An Experimental Investigation of Confined Cyclonic Flows and Ensuing Jet

by

Omer Khan

A dissertation submitted to the Graduate Faculty of
Auburn University
in partial fulfillment of the
requirements for the Degree of
Doctor of Philosophy

Auburn, Alabama
May 1, 2021

Keywords: Confined cyclonic flows, bidirectional vortex, liquid rocket, swirling jet

Approved by

Anwar Ahmed, Chair, Professor of Aerospace Engineering
Joseph Majdalani, Professor and Francis Chair
Jeyhoon M. Khodadadi, Professor of Mechanical Engineering
Roy J. Hartfield, Walt & Virginia Woltosz Professor

Abstract

Confined cyclonic flows are being explored for their application in propulsion due to several advantages rendered by confined vortices which include, increased fuel residence time, turbulence, and propellant mixing, resulting in improved combustion efficiency. A number of analytical models have been presented that attempt to establish the inner flowfield of the confined cyclonic flows. However, in the absence of experimental data, these models remain unvalidated. Therefore the research work in this dissertation is motivated by the need to experimentally characterize the fluid dynamics of the vortex flows in the cyclonic chamber. Additional research focused on the swirling jets emanating from the cyclonic chamber and the role of vorticity on the jet characteristics.

Particle image velocimetry measurements were taken for a modular hydro cyclone with tangential injection as an analog of the cold flowfield of cyclonic chambers. The analysis of the velocity profiles showed the bidirectional vortex behavior in the complete range of the operating conditions. The trend of variation in the characteristic parameters of the tangential velocity profile such as the core thickness, maximum tangential velocity, and wall boundary layer were found in agreement with the analytical solution. However, two additional flow features in the form of the high exit-bound velocity region of the head-induced flow and the reverse flow region were established. The vortex breakdown and resulting reverse flow region were eliminated by allowing passive flow entrainment or active injection from the axial head port. Proper orthogonal decomposition revealed the presence of coherent structures in the vicinity of the head injection port that suggests efficient mixing of the injected fluid. In addition to head port configuration, the exit contraction ratio was also found to significantly affect the flow. The influence of both the exit contraction ratio and injection area can be characterized together with the help of Swirl no, whereas the effect of the chamber aspect ratio can be adequately characterized with the vortex Reynolds number, V, and the off-swirl number, κ. Jet emanating from the cyclonic chamber was observed to be swirl-dominated, indicating a strong influence of the fluid rotation inside the chamber that resulted in reduced axial momentum and rapid decay. The configuration and operating condition of the axial head port greatly influenced the flowfield of the jet. Opening of the head port and subsequent injection reduced the axial adverse pressure gradient, thereby eliminating the reverse flow region along the chamber centerline. However, the unconstrained expansion of the swirling flow in the radial direction outside the chamber led to the bubble-type vortex breakdown of the jet. Further increase in the axial injection ratio, inhibited the breakdown and an axial jet was observed. The proper orthogonal decomposition showed a progressive increase in the mean modal energy with a higher fraction of axial injection.

Acknowledgments

I am thankful to Allah Almighty who has bestowed upon me, all the faculties that were required to undertake this dissertation. There is no doubt that the journey that culminates with this dissertation has been extremely challenging, yet very rewarding. I have been very fortunate to share it with many, some of whom just crossed the path, whereas others ran the whole stretch along with me. I am extremely grateful for them all and especially those mentioned below.

First and foremost I would like to express my sincere gratitude to my supervisor, Dr. Anwar Ahmed, whose keen insight, invaluable advice, and continuous support, have been foundational in my PhD. I shall be indebted for his mentorship that instilled in me the value of hard work and pursuit of excellence. I would like to thank Dr. Joseph Majdalani, for his extremely valuable discussions and suggestions that formed this dissertation in its present form. His command over the subject of cyclonic flows helped explain many of the experimental observations detailed in this dissertation. To the rest of my dissertation committee, Dr. Jay Khodadadi and Dr. Roy Hartfield, I would like to thank you for your input throughout my PhD and for the knowledge you have imparted through various classes and discussions. I would also like to thank Dr. Sabit Adanur for serving as the university reader for my dissertation.

I am thankful to Dr. Brian Thurow and the Advanced Flow Diagnostics Laboratory for lending me the PIV equipment, without which, the current research would not have been possible. I would also like to acknowledge the members of the Advanced Propulsion Research Laboratory, especially Langston Williams and Gaurav Sharma, with whom I had many lengthy discussions on the subject of confined cyclonic flows. The academic and social support provided by the current and past members of the Vortex Dynamics Laboratory was invaluable in the successful completion of this dissertation. I am grateful to the Auburn University, Aerospace Engineering Department for supporting my academic endeavors and providing me with the opportunity to teach undergraduate classes, which has certainly given me the much desired academic experience. I would also like to mention Mr. Andy Weldon and Mrs. Priscella Goodson, for their continued technical and administrative support.

I can never be thankful enough to my parents, Dr. Jamil Akther Ali Khan and Rubina Jamil, who have been a fountain of love and a mountain of support, against which I can always lean. Their sacrifices for my growth and continued encouragement have made me what I am today. I am forever indebed to them. I am grateful to my siblings Amna Khan and Ali Khan who have always supported me.

My wife, Saba Omer, I would not have been successful in this endeavor without your unwavering support and unconditional love. I am thankful to you for putting my graduate studies ahead of your own career aspirations. You have endured this journey with me every step of the way, and I am so fortunate to have it shared with you. I am looking forward to many more adventures ahead alongside you. I love my daughters, Ayisha and Emaan for the patience they have shown over the last few months of this dissertation writing, I love you and I will make it up to you!

Table of Contents

List of Figures

List of Tables

List of Symbols

A_i	injection area
a	chamber radius
b	mantle location, outlet radius for analytical solutions
C_p	Coefficient of pressure
D	chamber diameter
d_e	exit diameter
d_h	hub diameter
d_{inlet}	inlet diameter
d_p	diameter of PIV seeds
d_t	dimeter of inner tube
G_x	axial flux of axial momentum
G_θ	axial flux of tangential momentum
J	Bessel function
L	length of chamber
l	chamber aspect ratio, L/a
l_t	eddy viscosity ratio
P	static pressure
Q	PIV correlation peak ratio
Q_i	injection volume flow rate
Re	Reynolds number
Re_V, Re_Γ	classic vortex Reynolds number

r	radial coordinate
S	Swirl number
Stk	Stokes number
t_{fl}	characteristic fluid time
t_p	characteristic particle time
U	velocity
V	vortex Reynolds number

Greek

β	contraction ratio, $d_e/2a$
δ_c	core thickness
δ_d	uncertainty in the PIV measurement
δ_w	thickness of wall boundary layer
κ_∞	Ekman number
κ	off-swirl number
λ	individual POD mode energy
Ω	vorticity, $(\frac{dV}{dX} - \frac{dU}{dY})\frac{d}{U_{inj}}$
Γ	circulation
Φ	vane angle
σ	modified swirl number, $\frac{a^2}{A_i}$
ρ	density
μ	dynamic viscosity
ν	kinematic viscosity
ω_f	solid body angular velocity

List of abbreviations

BV	bidirectional vortex
CFD	computational fluid dynamics
CL	Complex-Lamellar
CRZ	central recirculation zone
LB	Linear Beltramian
NB	Non Linear Beltramian
OFAT	one factor at a time
PIV	particle image velocimetry
POD	proper orthogonal decomposition
PVC	precessing vortex core
RANS	Reynolds averaged Navier-Stokes equation
TKE	turbulent kinetic energy, $(u'^2 + v'^2)/\, 2U_{inj}^2$
VCCWC	Vortex Combustion Cold-Wall Chamber
VIHRE	Vortex Injection Hybrid Rocket Engine

Subscripts and Superscripts

eff	effective
inj	injection
L	laminar
max	maximum
r	radial coordinate
ref	reference

rev	reverse flow
T	turbulent
z	axial coordinate
θ	tangential coordinate

1. Introduction

Vortical flows in cyclone chambers have been studied since the late nineteenth century. However, for the most part, the focus has been on utilizing the centrifugal forces as the driving mechanism for the removal of heavy particles or moisture [1–4]. Recent research has focused on using the vorticity dominated flow for confined combustion and propulsion [5–7]. Research presented by Knuth et al. [8], Chiaverini [9], and Majdalani [10–15]on the swirl-driven combustion and vortex engines are some of the major milestones.

Liquid rockets remain the most popular category of rocket engines due to their higher specific impulse and operational flexibility among other advantages. To further increase the performance of liquid rockets engines, various techniques of oxidizer injection in the combustion chamber have been investigated, with varying degrees of success, as the benefits are sometimes accompanied by undesirable factors such as instabilities, increased complexity, and oxidizer jet dissipation. Overall, however, the application of vortex flowfields through the use of tangential oxidizer injection has proven to be advantageous compared to other techniques. For this reason, combustion chamber configurations that employ this method are starting to attract more attention from both the academic and industrial research communities.

The tangential injection arrangement results in a co-swirling, bipolar flow configuration inside the chamber. The cold oxidizer, because of its higher molecular weight, centrifuges out towards the wall. While the fuel (hydrogen), with lower molecular weight, is injected from the headwall and remains inside the core where it is combusted. Mixing and combustion are therefore confined within the central region of the cyclonic chamber with the walls being shielded from the high temperatures as the oxidizer wraps around and blankets the combustion region. Figure 1.1 shows a conceptual sketch of the confined cyclonic combustion chamber.

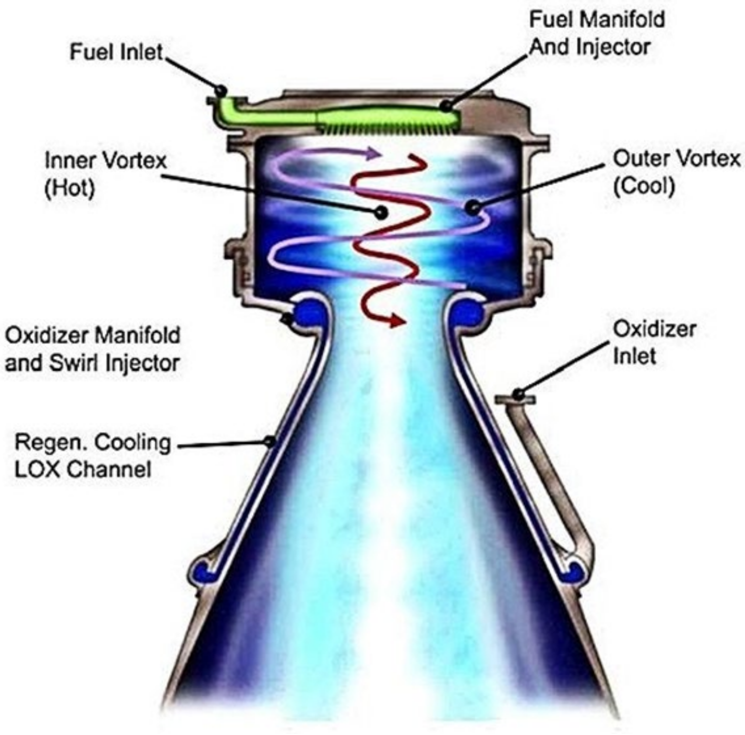

Figure 1.1 Schematic of a confined vortex engine [16].

The vorticity dominated flow inside the chamber increases fuel residence time, and in the presence of high turbulence levels, the propellant mixing is improved; these factors result in higher combustion efficiency. The spinning vortex core also provides an extended characteristic length much longer than the geometric length of the chamber, thus allowing for complete mixing to occur in shorter chambers. The increased flow path also results in increased residence time resulting in higher combustion efficiencies. Another important design feature of the cyclonic combustion chambers is the confinement of the combustion and associated heat release to the inner core; the latter remains shrouded by the outer vortex which consists primarily of cold oxidizer. This feature not only reduces the thermal loads and cooling requirements but also permits more flexibility in the material selection that can ensure durability and reduced weight [17][18].

The stability of the internal flow in cyclonic chambers is highly dependent on the coherence of the vortex core, which in turn is dependant on the conservation of the tangential momentum. A large number of analytical models for the “Bidirectional Vortex” have been advanced by Majdalani et al. [11,12,19–25] to characterize the internal flowfield of the confined cyclonic chamber, beginning from the bulk gaseous motion in an inviscid environment to the incorporation of viscous corrections, arbitrary wall injection, and compressibility. Although these analytical models remain an invaluable body of knowledge in the field of confined cyclonic flows, much work is needed to experimentally validate them. Few experimental efforts have been attempted to determine the feasibility of combustion within the confined vortex of the cyclonic chamber for propulsion. The experiments performed by Knuth et al. [26] and Ozawa et al. [27] on hybrid rocket motors focused on fuel regression rate as a measure of performance. Similar experiments conducted by Chiaverini et al. [9] on liquid vortex engines with oxygen, and hydrogen as propellants, used specific impulse as a measure of motor performance. These experiments established the feasibility of confined combustion within the central region of the cyclonic chamber but were unable to explain the flowfield in detail, which is essential to understand the flow kinematics and for subsequent improvements in design. Rom [28] and Wall [29] utilized particle image velocimetry (PIV) to determine the internal flowfield but only presented the velocity distribution in the transverse plane and in near-wall region, respectively. These efforts have been discussed in detail in Chapter 2. Additionally, the high tangential velocity that exists in the inner core of the chamber results in a swirl-dominated jet exiting the cyclonic chamber. As there is no mechanism in the nozzle to alter the tangential component, it becomes a major fraction of the net momentum of the emanating jet; under cold-flow conditions, it can results in the reduction of the axial momentum and therefore compromises the thrust production capability. This large tangential momentum component of the ensuing jet is unique to cyclonic chambers and stands in contrast with all other axial jets [30,31].

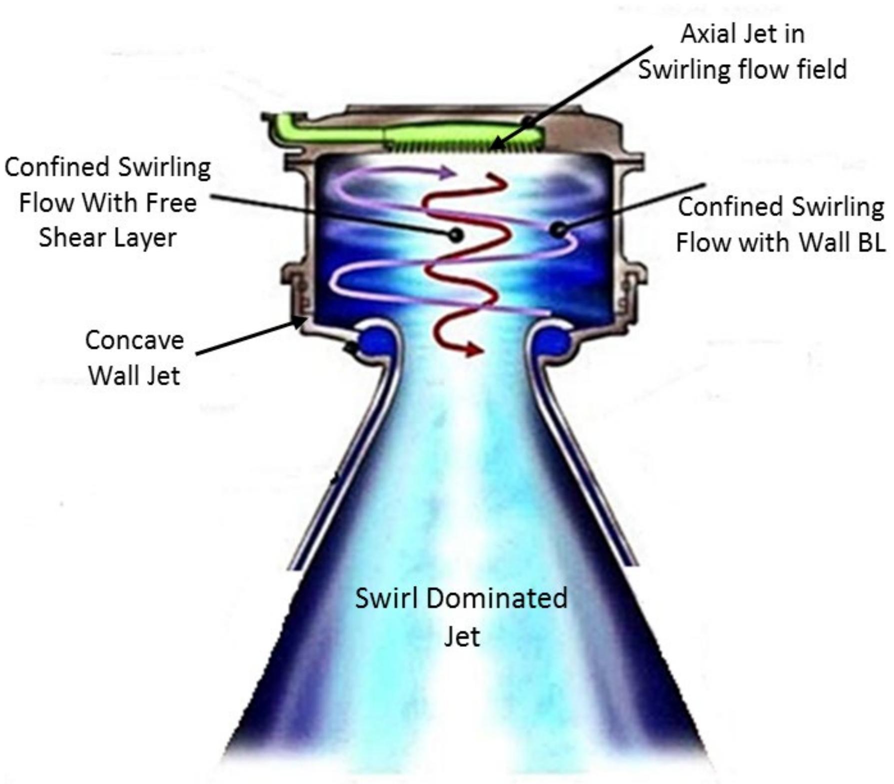

Figure 1.2. Fluid dynamics mechanisms in the confined cyclonic chamber.

The internal flowfield of the confined cyclonic chamber is a combination of various fluid dynamic mechanisms and their complex interactions as shown in Figure 1.2. This dissertation is motivated by the need to experimentally characterize the flowfield of confined cyclonic flows and emanating jets. The objective of the current work is to explain the fundamental fluid dynamics of the vortex flows in the cyclonic chamber and its dependence on the swirl number and vortex Reynolds number, which are highly dependent on the geometry of the chamber. Additional research work will focus on the swirling jet emanating from the cyclonic chamber and the role of vorticity on the jet characteristics.

To achieve these research objectives, particle image velocimetry (PIV) is used as the primary technique for obtaining quantitative data for a modular cyclonic chamber setup, whereas, flow visualization based on fluorescent dye is also conducted to obtain further insight. The remainder of the chapter serves as an overview of this dissertation.

Chapter 2 provides an extensive background and literature survey related to the research reported in this dissertation. In the beginning, the fundamental building blocks in the form of analytical models are presented, which are extended to the most recent bidirectional vortex models. Although the present study is experimental, the understanding of the foundational vortex models is necessary to explain the fluid dynamics of the vortex flows in the cyclonic chamber. This is followed by a review of major experimental efforts that have been undertaken to characterize the confined cyclonic chamber flowfield. The chapter concludes with a listing of relevant nondimensional parameters.

Chapter 3 details the experimental setup, choice of geometric and operating conditions, and the experimental approach. A significant portion of this chapter is then dedicated to the data processing, analysis, and correction methodology that must be implemented on the 2D-PIV data.

Chapter 4 presents the flow visualization and quantitative results for the baseline configuration. The fundamental flow dynamics that govern the formation of the cyclonic flowfield and its constituent components are then explained. The flowfield variation within the chamber and the effect of operating conditions in the form of the vortex Reynolds number are presented. The chapter concludes with a comparison of the experimental results with the analytical models.

Chapter 5 details the effect of cyclonic chamber geometry on the flowfield characteristics. It is then shown that the influence of various test parameters can be explained with the help of relevant nondimensional quantities.

Chapter 6 examines the effects of confined cyclonic motion on the emanating jet. The jet characteristics under various initial conditions are then detailed. The primary vortex breakdown mode for the swirling jet is identified. The effect of the shrouding tube on axial momentum recovery is then presented.

Chapter 7 summarizes the conclusions and contributions of this work, and provides recommendations for future work based on the present findings.

2. Literature Survey

Confined vortical flows are found in widespread applications and engineering devices such as cyclonic flow separators, dust collectors, swirl furnaces and vortex boilers, etc. Although a large number of devices rely on the characteristics of confined vortices there is relatively little information available concerning their fundamental fluid physics. From a design standpoint, attention is focused on the effectiveness of the devices rather than the underlying processes that allow them to operate. Confined vortical flows result in complex fluid motions that are affected by various fluid dynamic and geometric constraints; thus making it difficult to characterize the flow without an in-depth understanding of the physical mechanisms that affect their behaviour. Therefore, it is necessary to investigate these physical mechanisms in order to understand how confined vortices can be exploited to increase the effectiveness of cyclonic devices such as the vortex injection rocket engine.

In order to improve the performance of liquid rocket engines, investigations have been conducted to modify the flowfield within the combustion chambers, specifically, by the innovative injection of fuel and oxidizer combinations using different geometries. In this vein, the application of cyclonic flowfields through the use of tangential oxidizer injection has been shown to yield elevated efficiencies and enhanced performances. Salient features include increased fuel residence time, turbulence, and propellant mixing, thus improving overall combustion efficiency. The spinning vortex cores also provide an extended flow path much longer than the geometric length of the chamber, thus allowing for shorter chamber for complete mixing. This feature not only reduces cooling requirements but also permits more flexibility in material selection, thus promoting durability and reduced weight.

Although the use of confined swirling flows in propulsive devices is not a new concept, it was first introduced by Knuth et al. [26] in hybrid rocket applications such as the Vortex Injection Hybrid Rocket Engine (VIHRE) and the clean-burning Vortex Combustion Ramjet (VCRJ) [8][32]. It has since been utilized in various conceptual design and engines, including the Multiple Impinging Stream Vortex Injector by Michaels and Wilson [33]; the multi-mode Vortex Combustion Combined Cycle (VCCC) engine [34]; the In-Situ Resource Utilization (ISRU) hybrid propellant end burner suggested by Rice et al.[35]; and the Vortex Combustion Cold-Wall Chamber (VCCWC) developed by Chiaverini et al. [9].

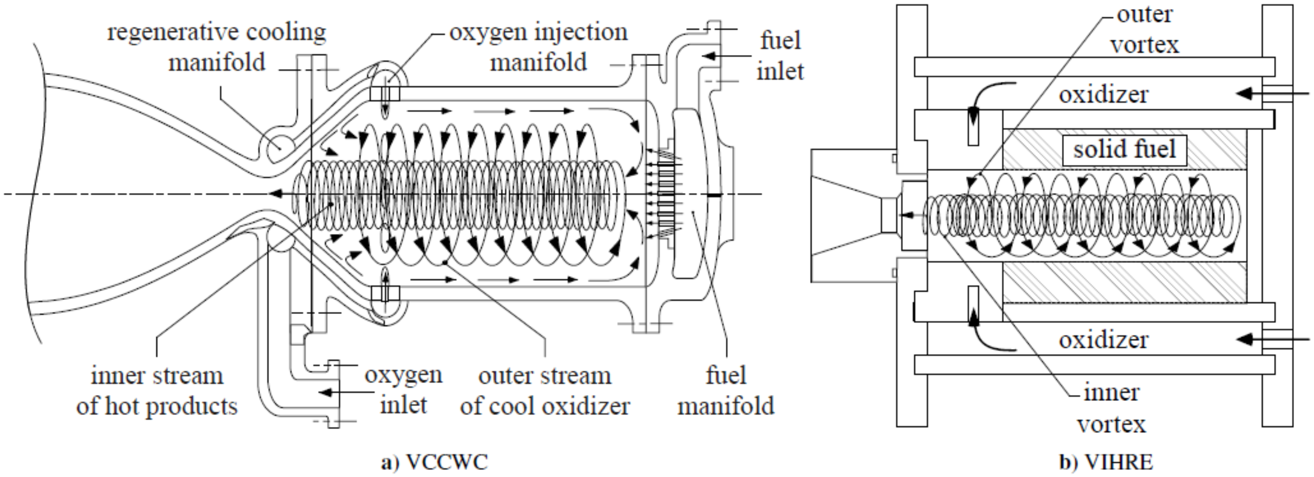

Figure 2.1 Schematics of (a) Vortex Combustion Cold-Wall Chamber (VCCWC), and (b) Vortex Injection Hybrid Rocket Engine (VIHRE). [10]

The common feature in most of these designs is the tangential injection of the oxidizer, which gives rise to a co-swirling, fully reversing, bipolar flow configuration in the combustion chamber. The corresponding flowfield structure comprises an outer, headwall-directed, annular vortex along with an inner, nozzle-directed, tubular vortex. These two coexisting cells remain separated by a rotating, axially non-translating fluid interface known as the mantle. The cold flowfield of such nature resembles closely that of a cyclone separator and has been explored both experimentally and analytically since the beginning of the 20th century. The first major contributions from the experimental investigations are presented by Shepherd and Lapple [36] in 1939, characterizing the flow patterns and pressure variations in cyclonic dust collectors. Thereafter, a continuously improving body of literature was formed with contributions from Ter Linden [1], Smith [37][38], Reydon and Gauvin [39], and Ogawa [40]; these researches utilized pressure probes and smoke flow visualization as experimental techniques. Later, Hoekstra [4] and Hu et. al. [41] exploited the advantages of non-intrusive techniques such as Laser-Doppler Velocimetry (LDV) to investigate the cyclonic flow features with minimum external interference. These studies helped to confirm the presence of a forced vortex near the axis of rotation, the prevalent axisymmetry and the axial invariance of the tangential velocity, the duality of mantle locations, the free vortex behavior in the farfield, and other relevant flow attributes. At this stage, the confined cyclonic flowfields were also investigated for their application in centrifugal burners for flame stabilization and to aid in the combustion of low caloric fuels in cyclonic chambers. The design of such devices is very similar to that of cyclone separators, with the only difference being the presence of a single outlet to exhaust the combusted hot gases instead of the two outlets that characterize the cyclone separators. In such applications, the experimental studies presented by Krepec [42] and Vatistas et al [43] formed the basis of the literature body. Later, the experimental studies by Knuth [44], Haag [45], and Anderson et al. [46] helped to characterize the advantages of confined cyclonic motion in hybrid rocket motors in terms of regression rate and specific impulse. These experiments established the feasibility of confined combustion within the central region of the cyclonic chamber but were unable to explain the flowfield in detail, which is essential for understanding the flow kinematics and for subsequent improvements in design. Moreover, experiments performed by Rom [28] [47] and Wall [29] utilized particle image velocimetry (PIV) to determine the velocity profiles in lab-scale cyclonic chamber for the purpose of characterizing the effects of compressibility and multiple mantles. However, their velocity distributions contained larger uncertainties, and Rom's velocity measurements were limited to the transverse plane only. In Rom's experimental study, the centrifugal forces on the seed particles presented a significant challenge in determining the vortex structure in the inner core region [48]. The out of plane velocity component was also suggested to be a limiting factor for 2-D PIV measurements.

The cold flowfield of such a bidirectional vortex chamber closely resembles that of a Ranque-Hilsch vortex tube as seen in Figure 2.2. The flow can be modeled as a Thomson-Rankine vortex, although it is commonly referred to as the Rankine combined vortex.

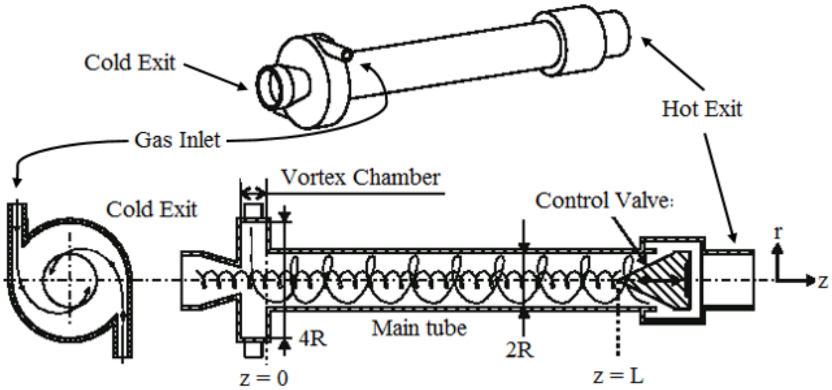

Figure 2.2 Ranque–Hilsch vortex tube [49].

Theoretical efforts have been made to model the confined cyclonic motion beginning from one dimensional, single-cell models such as the Thomson-Rankine vortex [40] and Oseen lamb vortex [50] to two-dimensional models including the Burgers-Rott Vortex [51], and the Two-Cell Sullivan [52] and Kuo vortex models [53]. In these endeavors, the Ogawa mixed model [40] for a cylindrical chamber and exact Bloor-Ingham Vortex [54] for conically-shaped chambers best represent the flowfield of the confined cyclonic motion but are only valid with significant simplifications and assumptions. Much more comprehensive and global solutions for cylindrical cyclonic chambers have been derived by Majdalani and coworkers [10–12,14,15,23]; their detailed review is presented in Sec 2.2.

In order to provide a comprehensive understanding to the reader of the subject matter, a brief overview of various analytical models and major experimental efforts undertaken to characterize the confined cyclonic flow in a cylindrical configuration are presented in subsequent sections. The literature presented in these sections will also seek to identify some of the shortcomings that the present research will try to address.

2.1 Analytical Models for Vortex Flows.

2.1.1 One-Cell Models

One of the most elementary, yet fundamental models that describe an unbounded vortex flow is the Thomas-Rankine Vortex. It is often referred to as a Rankine Combined Vortex [56] also, simply because it models the flow behavior as a piece-wise combination of two different profiles. It is pertinent to mention here that Rankine combined vortex is a one-dimensional model and thus it characterizes the tangential velocity (U_θ) only and does not account for velocity in the radial or axial directions. A representative tangential velocity profile for a Rankine combined vortex is presented in Figure 2.3. It is seen that it consists of a piecewise combination of a forced vortex core and of a free vortex tail, as it does not account for viscosity. A solid line that is representative of a physical vortex is also shown in Figure 2.3, for comparison, which shows the effects of viscosity. The Rankine models generally over-predict the peak tangential velocity, owing to its inviscid nature. The two different vortex profiles intersect each other at the maximum tangential velocity ($U_{\theta\,\max}$), the location of the maximum tangential velocity is referred to as core thickness (δ_c).

The inner region where the tangential velocity scales directly with the radius, r is called the forced vortex (Figure 2.3); it represents a solid body rotating at a constant angular velocity and generating axial vorticity. At the outer periphery of this solid body rotation region, the flow transitions to an irrotational free vortex tail, where the tangential velocity scales with $1/r$. As the flow in the free vortex tail remains irrotational, it exhibits a zero vorticity magnitude with constant circulation. As such, the vorticity remains confined to the forced vortex region. Despite being an elementary, one-dimensional model, the Rankine combined vortex model finds its utility in various applications, due to small relative magnitudes of radial and axial velocities to the tangential velocity. It will be later shown that this, in fact, is true for confined cyclonic motions as well.

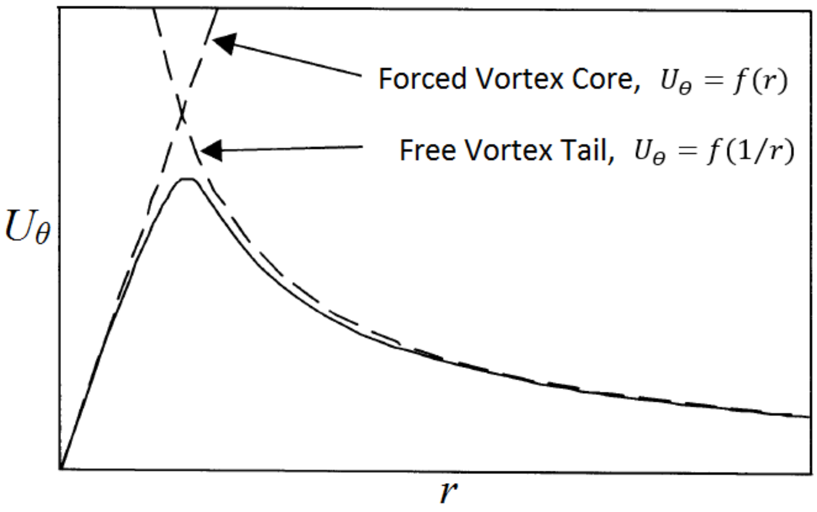

Figure 2.3 Constituent parts of the Rankine vortex [56]**.**

The extension of the Rankine combined vortex may be referred to as the Oseen-Lamb vortex model [50], which accounts for temporal effects that manifest themselves as the radial decay of the vortex under viscous shear. The Oseen-Lamb vortex is an exact solution of the incompressible, axisymmetric Navier-Stokes equations. The resultant velocity profile of the Oseen-Lamb vortex is shown in Figure 2.4, where it is compared with other similar flows. The radial decay under the effect of shear results in a relatively smooth transition between the forced vortex core and the free vortex tail; this also results in the outward shifting of the location of maximum tangential velocity.

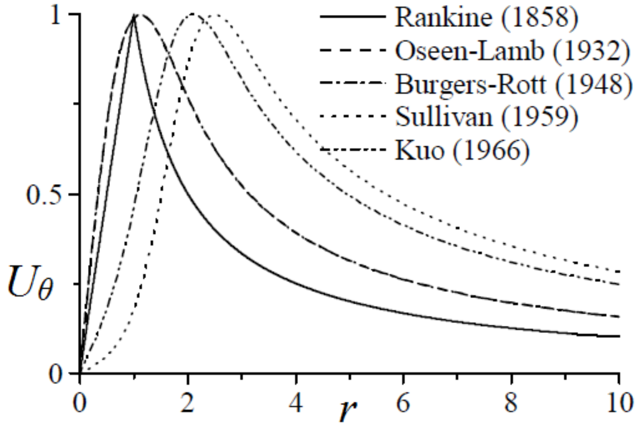

Figure 2.4 Radial distribution of tangential velocity for various models [10].

Since both models presented above remain one-dimensional, the natural extension to these is the Burgers-Rott vortex [51] which despite being a single-cell model, accounts for all three dimensions. In practice, the Burgers-Rott vortex has been of particular interest for modeling large-scale meteorological weather phenomena with naturally occurring helical motions. Another special feature of the Burgers-Rott vortex is the appearance of the kinematic eddy viscosity term that accounts for dissipation effects due to turbulence. Both the radial and axial velocities can be represented as a function of the ratio of viscosity and circulation, $\kappa_\infty \approx \nu/\Gamma$, which is a variant of the *Ekman number*. A large *Ekman number,* $\kappa_\infty \approx O(10^{-0})$ leads to higher off-swirl velocities which are dominated by the radial and axial components, whereas a small *Ekman number,* $\kappa_\infty \approx O(10^{-3})$ makes the flow tangentially dominated and therefore resembling the Oseen-Lamb vortex, as shown in Figure 2.5 [10].

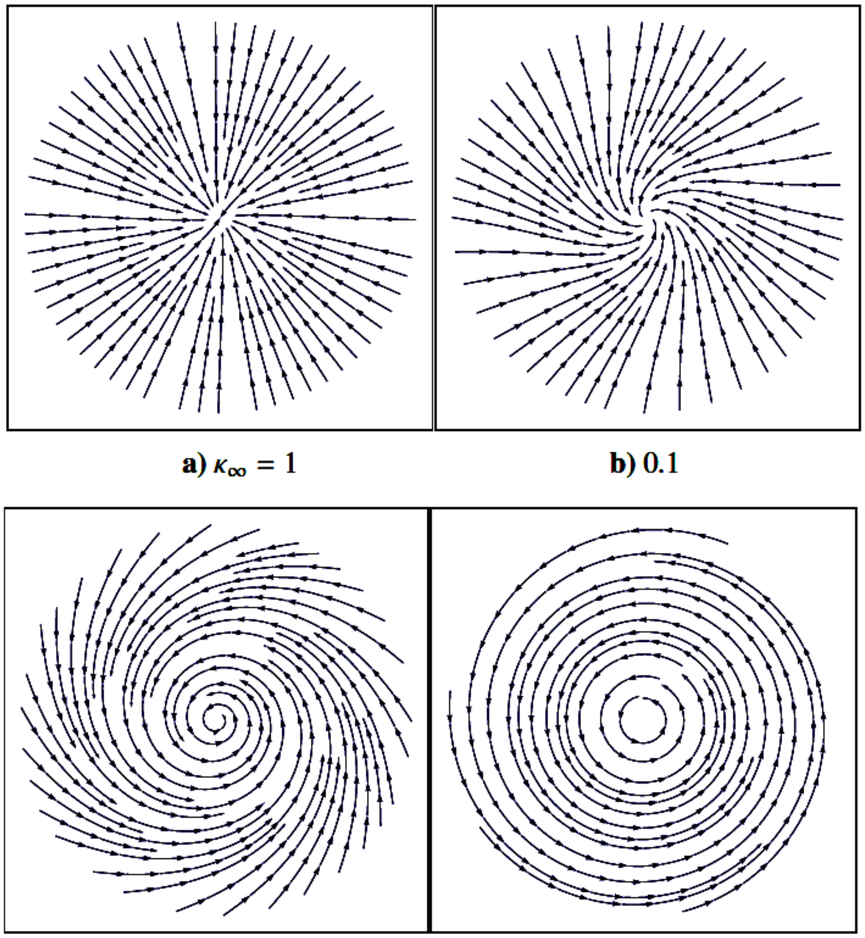

a) $\kappa_\infty = 1$ **b)** 0.1

c) 0.01 **d)** 0.001

Figure 2.5 Streamlines of the Burgers-Rott vortex at various off-swirl Ekman numbers K_∞ [10].

The models presented above are single-cell, which is evident by their unidirectional behavior. However, the desired confined cyclonic velocity profile in the cylindrical chamber is expected to be bidirectional, i.e. the axial velocity can assume both positive and negative values at different radial locations. The confined flow is typically head-bound in the outer free vortex region and exit-bound in the forced vortex region. Thus, in the subsequent section, a brief overview of two-cell models is presented.

2.1.2 Two-Cell Models

The Two-Cell Sullivan Vortex (1959)

Sullivan [52] presented an exact solution of the Navier-Stokes equations for a three-dimensional vortex flow with two cells, which enables it to model bidirectional behavior. It was found that the radial and tangential velocities are a function of the radial coordinate only, whereas the axial velocity varies with the product of the radial and axial positions. Its analytical solutions may be expressed as:

$$\begin{aligned} U_\theta(r) &= \frac{0.029890}{r} H\,(6.2381r^2) \\ U_r(r) &= 42.712\kappa_\infty\left\{-2.0794r + \frac{1}{r}\left[1 - \exp\left(-6.2381r^2\right)\right]\right\} \\ U_z(r,z) &= 177.63\,\kappa_\infty\, z\left[1 - 3\exp\left(-6.2381r^2\right)\right] \end{aligned} \tag{2.1}$$

The bidirectionality of the Sullivan model makes it a popular choice in the meteorological community, as it enables the modeling of the central reverse flow zone (CRZ) along the central axis; the latter can be representative of the central suction region in tornados and hurricanes [57]. The difference between the flow profiles of the Burgers-Rott and Sullivan vortices can be seen in Figure 2.6, which clearly shows the reverse flow along the central axis for the Sullivan vortex, thus demonstrating its two-cell nature. It also identifies the location where the axial velocity crosses the abscissa, thus separating the downward flow near the axis of rotation and the upward flow during its outward recovery; this location is referred to as mantle in the context of the bidirectional vortex engine by Majdalani [10].

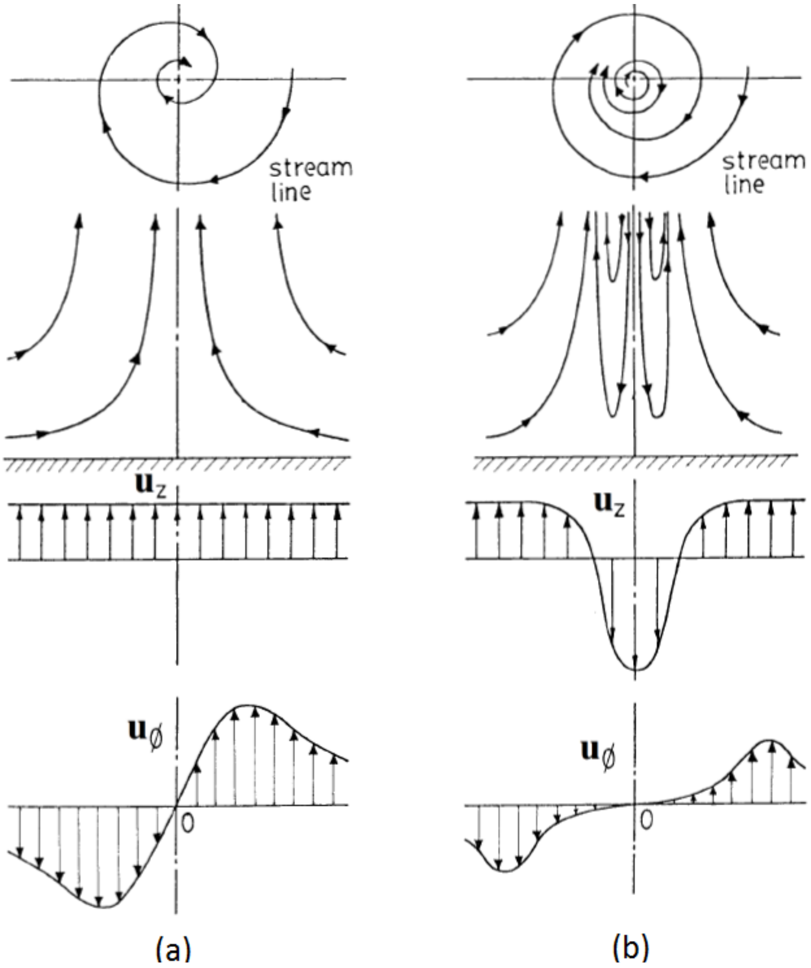

Figure 2.6 Flow characteristics of the (a) Burgers vortex (single-cell), and (b) Sullivan vortex (two-cell) vortex models [40]**.**

While comparing the tangential velocity profiles for various vortex models in Figure 2.7, it may be seen that the Sullivan vortex not only over-predicts the peak tangential velocity but also produces an outward shift in its location, to accommodate the CRZ. The over-prediction of the tangential velocity profile also shows less sensitivity of the Sullivan vortex to viscous effects as compared to the Burgers-Rott vortex.

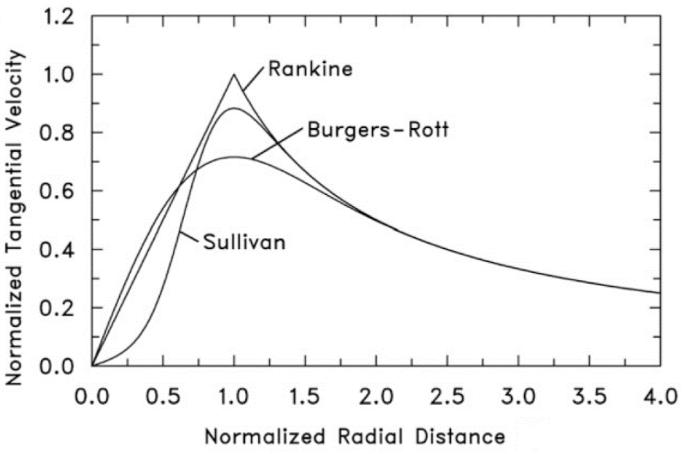

Figure 2.7 Normalized tangential velocity profiles for several vortex models [40]**.**

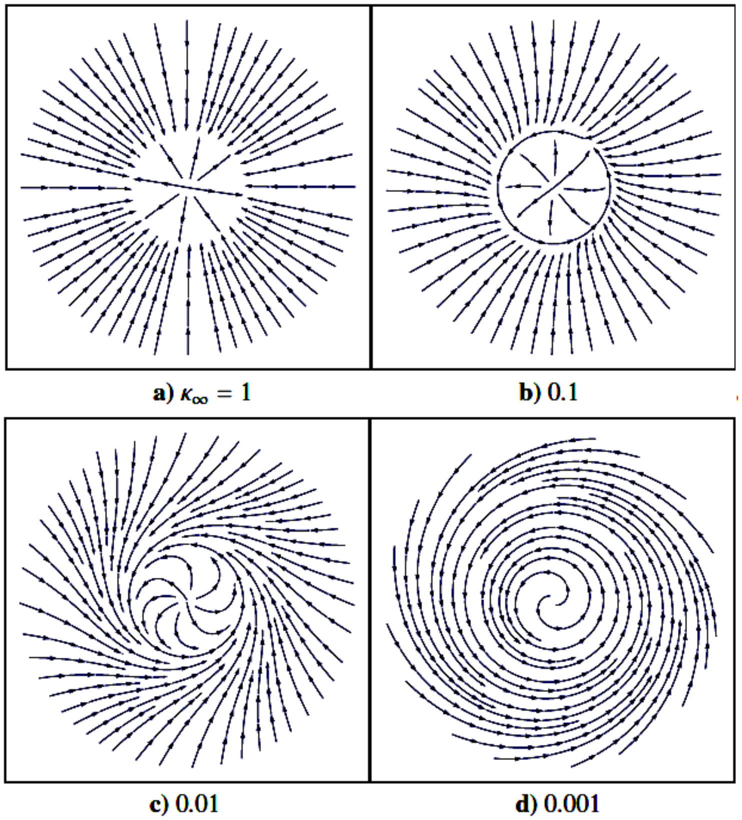
a) $\kappa_\infty = 1$ **b)** 0.1

c) 0.01 **d)** 0.001

Figure 2.8 Streamlines of the Sullivan vortex at various off-swirl Ekman number κ_∞ [10]**.**

The streamlines in the polar plane for the Sullivan vortex are shown in Figure 2.8, which show the effect of the Ekman number on the flow behavior. More importantly, the outward radial velocity in the central region is due to the reverse flow, which stands in contrast to the Burgers-Rott vortex streamlines presented in Figure 2.5. However, the effect of the Ekman number on the flow behavior remains unchanged. Although the above vortex models are unbounded, various devices have been engineered that use confined vortices. For example, the Bloor-Ingham vortex model [2] considers a bounded conical cyclone.

2.2 Bidirectional Vortex Models

Much more comprehensive and global solutions for cylindrical cyclonic chambers have been obtained by Majdalani and coworkers [10–12,14,15,23], for what is defined as the bidirectional vortex model, due to the bipolar nature of the vortex motion in the axial direction. In most studies, an integrated approach is used to combine the vorticity-stream function and the constant angular momentum assumption to produce exact solutions. In this context, Vyas and Majdalani [11] managed to obtain the first exact solution, named as the Complex-Lamellar model. Despite its inviscid, incompressible, and cold-flow nature, it formed the basis of an iterative increase in complexity to detail the step-by-step treatment of the coaxial bidirectional vortex flow in a cylindrical configuration. The over-prediction of velocity fields associated with the Complex-Lamellar solution was addressed by the introduction of a viscous boundary layer [19] or by the constant shear-stress model [12], with the latter giving rise to a piecewise solution for the swirl velocity. Majdalani also suggested utilizing a turbulent eddy-viscosity instead of the relatively smaller kinematic viscosity [12] especially at high-speed conditions to modify the vortex Reynolds number to a value that conforms to the experimental data. This approach will be utilized later to compare the results of the present experimental study with the analytical solution presented by Majdalani [10]. The incorporation of sidewall injection within the framework of these solutions led to their applicability to hybrid motor arrangements [58].

Majdalani proceeded to use a compact and less familiar Euler formulation known as the Bragg-Hawthorne equation [59], coupled with the Bloor and Ingham [54] angular momentum-stream function relation, to develop a series of solutions for cylindrically-confined cyclonic flows, known as the Beltramian vortex solutions. The Beltramian solutions resulted in exact expressions for the velocity, vorticity, pressure, and mantle location in a cylindrical cyclone. These solutions were adapted for arbitrary sidewall injection by Akiki and Majdalani [24][13], for compressibility effects and stability of cyclonic motions by Maicke and Majdalani [15][25][60] and, for the stability assessment, by Batterson and Majdalani [61][62]. The last set supported the notion that flow stability could be continuously enhanced with successive increases in the swirl velocity. The Complex-Lamellar and the Beltramian approach lead to qualitatively similar results but demonstrate differences in terms of peak axial and tangential velocities as well as the location of their mantles.

Before introducing and discussing the suite of results obtained by Majdalani [10], it is necessary to present the geometric configuration, presented in Figure 2.9, that is associated with this family of solutions. The model consists of a right-circular cylinder of radius a, and total length L, that leads to the aspect ratio of $l = L/a$. A cylindrical coordinate system is fixed at the head of the chamber with the positive z-axis running along the centerline and directed outward, the radial coordinate r pointing perpendicularly away from form the z-axis, and an azimuthal coordinate θ, representing the angular rotation about the z-axis. The chamber is equipped with an outlet of radius b at the opposing wall. The ratio of the outlet radius to the chamber radius is denoted by $\beta = b/a$, and is called the outflow fraction. The fluid is injected with an average tangential velocity U_i, from the opening at the base of the chamber with an injection area A_i, which results in an average volume flow rate of $Q_i = U_i A_i$.

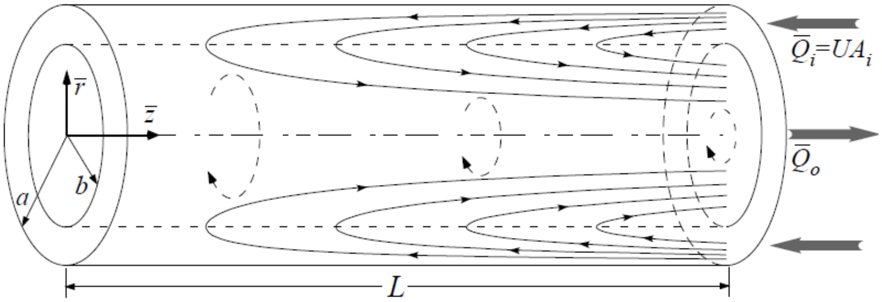

Figure 2.9 Geometry and reference frame for the bidirectional vortex chamber, [10]**.**

A comprehensive table of expressions for the stream function and the corresponding velocity components based on various solution approaches by Majdalani [10] are summarized in Table 2.1. The resulting velocity profiles are presented in Figure 2.10.

Table.2.1 Characteristic equations of various bidirectional vortex models of right-cylindrical cyclones, [10]**.**

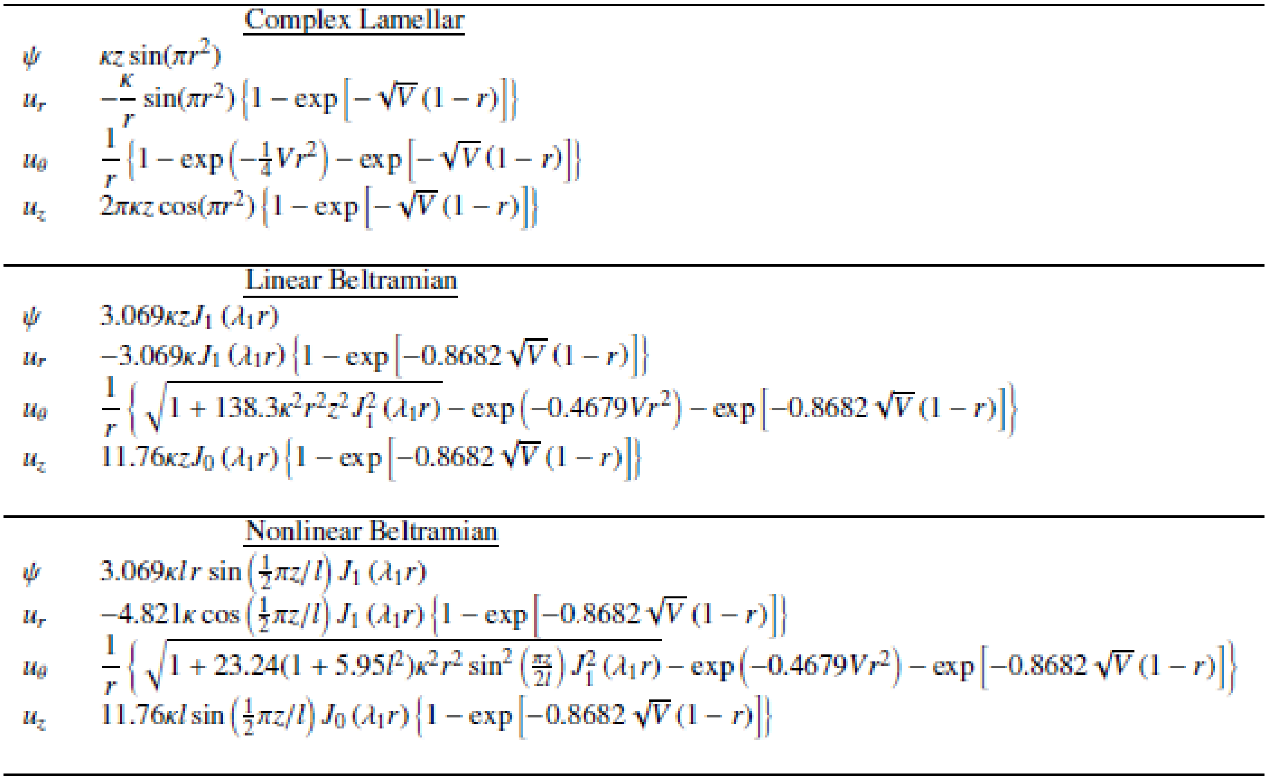

	Complex Lamellar
ψ	$\kappa z \sin(\pi r^2)$
u_r	$-\frac{\kappa}{r}\sin(\pi r^2)\left\{1-\exp\left[-\sqrt{V}(1-r)\right]\right\}$
u_θ	$\frac{1}{r}\left\{1-\exp\left(-\frac{1}{4}Vr^2\right)-\exp\left[-\sqrt{V}(1-r)\right]\right\}$
u_z	$2\pi\kappa z\cos(\pi r^2)\left\{1-\exp\left[-\sqrt{V}(1-r)\right]\right\}$
	Linear Beltramian
ψ	$3.069\kappa z J_1(\lambda_1 r)$
u_r	$-3.069\kappa J_1(\lambda_1 r)\left\{1-\exp\left[-0.8682\sqrt{V}(1-r)\right]\right\}$
u_θ	$\frac{1}{r}\left\{\sqrt{1+138.3\kappa^2 r^2 z^2 J_1^2(\lambda_1 r)}-\exp\left(-0.4679Vr^2\right)-\exp\left[-0.8682\sqrt{V}(1-r)\right]\right\}$
u_z	$11.76\kappa z J_0(\lambda_1 r)\left\{1-\exp\left[-0.8682\sqrt{V}(1-r)\right]\right\}$
	Nonlinear Beltramian
ψ	$3.069\kappa l r\sin\left(\frac{1}{2}\pi z/l\right)J_1(\lambda_1 r)$
u_r	$-4.821\kappa\cos\left(\frac{1}{2}\pi z/l\right)J_1(\lambda_1 r)\left\{1-\exp\left[-0.8682\sqrt{V}(1-r)\right]\right\}$
u_θ	$\frac{1}{r}\left\{\sqrt{1+23.24(1+5.95l^2)\kappa^2 r^2\sin^2\left(\frac{\pi z}{2l}\right)J_1^2(\lambda_1 r)}-\exp\left(-0.4679Vr^2\right)-\exp\left[-0.8682\sqrt{V}(1-r)\right]\right\}$
u_z	$11.76\kappa l\sin\left(\frac{1}{2}\pi z/l\right)J_0(\lambda_1 r)\left\{1-\exp\left[-0.8682\sqrt{V}(1-r)\right]\right\}$

here, κ is the off-swirl parameter that prescribes the order of the off-swirl velocities, z and r are the normalized axial and radial coordinates, V is the vortex Reynolds number that presents a combined effect of the tangential injection Reynolds number and chamber geometry, l is the aspect ratio of the chamber, and J is the Bessel function. A detailed description of κ and V is presented later.

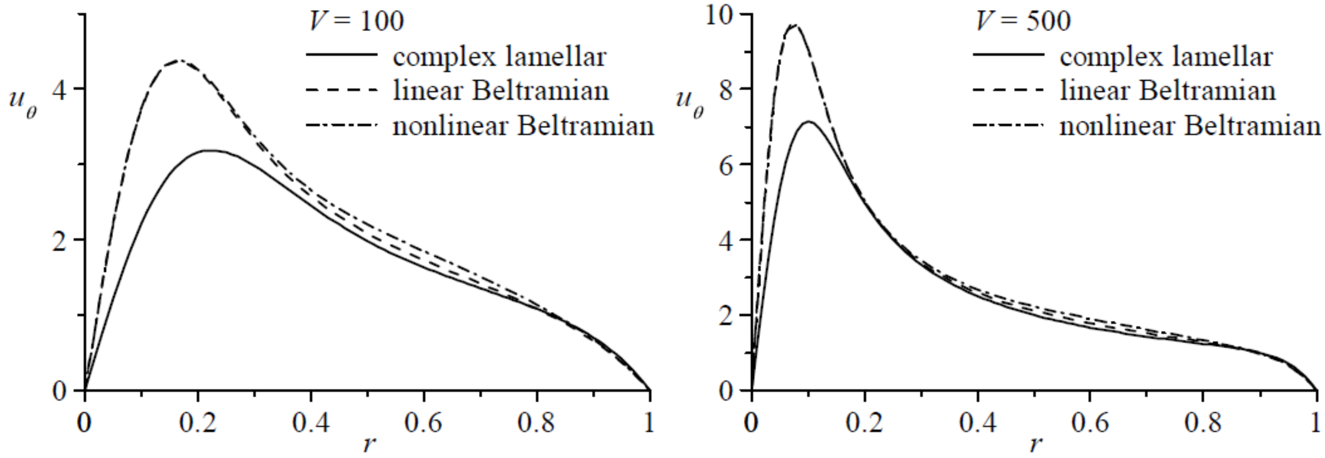

Figure 2.10 Tangential velocity profiles for Complex-Lamellar, linear, and nonlinear Beltramian models with κ = 0.1, z/L = 0.5, and V = {100, 500} [10]**.**

The tangential velocity profile for various models is presented in Figure 2.10. As with the analytical solutions of the unbound vortex models presented earlier, the existence of the forced vortex core and the free vortex tail is clearly evident. The only difference is presented by the fact that the bounded solution of Majdalani results in a sudden end to the free vortex tail at r = 1, whereas the same continues to infinity for the unbounded flows. The difference in the formulation of the models is also evident from the tangential velocity profile, where the Complex-Lamellar under-predicts the peak tangential velocity. An increase in the vortex Reynolds number by increasing tangential inlet velocity results in a more stable and intense coherent structure with higher $U_{\theta\,\max}$. The subsequent vortex stretching and conservation of angular momentum causes a reduced vortex core radius (δ_c) as seen from Figure 2.10 ($V = 500$).

The increase in vortex Reynolds number also dampens the viscous effects and results in thinner viscous boundary layers, both in the inner core (δ_i) and the wall region (δ_w). In a limiting case, an excessively large V will result in an inviscid solution. The variation of the maximum tangential velocity, core thickness, and wall boundary layer is presented by Majdalani [10] and is reproduced below, which is in agreement with the discussion above.

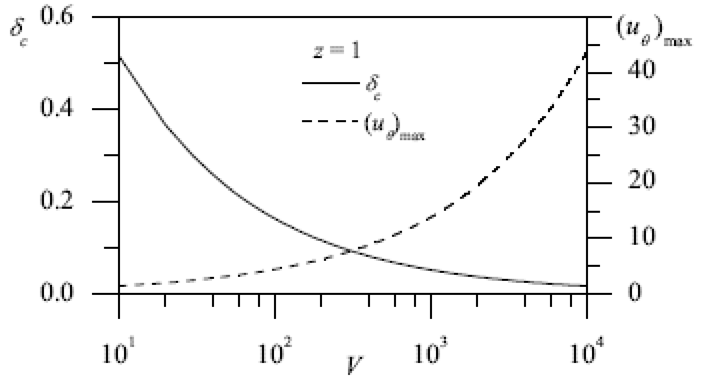

Figure 2.11 Variation of the tangential velocity viscous characteristics with increasing V [22].

According to Majdalani's theory, one obtains the following relations for the maximum tangential velocity ($U_{\theta\,\max}$), the core thickness (δ_c), and the forced vortex angular speed (ω_f) as a function of V [10].

$$U_{\theta\,\max} \approx 0.4365\sqrt{V}$$
$$\delta_c \approx 1.639/\sqrt{V}$$
$$\omega_f \approx 0.468\,V \tag{2.2}$$

These relations will be invoked later to compare the anlyitcal solutions with the present experimental study while accounting for the eddy-viscosity approach.

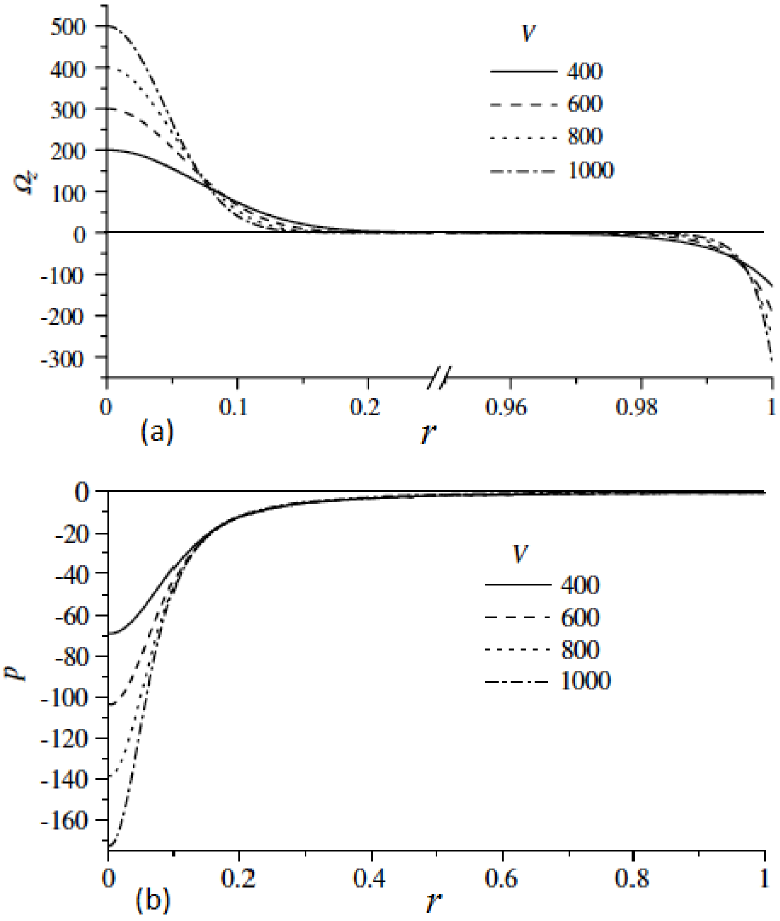

Figure 2.12 Variation of the (a) axial vorticity, and (b) pressure with increasing *V* [20]**.**

The distinction between the forced vortex core and free vortex tail can also be made with the radial distribution of the vorticity. By definition, a forced vortex is rotational and concentrates vorticity in its core as seen from the higher magnitudes of vorticity in Figure 2.12 (a) [20], in contrast, the free vortex tail is irrotational. The increase in vorticity magnitude in the close proximity of the sidewall at $r = 1$ depicts the Gortler type vortices that are characteristic of flow over a concave bounded wall [63]. As the vortex Reynolds number increases so does the magnitude of the axial vorticity.

Due to the peak tangential velocity concentrated at the outer periphery of the forced vortex, a significant radial pressure gradient is observed in the chamber. The variation of this pressure gradient has been shown to be axially invariant. Thus, a low-pressure region exists in the core of the chamber. This reduced pressure magnitude further drops with an increase in the vortex Re and also its locations shift inwards as the size of the forced vortex decreases with increasing V.

The radial velocity distribution is presented in Figure 2.13. The most significant feature of the radial velocity profile is a strictly negative sign, which also demonstrates the inward motion of the tangentially injected fluid. The radial velocity distribution has been shown to be independent of the axial distance. Another important feature of the radial velocity profile is that it also characterizes the oxidizer "spillage". Spillage or crossflow is defined as the oxidizer crossing the mantle from the outer vortex to the inner vortex away from the headwall. The spilled oxidizer will not be a part of the combustion process and will cause the thinning of the oxidizer blanket that protects the chamber outer walls from thermal effects. The invariance of the radial velocity with regard to the axial location suggests that significant spillage will be observed.

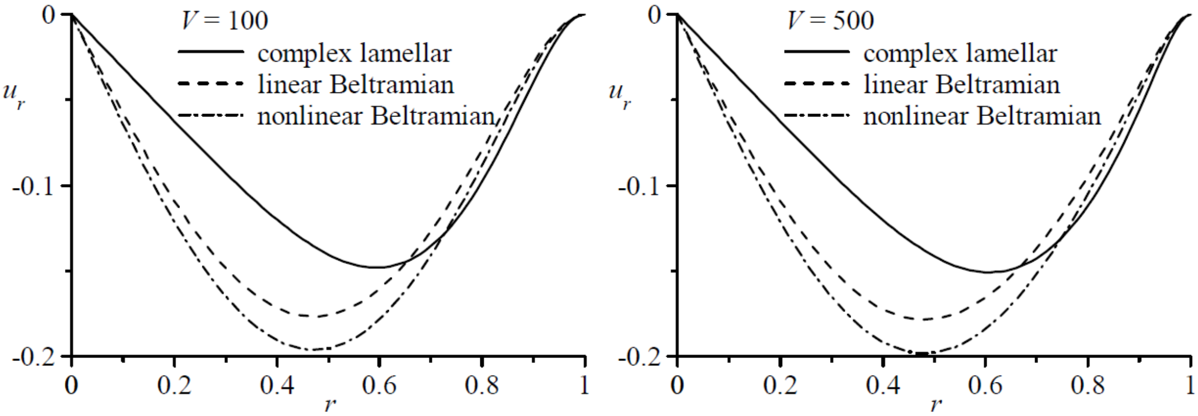

Figure 2.13 Normalized radial velocity profiles for Complex-Lamellar, linear, and nonlinear Beltramian models with $\kappa = 0.1$, $z/L = 0.5$, and $V = \{100, 500\}$ [10]**.**

This axial invariance stems from the dominant tangential component of the resultant velocity profile. The tangential and radial velocity components are affected by the axial coordinate to some degree but their axial sensitivity does not significantly influence the resultant velocity profile, which is reasonably valid, although physical flows do exhibit a small amount of axial invariance. This is most notable at the headwall of the chamber where the presence of a solid boundary causes increased radial flow and the structure of the vortex is not representative of that seen in the bulk of the fluid.

It has been shown by the above discussion that the tangential velocity remains invariant with the axial distance from the headwall. The radial velocity, despite the expectation to have axial dependence, especially in the near vicinity of the headwall, largely remains constant throughout. This is further masked by its much smaller magnitude as compared to the tangential velocity. However, the axial velocity is dependent on the axial distance from the headwall, as shown in Figure 2.14 [10], where the normalized radial distribution of the axial velocity is plotted for the Complex-Lamellar and Beltramian families of solutions at six evenly distributed axial locations and two vortex Reynolds numbers. A few observations that can be inferred from Figure 2.14 pertain to the axial velocity variation, as a function of axial distance, vortex Reynolds number, and model dependence.

The magnitudes of the axial velocity increase as the flow convects from the headwall towards the exit nozzle. The updraft in the proximity of the chamber walls and downdraft along the centerline confirm the bidirectionality of the flow for all of the models presented by Majdalani [10]; the location where the axial velocity changes its orientation and thus crosses the abscissa is known as the mantle. From Figure 2.14, it can be seen that the mantle location for the Complex-Lamellar model is at $r = 0.707$. For the Beltramian solutions, it is shifted towards the central axis and is located at $r = 0.628$. It is not coincidental that the classical experiments performed by J.L Smith [37] on the cyclone separator configuration also found these two values. However, the two cases presented by Smith vary in the geometric configurations, where the height of the inlet was the variable. The two families of solutions not only differ in the location of the mantle but also in the normalized magnitudes of the axial velocity, where the Beltramian solutions exhibit higher axial speeds. However, the effect of the vortex Reynolds number on both models is similar, where the increase in the V results in the diminishing of the wall boundary layer.

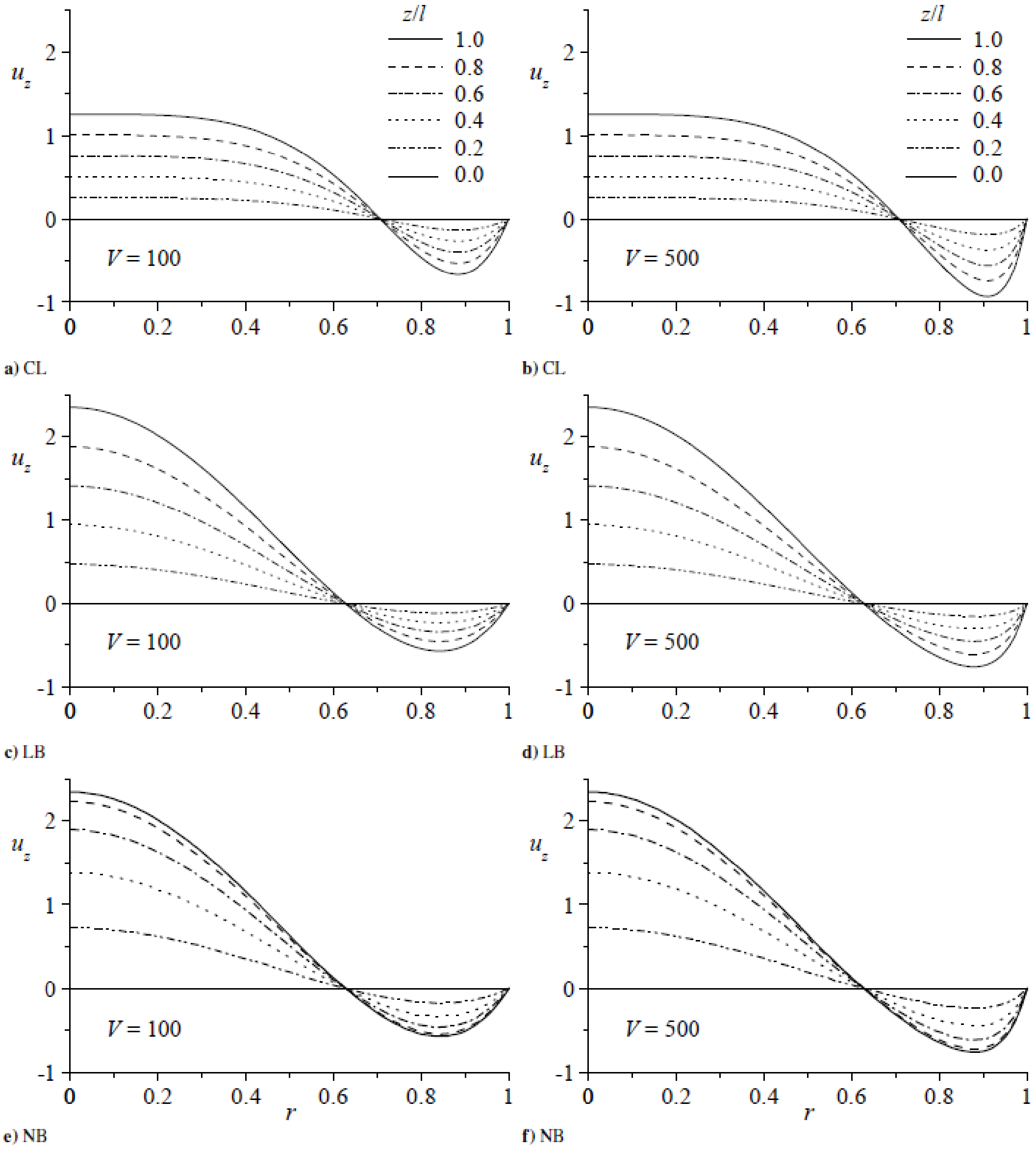

a) CL b) CL c) LB d) LB e) NB f) NB

Figure 2.14 Normalized axial velocity profiles for (a,b) Complex-Lamellar, (c,d) linear, and (e,f) nonlinear Beltramian models with $\kappa = 0.1$, and $V = \{100, 500\}$ [10]**.**

2.3 Experimental Studies of Confined Vortex Flows

As previously stated, experimental methods have been employed to understand the flow kinematics in the confined cyclones. Most of the earlier studies [1,4,36] have however focused on cyclone separators, which resemble the understudy configuration but have a noteworthy difference in the form of a spigot (exit at the headwall for removing heavier particles). Moreover, the inherent design of the cyclone separator is conical, which will skew the velocity profiles towards the centerline, thus making it difficult to compare them with a right-circular configuration, typically employed for confined combustion. More recently experimental studies have been carried out on the right-circular cylinder configuration with multiple tangential inlets, to dedicatedly determine the flowfield of the confined bidirectional vortex. In this section, a brief overview of these experiments is presented.

2.3.1 J. L. Smith

Smith [37] constructed a cylindrical cyclone chamber with a headwall equipped with a port to inject smoke for flow visualization. The tangential inlet velocity was achieved by drawing ambient air through eight guide vanes; the inlet height was set at two different values to explore the effect of inlet size. Measurements were made with slender pressure probes for magnitude and cobra probes for direction. The results presented for the two cases have an inlet area difference by a factor of 4. The resultant axial velocity plots at seven different axial locations for the two cases are presented in Figure 2.15 below.

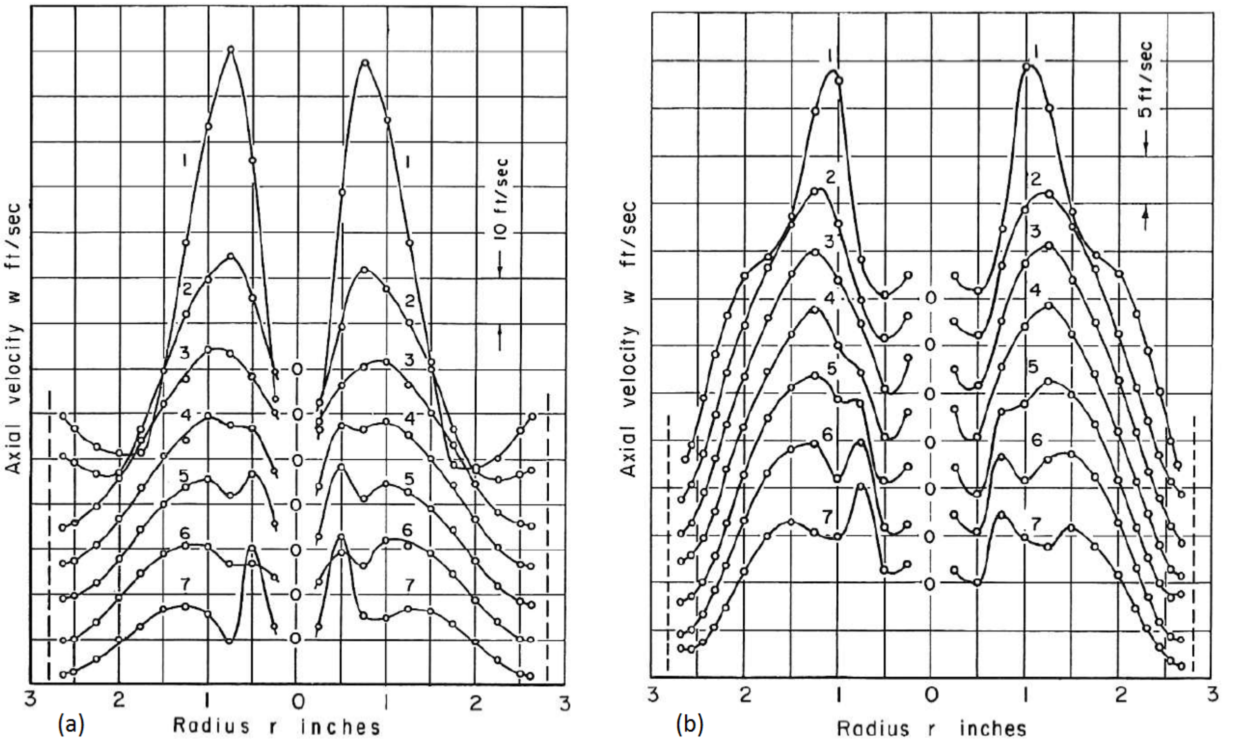

Figure 2.15 Radial distribution of axial velocity at seven different *z/L* locations, for inlet height of (a) 2 in, and (b) 0.5 in, according to Smith [37]**.**

The axial velocity plot clearly shows the bidirectionality in the chamber, but more interestingly it shows a drop in the axial velocity in the close proximity of the centerline. At few axial locations, the axial velocity assumes a negative value as well, which is a characteristic sign of the presence of the central recirculation zone (CRZ). The formation of CRZ has been reported in various other studies on such configurations but stands in contrast with the analytical models presented earlier with the exception of the Sullivan vortex. The plot of streamlines presented in Figure 2.16, shows a central hollow core or a CRZ. One can also infer the mantle location from Figure 2.16, by identifying the location where the axial velocity changes its direction. The shape of the mantle for the configuration with a smaller inlet height shows a conical shape with an average value of $\approx 0.63r$, whereas the larger height inlet shows a straight mantle with a fixed value of $\approx 0.7r$. These values are very similar to the ones arrived at by Majdalani [10], although they are obtained for two separate inlet conditions. Also, since, only two inlet heights were investigated, it is difficult to discern a correlation for the mantle as a function of the inlet height. But the inlet height/area can thus be identified as a design variable.

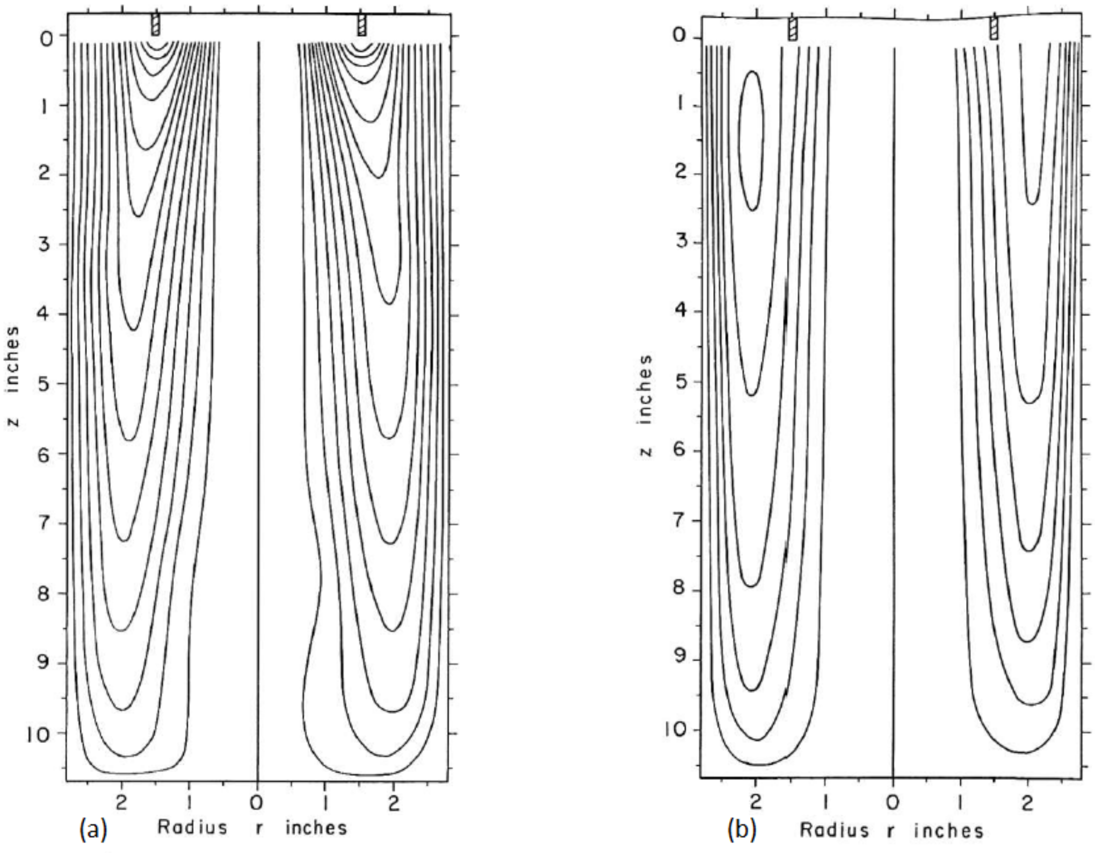

Figure 2.16 Streamlines projected on the *r-z* plane for inlet height of (a) 2 in, and (b) 0.5 in, according to Smith [37].

2.3.2 Akira Ogawa

Fujita and Ogawa [40] presented the Ogawa combined vortex model with particular consideration to the bounded cyclonic flows that model the physical characteristics of the tangential, radial, and axial velocity components and also the distributions of the static pressure and vorticity. Ogawa followed it with a set of experimental studies to determine these characteristics for the bidirectional configuration and the unidirectional configuration (Ogawa called them return flow type and axial type, respectively). The return flow type configuration and its resultant velocity distributions measured by a cylindrical pitot tube at *z/L* of 0.71 are given in Figure 2.17.

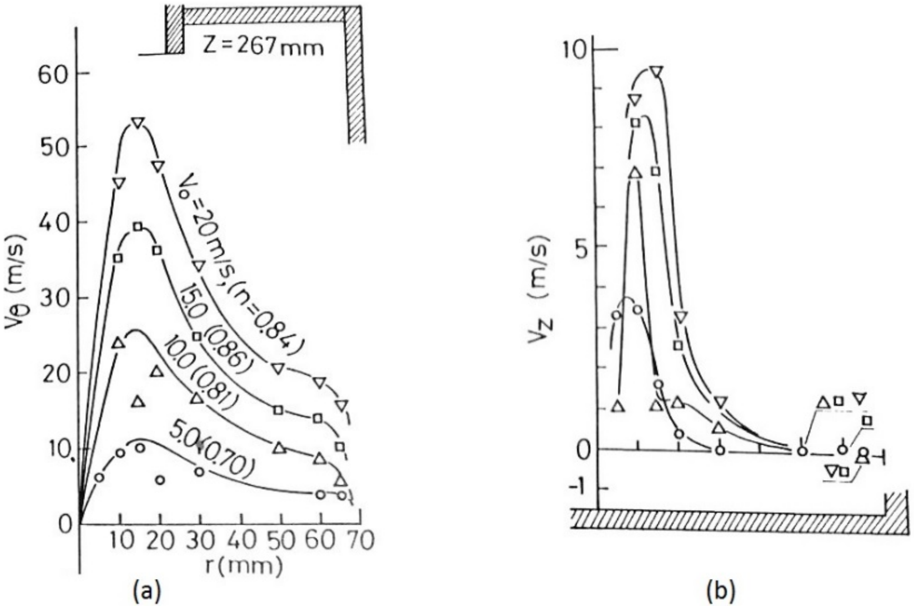

Figure 2.17 (a) Radial distribution of tangential, and (b) axial velocity as a function of inlet velocity, according to Ogawa [40].

The results of the tangential velocity fall exactly in line with the Beltramian family of solutions presented by Majdalani [10], discussed in Sec 2.2. The formation of forced vortex core and free vortex tail, as well as the thickness of the core, identified by the maximum tangential velocity, can be seen in Figure 2.17. The only observation that on a cursory look, does not agree with the Beltramian solution is the magnitude of the peak tangential velocity; here it is found to be 2.5 times the inlet velocity, whereas the Beltramina solution predicts it to be around 5 to 7 times the inlet velocity. The concept of eddy-viscosity can be invoked to address this dichotomy as explained by Maicke and Majdalani [12]. However, the axial velocity distribution which is similar to the one reported by Smith [37] in Sec 2.3.1 is different from the one predicted by Majdalani [10]. Specifically, the peak axial velocity is offset from the centerline and drops sharply as it approaches the centerline. It is hypothesized that this is due to the presence of the central recirculation zone which often evolves in a cyclonic flowfield. The presence of a pitot tube, which is used to measure the velocity along the centerline can also impact the distribution. In subsequent studies, Craig Rom [28] and Wall [29] utilize particle image velocimetry (PIV), which is a non-intrusive technique to investigate the bidirectional vortex behavior without the presence of any external object.

2.3.3 Craig Rom

In order to take the advantage of non-intrusive techniques such as PIV, Rom et al. [47] perform a number of experiments on the right-cylindrical cyclonic chamber equipped with eight tangential injectors and a nozzle to determine the velocity components of the cyclonic flowfield using Nitrogen gas as the operating fluid. Smoke particles with an average diameter of 0.2 μm are used to seed the flow. However, the high tangential velocities of the vortex chamber impart a radial acceleration under the effect of centrifugal forces on the particle; this effect, coupled with the out-of-plane axial velocity, compromise the ability to ensure sufficient seeding concentrations in the central core. The raw PIV images provided by Rom in [47] and the resultant velocity contour are presented in Figure 2.18 to demonstrate the seeding problem in the core region.

The scarcity of seeding particles in the core region is evident in the processed velocity vectors presented in Figure 2.18 (b), which shows a void region in the core. As a result, these researchers are unable to capture the forced vortex core, present in the confined cyclonic motion, as seen from Figure 2.19. Thus, they could not characterize the important features of the flow such as the maximum tangential velocity $U_{\theta\,\max}$ and thickness of the core, δ_c. The very high out-of-plane velocities in the form of tangential velocity on the *r-z* plane also restricted the use of 2-D planer PIV, and thus no results for the axial and radial velocities were presented.

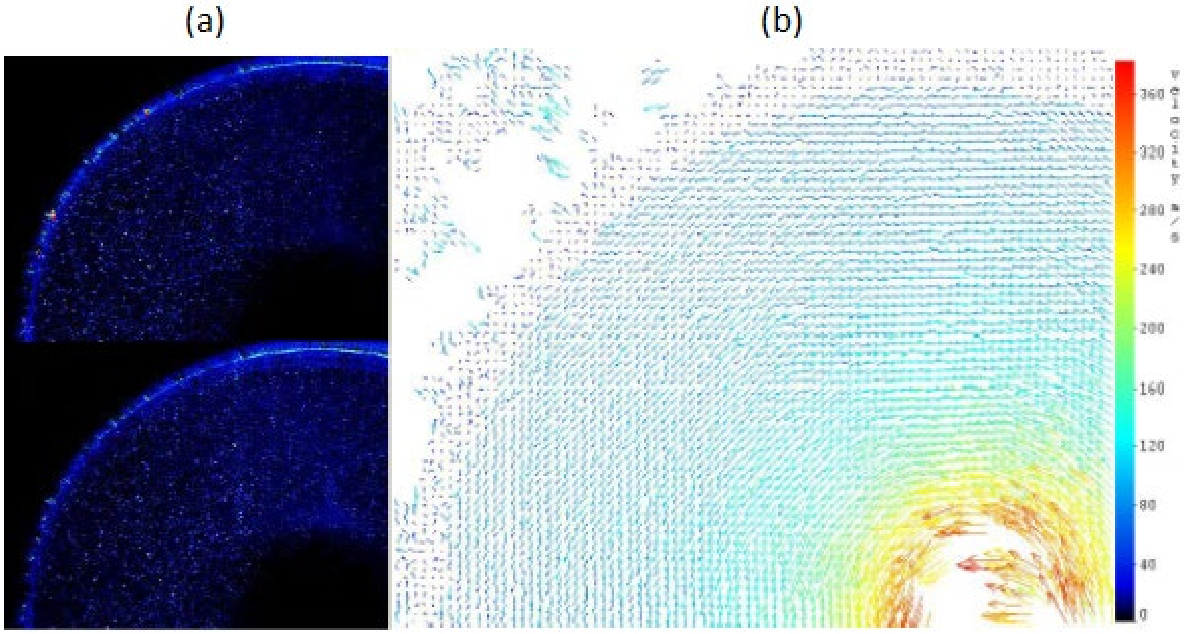

Figure 2.18 (a) Raw PIV image pair, and (b) processed velocity vector field according to Rom [47]**.**

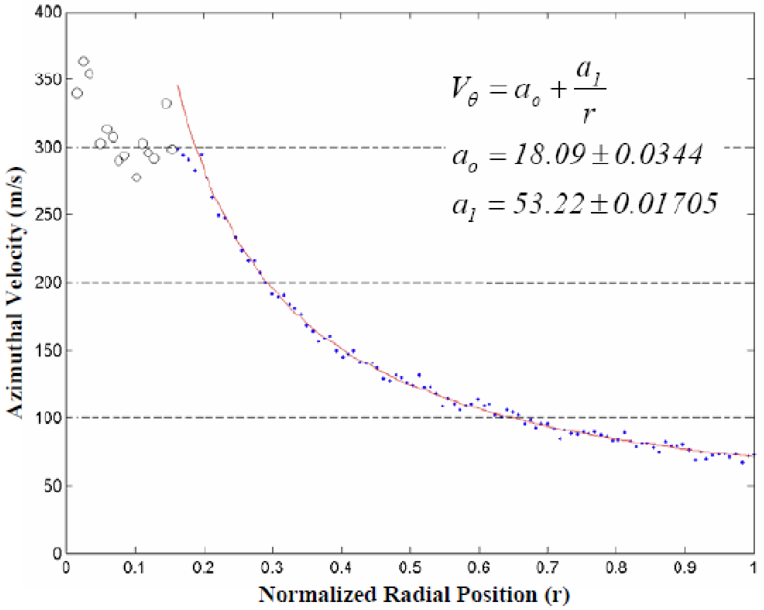

Figure 2.19 Radial distribution of tangential velocity according to Rom [28]**.**

2.3.4 Neil Wall

Recognizing the challenges faced by Rom and additionally, the limitations of the out-of-plane velocity component with the 2-D PIV measurements reported by Maicke [64], Wall [29] used a hydro cyclone instead as an analog. The simple substitution of the operating fluid from gas to water not only alleviates the problems faced by Rom [28] but also enables the use of much lower flow velocities while maintaining the same non-dimensional parameters such as *Re* and *V*. It also allows for a much simpler design of the fluid supply system and affords the flexibility of choosing a denser, lighter scattering seed particle. However, using water as the working fluid and the presence of intense vortical flow resulted in a hollow air core along the chamber centerline due to vortex breakdown and cavitation as shown in Figure 2.20.

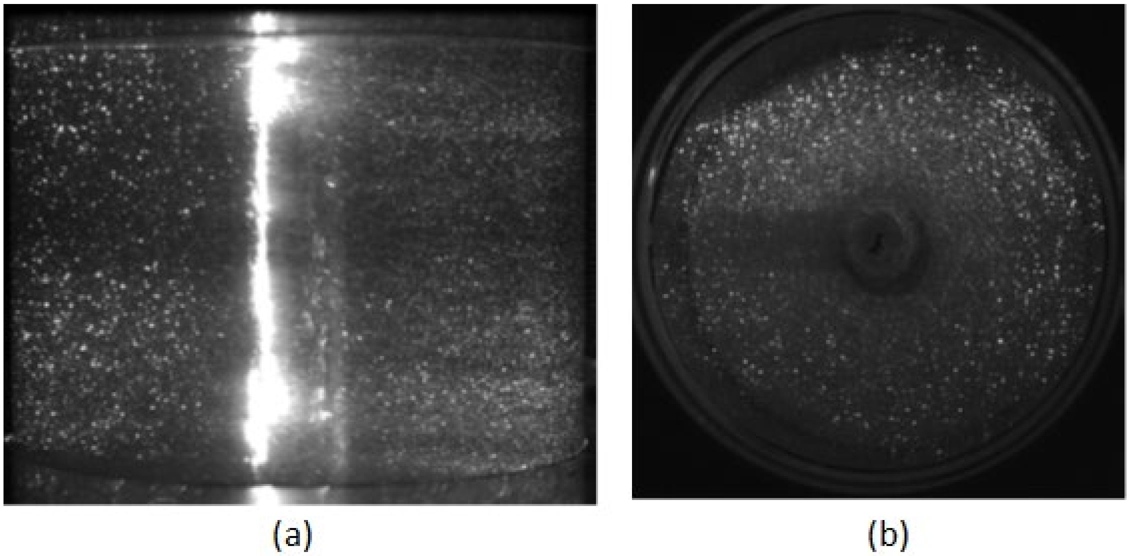

Figure 2.20 (a) Raw PIV images in *r-z* plane, and (b) *r-θ* plane, according to Wall, [29].

The resultant hollow core acts as a reflective surface for the laser sheet, which reduces the penetration of the light sheet past the hollow core limiting the effective field of view (FOV) due to the increased localized light pollution and the insufficient light scatter from particles; both situations result in an insufficient contrast. The *r-θ* plane was affected to a much lesser extent than the *r-z* plane. Wall employs a Computational Fluid Dynamics (CFD) approach coupled with experimental PIV measurements (sample results shown in Figure 2.21) to reach the following conclusions:

2D PIV measurements present challenges in the *r-z* plane that prevent the mantle location/structure from being resolved. However, the investigation of confined vortices in the azimuthal plane is sufficiently carried out. Wall also concludes that the CFD analysis of cyclonic flows can be analyzed using the RANS-based RSM turbulence model.

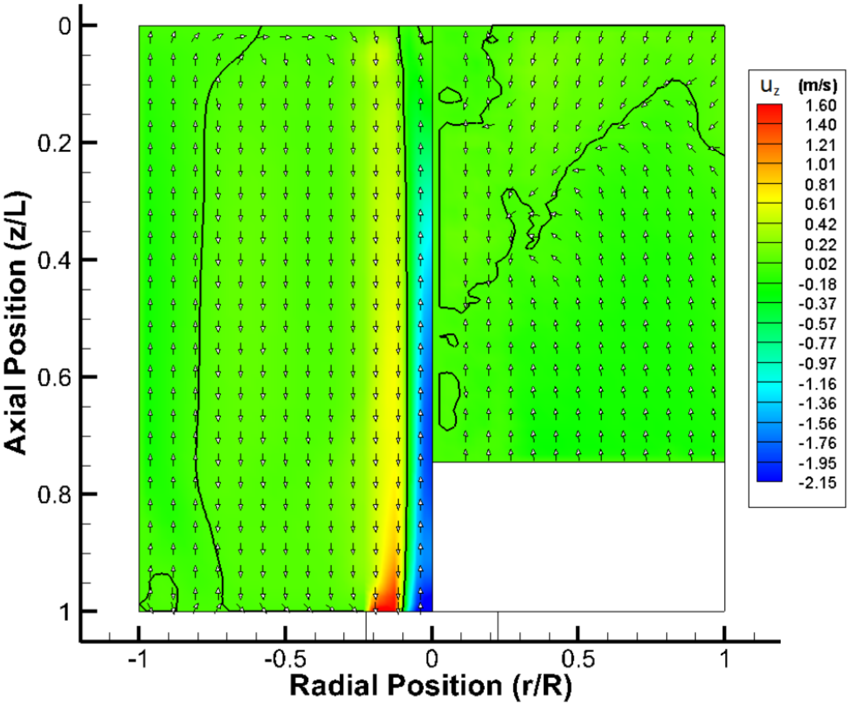

Figure 2.21 Axial velocity contour in the *r-z* plane, CFD results (left of centerline) and PIV results (right of the centerline), the solid line shows the mantle boundary, according to Wall [29]**.**

In terms of the parametric study, Wall finds that decreasing the exit radius, thus the chamber contraction ratio, results in increased intensity of the vortex and significantly affects the mantle structure. Conversely, he finds the chamber aspect ratio to have an opposite effect. Moreover, the inlet Reynolds number is found to influence the intensity of the confined vortex while having a minimal effect on the structure of the mantle.

Based on the schematics of the experimental setup presented by Wall in [29], it may be inferred that the primary reason for a large hollow core experienced by Wall, is due to the hydro cyclone discharging to ambient air, thus leading to a large region of cavitation in the precessing core. The observation made by Wall, regarding the suitability of 2D PIV as an investigation technique for the *r-z* plane also stems from the same reason. This can be largely avoided by submerging the hydro cyclone into a water bath. Using water instead of air at the outlet will ensure the consistency of the operating flow properties both inside and around the chamber exit. In fact, this strategy is used in the present study.

2.4 Dimensionless Parameters

It is important to identify the non-dimensional parameters that govern this flowfield. Three main nondimensional parameters consist of the swirl number, S, the vortex Reynolds number, V, and the off-swirl parameter, κ.

2.4.1 Swirl Number, *S*

Swirl is generated in a flow by three principal methods, all of these pertain to the injection of fluid in the domain. The degree of swirl is controlled either by controlling the ratio of axial to tangential entry, injecting the fluid through guided vanes like swirlers or helical impellers, or by direct rotation of the injection tube or the set of pipers. But with any method, the interest lies in knowing and describing the degree of swirl in the domain. For this purpose, the non-dimensional swirl number is used. Unfortunately, no global relation for calculating the swirl is agreed upon within the scientific community, and the swirl number has been defined based on operation and equipment; the starting point is often the ratio of the axial flux of tangential momentum and axial flux of axial momentum, as defined by Gupta [65]:

$$S = \frac{G_\theta}{G_x\, r} \tag{2.3}$$

here *r* is the reference length, whereas G_θ and G_x represent the axial flux of tangential momentum and the axial flux of axial momentum, respectively. These include the turbulent shear-stress terms and the pressure term.

The turbulent shear-stress terms are often difficult to measure with high confidence and as a consequence, the stress terms are dropped from the formulation of *S*. Similarly, the pressure term is modeled based on the velocity distribution, which also introduces errors where friction losses are high. Therefore, Eq. (2.3) is reduced to [65]:

$$S = \frac{G_\theta}{G_x\, r} = \frac{\int_0^r U_\theta U_z r^2 dr}{R \int_0^R U_z^2\, r\, dr} \tag{2.4}$$

If the axial and tangential velocity distributions are explicitly known, the swirl number can be calculated from Eq. (2.4), while simplifying for the pressure and turbulent shear-stress terms. However, often the velocity distributions are also unknown. In absence of the known velocity distributions, various relations for *S* have been derived based on simplifications, empirical data, and experimental observations. However such relations are very specific to the geometric configuration used to generate the swirl. In what follows, several examples are provided:

Lilley [66] defines the swirl number for a combustor with swirl vanes using

$$S = \frac{2}{3}\left[\frac{1-\ (d_h/d)^3}{1-\ (d_h/d)^2}\right] \tan\phi \tag{2.5}$$

here '*d*' and 'd_h' denote the nozzle and hub diameters of the vanes, and ϕ stands for the vane angle.

Hoekstra [4] and Gupta [65] define the swirl number for the cyclone separator configuration as

$$S = \frac{\pi}{4}\frac{d_e\, D}{A_i} \tag{2.6}$$

here d_e is the diameter of the vortex finder, D is the chamber diameter and A_i is the injection area.

For the treatment of bidirectional vortex flows, Majdalani defines the modified swirl number (σ) as

$$\sigma = {a^2}/{A_i} \tag{2.7}$$

This relates to the swirl number defined by Gupta as,

$$S = \frac{\pi}{4}\frac{d_e\, D}{A_i} = \frac{\pi}{4}\frac{2a\; 2b}{A_i} = \pi\beta\sigma \tag{2.8}$$

Since in the present study the mantle location is not known, and the exit diameter is a variable, the relation proposed by Gupta in Eq. (2.6) will be used.

2.4.2 Vortex Reynolds Number, *V*

For swirling flows, an analogous term to the Reynolds number is used to define the ratio of circulation to viscosity and is called the vortex Reynolds number Re_Γ or Re_V. It is given as

$$Re_\Gamma = Re_v = \frac{\Gamma_\infty}{v} \tag{2.9}$$

here Γ_∞ is the far-field circulation and v is the viscosity.

A more relevant definition for bounded vortical flows has been advanced by Majdalani [10], by relating the vortex Reynolds number, *V,* to the tangential injection Reynolds number, *Re*, the modified swirl number, σ, and the chamber aspect ratio, *l*. As a result, one gets:

$$V = \frac{Re}{\sigma l} \tag{2.10}$$

This expression can also be simplified in terms of the injection volume flowrate Q_i, chamber length, L, and fluid viscosity, v, as:

$$V = \frac{\overline{Q_\iota}}{v\, L} \tag{2.11}$$

In the present study, the vortex Reynolds number proposed by Majdalani in Eq. (2.11) will be used, as it will facilitate comparisons between experimental measurements and theory.

2.4.3 Off-Swirl Parameter, κ

In the context of a confined cyclonic chamber, Majdalani [10] prescribes an off-swirl parameter that governs the relative magnitude of the off-swirl velocity components i.e. U_r, U_z, and the swirl velocity component U_θ. It is defined in terms of the geometric parameters, the aspect ratio, l, and the modified swirl number, σ:

$$\kappa = \frac{1}{2\,\pi\sigma l} \tag{2.12}$$

A large value of the off-swirl parameter would result in a weekly rotating flow whereas a small value of κ will have a dominant tangential velocity.

3. Experimental Setup

An extensive body of knowledge detailing the analytical solutions has been formulated to gain an understanding of the fundamental fluid mechanics of the flow in confined cyclonic chambers [10,13–15]. The experimental proof of concept confirming the unique advantages afforded by the confined vortex motion in the bidirectional vortex engine, VIHRE, and VCCWC have also been presented [9,44]. However, there is a limited number of experimental studies that have focused on the flow inside a cyclonic chamber and its sensitivity to the geometric design parameters. This data deficiency has warranted a need to experimentally characterize the flowfield of confined cyclonic flows. The objective of the present work is therefore focused on explaining the fundamental fluid dynamics of the flowfield of confined vortex flows in the cyclonic chamber. In this process it is also hoped to elucidate the flow dependence on the swirl number, and vortex Reynolds number, which are highly dependent on the geometry. In addition, efforts will be devoted to characterize the swirling jet exiting the cyclonic chamber and the role of vorticity on the jet characteristics.

It should be mentioned that earlier experiments [37,40] conducted on cyclone separators used intrusive techniques such as pitot static tubes for the measurement of pressure and velocity in the chamber. Though a mean pressure and velocity were obtained, the intrusive nature of the measurement techniques often altered the flowfield. Later, the laser doppler velocimetry was successfully employed by Hoekstra et al. [4], but because of the point measurement nature of LDA, results had a low spatial resolution.

In the present study, planar PIV was selected as a primary experimental technique. Not only is it a non-intrusive technique but it also makes it possible to obtain data over large sections of the flow simultaneously. Although the advanced PIV techniques such as the volumetric and tomographic PIV could result in higher data resolution, these techniques are more susceptible to wall curvature and internal reflections compared to planar PIV. The biggest challenge in employing PIV for swirling flows is often faced in the form of achieving adequate seeding. The size of the seeding particle needs to be small enough that it can adhere to the flow accurately, especially in the vortex core region; and large enough to scatter sufficient light for detection. This has been well documented from the experiments performed by Rom [28] and Maicke et al. [48][64] for the bidirectional vortex engine. However, much more flexibility in terms of seed selection can be achieved by using a denser operating fluid. Therefore, in the present study, water was selected as the working fluid to counter the challenges outlined above, where the density difference in air and seeding particles resulted in low seeding density in the vortex core. The inherent three-dimensional nature of the cyclonic flowfield also results in errors due to the high out-of-plain velocities while implementing planar PIV. However, using water as the working fluid, made it possible to achieve the desired vortex Reynolds numbers at relatively lower velocities.

3.1 Geometric Configurations and Operating Conditions

A right-cylindrical chamber with multiple tangential inlets was chosen as the starting point, since it constitutes the most basic design capable of producing a confined cyclonic flow. Various geometric parameters were then identified with the help of the literature, both analytical and experimental, presented in the previous chapter, to carry out the parametric study needed to explain the variance in the flowfield and relevant characteristics.

The literature review suggests that the cyclonic flowfield is governed by the swirl number, S, the off-swirl parameter, κ, and the inlet velocity, which can be expressed as the vortex Reynolds number, V [4,10]. Although the swirl number expresses the ratio of the axial flux of tangential momentum to the axial flux of axial momentum, it can be expressed conveniently in terms of the relevant geometry [4,67]; the chamber exit area (contraction ratio, β), the inlet area, A_i, and the chamber radius, a [4], the latter two parameters were also used to define the modified swirl number, σ, by Majdalani [10]. The chamber aspect ratio, l, also appears in the formulation of both V and κ. Thus, it was expected that these design parameters will influence the bidirectional flowfield.

The influence of the geometry on the performance of hybrid rocked motors with swirling flowfields such as in the vortex injection hybrid rocket engine (VIHRE) by Knuth et al. [44] has also been investigated experimentally. These researchers statistically determined the sensitivity of the average regression rate for each design parameter and found the port diameter, port length, injection area, and throat area to be the most significant physical design variables [26]. Although VIHRE is a hybrid rocket motor, its internal flow is very similar to the understudy confined flow in a cyclonic chamber. During the research on swirling flow in gas cyclones, Hoekstra et al. [4] also found the diameter of the vortex finder to significantly affect both the axial and tangential velocity distributions. In an experimental study, Wall [29] also found the contraction ratio and chamber aspect ratio to influence the mantle structure.

Based on the above discussion, five quantities were selected for the parametric study to investigate their influence on the cyclonic flowfield. These include the vortex Reynolds number, V, head injector configuration, exit contraction ratio, β, the injection area, A_i, and the chamber aspect ratio, l. The chamber radius, a, of 1 inch, and the number of tangential injectors, ($n = 4$) were kept constant for the study. This enabled the design of a modular arrangement, where each of the above parameters could be changed individually. The selection of individual parameters has been discussed in detail in Chapter 5 and is summarized in the table below:

Table.3.1 Test Parameters.

S No.	Parameter	No. of variations	Values
1.	Vortex Reynolds number, V	5	1240, 2470, 3710, 4940 and 6180
2.	Contraction ratio, β	5	0.168 , 0.25, 0.305, 0.353, and 0.50
3.	Inlet area, A_i	4	0.25, 0.35, 0.42 and 0.5
4.	Chamber aspect ratio, l	3	1.0, 2.0 and 3.0
5.	Head injector configuration	3	Closed, Open, and Active injection

A full factorial test of the above test parameters, for three additional axial locations for the transverse (r-θ) plane, is extremely cost prohibitive. Therefore a baseline configuration, given in Table 3.2, was selected, and then one factor at a time (OFAT) approach was pursued. However, recognizing the limitations of the OFAT design, where interactions among the geometric variables cannot be studied, additional geometric combinations were identified and tested. Moreover, since multiple geometric variables are combined to define the various non-dimensional quantities, the combined influence can be expressed in terms of these non-dimensional numbers. For example, both the contraction ratio and inlet area are used to define the swirl number. Similarly, the vortex Reynolds number formulation includes the inlet velocity, inlet area, and the chamber aspect ratio. The results presented in Chapters 4 and 5 are also summarized as a function of these non-dimensional numbers.

3.2. Baseline Configuration.

Geometric Parameters		Operating Parameters	
Chamber radius, a	1 in	Vortex Reynolds number, V	3710
Chamber AR, l	2	Modified swirl no. $\sigma = a^2 / A_i$	2.6
Inlet diameter, d_{inlet}	0.35 in		
Total inlet area, A_i	0.385 in^2	Geometric swirl no. $S = (\pi d_e a) / (2 A_i)$	2.04
Contraction ratio, β	0.25		

In order to globalize the applicability of the findings of this study, and to facilitate the comparison with published data, all variables have been presented as nondimensional quantities. This not only makes the chamber configuration scalable but also enables independence from fluid-specific properties. All length scales have been non-dimensionalized by the radius of the chamber, a, and the velocities by the injection velocity, U_{inj}. The other non-dimensional quantities have been discussed in Sec. 2.4.

3.2 Experimental Setup

In what follows, the experimental setup is described in detail, including the design and specifications of the cyclonic chamber, and fluid supply system, followed by the flowfield visualization setup. A detailed discussion on the PIV setup and the choice of seeding particles and the time interval between the image pairs is then described.

3.2.1 Vortex Chamber Design

A modular approach is used to design the experimental setup as shown in Figure 3.1, that allowes testing of different geometric configurations. As such, each component can be independently changed to achieve the desired experimental configuration. The test setup is machined from transparent acrylic to maximize the optical accessibility for the flow visualization and PIV measurements. An acrylic tube of 0.25-inch wall thickness with varying lengths serves as the chamber sidewall. The coordinate system is attached to the headwall with the positive *z*-axis pointing outwardly along the chamber centerline.

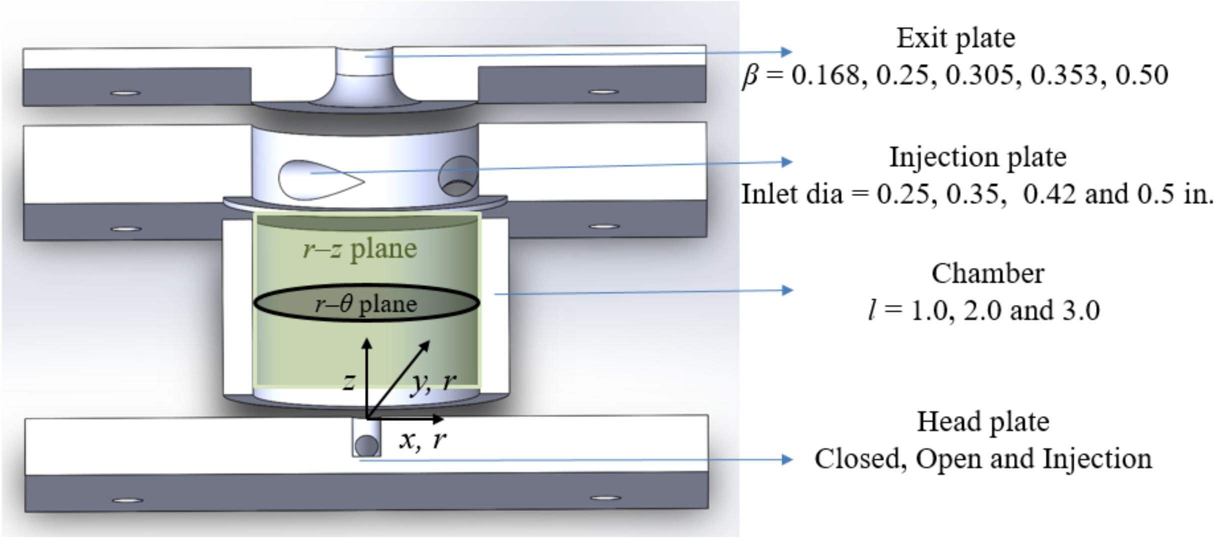

Figure 3.1 Sectional view of the modular vortex chamber.

Planar PIV is utilized to calculate the velocity fields on both the axial, *r-z* plane and the transverse, *r-θ* plane. It may be noted that the optical access in the axial plane is limited by the thickness of the injection plate. Therefore approximately 0.45 inches of the axial field of view (FOV) could not be recorded for PIV. This results in the available axial FOV equivalent to z/L = 0.55, 0.77, and 0.85 for the chamber aspect ratios of l = 1.0, 2.0, and 3.0 respectively. The curvature of the chamber walls also makes the outer 5% of the chamber radius optically inaccessible. Thus, the optical accessibility of the axial plane remains limited to ~ 70% in the axial direction and ~95% in the radial direction. Similarly, the head injector inhibits the optical access around the chamber centerline; however, for the baseline case (i.e. head injector closed configuration) the head injector plate is replaced with a clear acrylic plate, thus making the entire *r-θ* plane optically accessible.

The exit plate is equipped with an extruded boss that when aligned with the base of the tangential injectors acts as the chamber base wall. Converging exit nozzles of various exit diameters are machined on the exit plates to control the contraction ratio. However, each nozzle has a converging radius of 0.25 inches. The contraction ratio is defined as the ratio of the nozzle exit radius to the chamber radius. The complete assembly is held together with four threaded rods. The assembled experimental setup is shown in Figure 3.2.

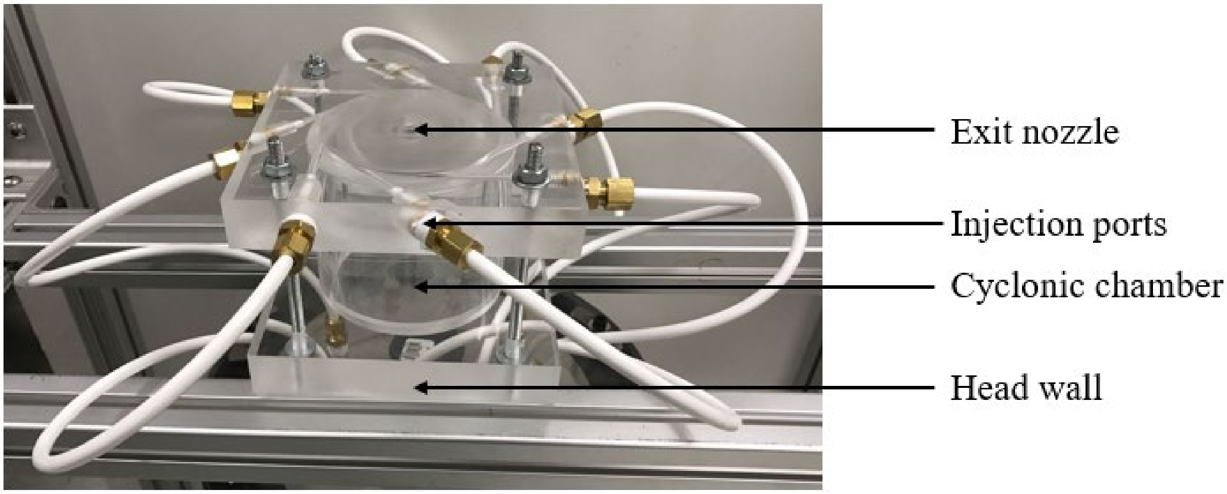

Figure 3.2 Assembled experimental setup.

The injector ports are connected to a flow conditioner equipped with a honeycomb and a series of screens of different porosities to ensure uniform fluid flow and to remove small-scale eddies generated by the pump. The flow conditioner and the cyclonic chamber assembly are fully submerged in the tow tank of the Auburn University Vortex Dynamics Lab, where the experiments are conducted. Water to the flow conditioner is supplied by a Lanchez QSB-JH-9003 variable speed pump and regulated through a rotameter. The supply to the head injector is regulated with a separate pump. Since the entire setup is submerged in water, it forms a closed loop system to maintain a uniform seeding density for PIV.

3.2.2 Flow Visualization

Flow visualization is performed by injecting a near-buoyant, Rhodamine-590 dye into one of the intake lines. A thin laser sheet generated by the Nd:YLF laser (Photonics Industries DM50-527, 55mJ/pulse, 10kHz max) is positioned either at the axial plane along the chamber centerline or at the transverse plane at $z/L = 0.5$ for the baseline configuration. The images are captured by a high-speed camera, PCO Dimax S4, 4Mpx. The camera is outfitted with the Tiffen, Orange 21, optical filter compatible with the fluorescence emission to minimize surface reflections.

3.2.3 Particle Image Velocimetry Setup

Particle image velocimetry (PIV) is employed to determine the flowfield in the r-z plane as well as in the r-θ plane, using a 200 mJ New Wave dual pulsed YAG lasers and 11 MP (4032 x 2688) BOBCAT 2.0 B4020, Imperx camera fitted with 85 mm focal length lens. A maximum possible FOV is relied upon to capture the area of interest. This results in a high spatial resolution of the order of ~43 pixels per mm. However, the circular area of interest for the r-θ plane and close to square for the r-z plane of the circular cylinder mean that post-processing in terms of masking/cropping has to be undertaken as discussed below.

As mentioned earlier, it is recognized that the swirl-dominated flows are three-dimensional in nature; therefore, the ideal investigative technique should be time-resolved, volumetric, tomographic PIV. In the absence of such a facility for the present study, the 2-D time-averaged PIV is utilized. However, dedicated efforts have been made to keep the errors incurred due to 2-D

PIV to a minimum by adhering to the conventions of PIV regarding the selection of seeding size, seeding density, pulse duration and separation, laser sheet thickness, and the interrogation window size.

The seeding size is governed by the Stokes particle number, which characterizes the behavior of particles suspended in fluid flow, while prescribing the fluid response time of the particle. It is defined as the ratio of the characteristic particle time, t_p, and the characteristic fluid time, t_{fl}. For acceptable tracing accuracy, the particle response time should be shorter than the shortest time scale encountered in the flow. When the *Stk* is much less than unity (*Stk* << 1), the motion of the particle is predominantly determined by the flow. If the *Stk* < 0.1, then the tracing accuracy errors are under 1% [68]. The selection of water as the operating fluid allows a much higher flexibility in the selection of the seeding particle. For the present study, the TSI (Model #10090) particles with a mean diameter of 55 microns are used. The polyamide spheres particle density is 1.03g/cm³. The *Stk* number is calculated using the Eqs. (3.1) and (3.2),

$$t_p = D_p^2 \frac{\rho_p}{18\,\mu} \tag{3.1}$$

$$Stk = t_p \frac{U}{l} \tag{3.2}$$

Based on the seeding particle specifications, properties of water, the maximum expected tangential velocity, and characteristic length, the *Stk* = 0.03 is calculated. It is concluded that the selected particles would follow the fluid motion.

The seeding density, Δt (pulse separation), and the interrogation window size are selected based on the PIV conventions, which state that there should be 5-10 particles per interrogation window, and the maximum displacement should not exceed 25% of the interrogation window. A pulse separation of 50 microseconds and the interrogation window size of 64 x 64 pixels for the first pass and a 32 x 32 pixel for the second pass are found appropriate for the PIV. Since the cyclonic chamber, flow conditioner, and pump are all submerged in water (Figure 3.3), they form a closed-loop system that maintains a uniform seeding density for PIV.

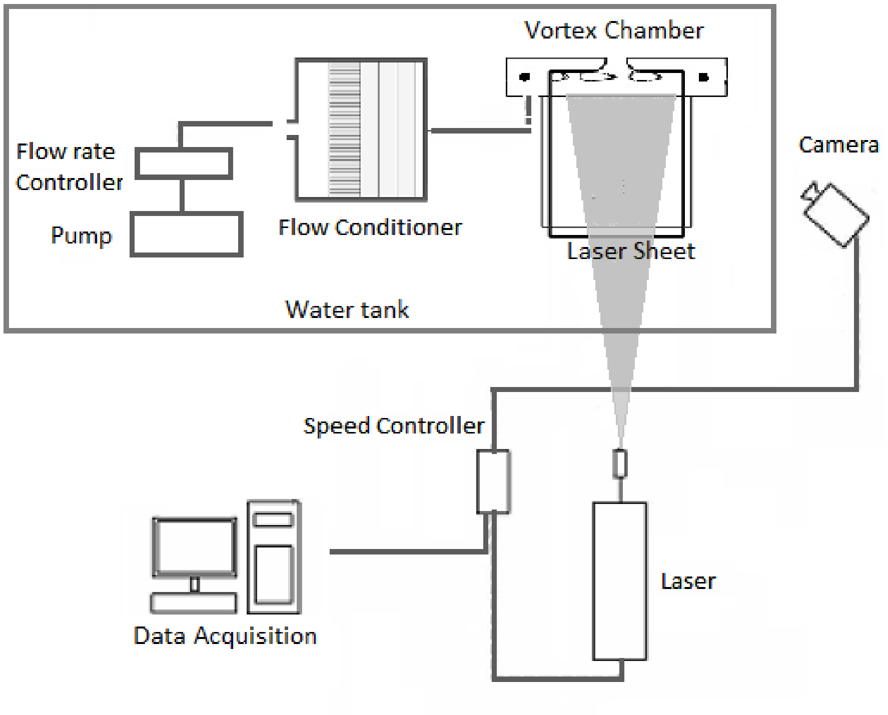

Figure 3.3 The layout of the experimental setup.

The cylindrical beam of the laser output is converted into a laser sheet of thickness 1 mm by using a Dantec Dynamics light sheet generator. The light sheet is aligned with the axial plane of the chamber to determine the flowfield of the *r-z* plane and is rotated by 90° for measurements in the transverse plane. The camera is always positioned in such a way as to remain perpendicular to the light sheet. The layout of the experimental setup is shown in Figure 3.3 and the raw PIV images acquired are presented in Figure 3.4.

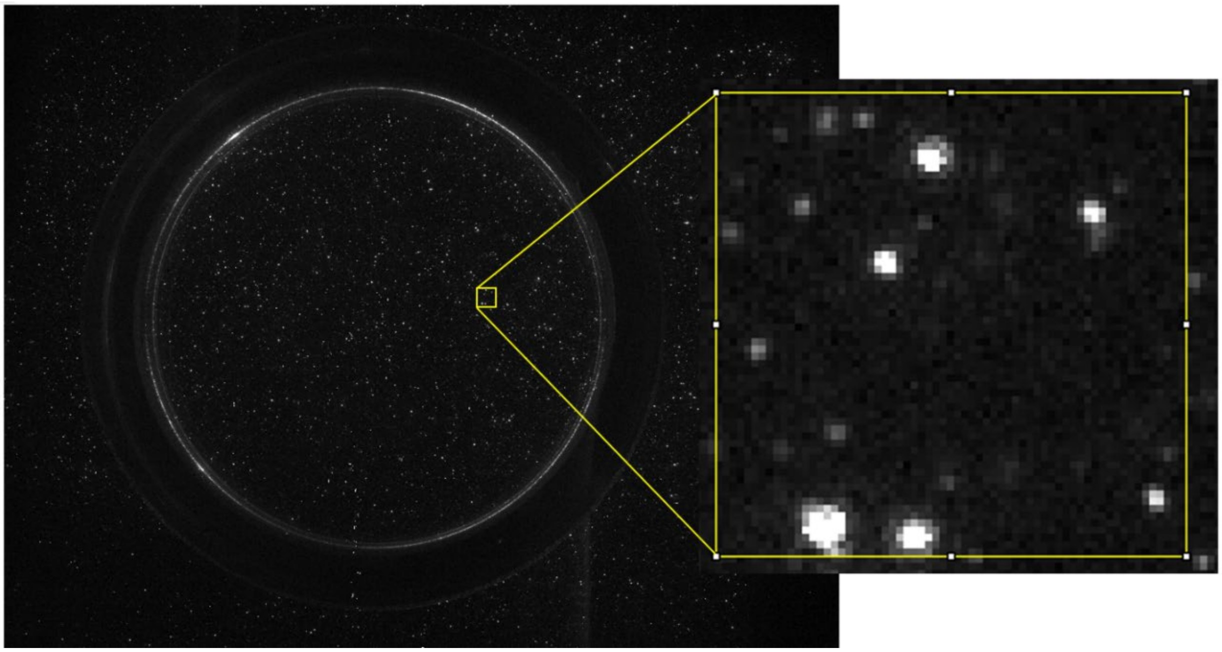

Figure 3.4 Raw PIV image of particle-laden flow and the magnified region showing a single interrogation window.

3.3 Experimental Data and Analysis

The PIV data is collected using the Bobcat CamConfig and FrameLink Express software. In this process, a Dantec Dynamics calibration plate is relied upon to focus the desired plane of interest. Two Quantum Pulse generators (Model no. 9514) are utilized to set the pulse separation and to synchronize the laser trigger and camera shutter operation. Prior to actual data acquisition, a few sample images are recorded to ensure adequate seeding density. A total of 1000 image pairs are recorded at 4 Hz for each test configuration.

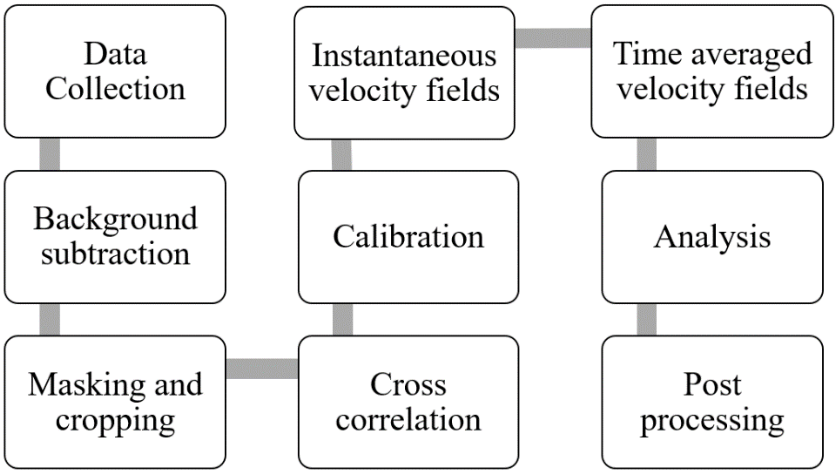

Figure 3.5 Flow chart of the data processing routine.

3.3.1 PIV Data Processing

The PIV data is processed according to the routine presented in Figure 3.5. Note, that the presence of chamber walls and internal reflections can result in unwanted artifacts in the acquired images. Moreover, a few dead pixels that have been noticed on the camera sensor, have resulted in stationary bright pixels in the raw images; they have been removed before processing the data. Also, the round shape of the region of interest in the r-θ plane has mandated masking/cropping. These two steps have been implemented using MATLAB algorithms. An example of the background subtraction for a raw PIV image (Figure 3.6 a) and its processed image (Figure 3.6 b) is presented below. The removal of artifacts and reflection from the chamber walls is apparent.

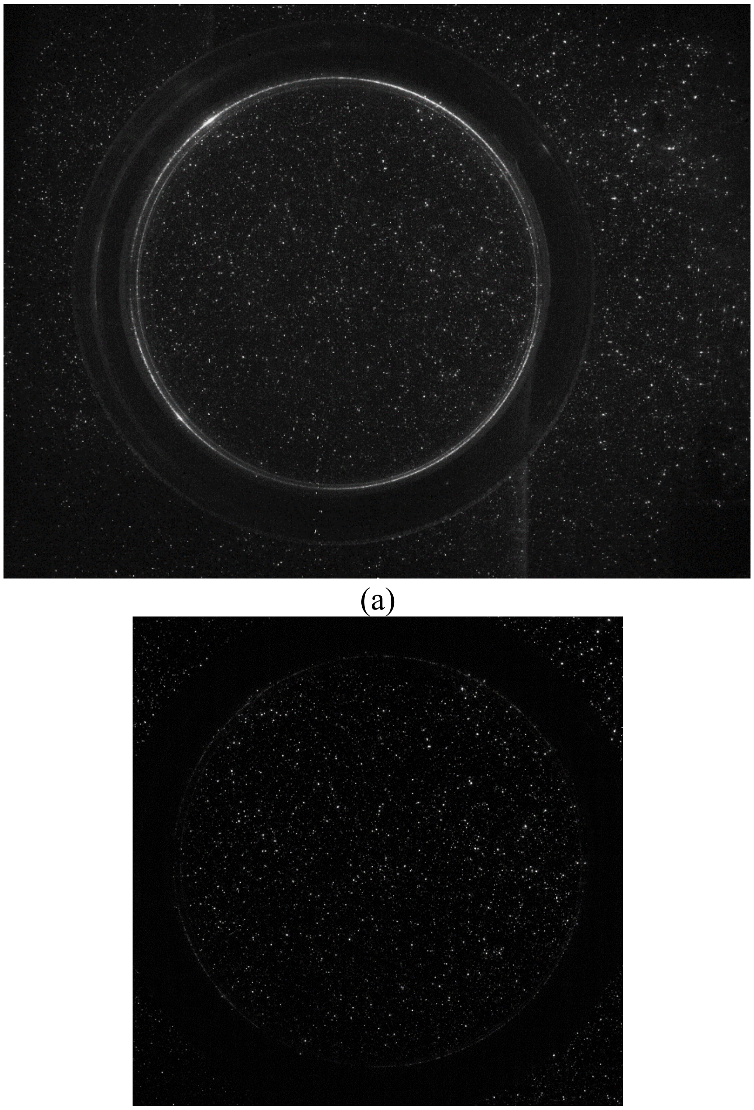

(a)

(b)

Figure 3.6. Illustration of background subtraction, (a) raw image, and (b) processed image.

The processed image pairs are cross-correlated using the open-source application “ Fluere 1.3” [69] over two passes of 64 x 64 pixels for the first pass and a 32 x 32 pixel for the second with 50% window overlap. The time and space calibration are also enforced during this step, which results in instantaneous velocity fields for each image pair. Although these instantaneous velocity fields are separated by a fixed time step, any time-dependent structure or its evolution cannot be ascertained from this data, due to its very sparse time resolution of ¼ second. Thus, the time-depending mechanisms such as the vortex core precession could not be characterized in the present study. PIV images at a given condition have been processed in the ensemble cross-correlation to yield a time-averaged velocity field (Figure 3.7). In fact, much of the discussion presented in this study is based on mean velocity profiles. However, instantaneous velocity fields can also be utilized to calculate the turbulent quantities such as turbulent kinetic energy, and Reynolds stresses. The post-processing of the data for the calculation of derivative quantities and the proper orthogonal decomposition are all carried out using Matlab and Tecplot 360. A detailed discussion on the uncertainly associated with the PIV correlation utilized in the present study is presented in Appendix "B". Based on the correlation peak ratio analysis of representative cases, it is determined that the standard uncertainty for the present experient remains below 3 percent.

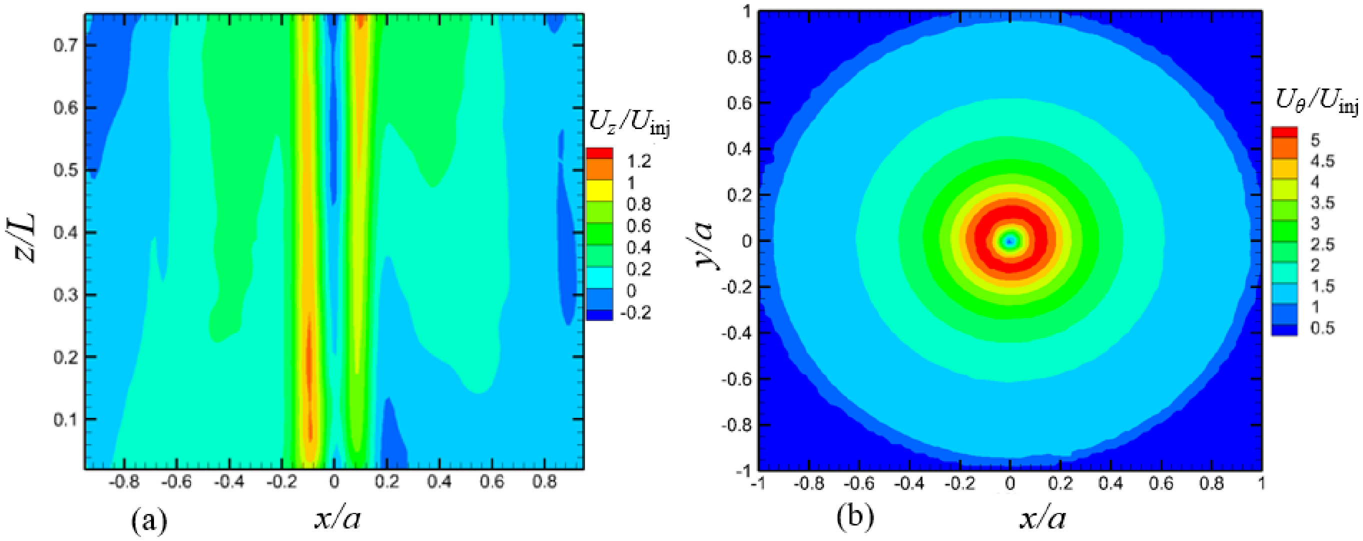

Figure 3.7. Time-averaged (a) axial velocity, and (b) tangential velocity.

3.3.2 PIV - Analysis, and Corrections.

The susceptibility of the 2D PIV to capture the flowfield with strong out of plane velocity is well documented. It is also known that the flowfield in the cyclonic chamber is highly three dimensional, with the dominant component being the tangential velocity. The strong tangential velocity remains perpendicular to the light sheet for the *r-z* plane measurement and thus induces bias in the respective radial and axial velocity components. These induced errors can be observed in the time-averaged axial velocity field presented in Figure 3.7a, which shows an asymmetric distribution of the axial velocity.

The aliasing effect of high out of plane velocity is explained in Figure 3.8, where the effect of uniform out-of-the-plane motion of a dot card is seen. At the center of the image along the horizontal dashed line, the vertical displacement of the dots, post rotation is zero. However, away from the center of the image and the axis of rotation the position of the dots depicts aliasing in both the radial and axial directions. The magnitude of displacement depends on the distance from the center and the magnitude of out of plane motion. In the PIV, although the plane of the light sheet is fixed, the seed particles move out of the planar light sheet, analogous to the dots in Figure 3.8. Thus an erroneous displacement and corresponding erroneous velocity added to the true axial velocity will be observed.

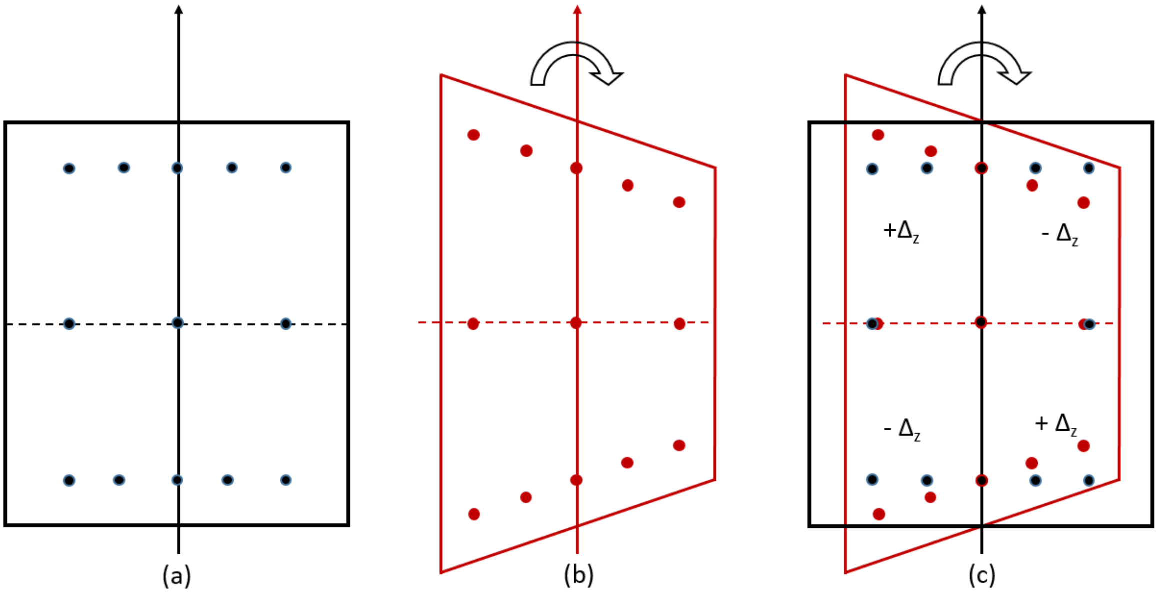

Figure 3.8. Effect of rotation on the perceived location of fixed dots.

The axial velocity profile of the understudy bidirectional cyclonic flow is axisymmetric as shown by multiple analytical solutions and experimental investigations of similar cyclone separators [10,12,15,70,71]. The tangential velocity is antisymmetric on any given *r-z* plane, where the flow is either directed into or out of the plane at a particular instant. This antisymmetric effect relative to the chamber axis results in an antisymmetric induced error in the axial velocity component, as shown above by the perceived change in position of the points. In a confined cyclonic motion, the observed velocity can be expressed as the sum of the true axial velocity and corresponding antisymmetric induced error at any given location (*r,zi*) as:

$$\left|(U_z)_{r,zi)}\right|_{observed} Right = \left|(U)_{r,zi)}\right|_{True} Right + \ \varepsilon\left|(U_z)_{r,zi)}\right| Right \qquad (3.3)$$

$$\left|(U_z)_{r,zi)}\right|_{observed} Left = \left|(U_z)_{r,zi)}\right|_{True} Left + \ \varepsilon\left|(U_z)_{r,zi)}\right| Left$$

Since the expected axial velocity is axisymmetric [10,11,20] and the induced error is antisymmetric with respect to the chamber axis as discussed above, it can be removed by adding the above equations. The resultant error-free axisymmetric axial velocity is given as:

$$\left|(U)_{r,zi)}\right|_{True} Right = \ \left|(U)_{r,zi)}\right|_{True} Left \qquad (3.4)$$

$$= \frac{1}{2}\left|\ \left|(U_z)_{r,zi)}\right|_{observed} Right + \ \left|(U_z)_{r,zi)}\right|_{observed} Left\ \right|$$

These corrections remove any errors induced due to the out of plane tangential velocity and produce a corrected axial velocity profile. This methodology is valid as long as the true nature of the flow is axisymmetric in the axial direction. The applicability of this method has been demonstrated by Liu et al. [72][73] on the cyclone separator, using both planar and stereo PIV. The comparison of the axial velocity contours calculated from the original 2-D planar PIV results and the 3-D stereo PIV is given in Figure 3.9.

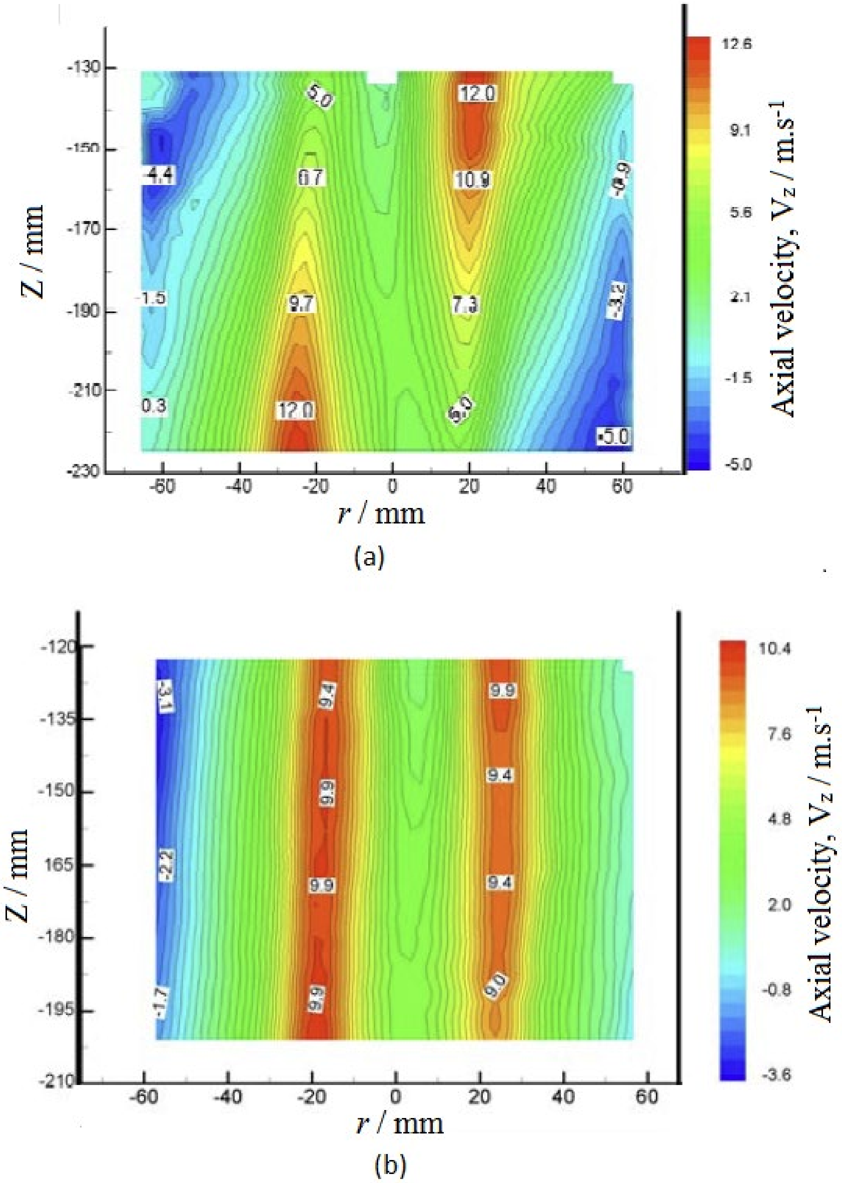

Figure 3.9 Axial velocity contours of cyclone separator acquired with (a) 2-D planar PIV, and (b) stereographic PIV [72].

The antisymmetric induced error due to the high out of plane velocity is evident in Figure 3.9a, whereas the actual axisymmetric axial velocity distribution is captured by the 3-D stereo PIV in Figure 3.9b. The corresponding axial velocity profiles at different *z/L* locations for original 2-D, corrected 2-D from planar PIV data, and 3-D stereo PIV are presented in Figure 3.10. The aliasing effect of the 2-D PIV is seen as the asymmetric velocity profiles in Figure 3.10a, which have been corrected, and compares well with the 3-D stereo PIV in Figure 3.10b.

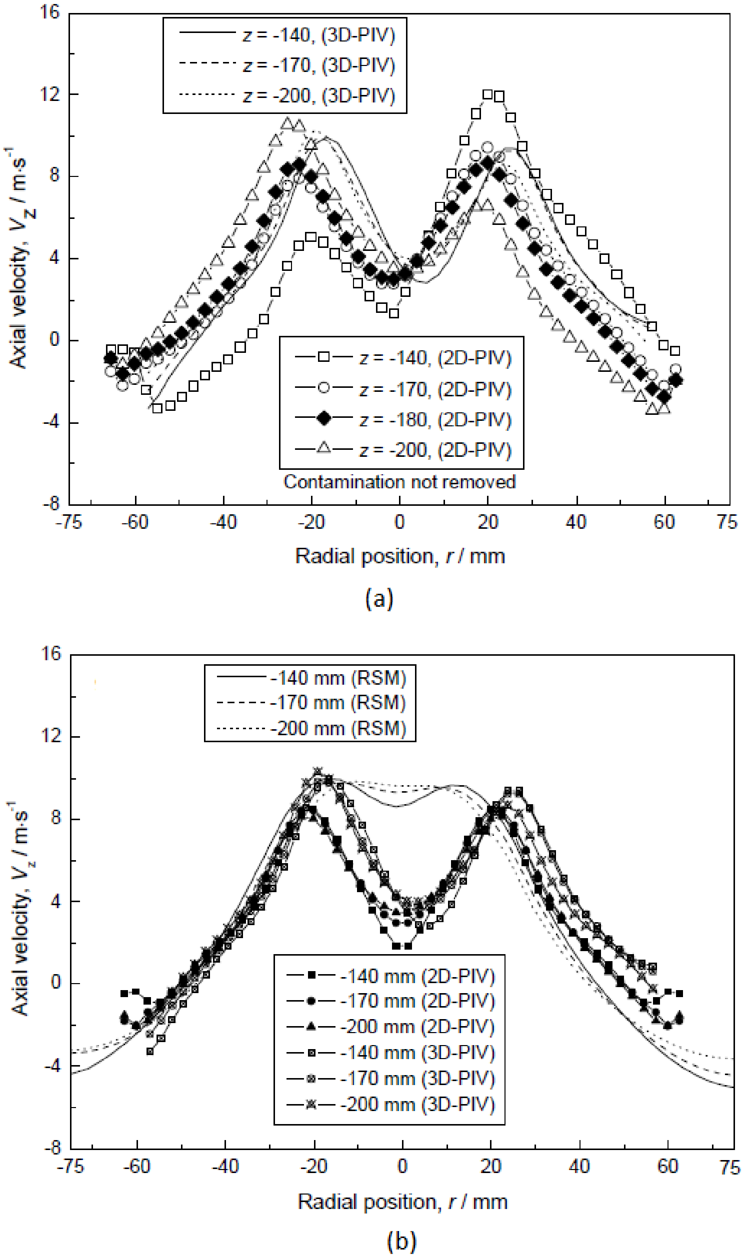

Figure 3.10 Comparison of uncorrected axial velocity profiles obtained by (a) planar PIV with (b) corrected and stereographic PIV data [72].

This correction methodology has been applied in the present work to all axial plane data. However, a similar correction is not necessary for the *r*-*θ* plane calculations. The out of plane velocity component for the *r-θ* plane is the axial velocity, which is comparatively much smaller than the dominant tangential velocity. Thus, the out of plane error on the *r-θ* plane is negligible. The original and corrected radial distribution of the axial velocity profiles is presented in Figure 3.11.

The antisymmetric nature of the out of plane velocity is clearly evident in Figure 3.11a. On the left side of the chamber axis (*x/r* =0) the velocity profiles appear to merge together due to the negative induced error for *z/L* = 0.75 and positive induced error for the z/L = 0.25, whereas on the right-hand side of the chamber axis, the velocity profiles become further apart because of positive induced error at *z/L* = 0.75 and negative induced error for *z/L* = 0.25. The velocity profile at *z/L* = 0.5 is almost symmetric even before the correction, as it is close to the horizontal axis of the raw images.

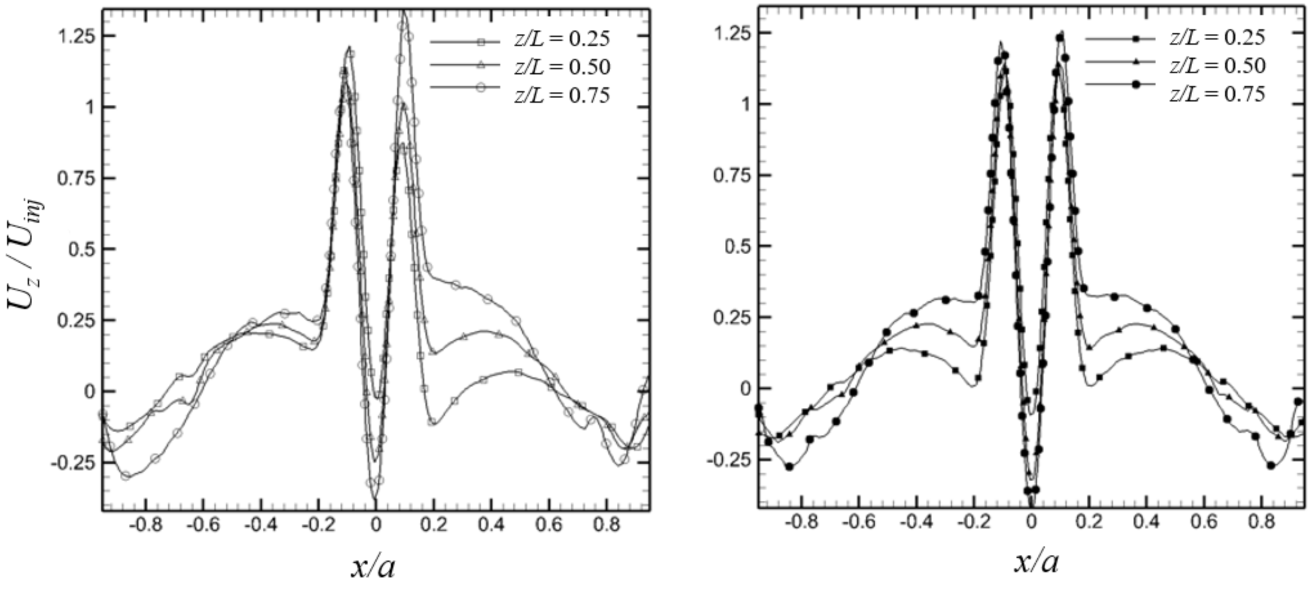

Figure 3.11. Distribution of axial velocity for (a) original, and (b) corrected 2-D PIV data.

The original and corrected axial velocity contours are presented in Figure 3.12. The symmetric nature of the corrected axial velocity contour in Figure 3.12b is a good representation of the expected axial velocity profile for the bidirectional cyclonic chamber and will be discussed later in Sec 4.2. The symmetry of the features seen in Figure 3.12b also compares well with the flow visualization result of a representative case presented in Figure 3.13.

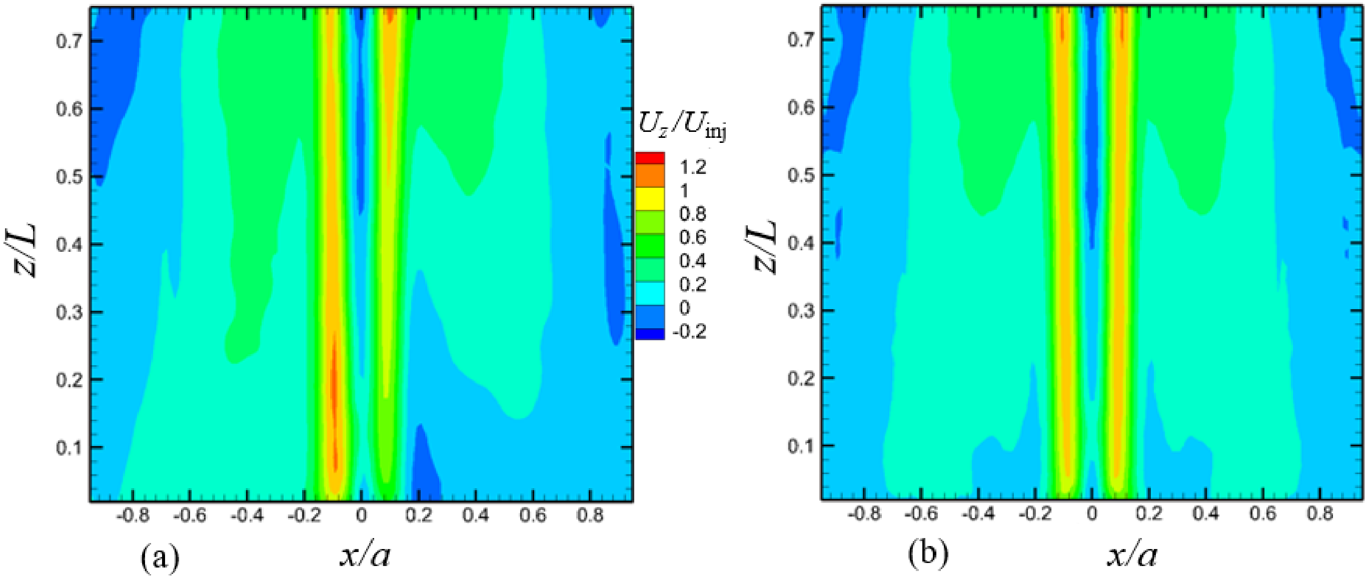

Figure 3.12. Axial velocity contours for (a) original, and (b) corrected 2-D PIV data.

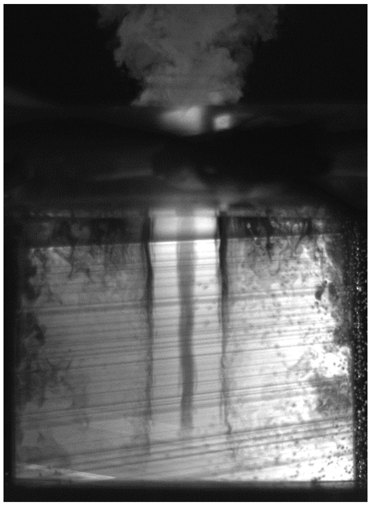

Figure 3.13. Fluorescent dye visualization of the flowfield of confined cyclonic chamber.

It is concluded that, although the out of plane velocity bias mainly affects the axial plane PIV, the same can be corrected by the above-presented methodology. The comparison of the planar and stereographic PIV [73] presented by Lui et al. and the agreement of the corrected axial velocity profile of the present study with the flow visualization results tend to confirm the efficacy of the correction methodology. However, this methodology will not be applicable when the actual velocity distribution is not axisymmetric; such a condition is not expected for the present study but can arise in confined cyclonic flows in the form of the precession of the vortex core. Therefore, the results presented in this research for the axial velocity must be interpreted keeping in view the correction methodology and its limitations. The results of the tangential velocity profile, however, are free of any such deficiency.

4. Results and Discussion

Before presenting the results of the baseline configuration of the confined cyclonic chamber, it is important to highlight the salient features and unique characteristics of the bidirectional vortex flow. The desired flowfield in the confined chamber is vortex-dominated and bidirectional. The presence of a vortex-dominated flow can be established by the tangential velocity field and the radial distribution of the vorticity. Moreover, the bidirectionality can be assessed by the axial velocity measured at several radial positions. The streamlines in a particular plane can be examined to determine the flow behavior and presence of secondary flow, if any. The embedded coherent structures can be identified by employing proper orthogonal decomposition and isolating the Eigen solutions based on the energy levels. Besides exploring the general flowfield, various quantifiable parameters that have been presented in the literature can be utilized to define and subsequently compare resultant flowfields at different operating conditions and geometrical configurations. These parameters include the mantle location, defined as the radial location of a rotating but not translating cylinder across which the axial velocity has opposite signs, the maximum tangential velocity $U_{\theta\,\mathrm{max}}$, which occurs at the junction of the forced vortex core and the free vortex tail (the location of this junction is called the thickness of the core δ_c), and the sidewall boundary layer thickness δ_w.

Figure 4.1 helps to identify these parameters (except for the mantle location) in the r-θ plane. The same convention will be used when discussing the result, for consistency and ease of comparison. It may be noted that the tangential velocity profile has little to no variation with the azimuthal location as evident from Figure 4.1a therefore, Figure 4.1b has been extracted at a preselected azimuthal location at $\theta = 0$ and will be consistent throughout the results presented here.

Moreover, the data presented here has been processed from a time average particle image velocimetry technique, which cannot resolve for the time-sensitive floe feature that can have asymmetric distribution, such as the precession of the core vortex or the central recirculation zone, if any.

Similarly, Figure 4.2 represents an example of the mantle location at the radial distance where the axial velocity distribution crosses the abscissa. The intersection of the axial velocity distribution and the *x*-axis near *x/a* = 0 is not considered as a dual mantle because it represents the formation of a central recirculation zone (CRZ), that will be later discussed. Owing to the limited optical access through the injector plate and near the sidewalls of the chamber due to the wall curvature at *x/a* = 1, the shaded portion of Figure 4.2 does not contain any data.

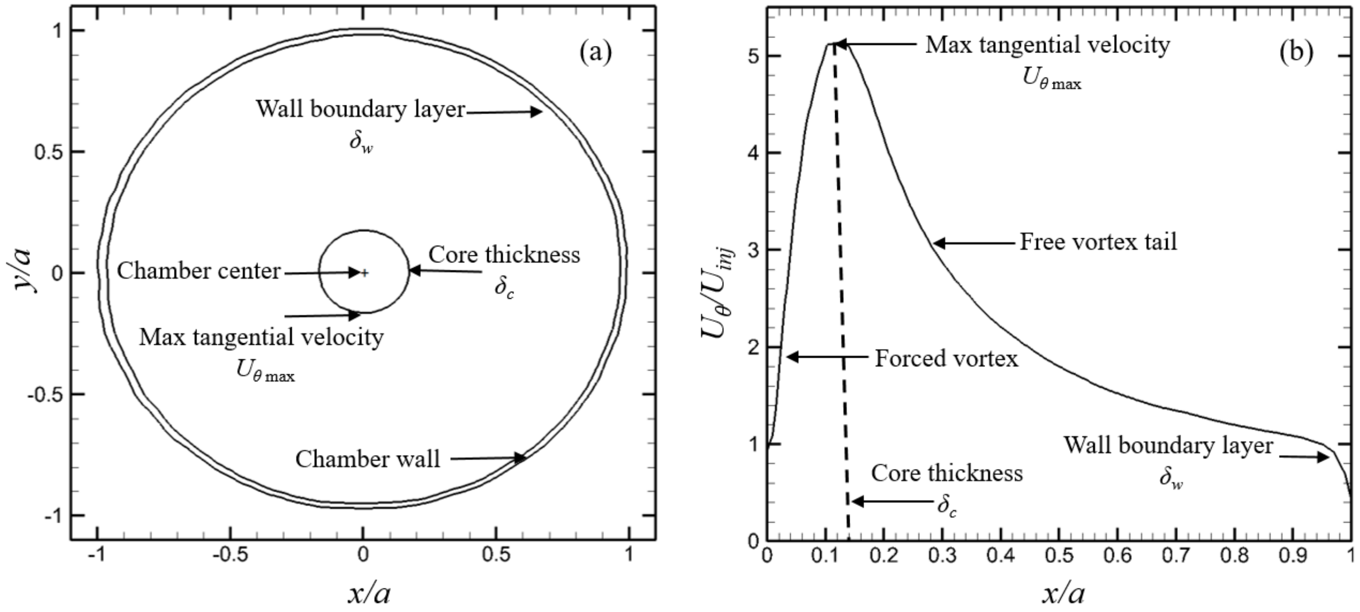

Figure 4.1 Sample presentation to identify the important parameters in the *r*-*θ* plane.

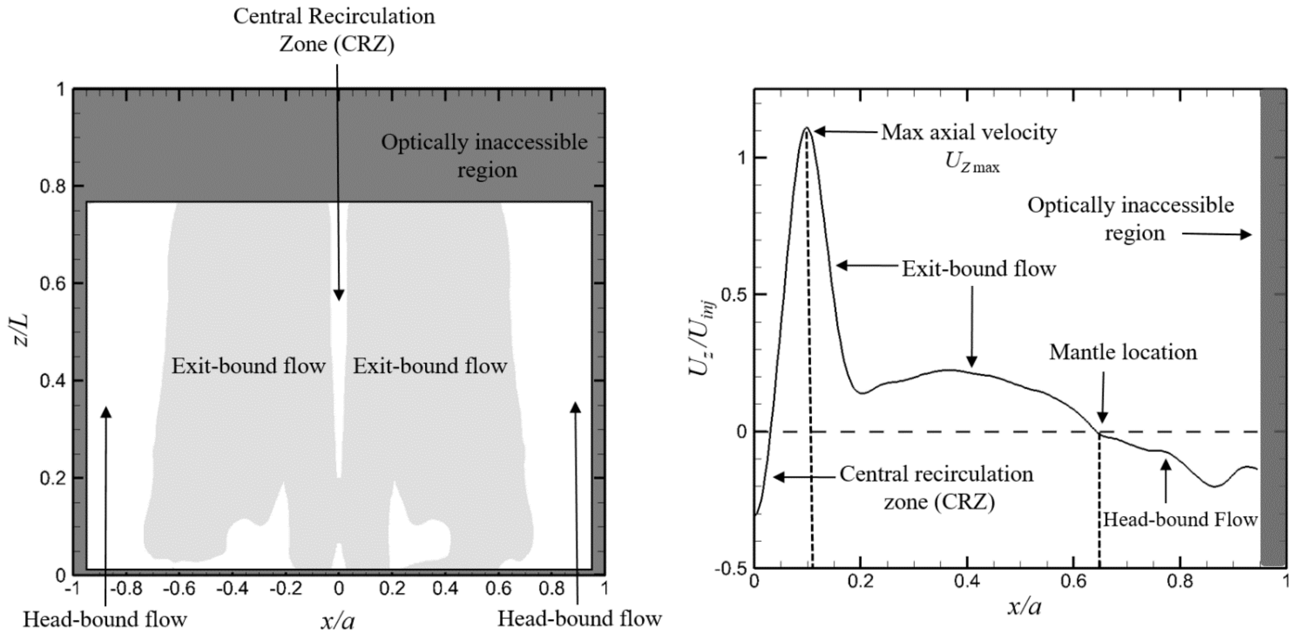

Figure 4.2 Sample presentation of results to identify the important features in the *r*-*z* plane.

4.1 Flow Visualization Results.

Planar flow visualization of the confined cyclonic flow is accomplished with the injection of Rhodamine dye that is illuminated with a 7 W Argon ion laser and OZ Optics light sheet generator. The laser light sheet and camera are positioned to capture either the transverse plane at *z/L* of 0.5 (midplane) or the axial plane along the centerline of the cyclonic chamber.

The effect of the tangential injection is highlighted in the flow visualization image presented in Figure 4.3 with the laser light sheet illuminating the transverse midplane of the cyclonic chamber. Following the direction of the injection, flow spirals clockwise along the concave walls of the circular chamber. The viscous interaction of the tangentially injected fluid and the concave wall results in the growth of a turbulent boundary layer and the onset of centrifugal instability in the form of Görtler vortices [63,74] visible in Figure 4.3. These vortices are swept towards the headwall due to the axial component of flow and after turning at the headwall, they convect radially inwardly towards the center where they amalgamated into braids. The flow visualization image clearly shows a highly turbulent boundary layer with large-scale structures that are typical feature of flow over a concave wall. The flow becomes more uniform towards the center due to the acceleration under the influence of a favorable radial pressure gradient between the wall and the center. The large eddies are significantly suppressed leading to finer scales turbulence near the central core. As the flow spirals towards the center it is amalgamated as braided vortices heading towards the exit nozzle.

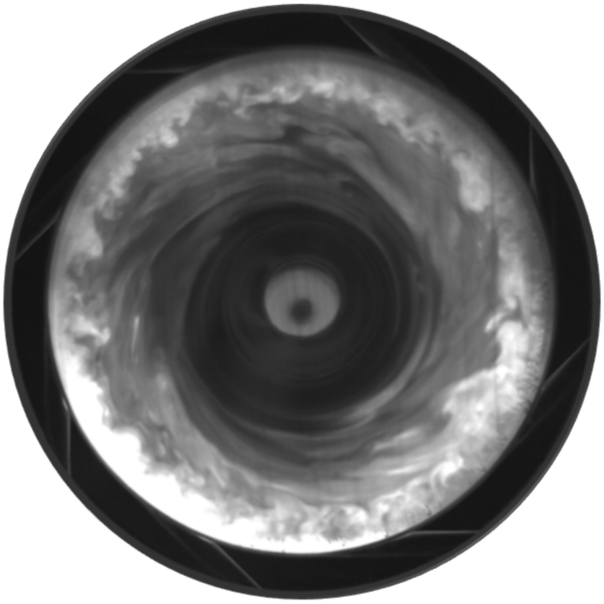

Figure 4.3 Flow visualization in the transverse plane at *z/L* = 0.5, depicting the formation of Görtler vortices on chamber walls.

The time history of the formation of a bidirectional vortex in the chamber is shown in Figure 4.4 a-f, in order of increasing time after injection. It represents the path followed by the fluid stream as it travels from the tangential injector to the exhaust nozzle. The fluid stream initially injected tangentially travels towards the headwall while remaining in contact with the chamber sidewall under the effect of the centrifugal forces. The injected fluid and its movement towards the headwall are evident from the illuminated dye in Figure 4.4 a-b. A closer look at the exhaust (center top section) of Figure 4.4 b, shows the presence of dye in the exit flow. However, the tangentially injected dye has not reached the headwall, which indicates the presence of crossflow. A qualitative statement about the size and structure of the mantle can also be ascertained from the structure of the head-bound flow (Figure 4.4 c).

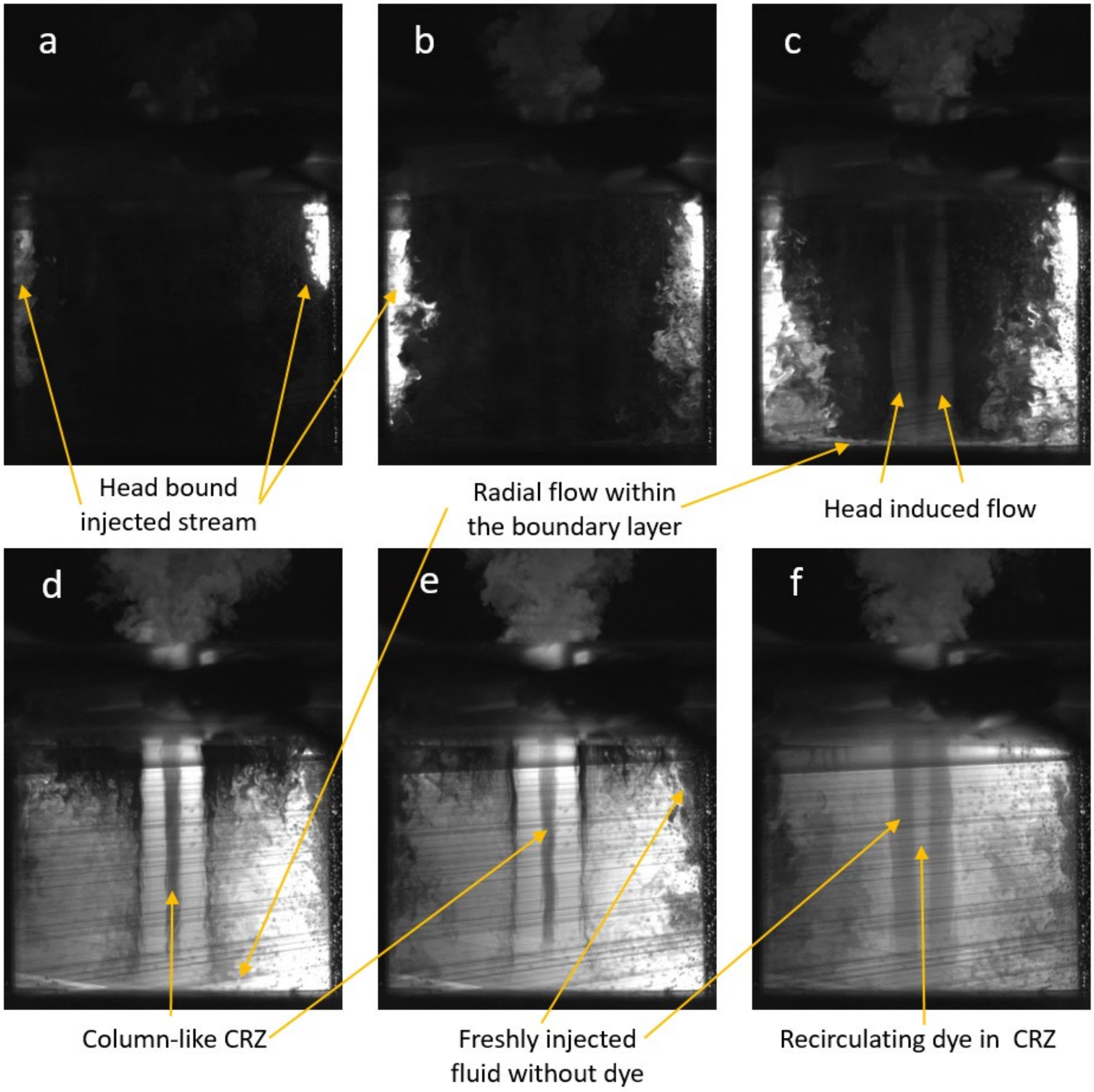

Figure 4.4 Time history of the formation of the bidirectional vortex.

The viscous interaction of the fluid stream and the chamber headwall results in a rotating boundary layer that gives rise to a secondary flow. This secondary flow, though being a coherent feature does not represent the bulk rotating motion of the fluid in the chamber, and has seldom been investigated and discussed in the literature. Neither for the cyclone separators because of their conical geometry of the bottom surface that ends in an open spigot, nor for the confined right-cylindrical cyclonic chamber due to inadequate spatial resolution of experimental studies to capture the thin boundary layer, and inherent inviscid nature of the analytical models.

In swirling flows, the centrifugal forces experienced by the rotating fluid are balanced by the radial pressure gradient. For a fluid element that is following a circular path in the chamber (Figure 4.5), the net centrifugal force and the Euler's equation in the radial direction can be written as:

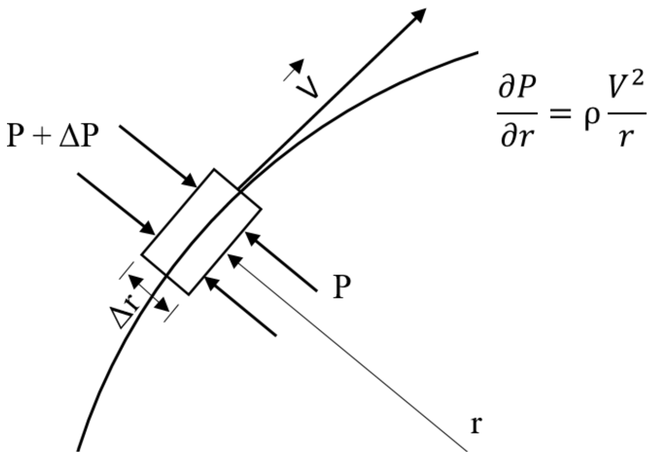

Figure 4.5 Pressure forces on a fluid element following a circular path.

$$\frac{dp}{dr} = \frac{\rho V^2}{r} \tag{4.1}$$

$$\sum F_c = \frac{m V^2}{r} \tag{4.2}$$

Equations (4.1) – (4.2) show that the centrifugal forces exerted on the fluid particles, which are balanced by the radial pressure gradient are proportional to the square of the tangential velocity. Moreover, it can be seen that for a given radial pressure gradient, the smaller the tangential velocity, the smaller the radius the particle must follow. At the headwall, due to viscous effects, the tangential velocity, and corresponding centrifugal forces decrease significantly, whereas the radial pressure gradient which is independent of height remains the same. The unbalanced equilibrium drives the flow, confined within the thin boundary layer, towards the center of the chamber. This behavior is precisely opposite to the Ekman layer that forms on a rotating wall and is responsible for Ekman pumping [75,76]. The headwall boundary layer and fluid motion towards the chamber centerline confined within this boundary layer, can be observed by the bright fluorescent dye layer on the chamber headwall in Figure 4.4 c-e. Subsequently, this fluid turns inwards along the centerline in a toroidal manner as seen in Figure 4.4 c-e. Another feature that makes this flowfield significantly interesting is the presence of the central recirculation zone (CRZ), represented by the dark region along the centerline in the above-referred figures. The CRZ is formed subsequent to the vortex breakdown when the adverse pressure gradient along the centerline is more than the kinetic energy of the flow. Among various types of vortex breakdown modes identified for swirling flows [77]; the most commonly observed ones are the bubble type or the spiral type. At high swirl levels, the breakdown evolves into a column-like CRZ [78,79], which is observed here. As the injected dye runs through the cyclonic chamber, Figure 4.4 f, the freshly injected fluid appears as dark regions by the chamber walls and the outward toroid. The remnant fluid with dye can still be seen in the chamber and more specifically recirculating in the CRZ in Figure 4.4 f. The formation of the CRZ is not captured by the basic analytical solution of

Majdalani [10] but closely resembles the unbounded two-cell Sullivan vortex model [52] as well as Majdalani's analytical solution for a wall-bounded cyclonic motion with a hollow core [80].

Since the confined cyclonic flowfield and its prominent features have been qualitatively investigated, the Particle Image Velocimetry (PIV) results are provided below to quantify these characteristics.

4.2 Identification and Evaluation of Vortex Dominated Flowfield.

This section of the results is dedicated to ascertaining the formation of the bidirectional vortex flowfield for the baseline case and identifying its important flow features. Once the bidirectional vortex flowfield is determined to exist, the characteristic parameters such as mantle location, $U_{\theta\max}$ and δ_c, and their variation within the domain of the chamber at different heights from the headwall, and the effect of the inlet vortex Reynolds number will be evaluated. The chamber geometrical parameters such as chamber diameter, aspect ratio, l, and the nozzle exit diameter d_e, are selected to size the geometry based on similar vortex rocket engine chamber designs [44] and are summarized in table 4.1.

Table 4.1 Baseline chamber geometrical and operating conditions.

Geometric Parameters		**Operating Parameters**	
Chamber radius, a	1 in	Vortex Re, V	3710
Chamber AR, $l = L/a$	2	Modified Swirl no. $\sigma = a^2 / A_i$	2.6
Inlet Diameter, d_{inlet}	0.35 in		
Total Inlet Area, A_i	0.385 in^2	Geometric Swirl no. $S = (\pi\, d_e\, a) / (2\, A_i)$	2.04
Contraction Ratio, β	0.25		

In order to ascertain the vortex-dominated flow behavior in the chamber, Figure 4.6 presents the tangential velocity with superimposed velocity vectors (a) and the radial distribution of the tangential and radial velocity at the chamber mid-plane, $z/L = 0.5$.

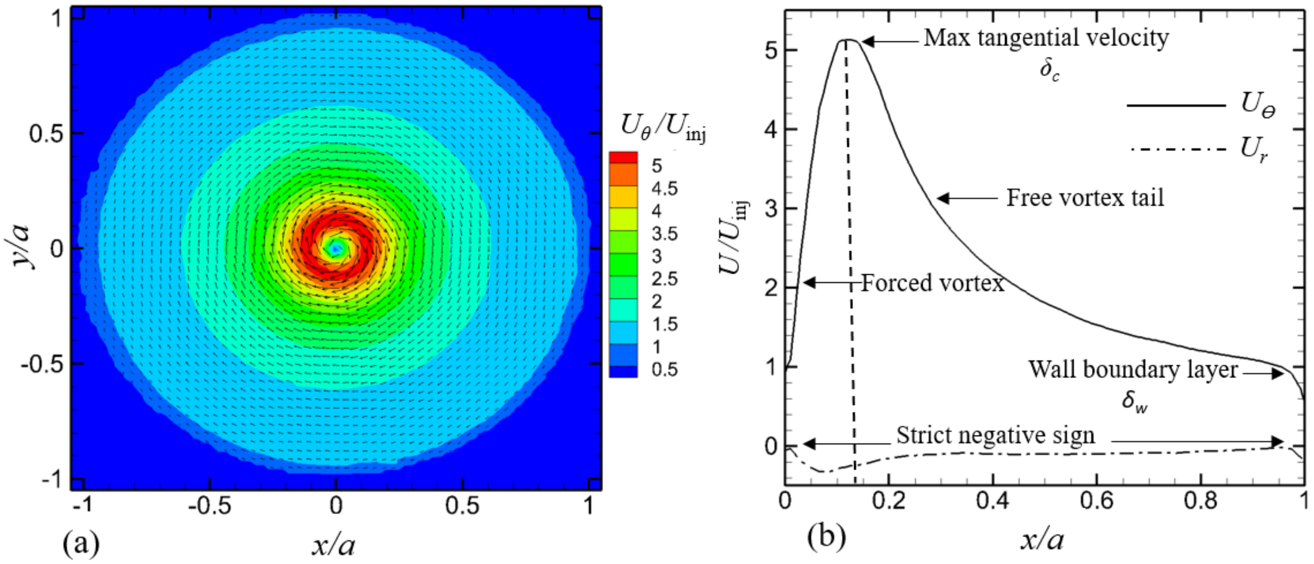

Figure 4.6 (a) The tangential velocity with superimposed velocity vectors, and (b) the radial distribution of the tangential and radial velocities at the chamber midplane.

Figure 4.6a clearly shows a clockwise bulk rotation, for which the magnitude can be estimated by the tangential velocity contours. It is observed that the maxima of the tangential velocity are neither located in the center, which is characteristic of a free vortex nor at the maximum r (radial distance), which would it characterize it as a forced vortex with a constant angular velocity. It can be seen that the tangential velocity initially increases to a certain radial distance and then starts to decrease, thus signifying two separate regions with different behaviors, precisely as described by Majdalani [10]. The inner forced vortex region where the tangential velocity scales directly with radius, r (Figure 4.6) undergoes a viscous dominated solid body rotation with constant angular velocity and is rotational. At the outer periphery of this solid body rotation region, the flow transitions to an irrotational free vortex tail, where the tangential velocity scales with $1/r$ and the viscous effects are negligible until the radial distance reaches the chamber wall. At the wall, due to the no-slip condition, the viscous interaction results in a boundary layer development and onset of a Görtler instability [63], as seen in Figure 4.3. It can thus be seen that the bulk motion in the chamber is vortex dominated.

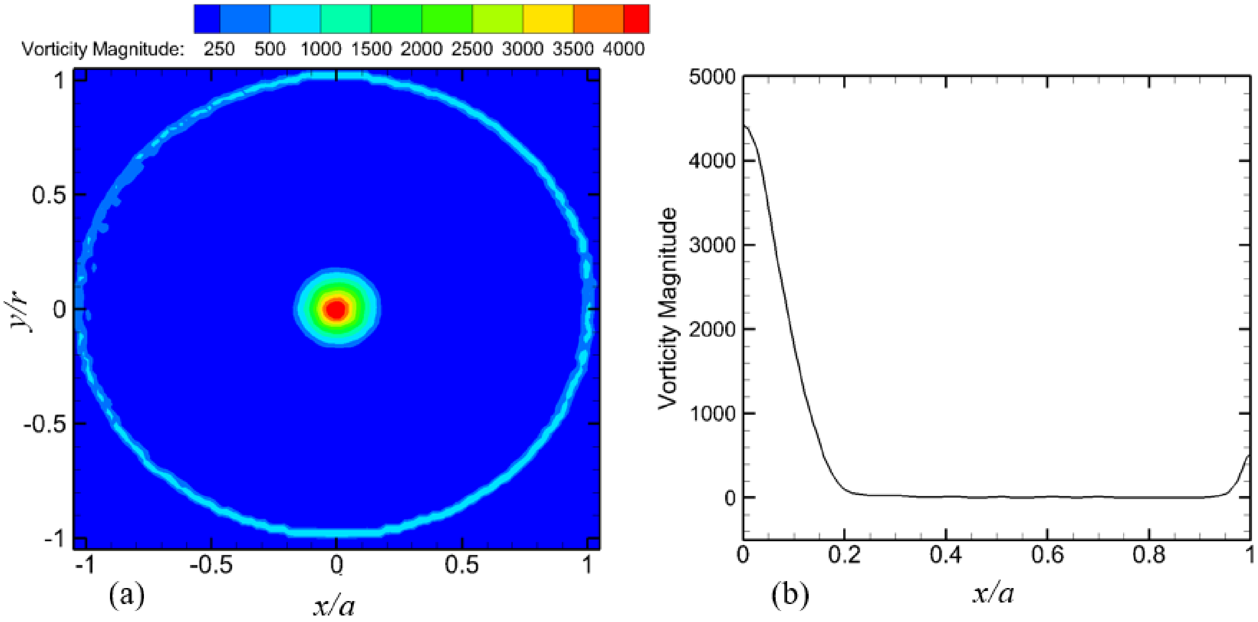

Figure 4.7 **(a) Contours of vorticity magnitude and, (b) the radial distribution of the axial vorticity magnitude at the chamber midplane, *z/L* = 0.5.**

The radial velocity profile showcases the relative inwards or outwards flow regions within the chamber. The radial distribution of the radial velocity in Figure 4.6b displays negative values, with zero radial velocity bounding it, both at x/*a* = 1 (chamber wall, no sidewall injection) and at x/*a* = 0 (chamber centerline). However, within the chamber, there is some crossflow of the fluid from the outer vortex into the inner vortex. The same observation has been suggested in the analytical solutions [10] presented in Sec. 2.2. The location of the maximum magnitude of the radial velocity, however, appears in the vicinity of the chamber centerline, which is different from the CRZ-free analytical models, which predict it to be around $r/2$.

The presence of the vortical flow can also be verified by the distribution of the axial vorticity magnitude, presented in Figure 4.7a, and its radial distribution in Figure 4.7b. The rotational forced vortex in the inner core concentrates the vorticity in the center of the chamber as shown in Figure 4.7 at *x/a* = 0. In contrast, the flow in the free vortex tail is irrotational with constant circulation. The viscous interaction at the chamber walls gives rise to vorticity in the wall boundary layer and is observed in Figure 4.7, at x/*a* = 1.

With the above discussion, it is established that the confined flowfield is vortex-dominated. In what follows, the bidirectional behavior is investigated with the axial velocity distribution presented in Figure 4.8.

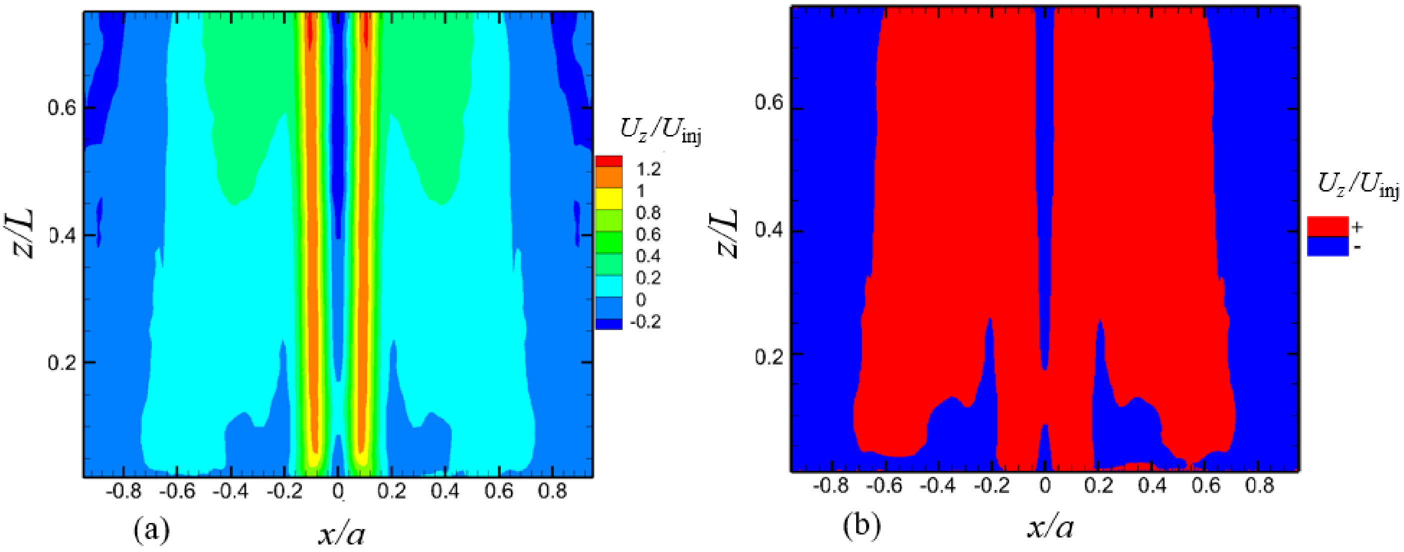

Figure 4.8 (a) Contours of axial velocity and, (b) the mantle structure.

It is reiterated that due to the experimental setup there is limited optical access near the chamber sidewalls and through the injection plate; as such, the entire cross-section of the chamber is not accessible, as shown in Figure 4.2a. However, the important features such as the location of the mantle and the formation of recirculation zones are not compromised in the experiments. The bidirectional behavior of the flow remains evident from the above figure, where the head-bound flow displays clear negative U_z, identified by the legend and the exit-bound flow is indicated by the positive U_z. The tangential injection at the injector plate leads to a cyclonic flow that travels towards the headwall while being drawn towards the chamber sidewall under the effect of the centrifugal forces. At the head-end, the flow turns inwardly under the influence of the headwall, ultimately changing its polarity before exiting the chamber. The two oppositely traveling fluid streams are separated by a rotating but not traversing free cylindrical boundary called the mantle, which can be easily identified in Figure 4.8b at the boundary of the red and blue contours. The mantle shape is slightly conical, whereas the analytical studies [10] suggest it to be at a constant radius and therefore a straight line. The experimental mantle lies within the bounds suggested by the analytical solutions (0.628r to 0.707r) depending on the solution model. The head-bound flow, colored in blue, in Figure 4.8b in the vicinity of the centerline, does not define the mantle, but is due to the secondary flow or due to the vortex breakdown.

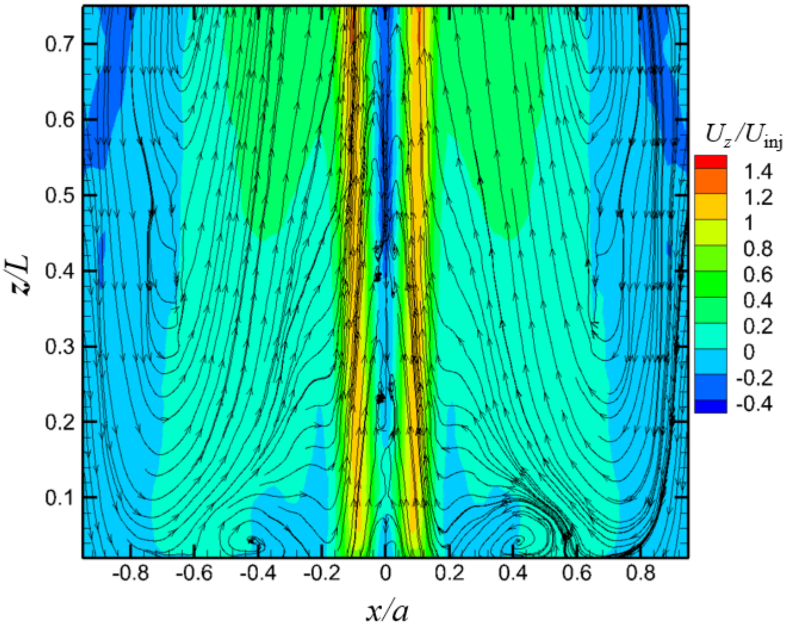

Figure 4.9 Projected streamlines in the *r*-*z* plane.

The flow pattern observed here is similar to the flow structure presented in the flow visualization results in Figure 4.4 d. The head-bound motion, followed by the turning of streamlines across the mantle and subsequent movement towards the exit is evident. However, two important features are noteworthy. First, the formation of the central recirculation zone (CRZ) along the axis of the chamber, and second, a stable focus that illustrates a cross-section of doughnut shape, that rotates with the bulk tangential velocity near the headwall of the chamber. The formation of CRZ is typically observed for flows with swirl no. above 0.6 [65]; for the presented case, we have $S = 2.04$, therefore the breakdown of vortex and formation of CRZ is expected. The formation of CRZ is a function of V, outlet radius, and swirl no. [78]; the results based on the variation of these parameters are presented later in Secs. 4.4, 5.3, and 5.5 respectively.

The tangential fluid stream that enters the chamber produces strong centrifugal forces, which push the flow towards the chamber walls as it travels towards the headwall. This coupled with the strong adverse pressure gradient along the chamber centerline, leads to the formation of a columnar axisymmetric recirculation zone, as seen in Figure 4.9. The outflow highlighted by the high axial velocity component surrounding the CRZ in Figure 4.9 represents the head-induced flow, which originates from within the headwall boundary layer. In the headwall boundary layer, the imbalance between the centrifugal forces and radial pressure gradient drives the flow radially towards the center before turning along the centerline. Due to the limited optical access very close to the headwall and the laser reflection, the headwall boundary layer in the above figure is obscured; however, it may be inferred from the flow visualization results presented in Figure 4.4. The head-induced axial flow separates the CRZ from the bulk motion in the chamber. Thus, the flow within the chamber consists of four major parts. These are the outer head-bound vortex, the inner exit-bound vortex, the head-induced flow, and the central recirculation zone, in the order of decreasing radial distance from the chamber centerline. The first two, the outer and inner counter flowing vortices are well documented in the literature [10]. However, the latter two components, i.e. the head-induced flow and the central CRZ motion do not appear in the analytical solutions that do not take into account viscous flow instability.

The shear between the high radial velocities in the headwall boundary layer and very low radial velocity in the bulk tangential motion of the chamber also give rise to the Kelvin-Helmholtz instability in the form of the doughnut structure shown in Figure 4.9 near the headwall. However, due to the much lower magnitude of this velocity difference as compared to the large velocity gradient that exists between the head-induced axial flow and the reverse flow in the CRZ, this instability is not evident in the vorticity contour plot presented in Figure 4.10.

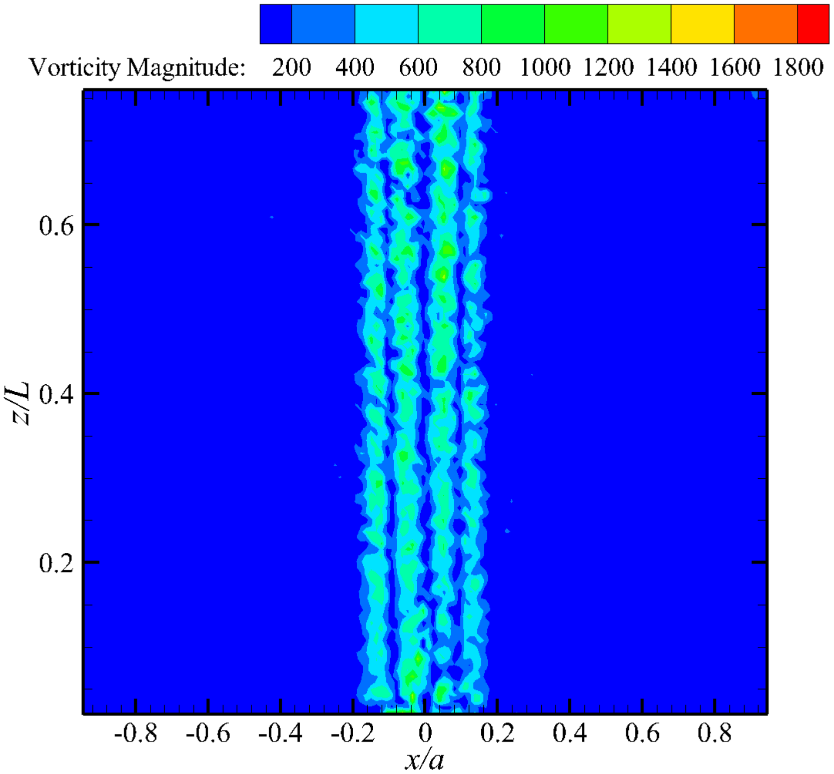

Figure 4.10 The magnitude of vorticity distribution in the *r-z* plane.

The outer pair of vorticity columns represents the free shear layer that exists between the inner vortex and the head-induced flow, whereas the inner pair of vorticity columns represents the interaction between the head-induced flow and the CRZ. The location of these vorticity columns is also corroborated with the gradients in the axial velocity contour presented in Figure 4.8 (a).

4.3 Variation with Height within the Chamber.

With the discussion in Sec. 4.2, it is established that the flowfield is bidirectional and is vortex-dominated. Although the variation in the flowfield along the length of the chamber can be seen in the *r-z* plane, this section is dedicated to quantitatively compare the variation in the flowfield at different *z/L* on both the axial plane and the tangential plane. Six equidistant z/L locations were selected to explore this effect, including *z/L* = 0.125 (close to headwall) and 0.75 (close to the injector plate) as shown in Figure 4.11.

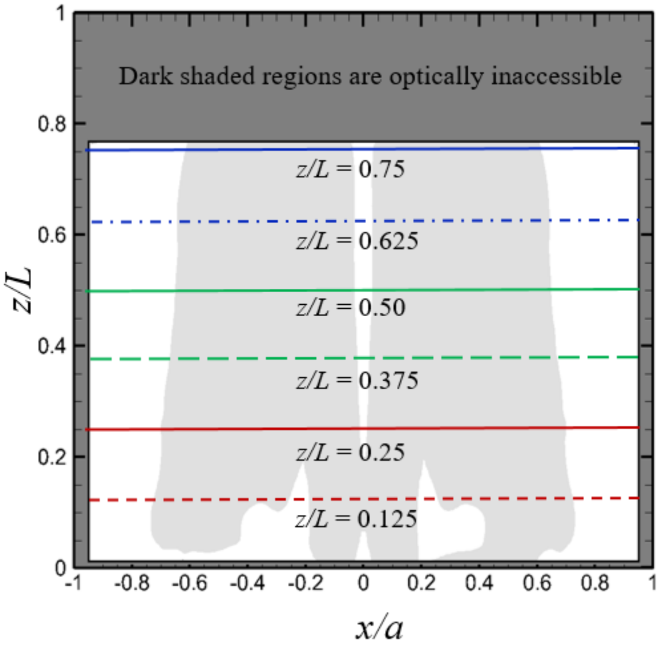

Figure 4.11 Location of *z/L* planes for investigation in the *r-z* plane.

The selection of these locations is influenced by the optical access limitations, highlighted earlier, where the excessive reflections from the headwall and the opaqueness of the injector plate become limiting factors. Figure 4.12 presents the axial velocity distribution at the six *z/L* locations in the chamber. A zero-line has also been included in the figure to identify the mantle location as it varies with the distance from the headwall. It is observed that the mantle location is not a straight line but follows a slightly conical shape as seen in figure 4.8b. The mantle location moves towards the chamber centerline near the exit plate, whereas closer to the headwall it moves towards the chamber sidewalls. The convergence of the outgoing flow near the centerline at the exit is due to the limited contraction ratio, $\beta = 0.25$ in this case. This is in contrast to the analytical models [10] which predict the mantle to be at a fixed radial position irrespective of the height in the chamber, though a much larger outlet radius that results in $\beta = 0.628$ or 0.707 is used in the analytical models. The variation of mantle structure with outlet size is presented and discussed later. Similar conical mantle shapes have been reported in various experimental studies on the cyclone separators and bidirectional vortex chambers, [37,40]. Its small deviation from a straight cylinder could be attributed to the viscous endwall effects that are not yet incorporated in the analytical models. Despite the variation of the mantle location with respect to the distance from the headwall, the mean location remains within the bounds of the analytical mantle location obtained by various solutions.

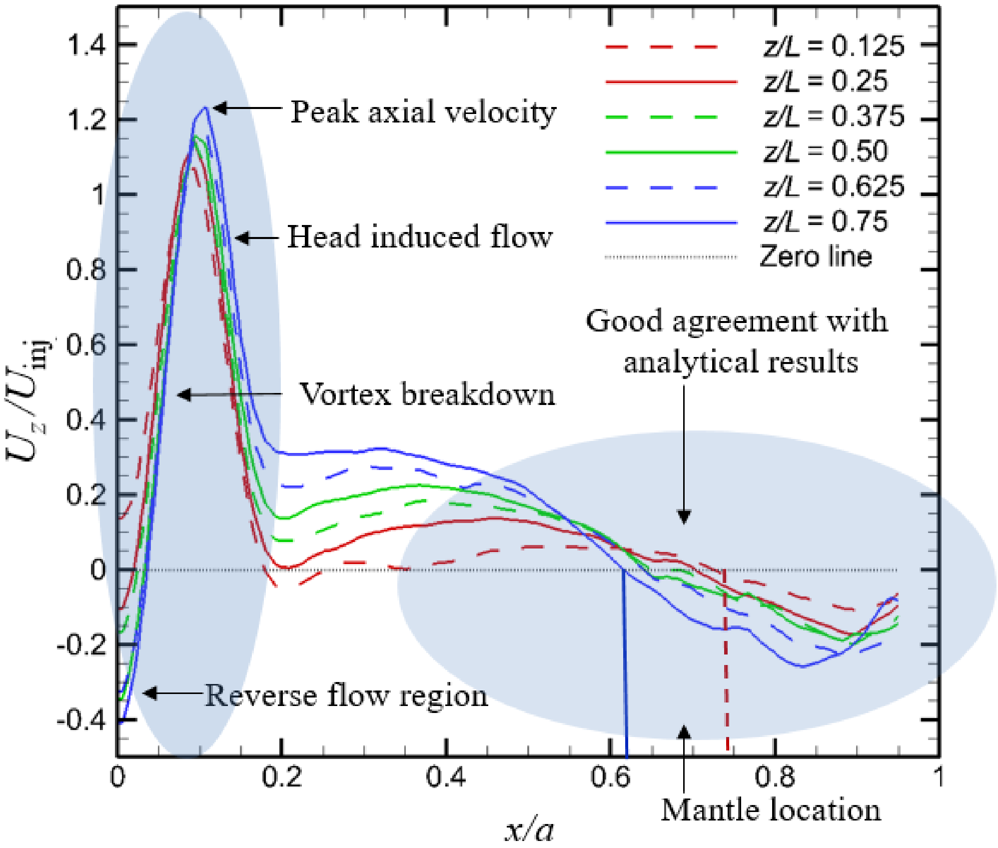

Figure 4.12 Axial velocity distribution at six different *z/L* locations.

The overall distribution of the axial velocity can be divided into two regions highlighted in Figure 4.12. The region towards the sidewall at (x/a = 0.4 to 1.0) agrees well with the analytical solutions presented in Figure 2.14, whereas, the region in the vicinity of the chamber centerline (x/a = 0 to 0.2) differs significantly, in the form of a sudden peak in the axial velocity and the reverse flow in the center. The operating conditions presented in Table 4.1 show that the swirl number is beyond the critical swirl number of S = 0.6, suggested in the literature [65,78,81,82]. Therefore, the vortex breakdown results in the formation of the CRZ, represented by the reverse flow along the centerline. The increase in the axial velocity is due to the head-induced flow which envelops the central recirculation zone along the chamber axis. The conservation of axial momentum also dictates a rise in the axial velocity to cater for the reverse flow. The peak axial velocity and the reverse flow both have higher magnitudes near the chamber exit.

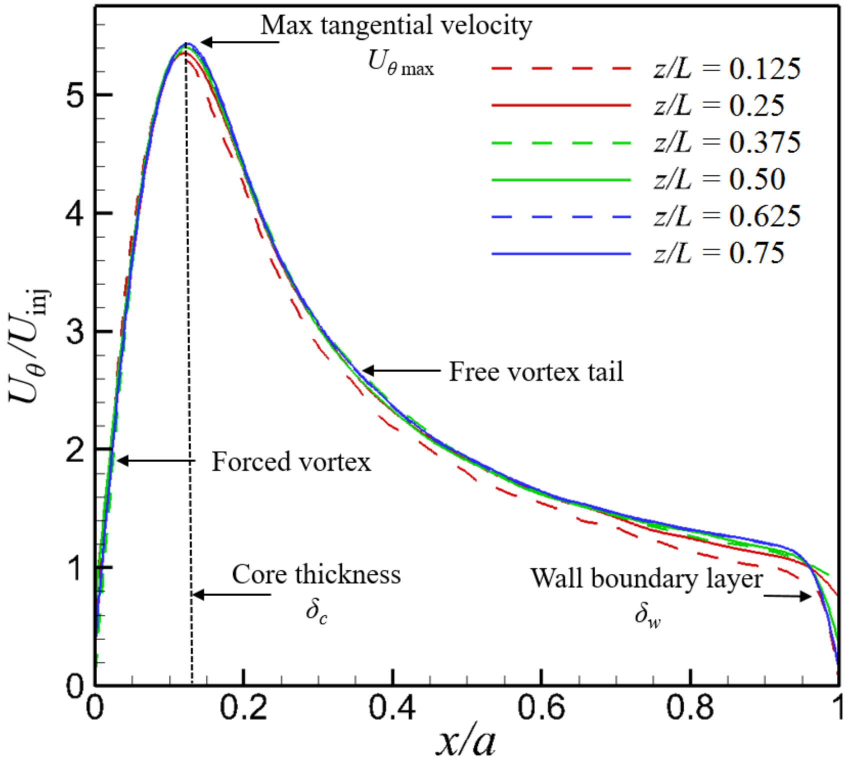

Figure 4.13 Tangential velocity distribution at different *z/L* locations.

The tangential velocity measured at the six *z/L* locations and its contours are presented in Figures 4.13 and 4.14, respectively.

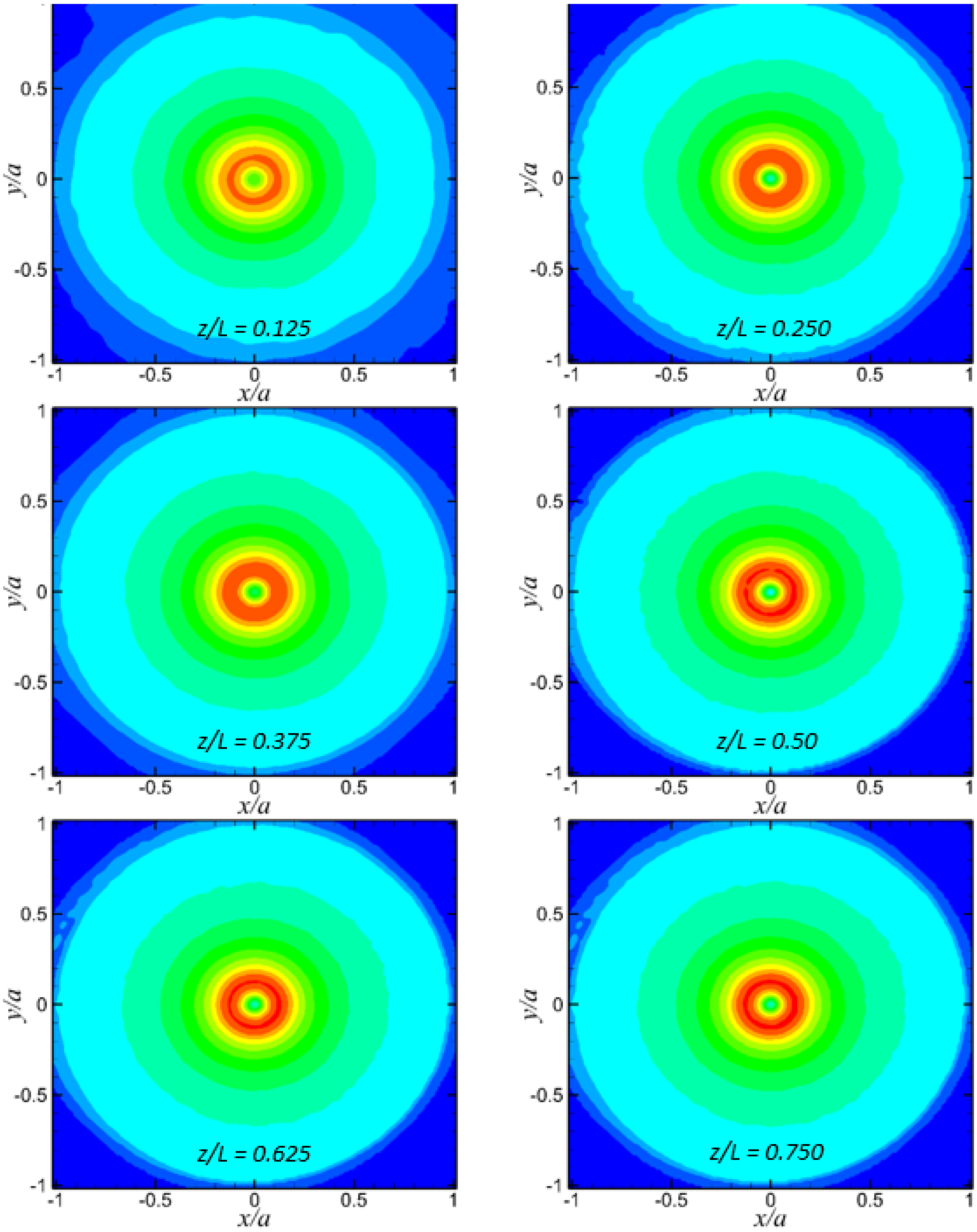

Figure 4.14 Tangential velocity contour on the *r*-*z* plane at different *z/L* locations.

From a comparison of Figures 4.13 and 4.14, it is observed that there is a negligible effect of the vertical location on the tangential velocity profile. This is also a very important stability consideration, as the coherence of the vortex structure depends on the conservation of the angular momentum. Thus, the axial invariance of the tangential velocity ensures the stability of the confined vortex structure. The six velocity profiles collapse together except in the viscous-dominated regions, both at the forced vortex and the wall boundary layer. The decrease in the $U_{\theta\,\max}$ and $U_{\theta\,\text{wall}}$ near the headwall at $z/L = 0.125$ with increased distance from the injection (near $z/L = 0.75$) is due to viscous diffusion and dissipation respectively. This very week dependence of the tangential velocity on the axial distance is also supported by the literature on the bidirectional vortex [10], where tangential velocity is found to be a function of $(z\,\kappa^2)$ with $\kappa \approx 10^{-2}$.

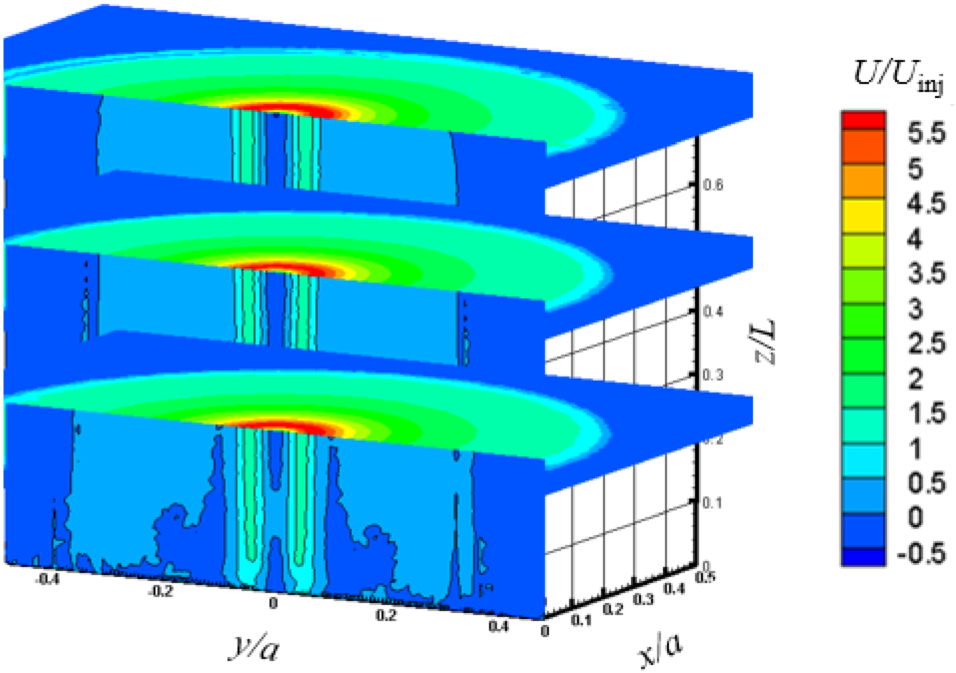

Figure 4.15 Contours at selected *z/L* locations plotted for comparison.

The cumulative flowfield is presented in Figure 4.15; the contours are colored by the tangential velocity in the r-θ plane, and by the axial velocity in the r-z plane.

In order to ascertain the pressure distribution in the chamber, the coefficient of pressure for the incompressible operating fluid is calculated by Eq. (4.3).

$$C_p = 1 - \left(\frac{U}{U_{inj}}\right)^2 \qquad 4.3$$

where U is the local velocity at any given location.

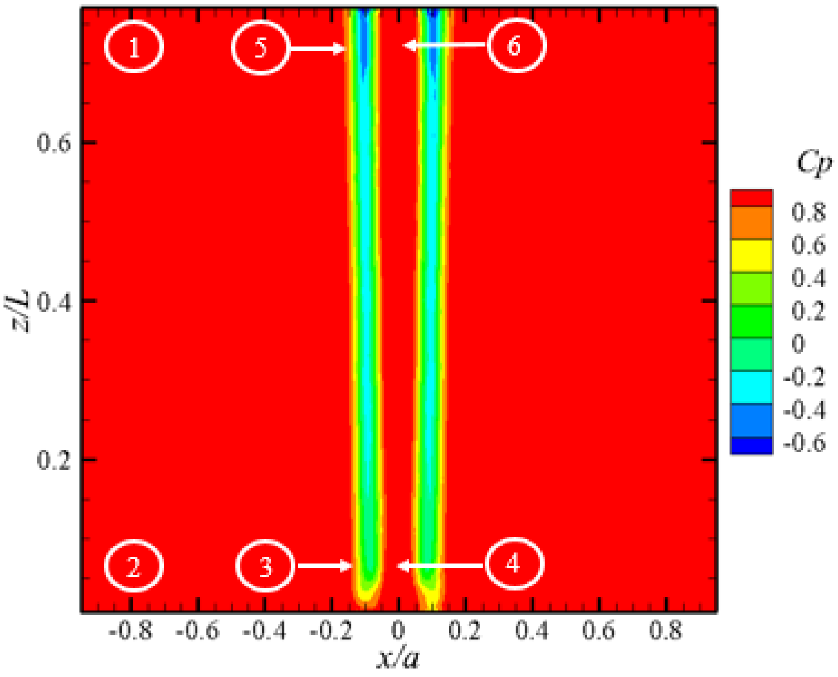

Figure 4.16 Contour of coefficient of pressure in the *r-z* plane.

The pressure distribution within the chamber can be seen in Figure 4.16, various locations have been marked to explain the pressure variation. The tangential fluid stream that enters the chamber produces strong centrifugal forces, which push the flow towards the chamber walls as it travels from the injection port at location 1, towards location 2 at the headwall. The pressure at location 3, is significantly lower than location 2 ($P_3 < P_2$), due to the very high tangential velocity near the chamber centerline as seen in Figure 4.14. However, the pressure at location 4, *x/a = 0*, headwall center is much higher and is close to stagnation pressure due to the formation of the recirculating zone. Along the chamber centerline, the pressure decreases from the headwall to the exit plate, such that $P_5 < P_3$, due to the higher tangential velocity close to the exit plate, at *z/L* = 0.75, as compared to the headwall, at *z/L* = 0.125, as seen in Figure 4.13. This axial pressure gradient is responsible for the flow to turn towards the exit plate from the headwall. The pressure at station 6 is much higher due to the reverse flow region as discussed earlier.

4.4 Variation with the Vortex Reynolds Number, *V*

Various studies [4,10,37] on flows in confined cyclonic chambers have shown that in addition to the geometrical parameters, the operating conditions also affect the magnitude of velocity components and their relevant characteristics. This section is dedicated to characterizing the effect of operating conditions in terms of the vortex Reynolds number on the flowfield. This is achieved by controlling the inlet volume flow rate, which affects the change of inlet velocity. In the present study, the results are obtained for five different vortex Reynolds numbers of 1240, 2470, 3710, 4940, and 6180. The results in the *r-z* plane are presented in Figures 4.17 and 4.18 for dimensional axial velocity, and Figures 4.18 and 4.19 for non-dimensionalized axial velocity.

Table 4.2 Geometric and operating conditions.

Geometric Parameters		Operating Parameters		
Chamber Radius, a	1 in	Modified Swirl no. $\sigma = a^2 / A_i$		2.6
Contraction Ratio, β	0.353			
Inlet Diameter, d_{inlet}	0.35 in	Geometric Swirl no. $S = (\pi d_e a) / (2 A_i)$		2.89
Chamber AR, $l = L/a$	2			
Vortex Re ($Qi / \nu L$)				
1240	2470	3710	4940	6180

First, it is observed that whereas the axial velocity magnitudes scale directly with the vortex Reynolds number, the distribution of the velocity does not change. For the five cases, the basic flowfield and the shape of the mantle are the same, where the four constituent parts of the flowfield, the outer head-bound vortex, the inner exit-bound vortex, the head induced flow, and the central recirculation zone are observed irrespective of V. In a numerical study for a unidirectional confined cyclonic motion by Wang et al. [78], the constituent parts are found to vary with the tangential Reynolds number. However, the range of the Re_θ, where $\left(Re_\theta = \frac{U_{inj} D}{\nu}\right)$, for which the CRZ does not appear is below 220. This tangential Reynolds number corresponds to a vortex Reynolds number of less than 10. Such a low value could not be reproduced with the present experimental setup. We concluded that the flow structure in the axial velocity, especially within the range of the vortex Reynolds number studied here, does not change significantly with V.

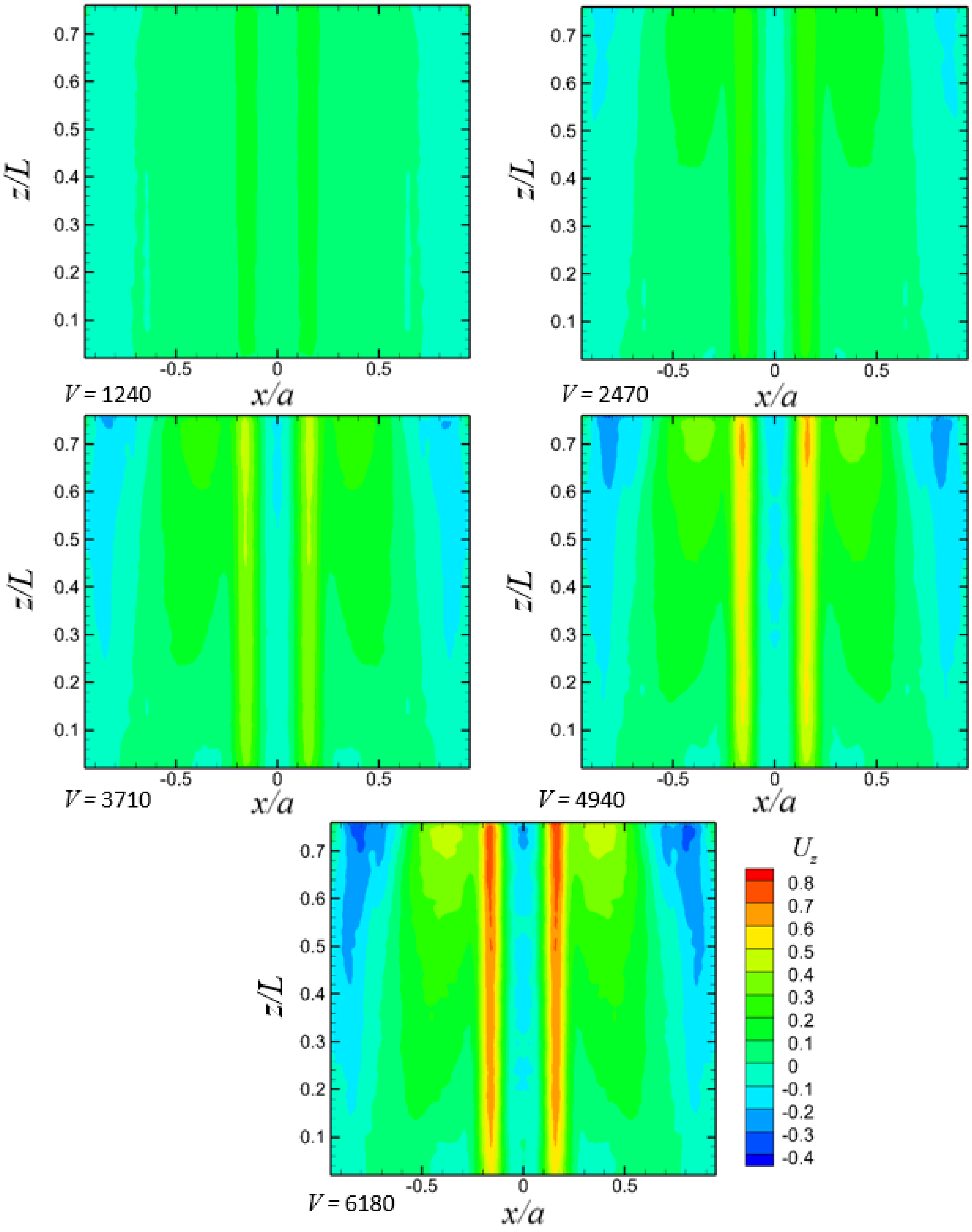

Figure 4.17 Contours of axial velocity for different values of *V*.

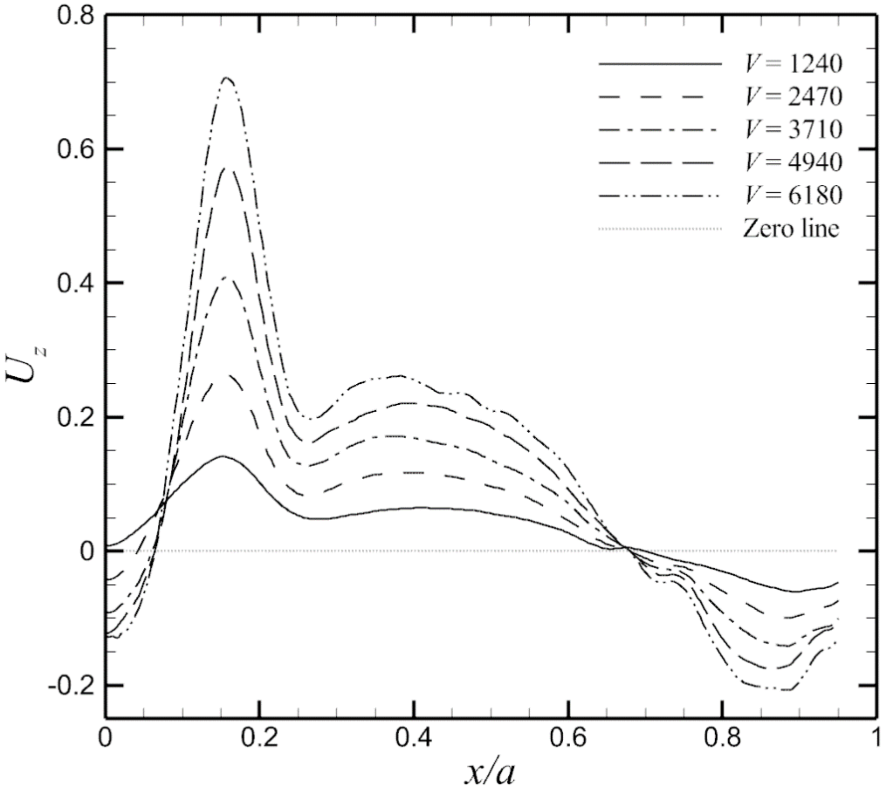

Figure 4.18 Radial distribution of axial velocity for different values of *V*.

To make a better comparison among the five cases, contours of the non-dimensional axial velocity are presented in Figure 4.19-20. It can be seen that not only the velocity magnitudes collapse together but the location of the maximum axial velocity in the head-induced region and mantle also do not vary with *V*. The only quantifiable difference is in the magnitude of the maximum reverse flow velocity within the CRZ, which can be attributed to the imbalance between the centrifugal forces exerted on the fluid particles that are proportional to the square of the tangential velocity and the adverse pressure gradient. These do not scale linearly with *V* and manifest themselves as the change in the reverse flow velocity magnitude.

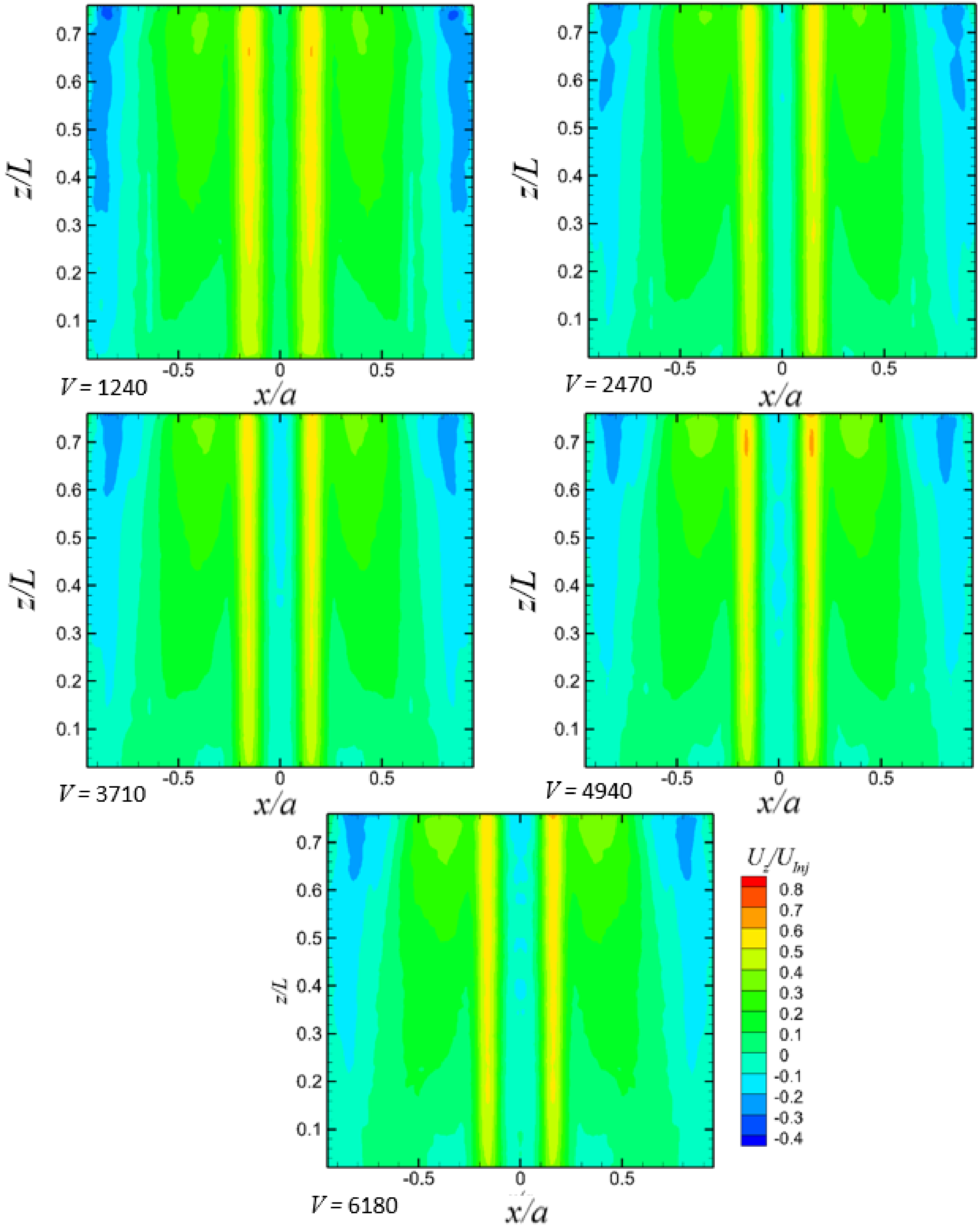

Figure 4.19 **Non-dimensional axial velocity contours for different values of *V*.**

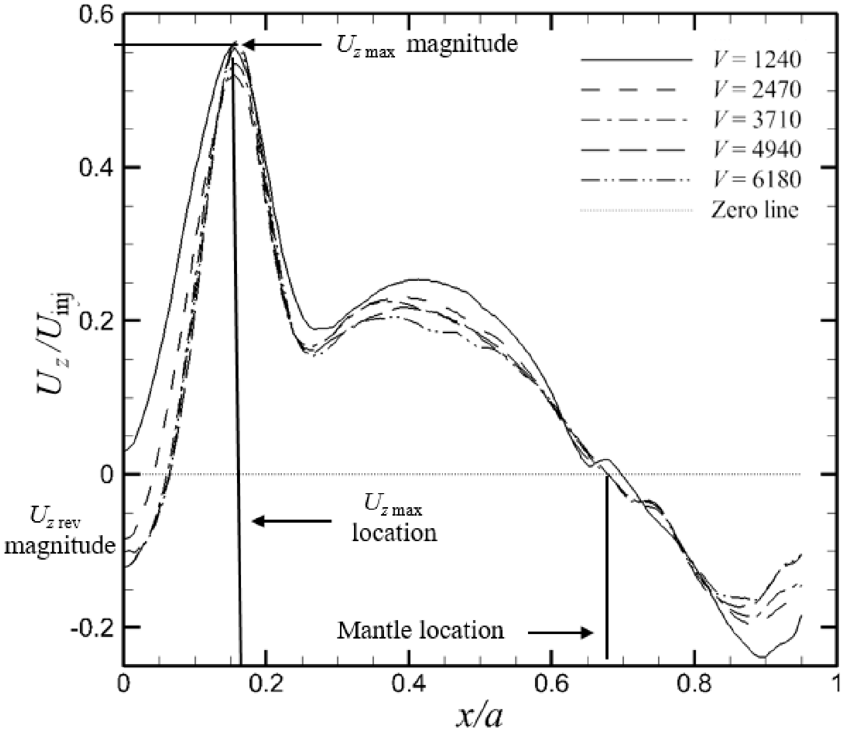

Figure 4.20 Radial distribution of the non-dimensional axial velocity at different values of *V*.

The influence of the *V* on the tangential velocity profile is rather more pronounced, where it affects not only the magnitude but also the distribution and relevant characteristic dimensions. The *V* not only scales with the magnitude of the inlet velocity but also prescribes the viscous behavior in the cyclonic chamber. The increase in *V* represents an increase in the ratio of inertial to viscous forces as well. As the characteristics such as core thickness δ_c, and wall boundary layer thickness δ_w, are prescribed by viscous effects, the vortex Reynolds number is expected to influence these via viscous damping. It has been shown in the literature [10] that for a given geometrical configuration the maximum tangential velocity $U_{\theta\max}$, relates directly to $\sqrt{V}$, whereas the core thickness δ_c and the wall boundary layer thickness δ_w, scale inversely with $\sqrt{V}$.

The contours of tangential velocity in the midplane at $z/L = 0.5$ for the five different *V* are presented in Figure 4.21. The variation in tangential velocity with *V* is obvious; higher *V* results in higher tangential velocity and vice versa. Moreover, the presence of a forced vortex core and of a free vortex tail is observed for all values of *V*.

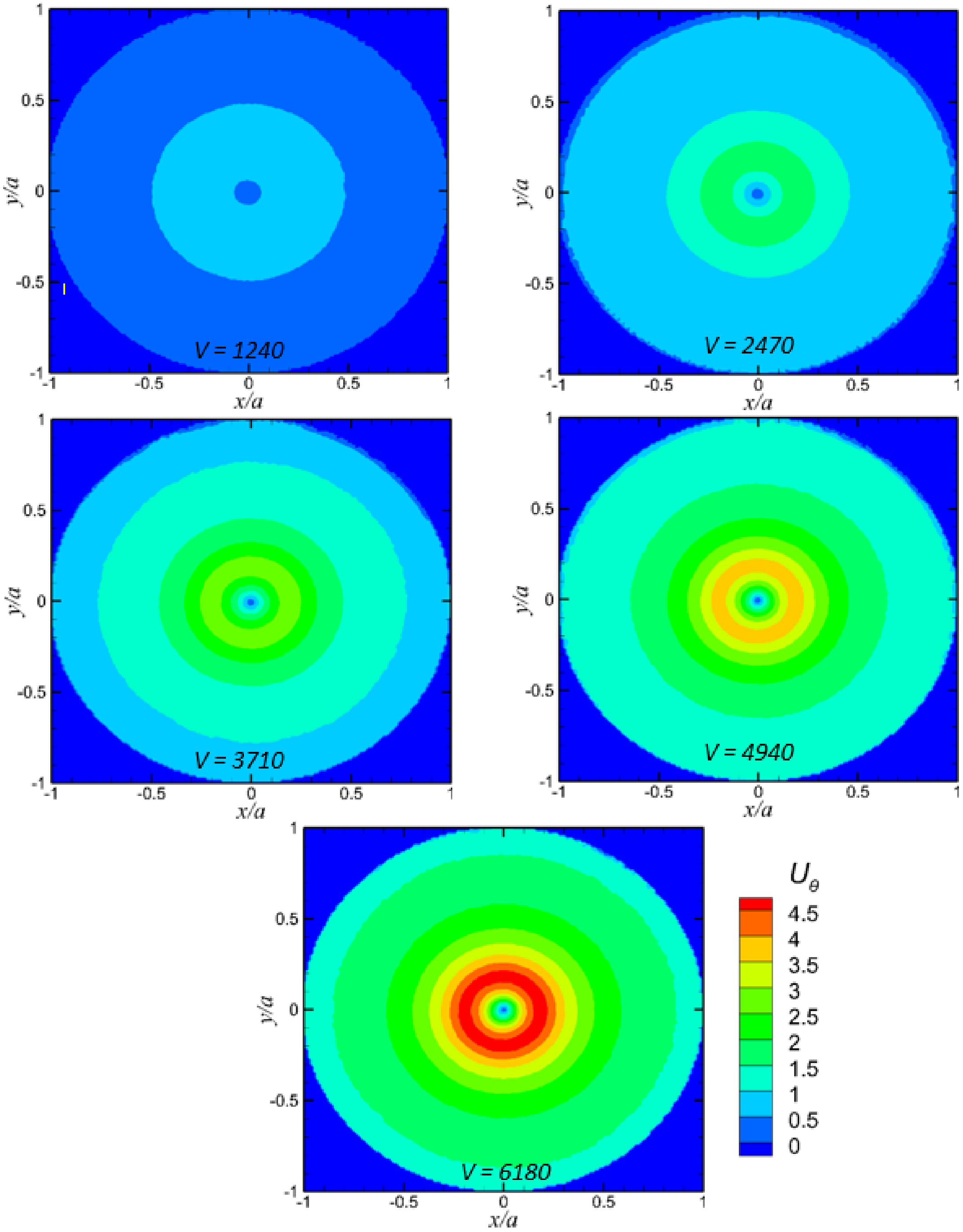

Figure 4.21 Tangential velocity contours on the mid-plane at different values of *V*.

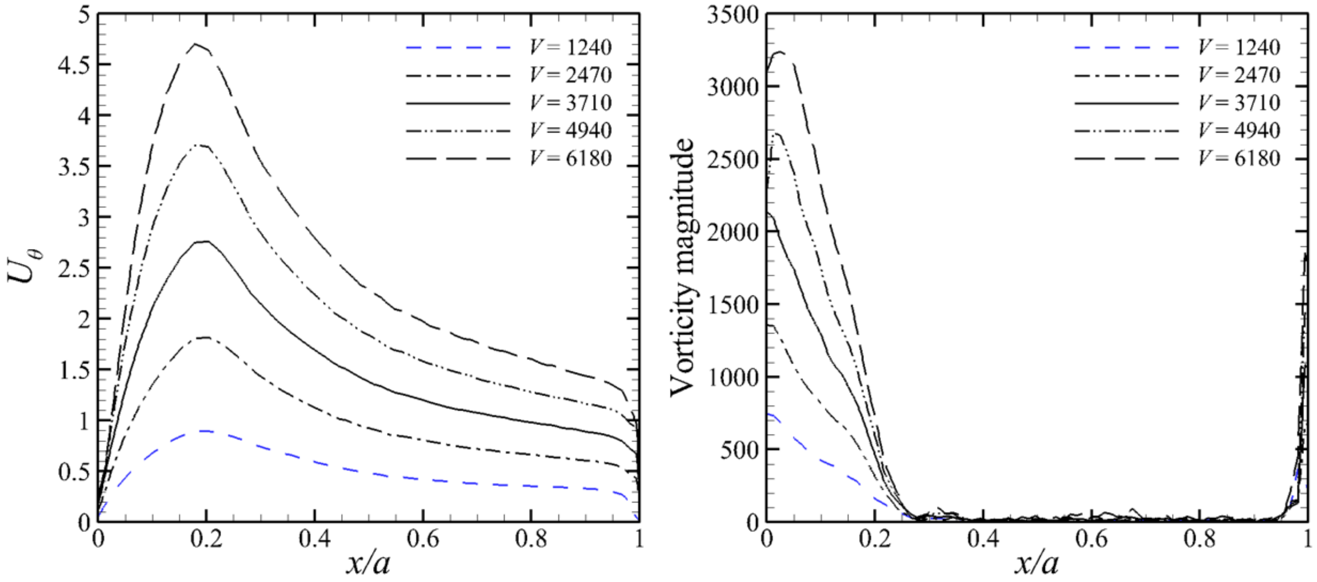

Figure 4.22 The tangential velocity and vorticity magnitude at different values of *V* at the midplane of the chamber.

Figure 4.22 presents the radial distribution of the tangential velocity and vorticity magnitude at the mid-plane of the chamber. It was observed that both the tangential velocity and the vorticity magnitude both in the forced vortex core and the wall boundary layer scale directly with the increase in *V*. The vorticity in the free vortex remains zero showing its irrotational behavior and is not affected by *V*.

The locations of peak tangential velocity and the wall boundary layer are affected by *V*; however, their variation is difficult to compare from a dimensional plot such as in Figure 4.22 Therefore, the radial distribution of the non-dimensional tangential velocity is presented in Figure 4.23.

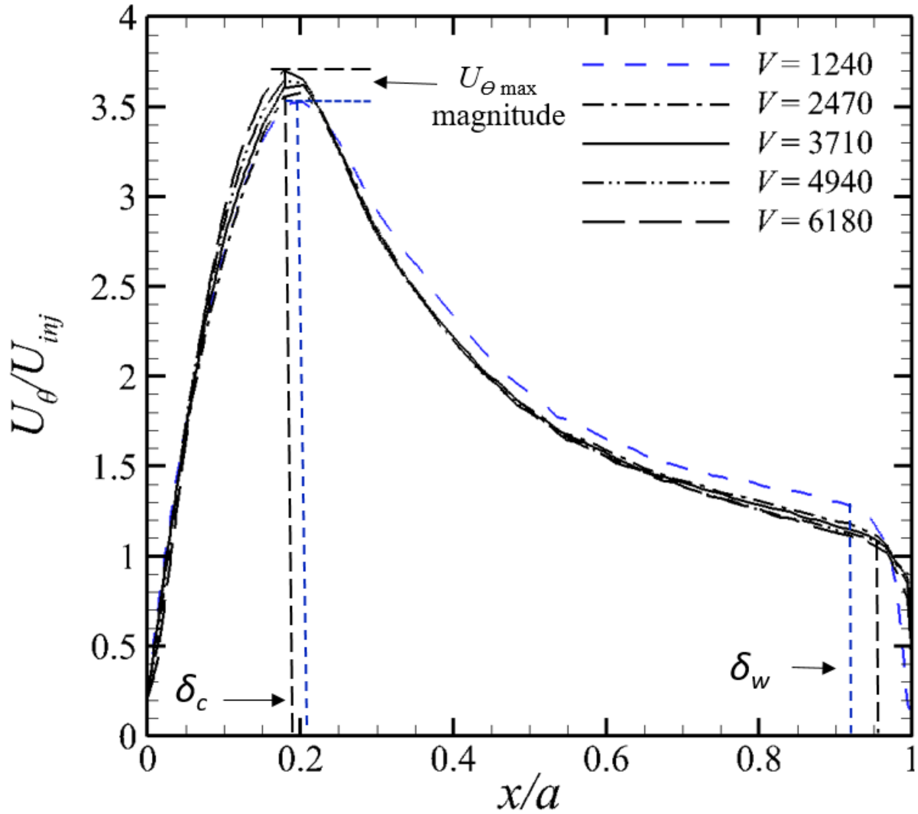

Figure 4.23 Tangential velocity distribution at different values of *V*.

The increase in the injection velocity as a consequence of an increased *V* results in a higher tangential velocity in the chamber which gives rise to a more coherent vortex. It is observed from Figure 4.23 that a higher vortex Reynolds number leads to a higher peak of the non-dimensional tangential velocity. This increase in the peak tangential velocity results in reduced pressure along the centerline which, in turn, results in vortex stretching in the axial direction. The vortex core thickness is reduced as a consequence of the conservation of angular momentum and vortex stretching. The location of the peak tangential velocity also shifts towards the chamber centerline which reflects the role of the vortex Reynolds number in controlling the thickness of the viscous dominated core. The viscous boundary layer that develops along the walls of the chamber also diminishes with the increase in *V*. Thus, a higher vortex Reynolds number leads to a thinner δ_c and δ_w.

4.5 Comparison with Analytical Models

The observations noted above are in line with the results presented by Majdalani [10]; however, a direct quantitative comparison can not be made without realizing that the analytical models are inviscid, and are only modified by viscous corrections that are obtained asymptotically from the laminar Navier-Stokes equations. In this experiment, however, the high velocities result in increased turbulent viscosity. Thus, there is a need to calculate the effective vortex Reynolds number that takes into account the increased eddy-viscosity. However, the eddy viscosity for the current experimental operating conditions is unknown, and measuring it remains a universal problem and an area of active research. Also, the eddy viscosity is expected to change within the domain of the experiments as well. However, an approach to this effect has been presented by Maicke and Majdalani [12] where the effective vortex Reynolds number is calculated based on the eddy viscosity ratio, l_t, a constant value that is appropriate for the given conditions. Although this is a first-order approximation, it has proved to work well [12] in the absence of a more sophisticated approach. A similar approach has been developed independently by Faler and Leibovich [83] and Escudier et al. [84]. The relation for l_t is given as:

$$l_t = \frac{\mu_t}{\mu_l} = \frac{\nu_t}{\nu_l} \tag{4.3}$$

here μ and v are dynamic and kinematic viscosity, with the subscripts t and l represent turbulent and laminar conditions, respectively. This yields the effective vortex Raynolds number, V_{eff} as [19]:

$$V_{eff} = \frac{\rho U A_i}{\mu_t \, L} = \frac{\rho U A_i}{\mu \, l_t \, L} = \frac{V}{l_t} \tag{4.4}$$

In order to determine the eddy viscosity ratio such that the experimental and analytical results could be matched, a constant value for l_t was initially determined, such that the analytical solution for effective V_t, will yield the same $U_{\theta\max}$ as the experimentally determined value at $V = 3710$ (the median value in the range of V tested). It yielded $l_t \approx 54$. Maicke and Majdalani [10] found an average value of $l_t \approx 152$, for a similar experiment [28] by using a modified least-squares method on matching radius. However, those experiments [28] were at much high values of V (22000 to 48000), which is an order of magnitude larger than the present experiment. As the eddy viscosity ratio is expected to change over a large variation in V, the lower value determined in the current experiment seems appropriate. Thus, the $U_{\theta\max}$ and δ_c are calculated using $l_t \approx 54$ for the linear Beltramian solution (Eq 2.2) while replacing V with V_{eff}. The experimental and analytical results are tabulated in Table 4.3 and presented in Figures 4.24-25.

Table 4.3 The characteristic values for the analytical solution and the experimental data presented in Figure 4.22.

V	**Experimental**		**From Eq (2.2), Linear Beltramian solution**			
			l_t = constant ≈ 54		$l_t = aV^b$, $a = 0.022$, $b = 0.95$	
	$U_{\theta\max}$	δ_c	$U_{\theta\max}$	δ_c	$U_{\theta\max}$	δ_c
1236	3.513	0.208	2.089	0.343	3.516	0.203
2471	3.581	0.203	2.953	0.242	3.578	0.200
3707	3.617	0.198	3.617	0.198	3.614	0.198
4943	3.642	0.189	4.177	0.171	3.640	0.197
6179	3.701	0.178	4.670	0.153	3.661	0.195

Since $V = 3710$ is used to determine the eddy viscosity ratio, the analytical and experimental results were matched for $V = 3710$, however for the remaining data points, the constant $l_t \approx 54$ does not yield a good agreement as evident, from Figures 4.23-4.24. The trend observed in the figures suggests that the eddy viscosity ratio must be expressed as a function of V; as such, the eddy viscosity is recast as a function of V with the following form:

$$l_t = a\,V^b \tag{4.5}$$

here a and b are constants.

The values of the coefficients a and b can be determined by matching the analytical and experimental $U_{\theta\,\max}$ values for $V = 2470$ and 3710. This yields $a = 0.022$ and $b = 0.95$. The results for $U_{\theta\,\max}$, δ_c and ω_f (solid body angular velocity) are plotted in Figures 4.23, 4.24, and 4.25 respectively.

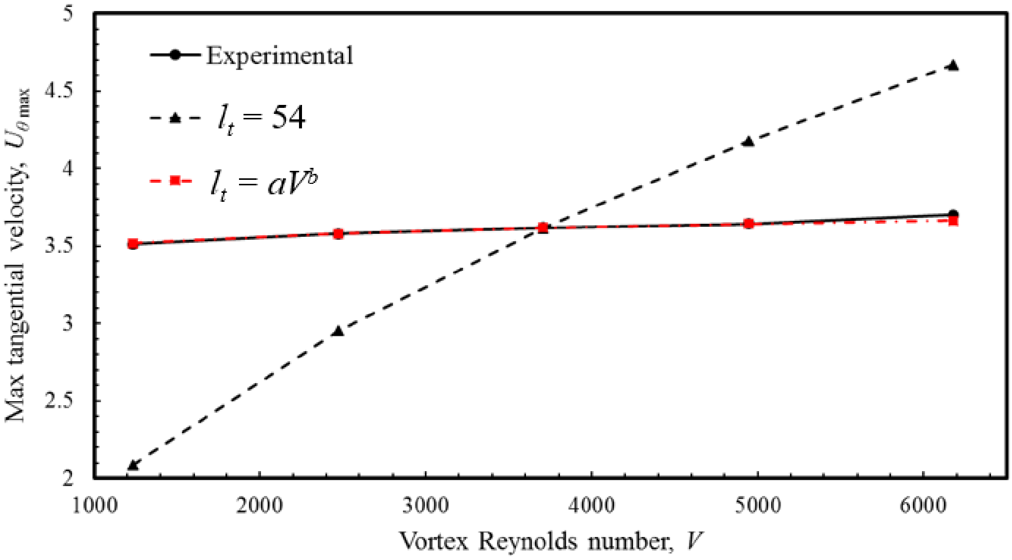

Figure 4.24 Comparison between experimental and analytical results for $U_{\theta\,\max}$.

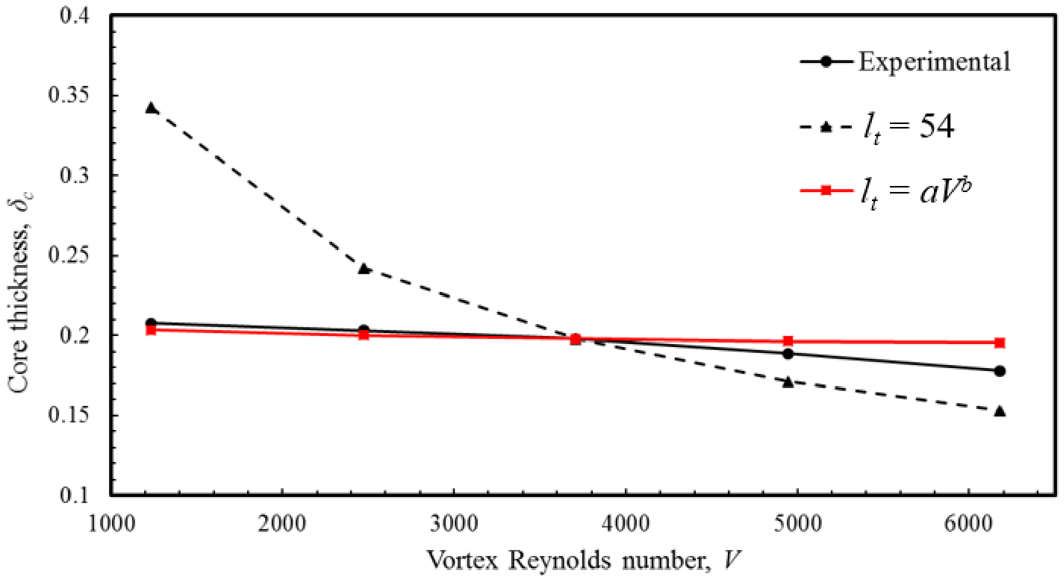

Figure 4.25 Comparison between experimental and analytical results for δ_c.

The angular velocity of the forced vortex was computed from the tangential velocity distribution and compared against two different analytical models, the Complex-Lamellar and the Linear Beltramian, using the eddy viscosity approach.

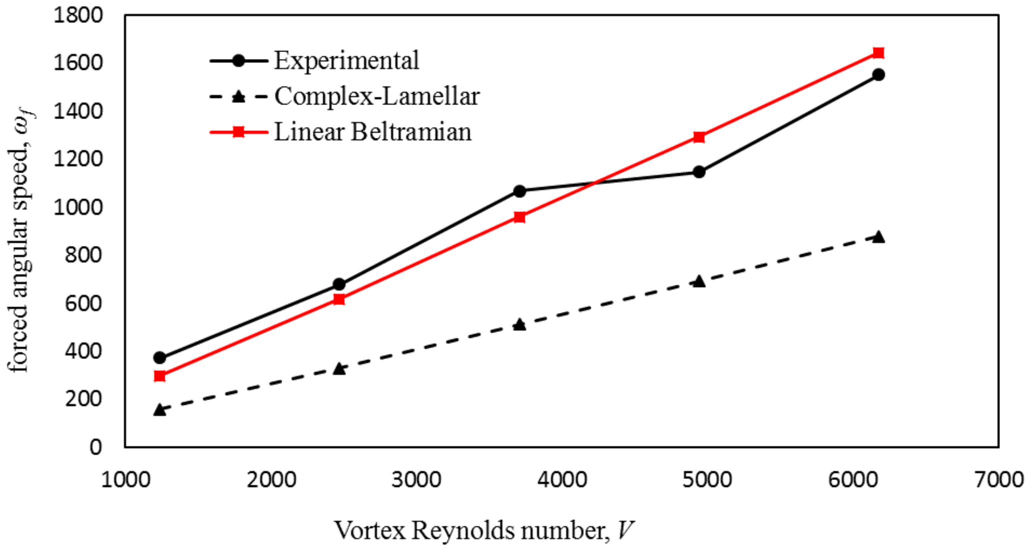

Figure 4.26 Comparison between experimental and analytical results for ω_f.

The calculation of wall boundary layer thickness from the measured tangential velocity profile presented significant challenges, due to higher viscous forces on the seeding particle and higher measurement uncertainty in the near curved wall region. However, an estimate of the wall boundary layer thickness based on the tangential velocity distribution is presented in Figure 4.27, where the vertical lines near *x/a* = 0.9 identify the experimentally determined wall boundary layer thickness.

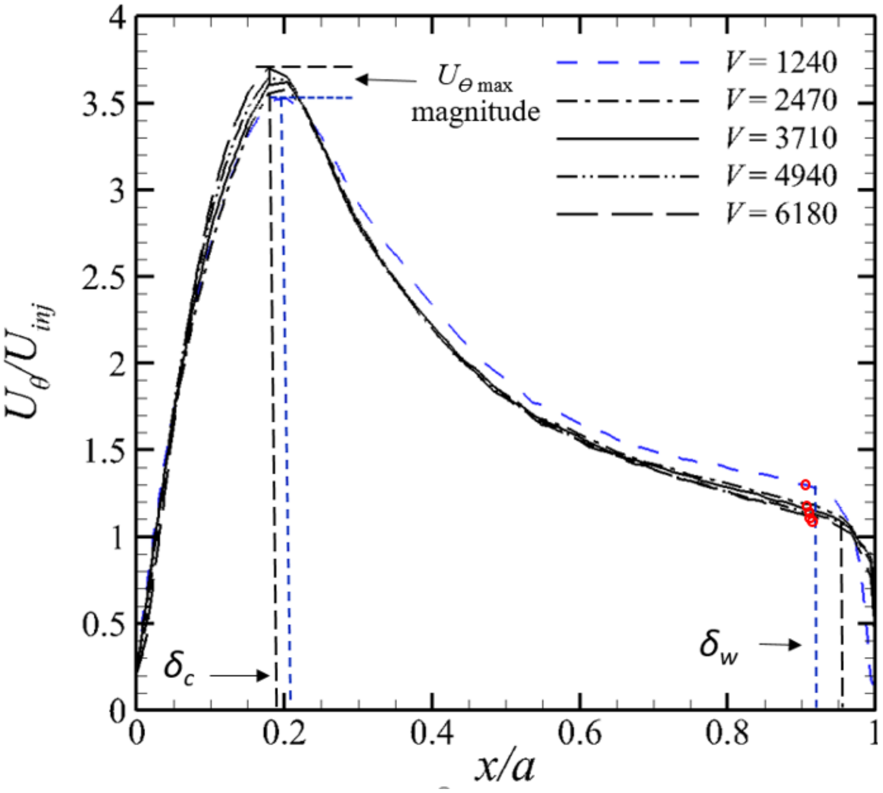

Figure 4.27 Tangential velocity profile, highlighting wall boundary layer thickness for various vortex Reynolds numbers.

It is observed that the wall boundary layer thickness reduces as the vortex Reynolds number is increased, demonstrating the dominance of inertial forces for higher *V*. The red circles superimposed on the velocity profiles represent the calculated wall boundary layer thickness from the Eq. (4.6), presented in [22].

$$\delta_w = \frac{5.8915}{V} \tag{4.6}$$

It is evident that defining the eddy viscosity ratio, l_t, in terms of the vortex Reynolds number yield an excellent agreement between the analytical and experimental results. Also, the values for the coefficients a and b were determined for $U_{\theta\,\max}$, but the same values yield excellent agreement for the core thickness and the solid body angular velocity as well. The experimental results for the forced vortex angular speed match well with the Linear Beltramian model as compared to the Complex-Lamellar model. The wall boundary layer thickness also yields a good match with the analytical results.

However, the correlation developed between eddy viscosity and vortex Reynolds number should be substantiated or investigated further with the experimental data over a larger range of V than can be undertaken with the present experimental setup; such study would represent a good extension to the present investigation.

4.6 Summary

The formation of a bidirectional vortex flowfield has been observed in the cyclonic chamber with tangential inlets under varying operating conditions. In addition to the two characteristic flow features of the bidirectional vortex, namely, the bidirectional axial velocity and the combination of the free-forced vortex, two additional flow features have been identified. These are the head-induced flow that surrounds the combination of the central recirculation zone and the reverse flow region which extend from the headwall to the exit nozzle along the chamber centerline. A good qualitative agreement with the analytical solutions has been observed in the outer head-bound distribution of the axial velocity, including the location of the mantle. However, the high exit-bound velocity region of the head-induced flow and the reverse flow region have not been discussed in the existing literature for bidirectional cyclonic chambers except for those that consider the presence of a hollow core [80]. The variation in the flowfield with the vortex Reynolds number and axial location has also been characterized. The tangential velocity profile shows independence concerning the *z/L* location but varies with the vortex Reynolds number. The trend of variation in the characteristic parameters of the tangential velocity profile such as the core thickness, maximum tangential velocity, and forced vortex angular speed is in agreement with existing analytical solutions by Majdalani and coworkers. An attempt has been made to use the eddy-viscosity approach to quantitatively compare the current experimental results with the analytical solutions. This attempt was successful.

5. Effect of Geometric Parameters on Bidirectional Flowfield and Associated Characteristics

Results presented in the previous chapter established that a bidirectional vortex flowfield develops in the cyclonic chamber for a range of the inlet vortex Reynolds number. Vortex breaks down in the form of a CRZ, and an associated reverse flow region was observed over the entire range of the vortex Reynolds number. Although, the formation of CRZ has advantages for its flame holding capability in applications that use swirling injectors, it is undesirable for the bidirectional vortex flowfield. The formation of CRZ is due to the very high geometric swirl number for the present chamber design and its geometric parameters. Although, the swirl number is defined as the ratio of the axial flux of the tangential momentum to the axial flux of the axial momentum. It is often found to be closely related to the geometric features of the chamber. For example, Hoekstra [4] described the dependence of the geometric swirl number in terms of the chamber exit area (contraction ration, β), the inlet area, A_i, and the chamber radius, a; the latter two are also used to define the modified swirl number, σ, by Majdalani [10]. This shows that the geometric design variables strongly influence the bidirectional flowfield. Moreover, the variation in the axial velocities with the relative distance from the headwall has been presented earlier, which suggests that the length of the chamber, L, and therefore the chamber aspect ratio, l, will also affect the flowfield, especially the mantle location.

The influence of the geometry on the performance of hybrid rocked motors with swirling flowfields such as the vortex injection hybrid rocket engine (VIHRE) has been investigated by Knuth et al. [44]. They later statistically determined the sensitivity of the average regression rate for each design parameter and found that the port diameter, length, injection area, and throat area to be the most significant geometric design variables [26]. Although VIHRE is a hybrid rocket motor, its internal flow dynamics are very similar to the understudy confined cyclonic chamber. During the research on swirling flow in gas cyclones, Hoekstra et al. [4] also found that the diameter of the vortex finder significantly affects both the axial and the tangential velocity distributions. The parallels between the vortex finder diameter to the chamber exit diameter in the present work are obvious. Experimental results also show the influence of the contraction ratio β, and the chamber aspect ratio l, on the mantle structure [29].

5.1 Selection of Geometric Variables

Based on the above discussion and the fact that the development of CRZ motion is undesirable in the bidirectional flowfield, four parameters are chosen for the parametric study to investigate their influence on the cyclonic flowfield. These include the head injector configuration, the exit contraction ratio, the injection area, and the chamber aspect ratio. Variation in these parameters is achieved by replacing the constituent parts of the modular design shown in Figure 5.1.

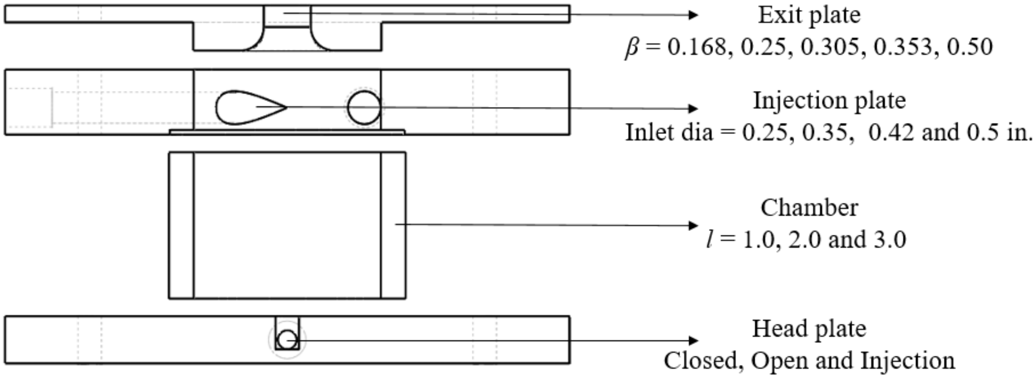

Figure 5.1 Schematic of the modular test setup.

5.2 Variation with Headwall Configuration

The results presented in Secs. 4.2 and 4.4 show vortex breakdown represented by the formation of the CRZ along the chamber centerline at different vortex Reynolds numbers. Although the CRZ can be advantageous in terms of high mixing characteristics, its effects on the bidirectional flowfield are not well understood. The formation of CRZ stems from the imbalance of the axial kinetic energy of the fluid stream and the adverse pressure gradient along the centerline [78]. In the limiting case, due to significantly low pressure in the core, the flow from the chamber exit is entrained to form a region of reverse flow. This reverse flow region blends with the CRZ and results in a complex flowfield around the axis of rotation.

It was hypothesized that if an inlet port is designed on the head-end such that its diameter is less than the head-induced secondary flow surrounding the inner reverse flow region, the low pressure in the core would entrain the fluid from this head port rather than the larger diameter exit port on the injector plate. The resultant increase in the kinetic energy and the reduction in the adverse axial pressure gradient would lead to the flushing of the CRZ from the chamber. In such a case the reverse flow in the center will be replaced by an axially accelerating fluid stream along the centerline, resulting in the desired bidirectional vortex flowfield.

In order to test this hypothesis a circular port of diameter 0.1 D (chamber diameter), aligned with the chamber centerline, was machined on the head plate as shown in Figure 5.1. The chamber was operated under various operating and geometric conditions. In addition to entrainment of fluid, active injection from the head port was also tested. The results are presented in this chapter while discussing the effects of geometric variables. Results of a representative configuration in the r-z plane of the baseline case under the operating conditions tabulated in Table 5.1 are presented in Figures 5.2 and 5.3.

Table 5.1 Headwall geometry and operating conditions.

Geometric Variables		Operating Conditions	
Chamber radius, a	1 in	Vortex Reynolds number	3710
Chamber AR, $l = L/a$	2	Modified Swirl no. $\sigma = a^2 / A_i$	2.6
Inlet Diameter, d_{inlet}	0.35 in		
Contraction ratio, $\beta = d_e/2a$	0.25	Geometric Swirl no. $S = (\pi\, d_e\, a) / (2\, A_i)$	2.04
Head Port	Closed	Open	Injection

It can be seen from Figure 5.2 that the operating condition of the head port significantly influences the flowfield along the chamber centerline, whereas, it has a negligible effect on the rest of the flow inside the chamber. The outer head-bound vortex remains unaltered but the polarity of the core flow is reversed, i.e the complete reverse flow region is replaced by an outward-directed flow. The adverse axial pressure gradient that causes the vortex breakdown and subsequent reverse flow now encourages the ambient fluid entrainment from the headwall port and increases the kinetic energy of the flow along the centerline. This eliminates the conditions favorable for vortex breakdown, and results in an outward flow. Since this outward-directed flow simply replaces the reverse flow region in the core, its effects do not propagate towards the sidewalls, and the mantle location remains unchanged. This is evident in Figure 5.4 (b), which shows the overlap of the mantle structure for the three cases.

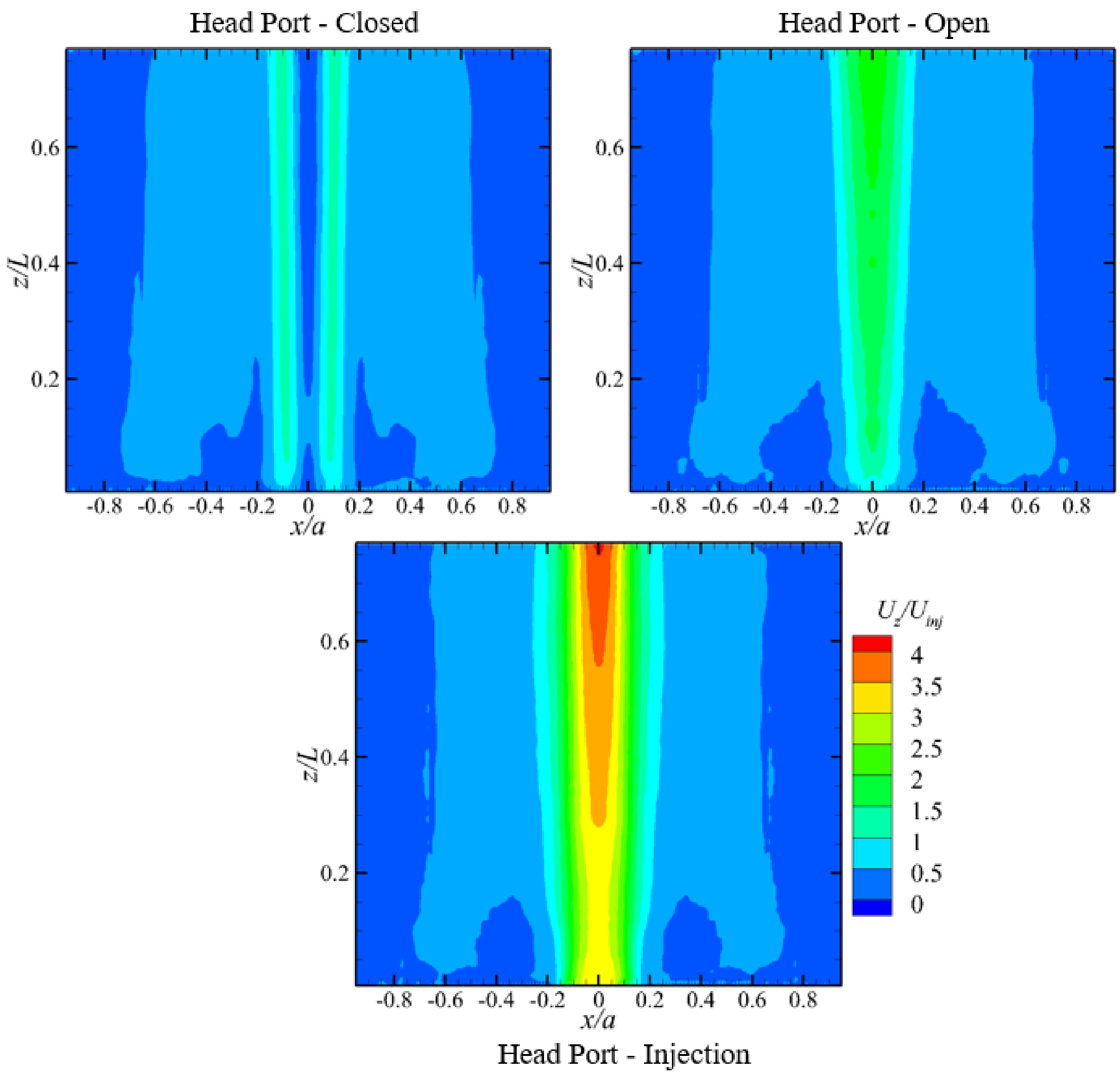

Figure 5.2 Contours of axial velocity for three different head port conditions.

An active injection from the head port at 1/4th the volume fraction of the tangential injection results in a further increase in the outbound velocity near the exit as seen in Figure 5.4 (a). Since the injection results in a higher mass flow rate through the chamber, it was reflected by an expansion in the outward-directed flow region near 0.2 *x/a*; this expansion, however, does not affect the mantle position.

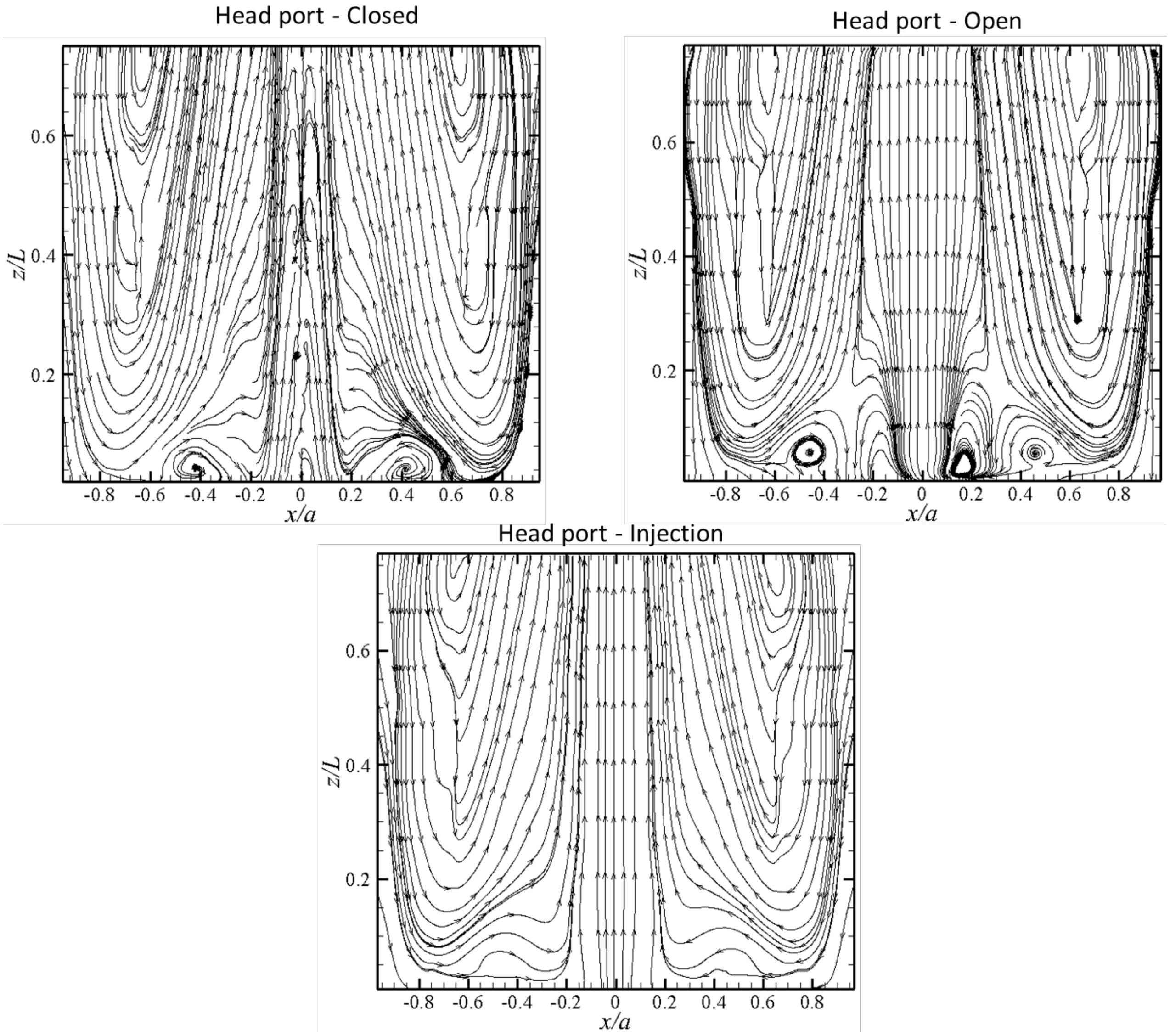
Head port - Closed

Head port - Open

Head port - Injection

Figure 5.3 Streamlines on the *r*-*z* plane for three different head port conditions.

In order to compare the flow structure for the three different head wall configurations, the streamline plots are presented in Figure 5.3. The formation CRZ and a toroidal structure represented by a doughnut shape for the head port-closed configuration has been discussed in detail in Sec. 4.2. The opening of the head port, allows the ambient flow to be naturally entrained due to the low pressure that exists along the chamber centerline, this entrained flow results in the removal of the CRZ and associated reverse flow region along the chamber centerline. However, the interaction of this low velocity entrained fluid and the rotating flow in the chamber results in additional instabilities in the vicinity of the headwall port as seen from the presence of an additional recirculating zone between the initial toroid and the entrained fluid stream in Figure 5.3. Whereas, an active injection from the head port, results in stretching and removal of this toroidal structure from the chamber.

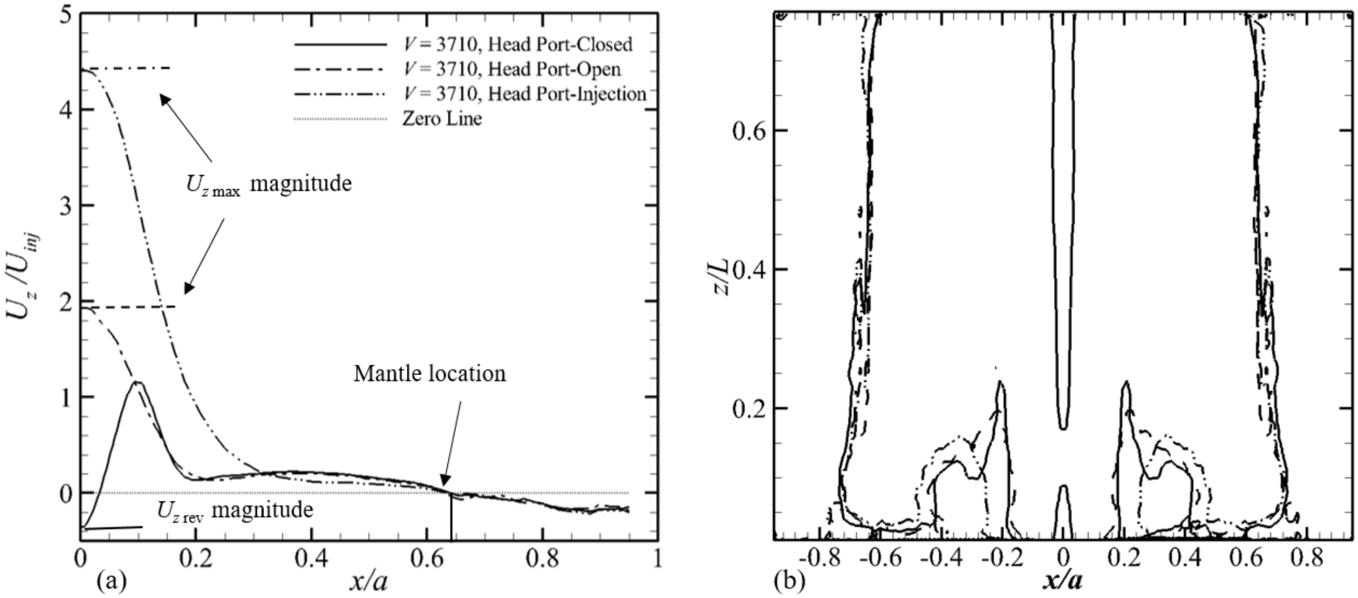

Figure 5.4 Distribution of the (a) axial velocity and (b) the corresponding mantle structure for three different head port configurations.

The injection of fluid through the headwall port does not compromise any of the advantages afforded by the bidirectional vortex flow but present a more realistic design of a cyclonic chamber for propulsive purposes, where the simulated oxidizer is injected through the tangential injectors and the simulated fuel is supplied from the axial port at the headwall. As stated earlier, one of the design features of the swirling injectors is to promote mixing through the formation of CRZ and subsequent increase in vorticity. In the present chamber design, although the formation of CRZ is undesirable, the mixing between the simulated oxidizer and fuel streams is desirable. In order to characterize the effect of head port configuration on the mixing and vorticity distribution in the core, the vorticity magnitude contour plots are presented in Figure 5.5.

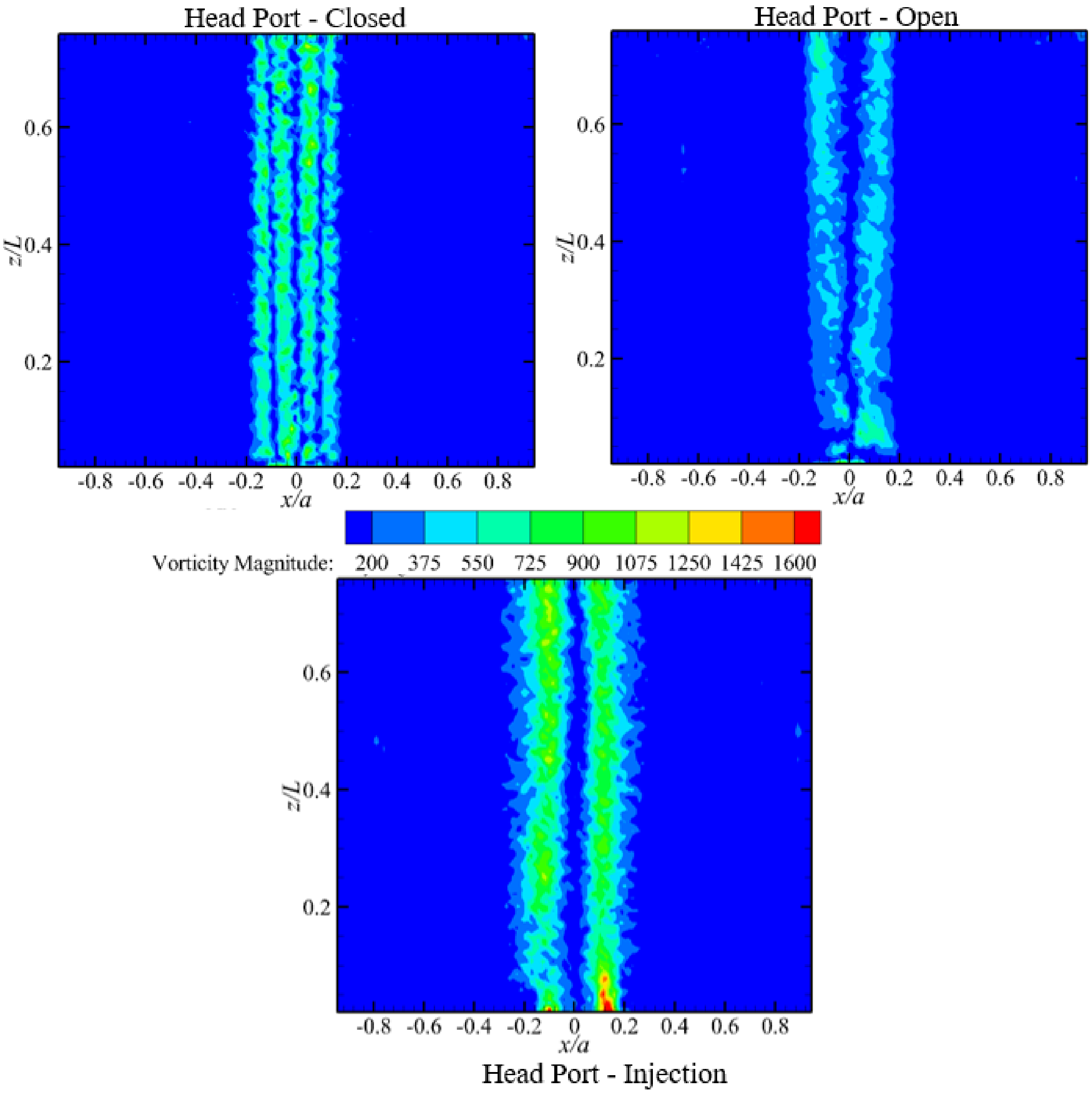

Figure 5.5 **Contours of tangential vorticity for various head port configurations.**

On the other hand, four distinct columns showing high vorticity levels are observed for the closed head port case, whereas, the configuration with injection from the open head port results in two distinct high vorticity columns. The four columns observed for the closed head port configuration represent the viscous interaction of three constituent parts of the overall axial flowfield. The outer pair of vorticity columns represent the free shear layer that exists between the inner vortex and the head-induced flow, whereas the inner pair of vorticity columns represent the interaction between the head-induced flow and the CRZ. Since the opening of the head port and subsequent injection results in flushing of the CRZ, the only shearing interaction is between the high-velocity outward-directed flow along the centerline and the outward-bound inner core. Although both of these motions are directed outwards, a high axial velocity gradient is present between them. This results in the formation of a free shear layer that is characterized by high vorticity as seen from Figure 5.5. This high vorticity shear layer and corresponding Kelvin-Helmholtz instability result in the formation of small-scale structures and eddies between the two outward-directed fluid streams.

To further investigate the effect of headwall injection and to visualize the coherent structures which enhance mixing in the core, the snapshot Proper Orthogonal Decomposition (POD) method is applied to the PIV data to extract the eigenfunctions or modes from an autocovariance matrix of the fluctuating velocity components. Modal decomposition is an efficient method of capturing the dominant components (modes) in the reconstructed velocity fields and thus represents a complex flow with a lower-dimensional model [85]. The total energy of the flow can be represented by the sum of all eigenvalues ($\sum \lambda_i$), with the largest energy fraction ($^{\lambda_i}/_{\sum \lambda_i}$) contained by the mean mode (Mode-0, λ_1). The cumulative sum of energy contents of the POD modes extracted from 1000 PIV image pairs in the axial plane is presented in Figure 5.6. The Mode-0, which represents the mean flow of the closed head configuration, constitutes ~60% of the total energy compared to ~86 % for the head port open and ~ 70% for the head injection configuration.

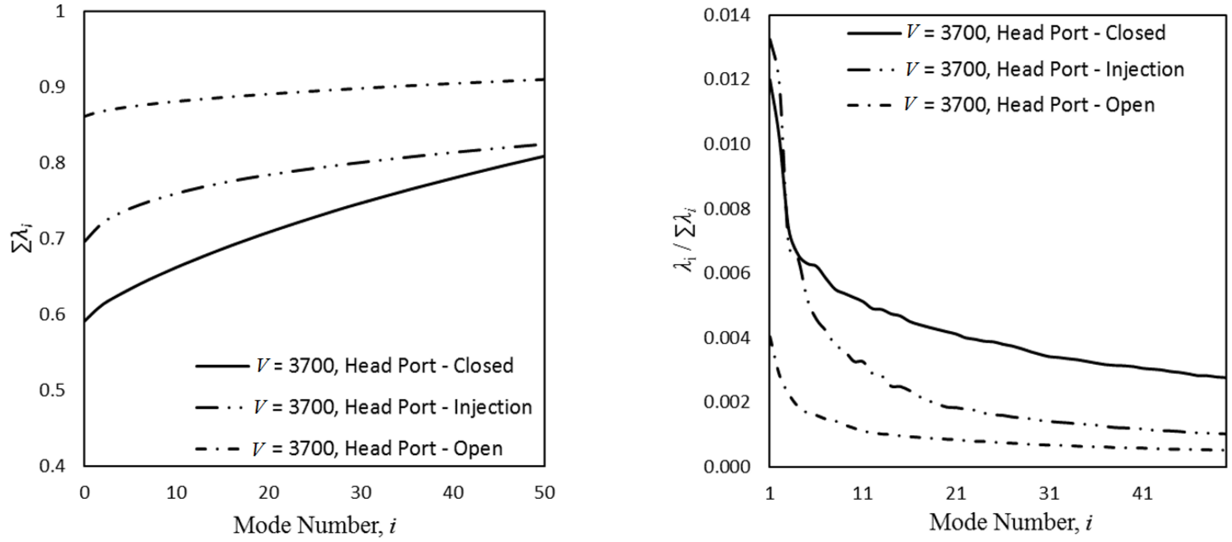

Figure 5.6 The energy content of the axial POD modes. (a) Cumulative, and (b) Individual.

The trend displayed by the mean mode (Mode-0) energy leads to an interesting observation: the maximum energy of the mean mode (mean flow) corresponds to the head port-open configuration, rather than the head injection configuration. Opening the head port allows for equilibrium to be naturally established in the chamber, by entraining the required amount of fluid to counter the low pressure developed along the chamber centerline. This reduces the force imbalance that can create strong shearing effects and, therefore, higher vorticity and other small-scale structures. Along similar lines, a forced injection through the head port acts as an axial jet immersed in a swirling flowfield; it leads to the development of a strong shear layer as seen in Figure 5.5 and subsequent structures caused by the Kelvin-Helmholtz instability. The minimum energy in the mean mode is observed for the closed head port case and is attributed to the presence of the reversed flow region, CRZ, and associated flow structures.

In order to ascertain the presence of coherent structures, the velocity fields of selected modes are reconstructed and shown in Figure 5.7. The plots span the entire optically accessible region of the *r*-*z* plane in the *z*-axis, although only the centrally located 50% of the chamber is shown in the radial direction. This is chosen because the coherent structures primarily exist in the vicinity of the chamber centerline, where the vorticity is at its maximum according to Figure 5.5. From the vector field of Mode-1 of the head port-closed configuration, it is seen that the coherent structures are distributed both near the headwall and the chamber exit. These coherent structures represent the shear layer created by the CRZ and the reverse flow, respectively. In contrast, Mode-1 for head port-open configuration has the concentration of coherent structures near the headwall only, thus representing the entrained flow as it interacts with the swirl-dominated flow inside the chamber. The Mode-1 vector fields for the active injection configuration clearly show the presence of the Kelvin-Helmholtz vortices in the shear layer of the injected jet. A similar distribution is seen in the Mode-2 of all the configurations. However, the presence of coherent structures along the chamber centerline for higher modes, such as modes 5 and 20, may be attributed to the diffusion of the vorticity and the distribution of energy to lower modes.

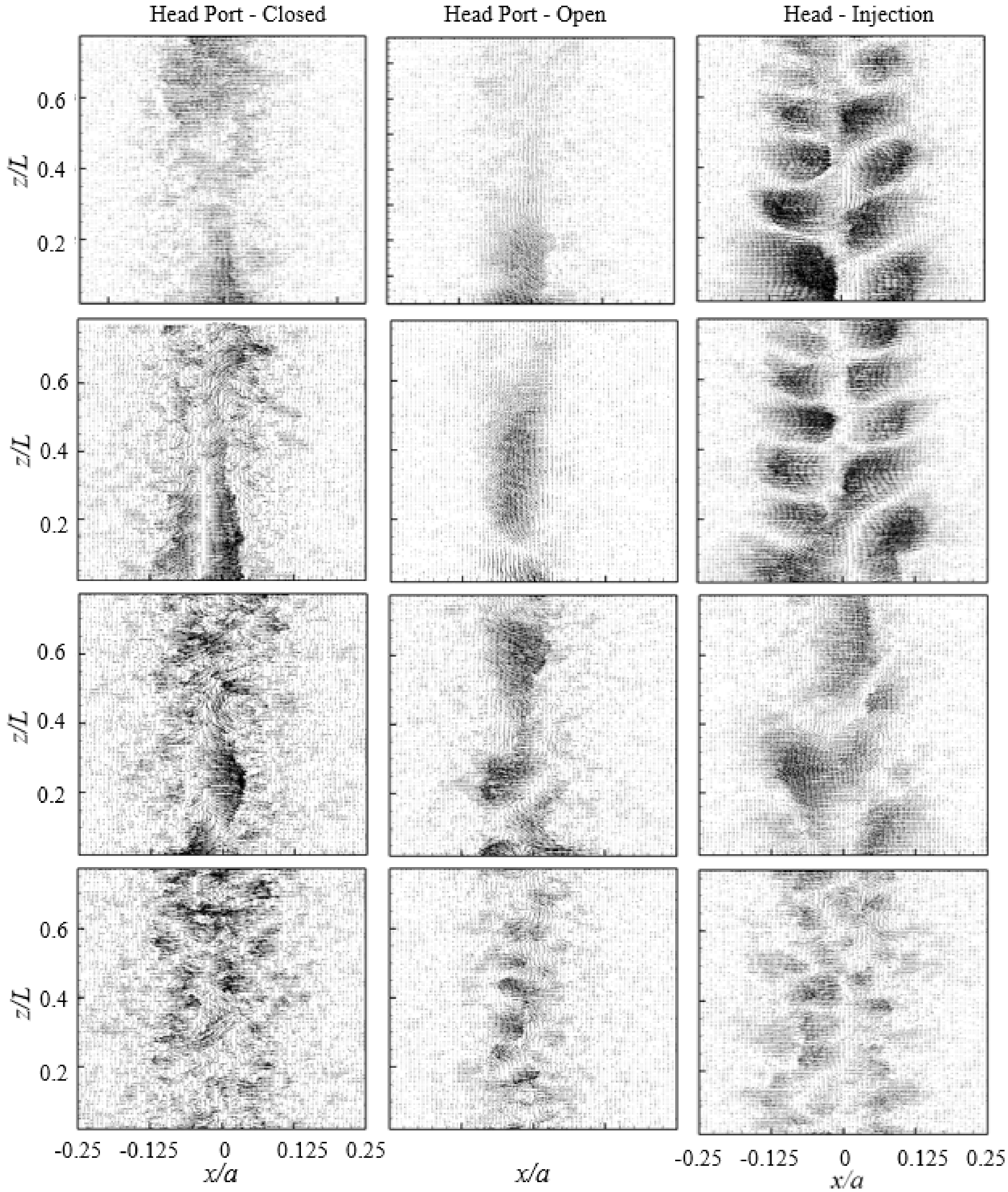

Figure 5.7 Reconstructed vector fields for Modes 1, 2, 5, and 20 (top to bottom).

The turbulent kinetic energy represents the measure of the turbulent intensity. It is evident from Figure 5.8, that two separate highly turbulent regions are formed for the head port-closed case. These two regions represent the CRZ close to the headwall and the reverse flow towards the chamber exit. However, the entrainment of ambient fluid for the head port-open configuration weakens the reverse flow, thus reducing the TKE near the exit, but the interaction between the entrained fluid at the head port and the swirling flow in the chamber creates a local region of high TKE. The injected stream from the head port for the head injection configuration creates a TKE distribution similar to the axial jet.

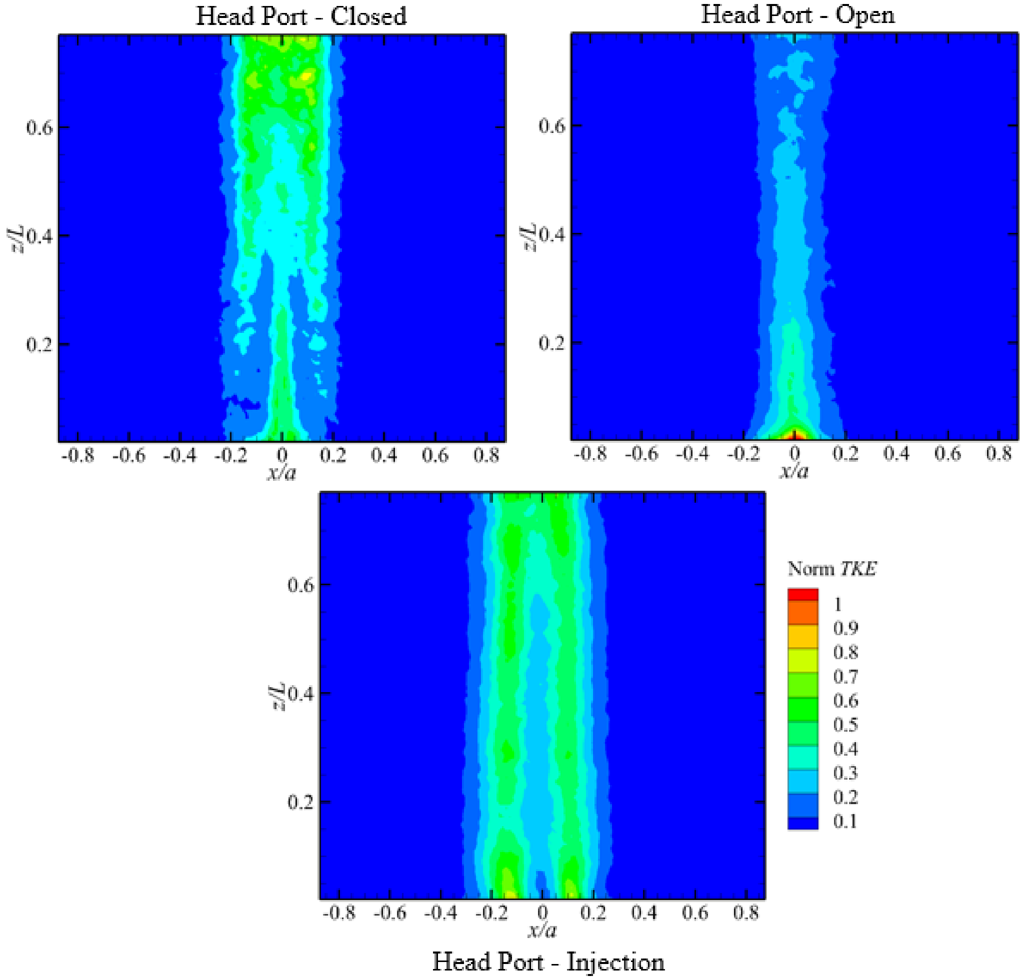

Figure 5.8 Contours of normalized TKE for various head port configurations.

As discussed in Sec 4.4, an increase in vortex Reynolds number results in a proportional increase in the magnitude of the tangential velocity and reduction in the core thickness. This leads to a further drop in the pressure along the chamber centerline and increases the relative magnitude of the reverse flow due to the locally adverse pressure gradient. The driving mechanism for entrainment of the ambient fluid from the headwall port, if open, is this reduced pressure in the core region. Therefore, as the inlet vortex Reynolds number is increased, the entrainment through the head port and the resultant normalized axial velocity along the chamber centerline also increases as seen in Figure 5.9. The invariance of mantle location with the vortex Reynolds number and head port configuration is also observed.

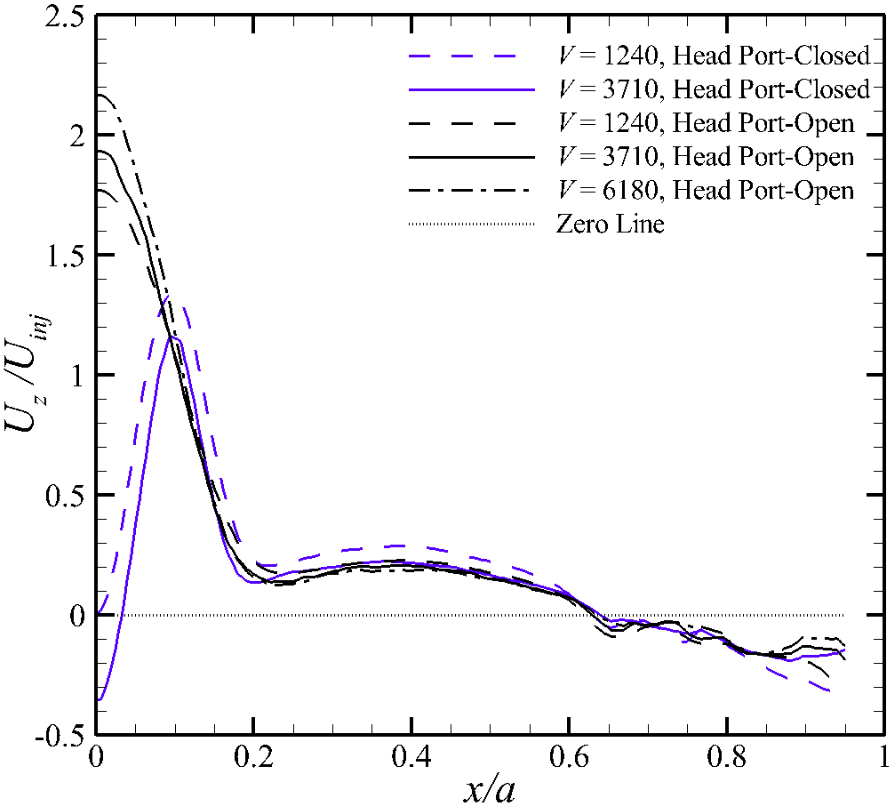

Figure 5.9 Distribution of the axial velocity for different vortex Reynolds numbers and head port configurations.

With the above discussion, it is concluded that the desired bidirectional vortex flowfield can be achieved in the cyclonic chamber by incorporating an inlet port at the headwall along the chamber centerline. The fluid entrained from the head port results in flushing the CRZ and associated reverse flow region out of the chamber. The vorticity and TKE distribution are also modified in the vicinity of the chamber centerline and depend on the amount of fluid entrained. However, this only affects the flowfield in the near vicinity of the chamber centerline and does not alter the mantle location or the updraft near the chamber sidewalls.

5.3 Effect of Contraction Ratio, β

Next, the effect of the contraction ratio, β, on the flowfield is characterized by varying the nozzle exit diameter. The choice of the contraction ratio values, displayed in Table 5.2, is guided by the devices that are used to model the confined cyclonic flowfields such as the vortex combustion cold wall chamber, VCCWC [10,28], and the vortex injection hybrid rocket engine, VIHRE [6,44]. It should be noted that the variation of the exit diameter also affects the swirl number, S. The swirl number is defined as the ratio of the axial flux of the tangential momentum to the axial flux of the axial momentum, and is expected to significantly impact the internal flowfield of the cyclonic chamber. However, S is often expressed in terms of the design and geometrical parameters of the specific experimental setup. In the present series of experiments, the swirl number is calculated using the relation presented by Hoekstra [4], given in Eq. (2.6), and reproduced below as:

$$S = \left[\frac{\pi \ d_e \, D}{4A_i}\right] \tag{5.1}$$

Here d_e denotes the diameter of the exit, D stands for the chamber diameter, and A_i represents the total injection area.

Table 5.2 Geometic and operating conditions used in the contraction ratio characterization.

Geometric Parameters		**Operating Parameters**	
Chamber Radius, *a*	1 in	Vortex Re, *V*	3710
Chamber *AR*, $l = L/a$	2	Modified Swirl # $\sigma = a^2 / A_i$	2.6
Inlet Diameter, d_{inlet}	0.35 in		
Total Injection Area, A_i	0.385 in^2	**Contraction ratio, $\boldsymbol{\beta}$**	**Geometric Swirl No, $\boldsymbol{S}$**
Exit Diameter, d_e	0.336 in	0.168	1.37
	0.5 in	0.25	2.04
	0.61 in	0.305	2.53
	0.707 in	0.353	2.89
	1.0 in	0.5	4.08

The tangential velocity contours for various contraction ratios are presented in Figures 5.10. It can be seen that a decrease in the contraction ratio using smaller radii exit port results in much higher tangential velocities in the vicinity of the chamber centerline, whereas the tangential velocity is not affected away from the centerline; none the less the location of the peak tangential velocity, which denotes the core thickness, also shifts inwardly to adhere to the decreasing exit port radius.

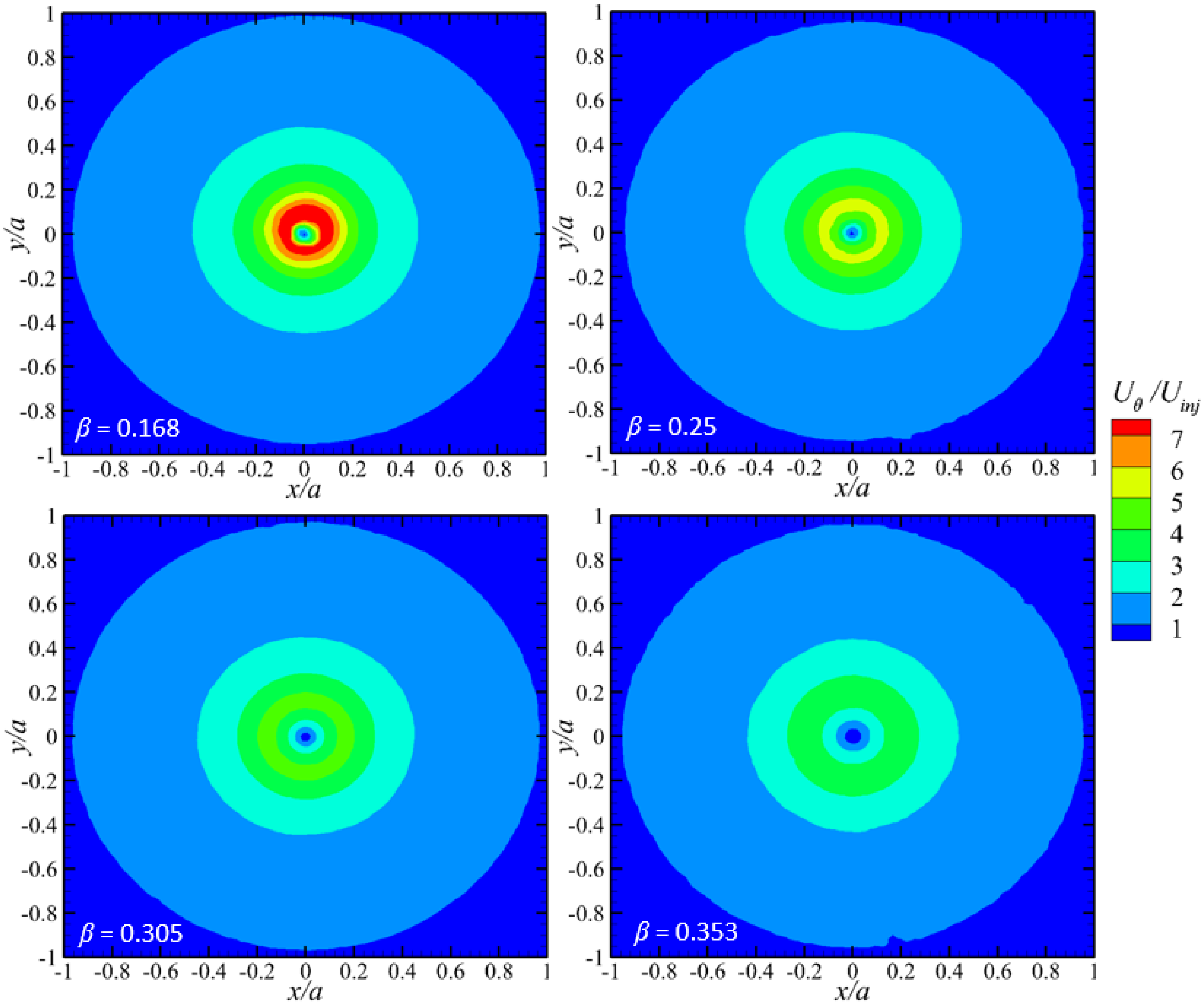

Figure 5.10 Contours of tangential velocity for different contraction ratios.

To quantitatively compare the effect of the contraction ratio, the radial distribution of the tangential velocity is presented in Figure 5.11. It can be seen that the peak tangential velocity, as well as the core thickness, are strongly affected by the exit radius. We start by noting that $U_{\theta\max}$ at $\beta = 0.168$ is twice as high as that at $\beta = 0.353$, while the core thickness is reduced by half approximately. The increase in $U_{\theta\max}$ is the consequence of the conservation of angular momentum. Reducing the exit diameter concentrates the angular momentum in a much smaller region around the chamber centerline, thus leading to a higher tangential velocity. This extends the region in which the free vortex behavior is observed, as the tangential velocity increases with decreasing radius. In a limiting case and absence of viscosity, it would result in the characteristic singularity of the free vortex. The axial stretching of the vortex affects both the pressure and the axial velocity in the chamber.

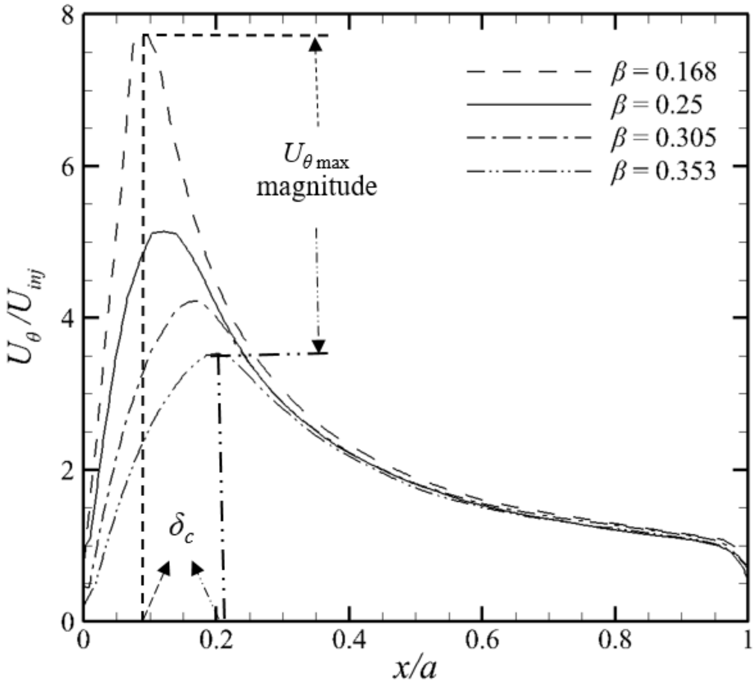

Figure 5.11 Distribution of the tangential velocity for different contraction ratios.

The axial velocity contours for various contraction ratios are presented in Figures 5.12 and 5.13 for head port close and open configurations respectively. The variation with head configuration has been discussed in the previous section. The conservation of mass and the incompressibility of the fluid (water) prescribe that the decrease in exit diameter results in an increase in the outwards directed velocity, especially in the head-induced region for the head port-closed configuration and along the centerline for the head port-open configuration. However, the reduced pressure in the core for the head port-closed configuration results in an increased magnitude of the reverse flow as well.

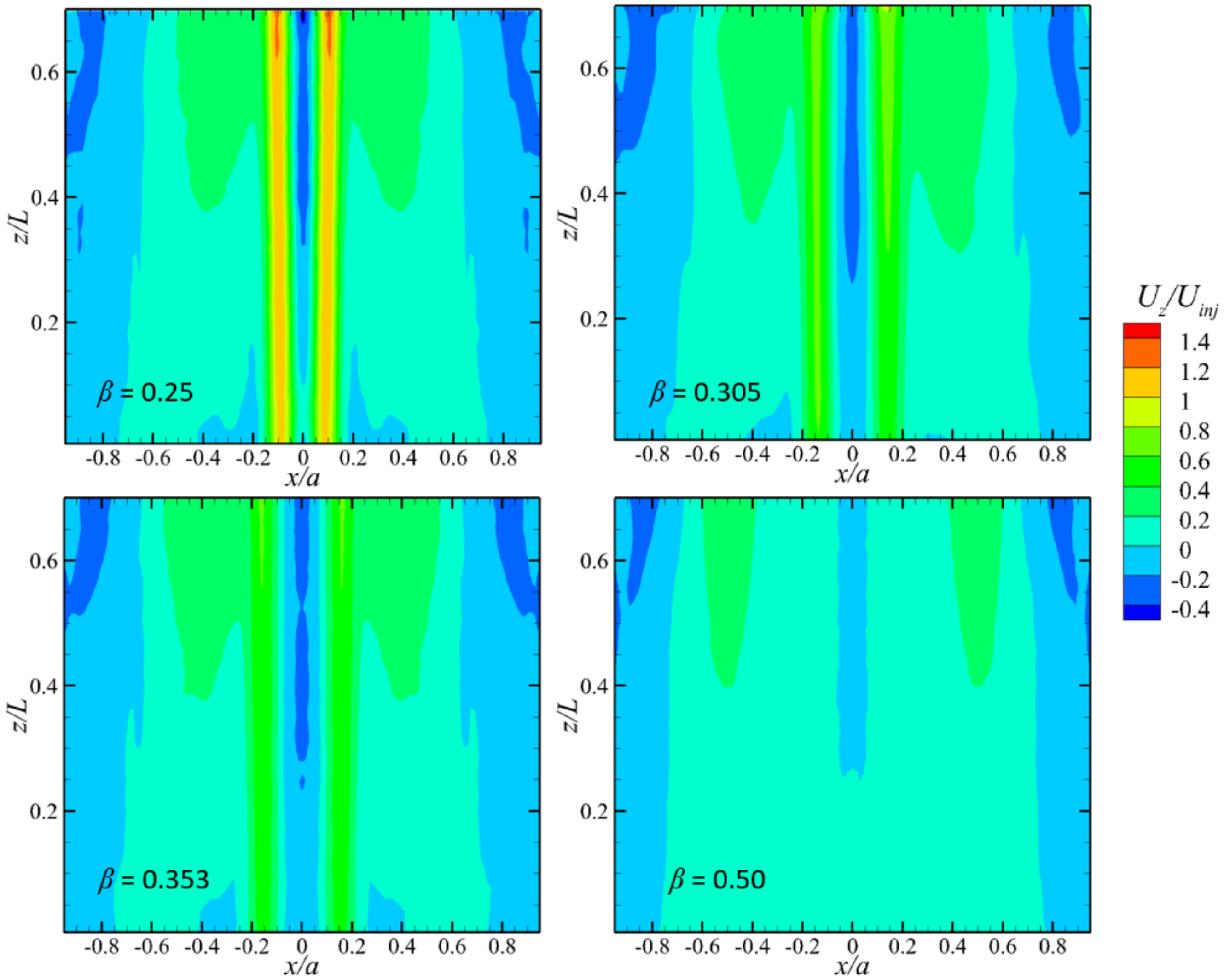

Figure 5.12 Axial velocity contours for different contraction ratios for head port-closed configuration.

An interesting observation is made for $\beta = 0.50$ from Figures 5.12 and 5.13, where a region of high axial velocity magnitude is seen around $x/a = 0.5$ and is disconnected from the chamber centerline. The location of the high outward-directed velocity region aligns with the exit port, which also extends to $x/a = 0.5$. This demonstrates much higher spillage for larger outlet diameters.

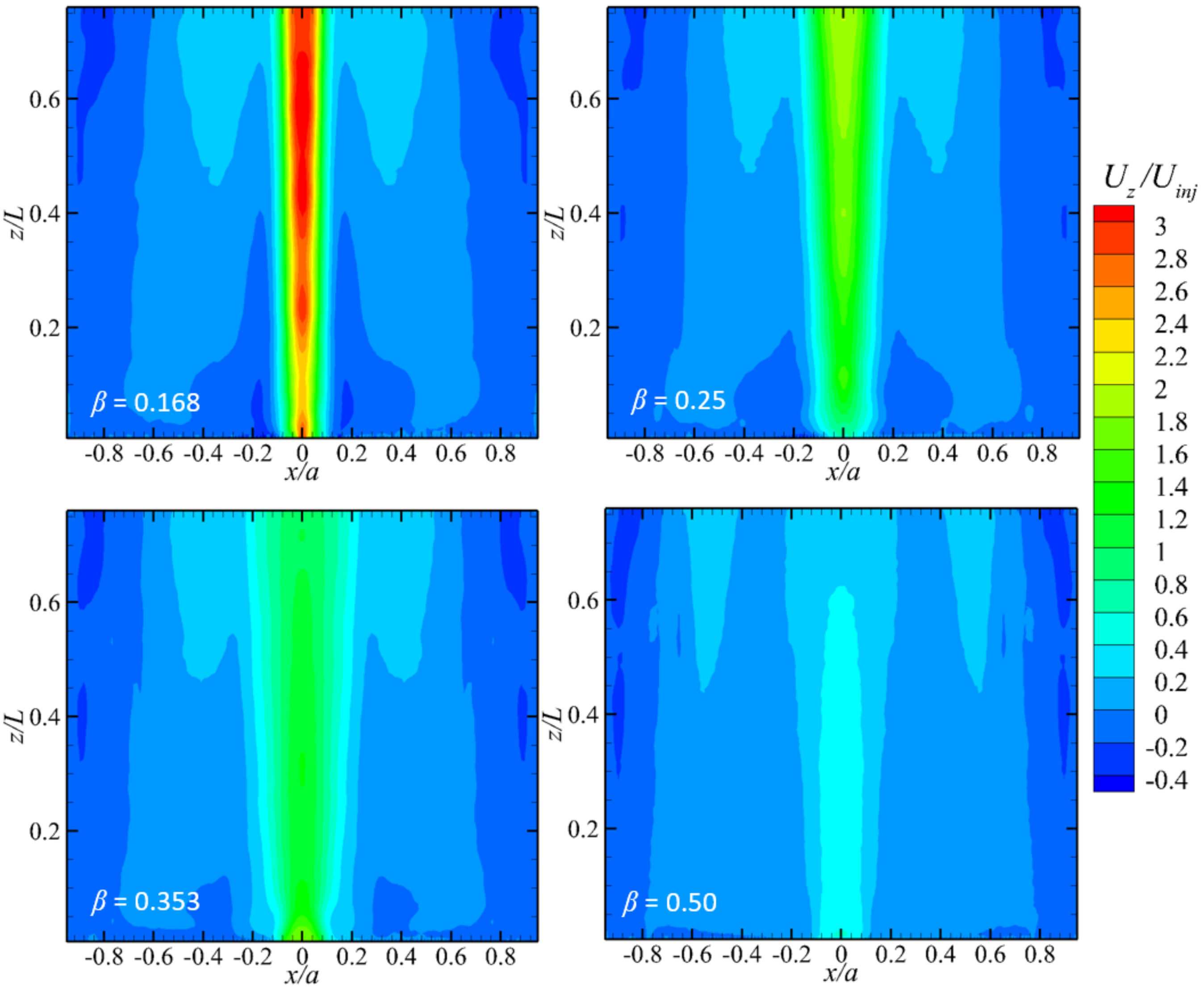

Figure 5.13 Axial velocity contours for different contraction ratios for head port-open configuration.

The variation in contraction ratio not only affects the magnitude of the axial velocity but also significantly alters the mantle location as seen in Figures 5.14 and 5.15. The overall mantle shape remains slightly conical as seen before, but the mantle converges towards the centerline as the exit radius is reduced. The overall mantle at the location *z/L* = 0.5 varies within the range of 63% to 74% of the chamber radius depending upon the exit radius.

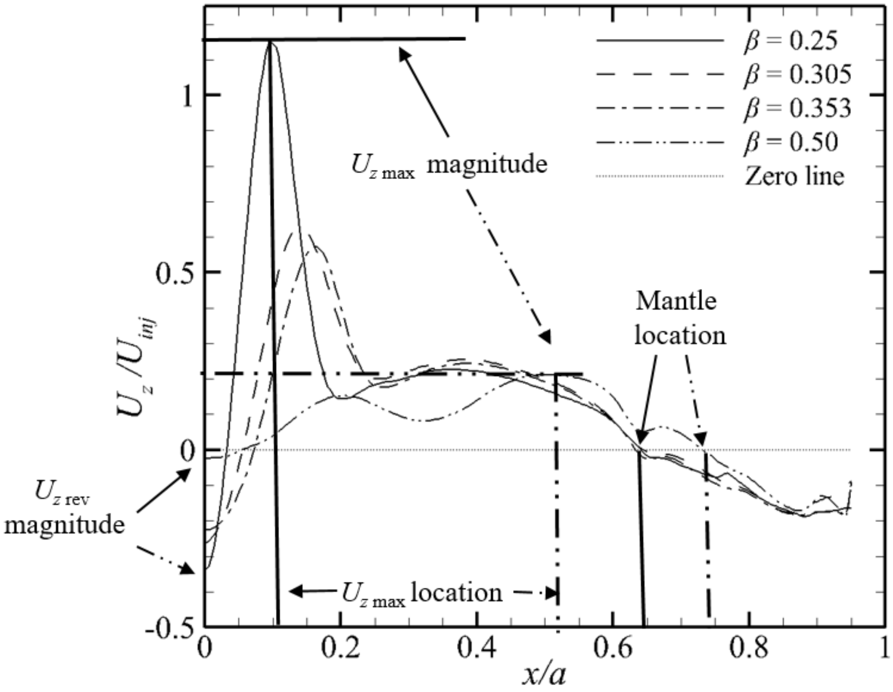

Figure 5.14 Distribution of the axial velocity for different contraction ratios for head port-closed configuration.

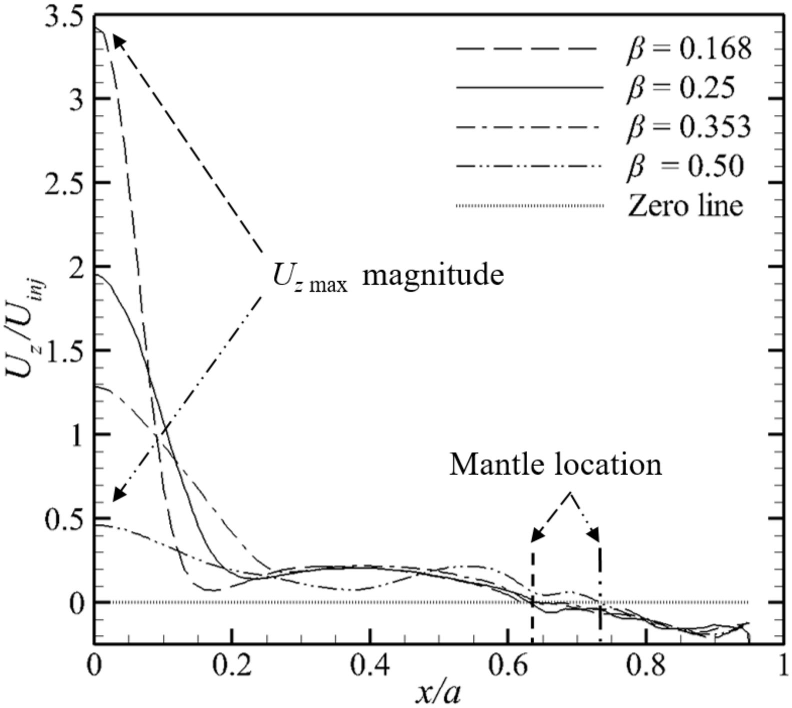

Figure 5.15 Distribution of the axial velocity for different contraction ratios for head port-open configuration.

The results presented above are consistent with the analytical solutions of Majdalani [10,22] which reported the mantle location at $\beta = 0.628$ for the Beltramian model and $\beta = 0.707$ for the Complex-Lamellar model. This is also accompanied by the lower magnitudes of both the axial and tangential velocity components for the Complex-Lamellar model, which has a higher β value than the Beltramian model. The direct relation of core thickness, δ_c, with the β value, is also validated by the results of the present experiment.

It should be noted that the analytical models that are developed for a perfect outlet that matches the mantle location do not account for arbitrary exit size. Although the possibility of multiple mantles is discussed by Vyas and Majdalani [86], this solution results in discrete β values. Most of their solutions use a constant β. The various nondimensional parameters such as the modified swirl number, σ, the vortex Reynolds number, V, and the off-swirl parameter, κ, which appear in the analytical models, do not account for the exit diameter variation. However, the formulation of the swirl number presented in Eq (5.1), includes the exit diameter and is often utilized with reference to cyclone separator studies. Hoekstra et al. [4] also demonstrate that the flowfield variation of the cyclone separator depends on the swirl number based on the vortex finder diameter. Their results are found to be in agreement with the present experiments.

From the above discussion, it is concluded that the exit size is an important design variable because it significantly affects the flowfield and therefore, should be reflected in the governing nondimensional numbers.

5.4 Effect of Inlet Size

Results presented previously show the presence of reverse flow along the chamber axis when the head port is closed. In addition to other factors pertaining to the formation of the reverse flow region, the most apparent cause remains the high range of the operating swirl number. The motivation behind varying the inlet size is to control the swirl number. As seen from Eq (5.1), an increase in the inlet area will result in the reduction of the swirl number. The initial selection of the injection area and the number of injectors was influenced by the earlier studies that have been carried out on similar cyclonic chamber configurations [28]. However, the orientation and the number of the tangential injectors have limited the possibility of an increase in the injection area. It can be seen from Figure 5.16a that any increase in the inlet port diameter will cause interference among the tangential injectors. To overcome this limitation, it was decided to reduce the number of injectors while increasing the inlet port area such that the total inlet area of the baseline configuration remained the same as the initial configuration.

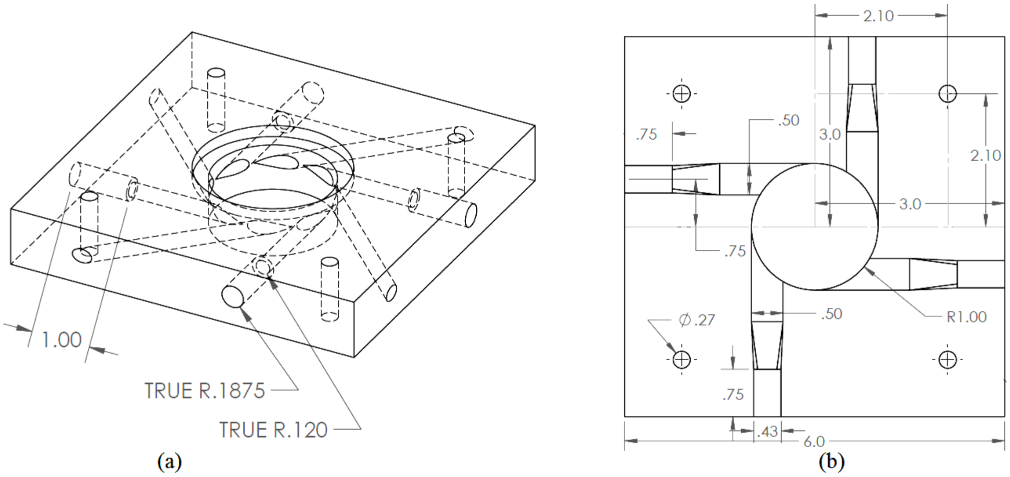

(a) (b)

Figure 5.16 Drawings for the (a) initial design and (b) modified design.

The salient features of the injector plate and resulting swirl numbers are presented in Table 5.3. The range of geometric swirl numbers for the selected injector port diameters spans from $S = 1$ to

4. The upper limit of the inlet port diameter is restricted due to the increasing proximity of the inlet stream to the chamber exit, which could result in excessive spillage.

Table 5.3 Geometrical and operating conditions for the effect of the inlet area.

Chamber		Injection Plate				Geometric Parameters	
Radius (in)	Height (in)	Inlet Port Diameter (in), d_{inlet}	Single Injector area (in^2)	No. of Injectors	Total Injection Area (in^2)	Swirl No. S	Modified Swirl No. σ
1	2	0.25	0.0490	4	0.1962	4.00	5.10
1	2	0.35	0.0961	4	0.3846	2.04	2.60
1	2	0.42	0.1451	4	0.5805	1.35	1.72
1	2	0.5	0.1962	4	0.785	1.00	1.27

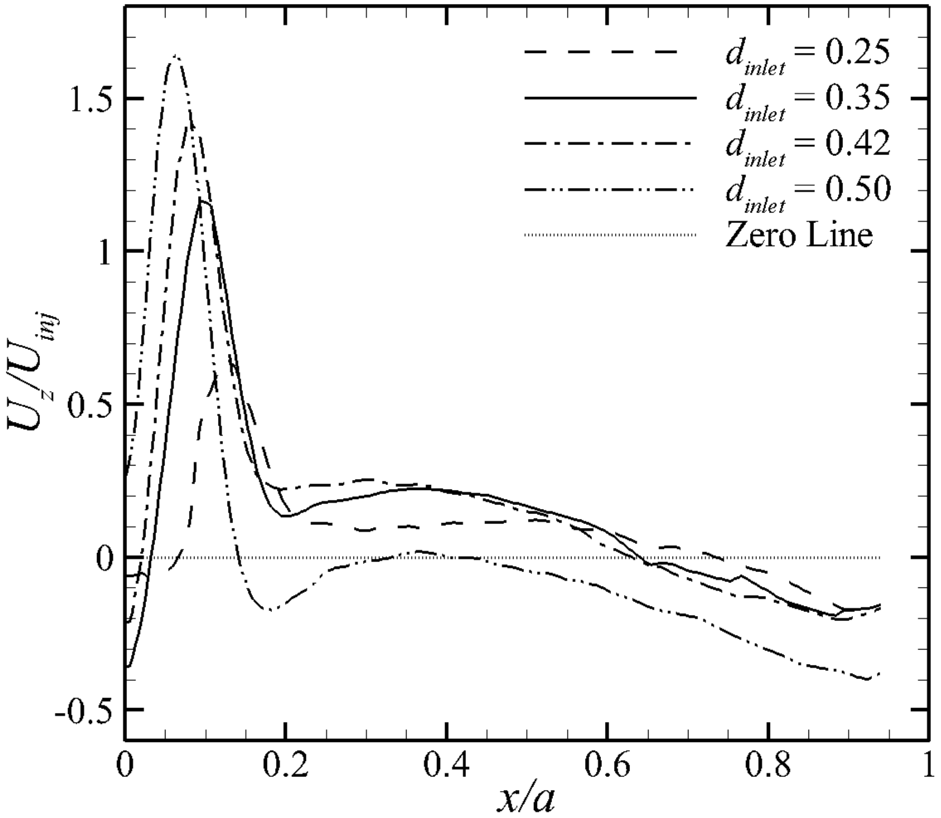

Figure 5.17 Distribution of the axial velocity for various inlet areas.

The axial velocity distribution for various inlet areas is presented in Figures 5.17. It can be seen that the increase in the injector port diameter results in a successive reduction in the mantle location. This is a consequence of the broader size of the injection stream, which radially displaces all of the flow characteristics towards the centerline, including the location of the maximum axial velocity. The formation of CRZ and the reverse flow are still observed for all the cases as evident from Figure 5.18. The variation of the inlet area thus has a significant effect on the axial velocity profile.

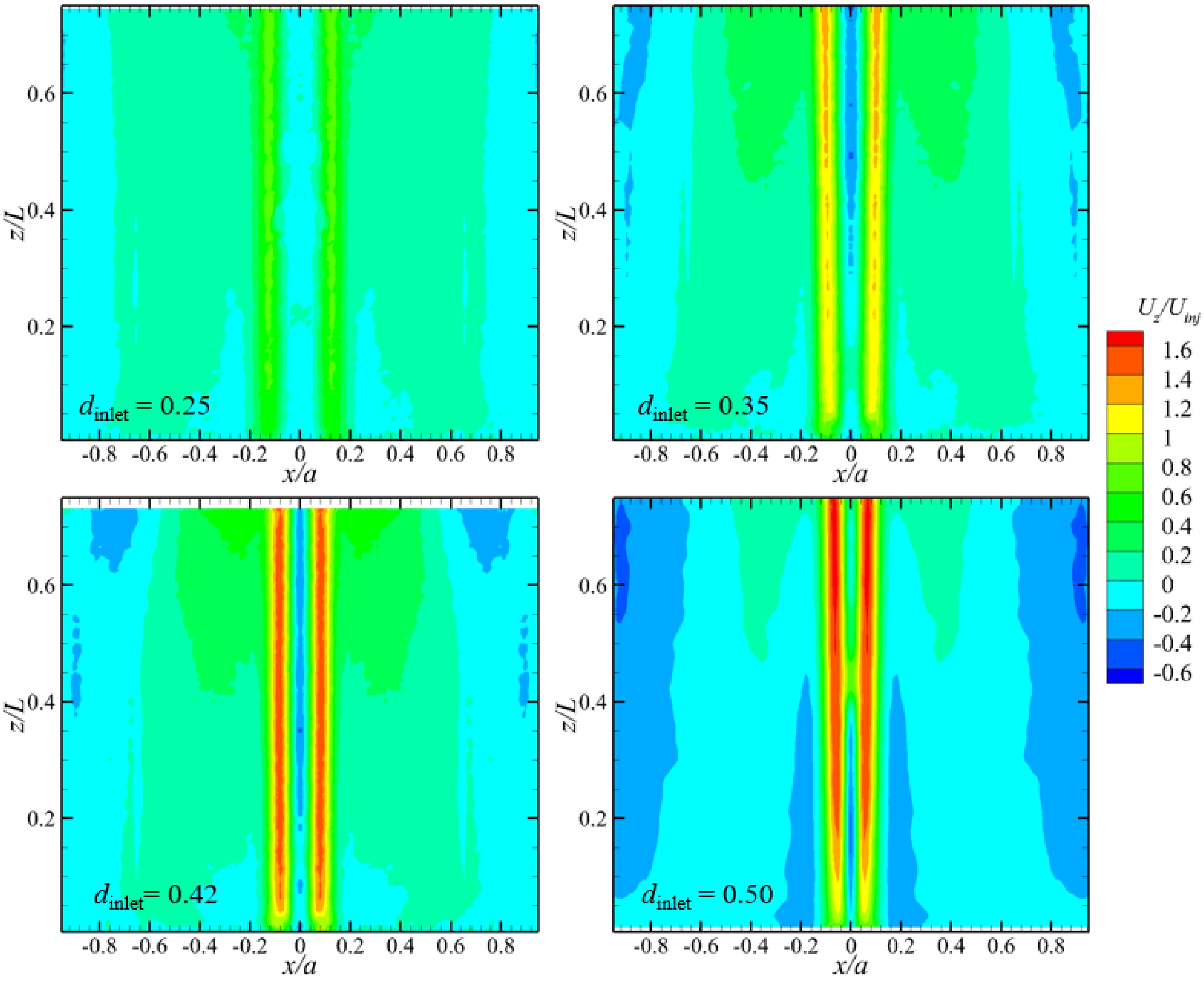

Figure 5.18 Axial velocity contours for different inlet areas.

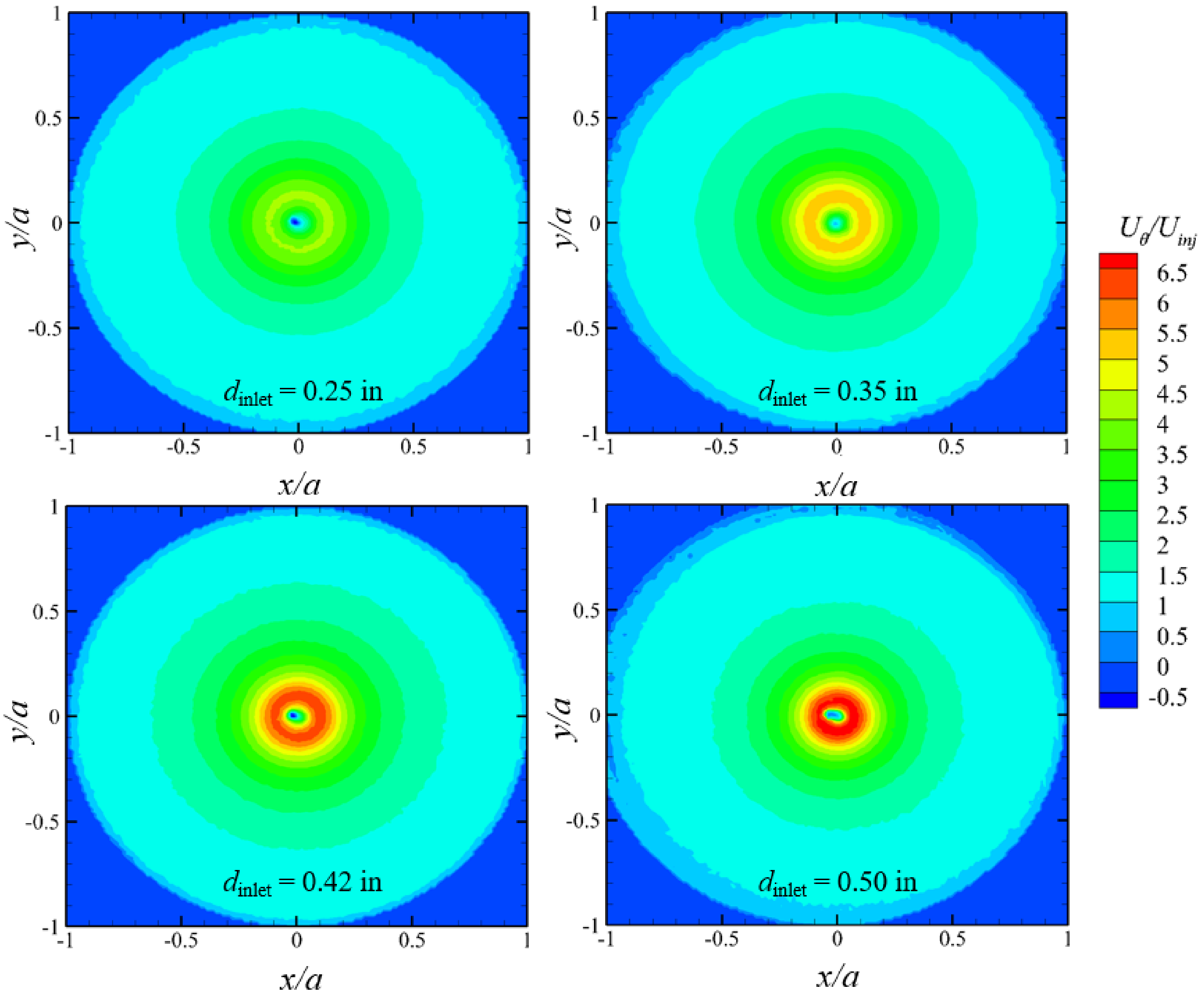

Figure 5.19 Contours of tangential velocity for different inlet diameters.

The tangential velocity contours for the four different inlet port diameters are presented in Figure 5.19. Similar to the axial velocity, the broader inlet streams from the larger inlets, radially displace the core thickness location towards the chamber center as seen in Figure 5.20. This also results in the increased nondimensional maximum tangential velocity.

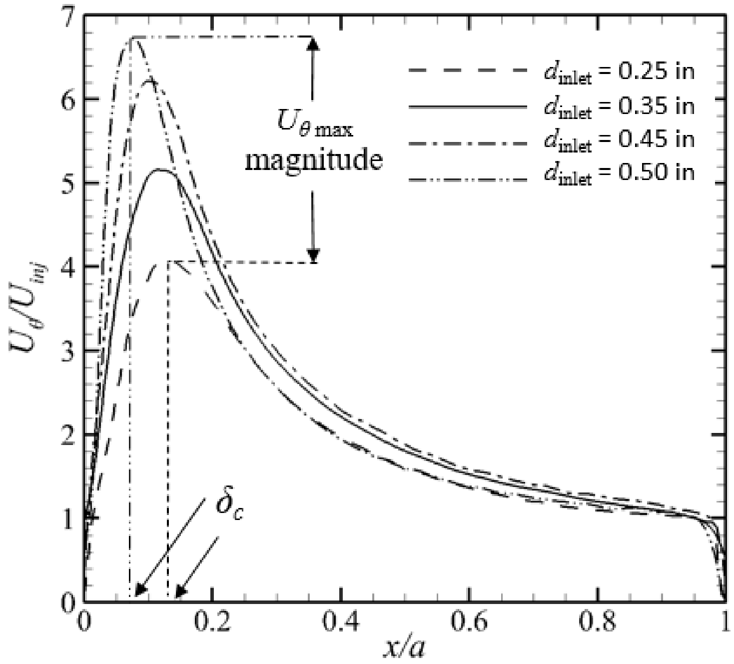

Figure 5.20 Distribution of the tangential velocity for different inlet diameters.

5.5 Effect of the Swirl Number

It has been seen that both the inlet area and the contraction ratio (exit diameter) have a significant effect on the flowfield. Although we have examined the effects of both these factors independently, their combined effects can be reflected in the form of the swirl number, as both of these parameters are used to define the swirl number in, Eq. (5.1). Results for different swirl numbers and contraction ratios are summarized in Table 5.4.

Table 5.4 Summary of the relevant characteristic parameters as a function of swirl number.

Geometrical Configuration	d_{inlet} = **0.50**	d_{inlet} = **0.42**	β = **0.168**	β = **0.25** d_{inlet} = **0.35**	β = **0.305**	β = **0.353**	d_{inlet} = **0.25**	β = **0.50**
Characteristic parameter	$S = 1$	$S = 1.35$	$S = 1.37$	$S = 2.04$	$S = 2.53$	$S = 2.89$	$S = 4$	$S = 4.08$
Mantle Location	0.408	0.632	0.634	0.638	0.645	0.631	0.734	0.733
$U_{z\,\max}$	1.641	1.420	*	1.161	0.627	0.573	0.649	0.200
Location of $U_{z\,\max}$	0.063	0.082	*	0.098	0.141	0.159	0.124	0.150
$U_{\theta\,\max}$	6.72	6.214	7.785	5.134	4.225	3.525	4.090	1.99
δ_c	0.077	0.101	0.092	0.119	0.172	0.199	0.135	0.289

* The measurements for $U_{z\,\max}$ and its location for $\beta = 0.168$ are not avaliable due to cavitation experienced during the experiment.

Results indicate that all the non-dimensional flow characteristics are highly dependent on S irrespective of the geometrical parameter used to vary the swirl number. For example, The characteristic locations including the mantle location, the location of maximum axial velocity (with the exception of the inlet diameter of 0.25 in), and core thickness, δ_c, have a direct relationship with S, whereas both the velocity components, $U_{z\,\max}$ and $U_{\theta\,\max}$, decrease with increasing S.

5.6 Effect of Aspect Ratio, *l*

The effect of the chamber aspect ratio on the flowfield was characterized by varying the length of the cylindrical chamber, whereas the diameter was held constant. An important feature of the aspect ratio is that it shows up in the formulation for the vortex Reynolds number, V, and the off-swirl parameter, κ. κ acts as a multiplier for the off-swirl velocities, therefore its impact is much more prominent on the axial velocity compared to the tangential velocity. In the present investigation, the chamber inlet velocity, and thus the vortex Reynolds number was controlled by regulating the injection volume flow rate. Therefore, once the aspect ratio was changed, it resulted in the change in both the off-swirl parameter and the vortex Reynolds number, for the same injection flow rate. The operating conditions for the aspect ratio study are presented in Table 5.5.

Table 5.5 Geometrical and operating conditions for the effect of aspect ratio.

Geometric Parameters		**Operating Conditions**	
Chamber Radius, a	1 in	Modified Swirl no. $\sigma = a^2 / A_i$	2.6
Contraction Ratio, β	0.353		
Inlet Diameter, d_{inlet}	0.35 in	Geometric Swirl no. $S = (\pi d_e a) / (2 A_i)$	2.89
Total Inlet Area, A_i	0.385 in^2		
Chamber Aspect Ratio, $l = L/a$		Vortex Re, $Qi / (\nu L)$	$\kappa = 1 /(2\pi\sigma l)$
1.0		7410	0.061
2.0		3710	0.0306
3.0		2470	0.0204

The distribution of the axial velocity for the three aspect ratios is presented in Figures 5.21. It can be seen that the increase in the aspect ratio results in a successive increase in the radial location of the mantle, and the magnitude of maximum axial velocity. However, it has been noted earlier in Sec 4.4 that these characteristics do not vary significantly with the vortex Reynolds number.

The variation of the $U_{z\,\max}$ also does not conform according to the off-swirl parameter, which would result in a successive increase in U_z with κ. The range of variation in the value of κ for the present study is very small, which makes it difficult to infer any appreciable trends with it. The variation in the characteristics of the axial velocity, however, can be explained by the proximity of the chamber walls for the low aspect ratio configuration. The resultant flow for the short aspect ratio chamber does not fully develop; the mantle location at the chamber midplane remains in very close proximity to the injectors as seen in Figure 5.22, and is, therefore, pushed towards the center. Similarly, the low value of the axial velocity in the head-induced flow region and the shallow dip at $x/a = 0.22$ also suggest that the flow did not develop completely.

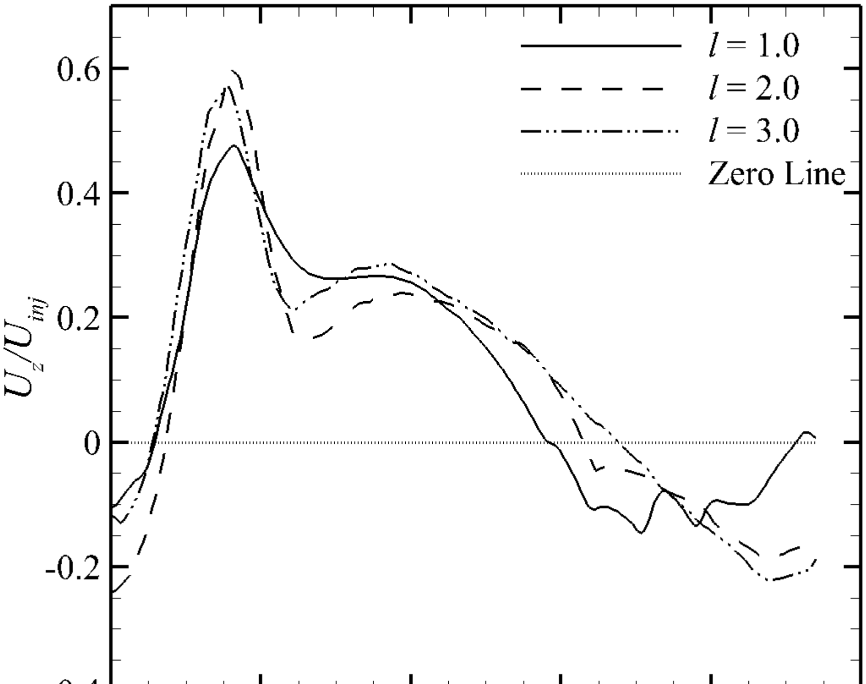

Figure 5.21 Distribution of axial velocity for various chamber aspect ratios.

The distribution of the tangential velocity for the three aspect ratios is presented in Figure 5.23. Here also, the effect of the proximity of the chamber wall is evident from the profile of the free vortex region for the shortest aspect ratio chamber. However, the tangential velocity characteristics such as the $U_{\theta\max}$ and the δ_c scale appropriately with the vortex Reynolds number when compared to results presented in Sec 4.4., reproduced with additional data of aspect ratio variation in Figure 5.24.

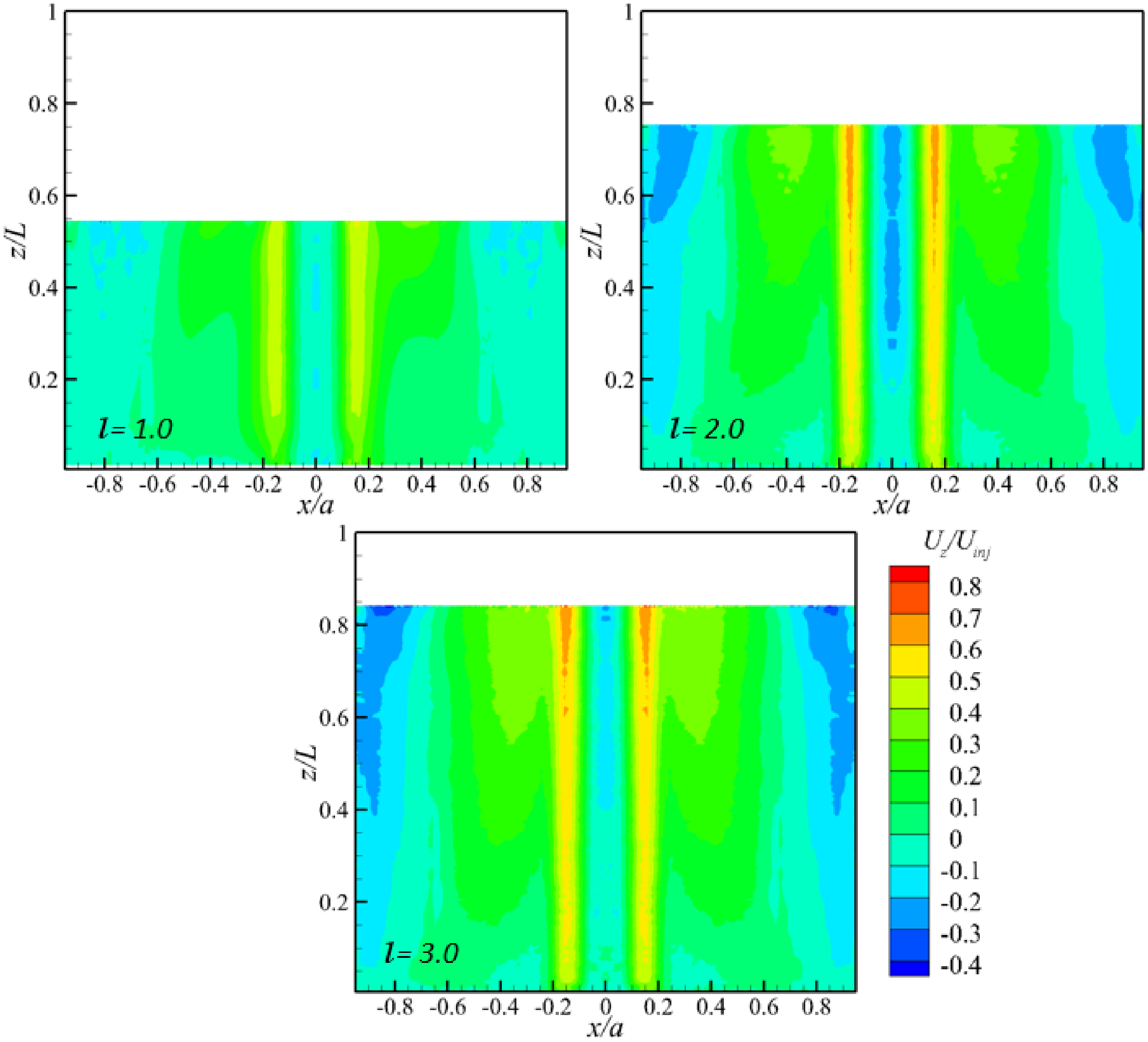

Figure 5.22 Axial velocity contours for different chamber aspect ratios.

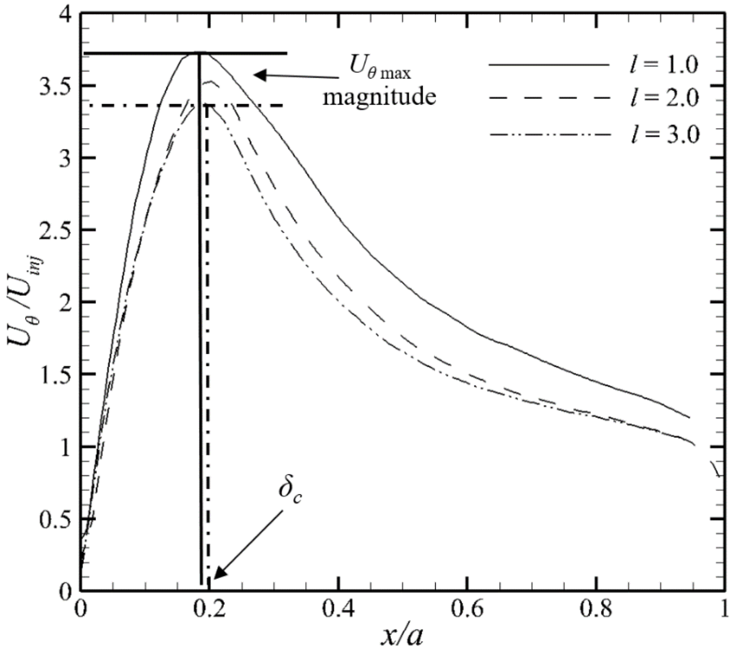

Figure 5.23 Distribution of tangential velocity for various chamber aspect ratios.

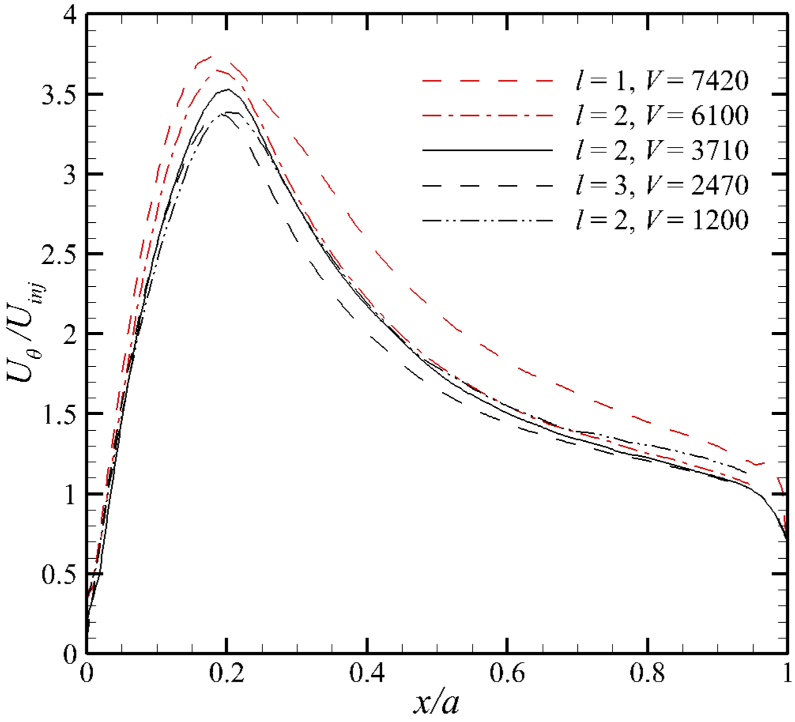

Figure 5.24 Distribution of the tangential velocity for various chamber aspect ratios and vortex Reynolds numbers.

Thus, it is concluded that the chamber aspect ratio influences the velocity characteristics, but the same can be adequately captured with the nondimensional parameter such as the vortex Reynolds number, V, and the off-swirl parameter, κ, provided the chamber aspect ratio is sufficient for the flow to develop.

5.7 Summary

In this chapter, the effect of the geometric parameters on the flowfield and associated characteristics have been presented. Based on the available literature, four geometric parameters, including the head injector configuration, exit contraction ratio, injection area, and chamber aspect ratio, were identified to investigate their influence on the cyclonic flowfield. The head-port configuration had a significant effect on the reverse flow region along the chamber axis, whereas, it did not alter the mantle location. The low pressure along the chamber centerline, which is responsible for creating the reverse flow region, causes the entrainment of the ambient fluid from the open head port, thus eliminating any reverse flow. In addition to the head port configuration, the exit contraction ratio was also found to significantly affect both the axial and tangential velocity profiles, in magnitude as well as distribution. The influence of both the exit contraction ratio and the injection area can be characterized together with the help of the swirl number. Although considerable variation in the flowfield was observed with the swirl number, the effect of swirl is normalized in the analytical solutions. Also, the effect of the chamber aspect ratio can be adequately characterized with the help of nondimensional parameters such as V and κ.

6. Effect of Swirl on the Jet

Swirling jets are often used in applications where mixing and mass transfer between the jet and the ambient fluid is desired. Unlike axisymmetric jets, shear layer of the swirling jets consists of helical vortical structures that are responsible for the increased mixing. However, when the swirl increases beyond a critical value, jet breakdown occurs, which is characterized by a stagnation/recirculation zone along the jet axis. This property of swirling jets is exploited in flame holders and fuel injectors. In the present work, a similar swirling jet was observed at the exit of the cyclonic chamber. The swirling jets have been investigated in the past [87,88][19-20], where most swirling jets are produced with mechanical devices such as helical impellers, etc. The reported research to date does not address the characteristics of jets exiting cyclonic chambers. In this chapter, a jet exiting a cyclonic chamber and the effect of injection from the chamber headwall will be discussed.

6.1 Swirling Jet Exiting a Cyclonic Chamber

The flowfield within the cyclonic chamber is highly swirl-dominated with the peak tangential velocity of three to four times the axial velocity. The maximum tangential velocity is located in the vicinity of the chamber centerline and has a profound influence on the characteristics of the emanating jet. Furthermore, a reverse flow region develops along the chamber centerline and spans the entire length of the chamber. Since jets are sensitive to the initial conditions [30], the ensuing jet from a cyclonic chamber is strongly coupled to the dynamics of the internal flow and was therefore investigated.

For this purpose, the jet emanating from the baseline cyclonic chamber is first characterized utilizing PIV in both the axial (r-z) and the transverse (r-θ) planes. In the transverse plane, the laser sheet is positioned at three axial distances of $z/d_e = 2$, 4, and 6 downstream of the jet exit to observe the spread of the jet.

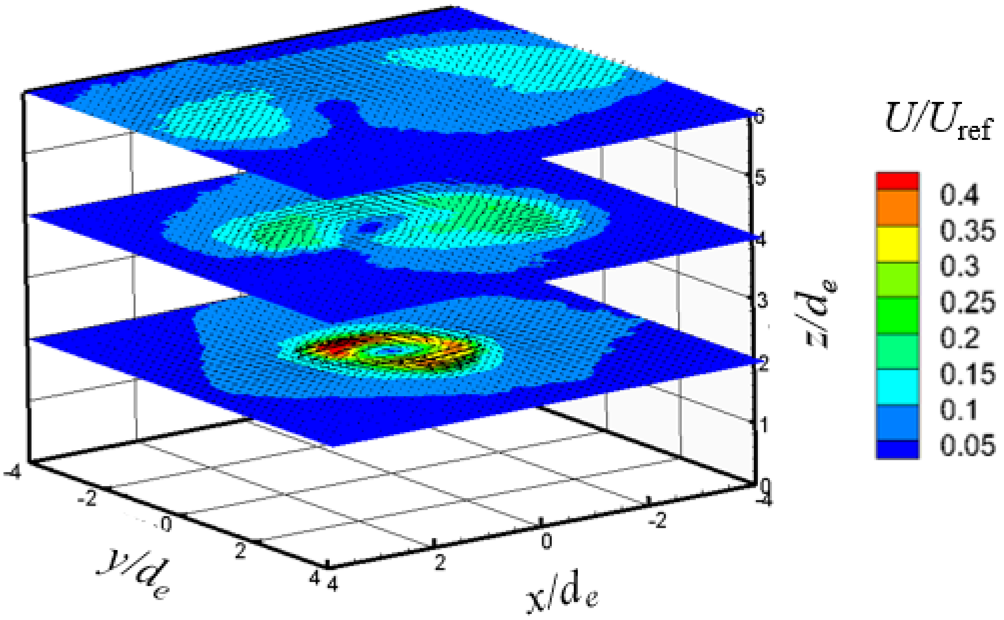

Figure 6.1 Velocity distribution in the transverse (r-θ) plane for the baseline nozzle at V = 3,710.

The velocity distribution in the transverse plane (r-θ) was plotted and presented in Figure 6.1. The velocity distribution at $z/d_e = 2.0$ is similar to that of a ring vortex resulting from an axisymmetric jet. However, on closer inspection of the velocity vectors, the rotation of the jet in the direction determined by the flow inside the chamber is evident. Moreover, as the jet spreads downstream ($z/d_e = 4$, 6) the magnitude of the tangential velocity diminishes as it interacts with the quiescent surroundings and entrains more fluid and finally bifurcates.

Figure 6.2 presents the reconstructed velocity fields for selected POD Modes for the baseline configuration in the transverse plane at $z/d_e = 2.0$. The bulk rotation of the jet is evident from the velocity vectors of the mean mode (Mode-0), whereas the secondary vortices created in the outer shear layer are clearly visible in Mode-2. However, the internal mixing and the interaction due to reversed flow persists at higher modes (Mode-20).

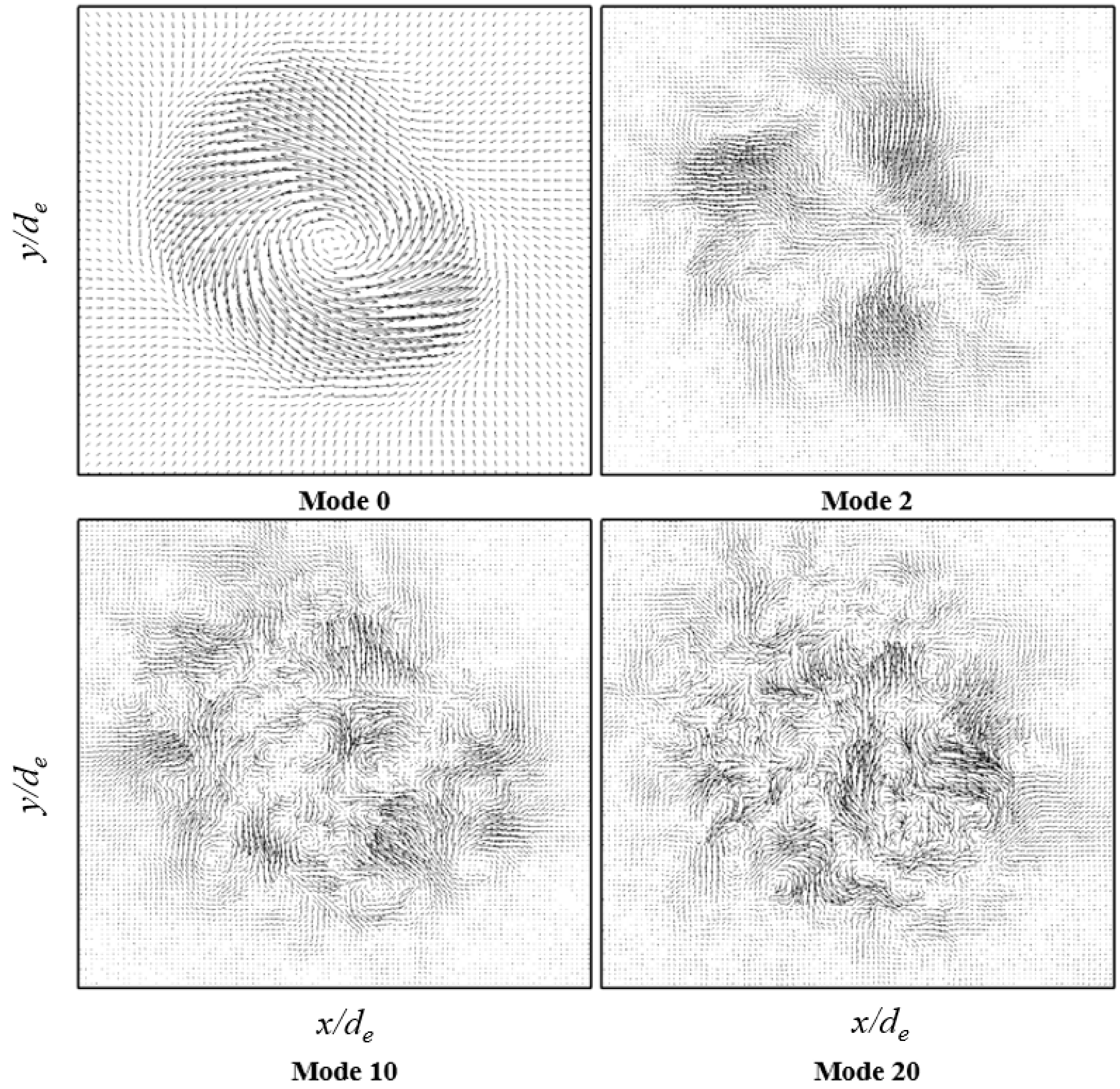

Figure 6.2 The reconstructed velocity distribution in a transverse (r-θ) plane at $z/d_e = 2$ for the baseline nozzle at $V = 3{,}710$.

Outside the cyclonic chamber, the swirling flow is not confined by the chamber walls, and as such, the swirling jet arms spread outwardly. The conservation of circulation implies an axial increase in pressure in the vortex core which leads to an axial deceleration. When the axial increase in pressure is sufficient to bring the axial velocity to zero, a stagnation point appears and a vortex breakdown can take place. In this context, various types of vortex breakdown in swirling jets have been identified. The main types consist of the axisymmetric bubble "B-type" and Cone "C-type" [88], as well as, the asymmetric spiral "S-type" [83]. At higher Reynolds numbers, the B-type and C-type breakdowns can assume asymmetric behavior due to the precession of the stagnation point which is located on the axis. In such case, the modes are referred to as the asymmetric bubble and the asymmetric cone. The primary difference between the B and C type breakdowns stands in their marked dissimilarities in the flow downstream of the stagnation point.

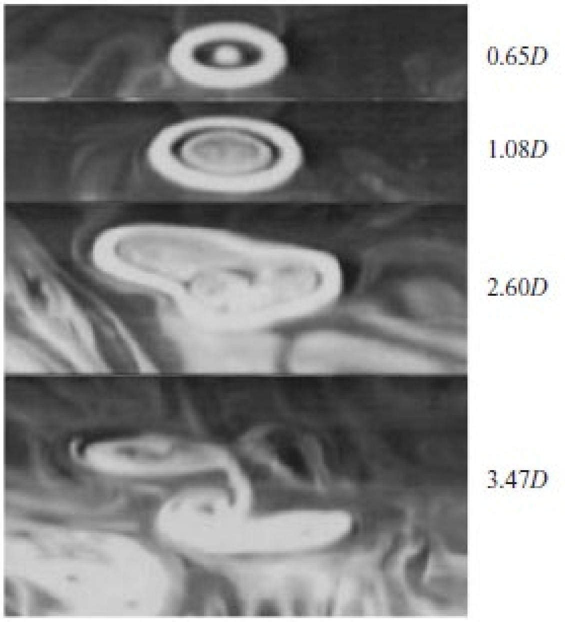

Figure 6.3 Axial evolution of the azimuthal structure at different axial locations following a bubble type vortex breakdown mode [88]**.**

The formation of helical disturbances is evident from Figure 6.1 beyond the $z/d_e = 2.0$, after the jet has undergone the bubble type vortex breakdown. The same phenomenon was observed by Billant et al. and has been shown in Figure 6.3 [88]; it is referred to as the "two-tailed bubble" type breakdown by Faler [89].

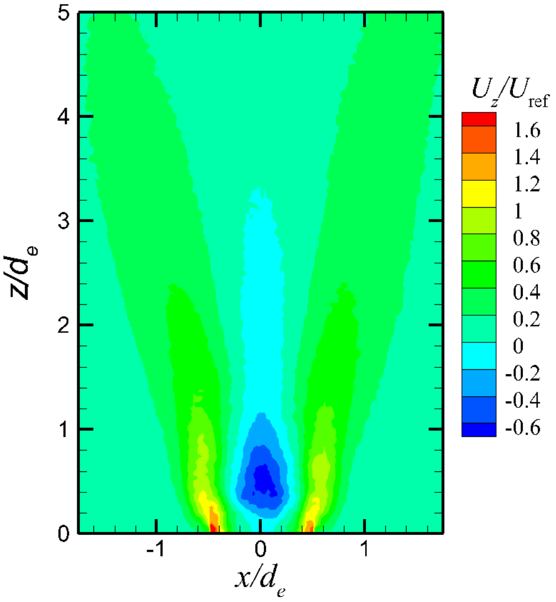

Figure 6.4 Axial velocity distribution of a baseline jet for a cyclonic chamber vortex Reynolds number, V = 3710.

Figure 6.4, shows the axial velocity of the jet for the cyclonic chamber at the vortex Reynolds number of $V = 3{,}710$. The reverse flow region in the core of the jet at the nozzle exit is created due to the drop in pressure near the exit caused by high tangential velocities. The reverse flow region also causes a significant loss of axial momentum. Due to the presence of the reverse flow region at the center, the centerline velocity could not be employed as a reference velocity for non-dimensionalization. Instead, a reference velocity, V_{ref}, was calculated for the given volume flow rate and the jet exit area, and then used for non-dimensionalization.

The flowfield of the post breakdown swirling jet is characterized by two separate shear layers. The outer shear layer between the swirling jet and the quiescent surroundings, and the inner shear layer between the swirling jet and the inner reverse flow. Similar results have been reported by Cala et al. [90]. The swirl-dominated jet also results in a greater spreading angle. Additionally, the inner and outer shear layers are also susceptible to the development of Kelvin-Helmholtz instabilities due to shear in both azimuthal and axial directions. The increase in inlet velocities in the chamber results in a stronger jet but the reverse flow remains intact, thus resulting in a complex flowfield with higher turbulence and rapid decay of the jet. Due to a significant loss in the axial momentum, the swirling jets are not ideal for propulsive purposes.

6.2 Effect of Headwall Injection on the Jet

It has been observed from the results presented in Sec 5.2. that the headwall configuration has a significant effect on the cyclonic chamber flow, where the opening of the headwall port and subsequent injection lead to the elimination of the reverse flow along the chamber centerline. Since it is observed from the above results that the same reverse flow region extends along the jet centerline, it is expected that the headwall configuration will have a substantial effect on the emanating jet as well.

In order to explore the effect of axial injection at the chamber headwall on the jet emanating from the cyclonic chamber, the following five cases are identified. The primary variation is in the ratio of the volume flow rate between the tangential injectors to the headwall axial injector while keeping the net volume flow rate constant ($\dot{Q}$ required for a Vortex Reynolds number of V=3710). Therefore, the limiting cases consist of pure tangential injection in Case 1 and pure axial injection in Case 5. These five cases are summarized below.

Table 6.1 Operating conditions of headwall injection.

Case	Tangential Injection	Headwall Injection
1	$\dot{Q}$	0, Closed
2	$\dot{Q}$	0, Open
3	$2\dot{Q}/3$	$\dot{Q}/3$
4	$\dot{Q}/3$	$2\dot{Q}/3$
5	0	$\dot{Q}$

Figure 6.5 shows the time-averaged axial velocity field for the five cases. For Cases 1 and 2, a central recirculation zone is formed along the jet axis where the axial velocities are negative and

are represented by blue contour level. Although the opening of the headwall port in Case 2 leads to the weakening of the CRZ, it is not large enough to allow pressure equilibrium, consequently, the negative axial velocities persist. The maximum negative axial velocities occur at a distance of about 0.5d_e outside the jet exit. Instantaneous PIV images provide an insight into the random motions in the jet by preserving the spatially frozen structures that are otherwise washed out in "long exposures" or in the averaging processes.

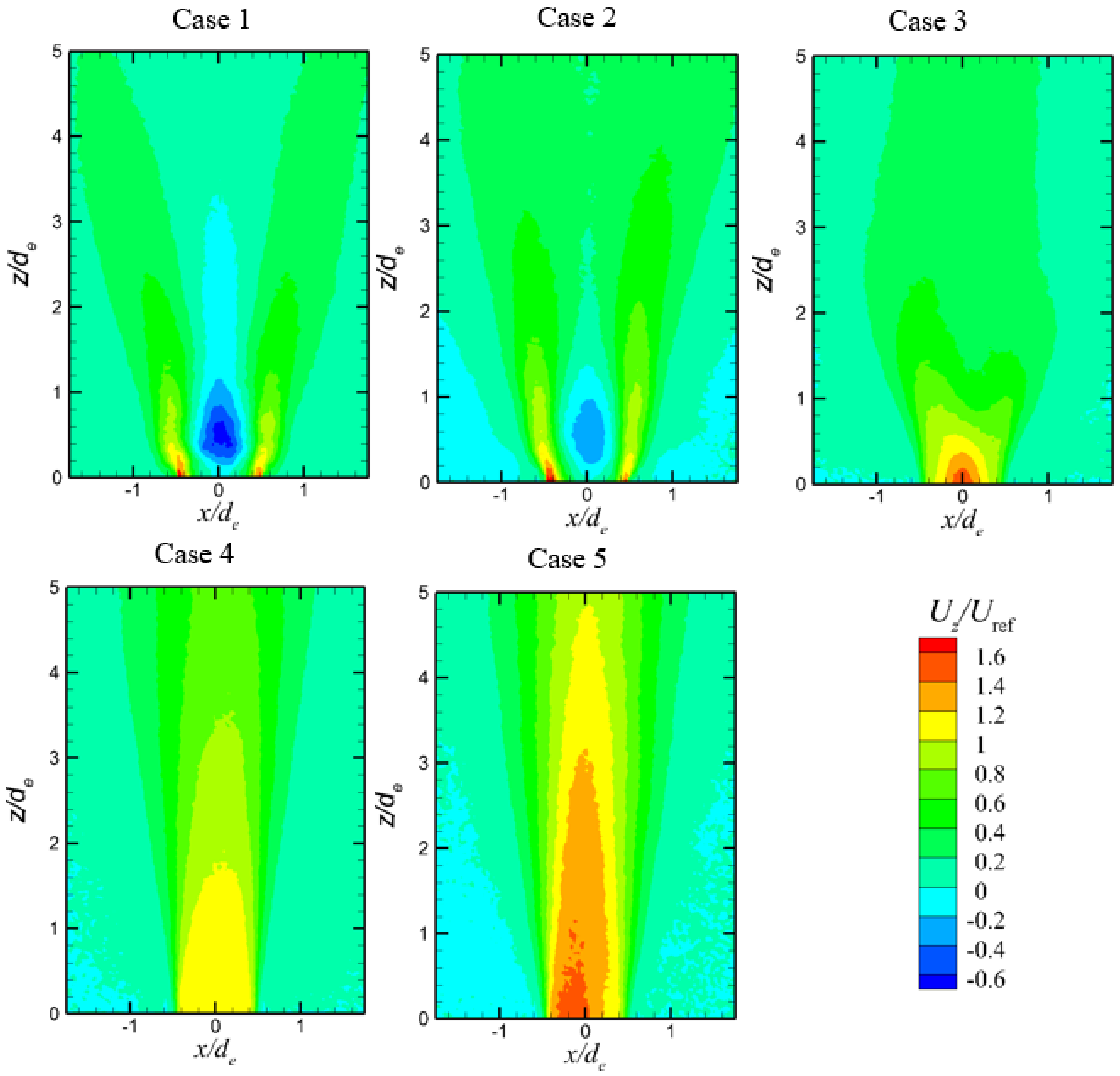

Figure 6.5 Time-averaged axial velocity contours for the five cases.

Figure 6.6 shows the instantaneous velocity distributions in the axial plane for Cases 1,3, and 5. It is evident that the reverse flow in the central region of Case 1 continues inside the nozzle. This shows that the reverse flow of the jet is the extension of the reverse flow region observed along the chamber centerline as discussed in Sec 4.2. For Case 3, a wake region is formed at the jet axis approximately one diameter downstream of the exit, which showcases the critical condition for jet breakdown as seen in Figure 6.5.

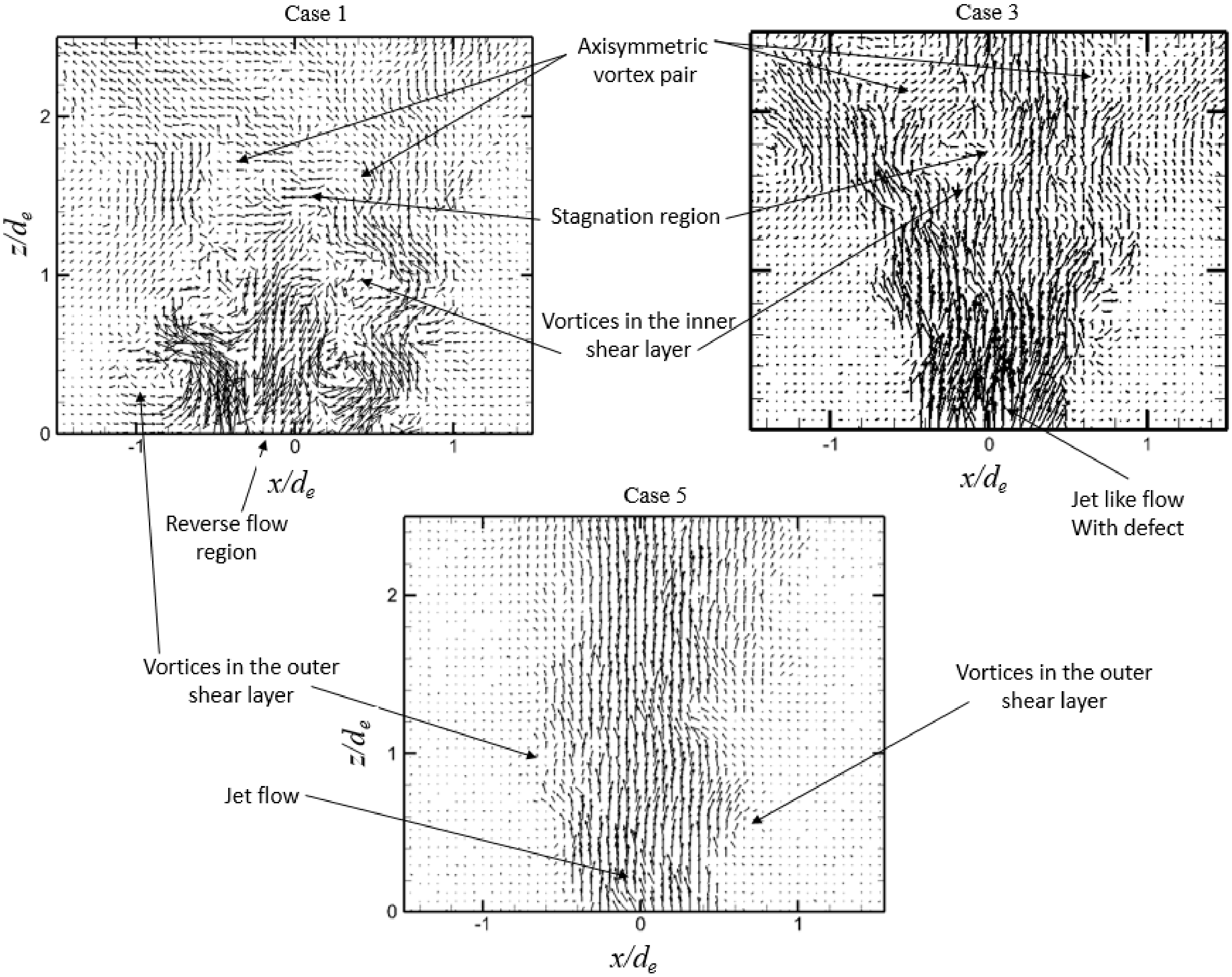

Figure 6.6 Instantaneous velocity vector distributions on the axial plane.

The velocity distribution in Figure 6.5 indicates a slightly positive velocity downstream of the wake region, whereas the instantaneous vector field in Figure 6.6 shows a jet-like flow from the exit, followed by a stagnation region at 1.5 d_e and subsequent formation of an axisymmetric vortex pair, which is characteristic of the onset of bubble-type vortex breakdown [82]. The flow around the wake region in Figure 6.5 (Case 3) represents the contraction of the stagnation region, which is also a feature of the bubble-type vortex breakdown. Since the operating conditions in Case 3 are indicative of the critical flow condition for breakdown, the subsequent increase in the injection from the head port results in a flowfield that resembles an axisymmetric jet as shown in Figures 6.5 and 6.6. The higher injection from the head port also results in a progressive decrease in the spread of the jet.

The presence of reverse flow in Cases 1 and 2, as well as the vortical structures in the core, indicate the formation of two separate shear layers. The velocity difference across these shear layers gives rise to Kelvin-Helmholtz instability and associated vortices. These vortices are evident in the instantaneous vector field presented in Figure 6.6. This also causes the concentration of vorticity in the vicinity of the jet exit as shown in Figure 6.7. Two separate regions of high vorticity at the exit nozzle are observed in Figure 6.7 for Cases 1-3, representing the turbulent interaction between the three different flow regions, i.e., the reverse flow in the center, the jet fluid stream emanating from the exit, and the ambient fluid at rest. However, for Cases 4 and 5, a single shear layer exists extending from the sidewalls of the nozzle, between the jet fluid and the quiescent ambient fluid. The magnitude of vorticity in the shear layer of Cases 4 and 5 is also lower than that concentrated in the shear layers of flows with vortex breakdown.

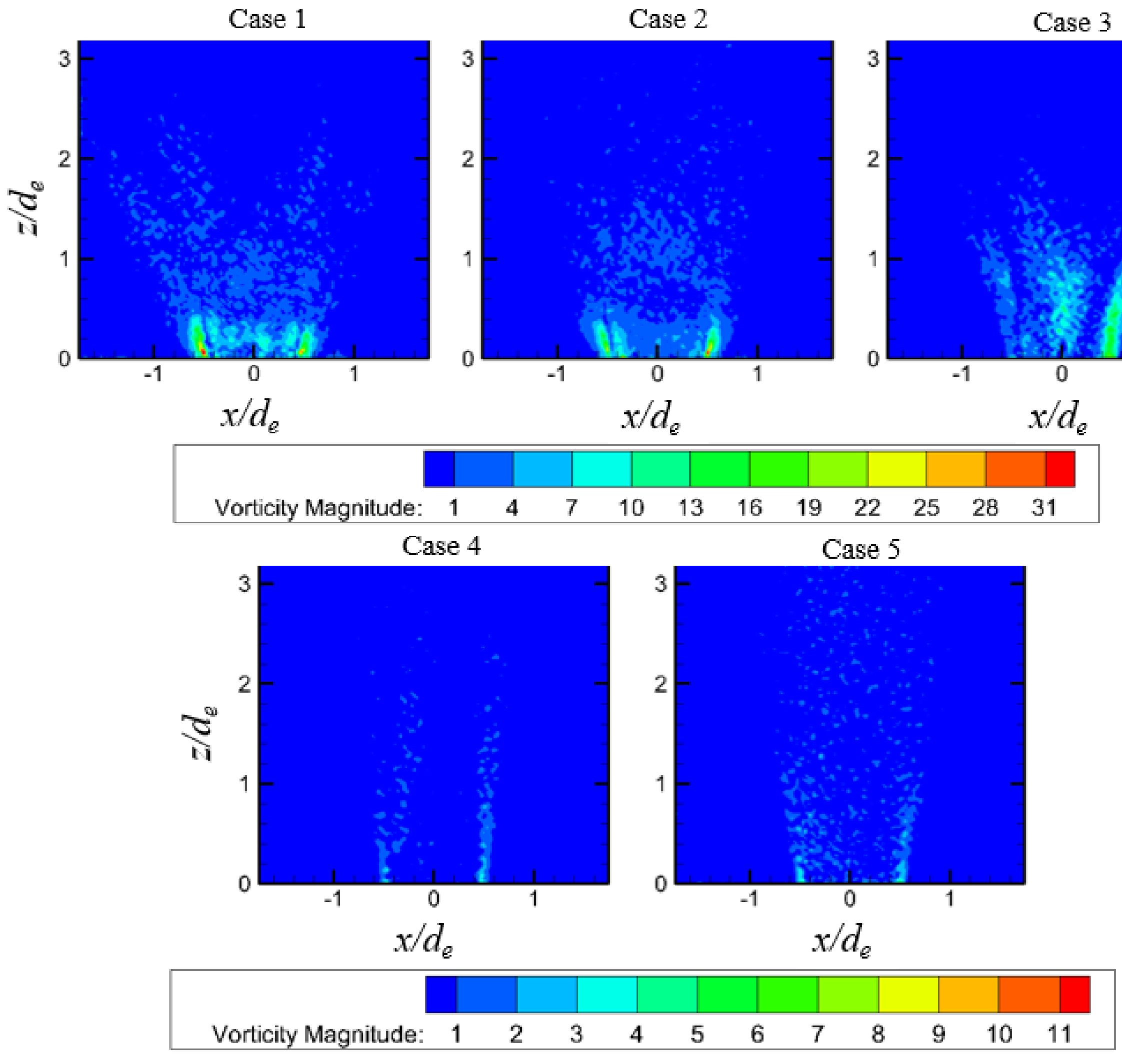

Figure 6.7 Vorticity magnitude contours in the axial plane for the five cases.

For Cases 4 and 5, where the injection from the headwall axial injector in the cyclonic chamber dominates, it is expected that the vortex cores in the mixing layer correspond to ring-like vortices and are the primary means of entrainment and mixing with the surrounding fluid, whereas the jet core remains almost unmixed. For Cases 1-3, which are significantly influenced by the tangential injection in the cyclonic chamber, the mixing is more efficient due to the wider spread and stronger vortices. During the mixing in the high-swirl jets, some entrained fluid of the surroundings is captured by the central recirculation zone and mixed with the annular jet. Thus, the contribution of large-scale vortical structures to jet diffusion in the inner mixing layer increases with increasing swirl rate.

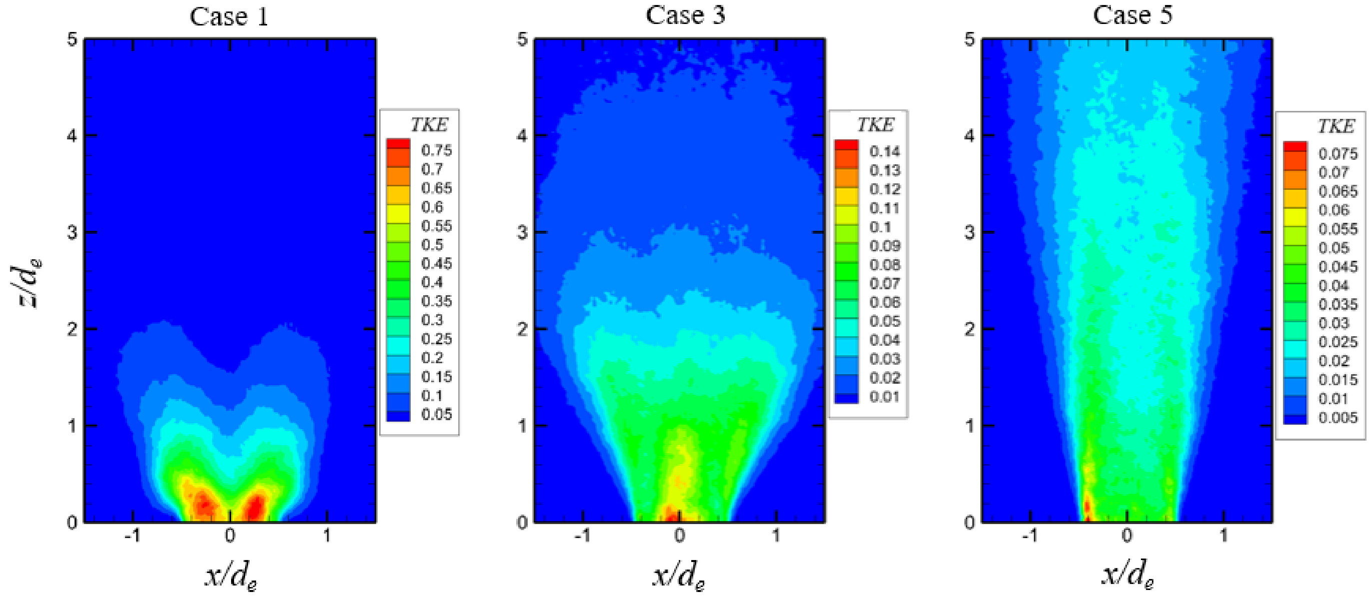

Figure 6.8 Distribution of the turbulent kinetic energy.

The same behavior can be visualized in the distribution of the turbulent kinetic energy for the three representative cases shown in Figure 6.8. The turbulent kinetic energy for Case 1 is much higher in magnitude and is concentrated in the close vicinity of the jet, where all mixing and diffusion take place. On the other hand, the TKE magnitude for Case 5 is not only lower in magnitude but also extends further downstream.

To reveal coherent structures in the flows and to analyze their contribution to mixing, Proper orthogonal decomposition (POD) is employed. The cumulative sum of energy contents, $\sum \lambda_i$, of the POD modes extracted from 1000 PIV image pairs in the longitudinal plane is presented in Figure 6.9. The energy content of Mode-0, which represents the mean flow for Case 1 constitutes only 40% of the total energy. The reduced energy in the mean flow is attributed to the presence of the reversed flow region and associated flow structures, which results in reduced axial momentum. The mean mode energy increases progressively with the configuration and injection from the head port, and reaches a maximum value of ~ 88 % for Cases 4 and 5. A similar magnitude of mean mode energy has been reported for a pure axial jet [30], which shows the close resemblance of Case 5 with an axial jet. The transfer of energy from the mean mode to lower modes for Cases 1 and 2 is also evident from the individual mode energy content presented in Figure 6.10. Also note that the energy of modes 1-3 for Cases 1 and 2 is an order of magnitude higher than the corresponding modes of Cases 3-5.

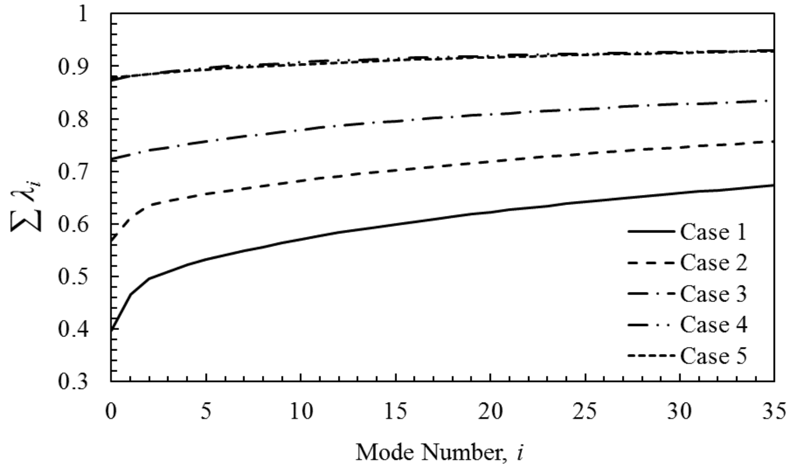

Figure 6.9 Cumulative sum of the energy content of the axial POD modes.

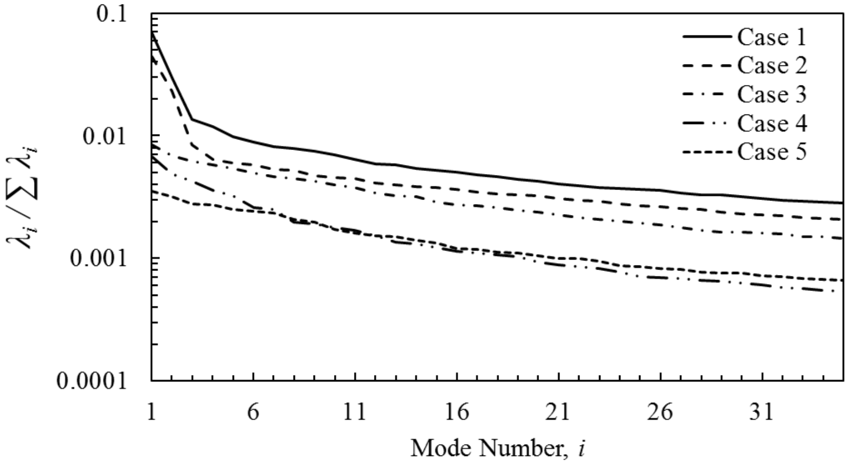

Figure 6.10 Individual energy fraction of the axial POD modes.

Figures 6.11-12 show the reconstructed velocity vector fields for the selected modes for Cases 1, 3, and 5. The mean mode vector field in Figure 6.11 shows the bulk motion of the fluid, where the central reverse flow is evident for Case 1, whereas the jet-like flowfield is observed for Cases 3 and 5. However, more noteworthy structures are present in modes 1 and 4 presented in Figures 6.11 and 12, respectively. These are the primary source of mixing with the ambient fluid and diffusion of the jet. However, the location of these coherent structures greatly varies from case to case depending on the swirl magnitude. The reverse flow observed in Case 1, which extends into the nozzle, gives rise to the double shear layer initiating from the exit orifice at $z/d_e = 0$. As a result, high-energy vortex pairs are observed in both the inner and outer shear layers. These are also responsible for the higher energy fraction of mode 1 observed for Case 1 in Figure 6.9. The breakdown of the swirling jet in Case 3 is evident from the vortex pair forming along the jet axis at $z/d_e = 1$. For Case 5, the large structures with alternating fluid advection patterns are visible with the longitudinal velocity and represent the vortex rings. These vortical structures appear weak near the exit $z/d_e = 1$ but become more pronounced as they convect downstream ($z/d_e = 3\text{-}4$). Because of entrainment of the surrounding fluid and mixing, these structures lose coherence and diffuse outwardly as observed for all the cases in Figure 6.12 (mode-10).

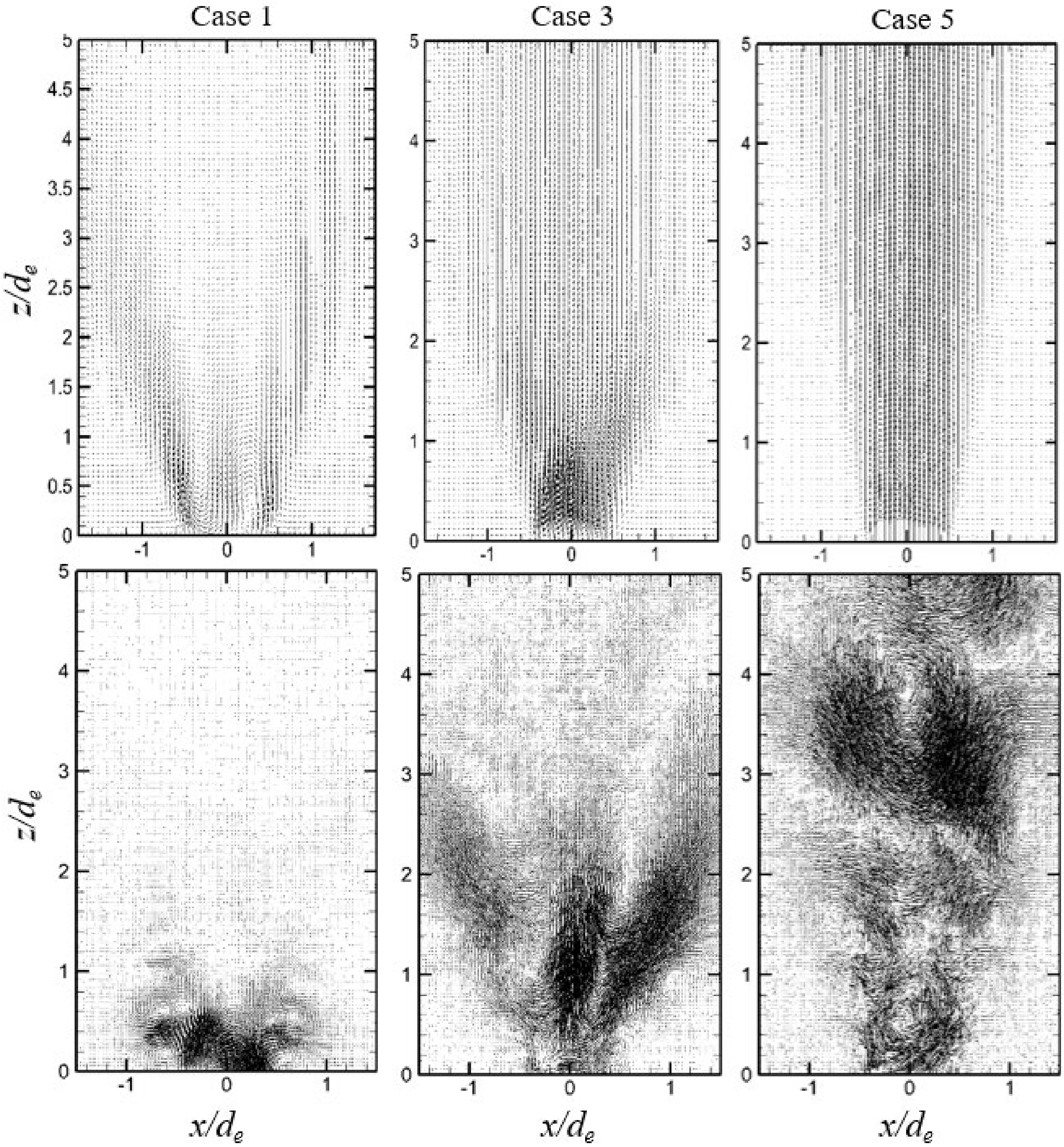

Figure 6.11 Reconstructed velocity field for POD modes, mode 0 (top) and mode 1 (bottom).

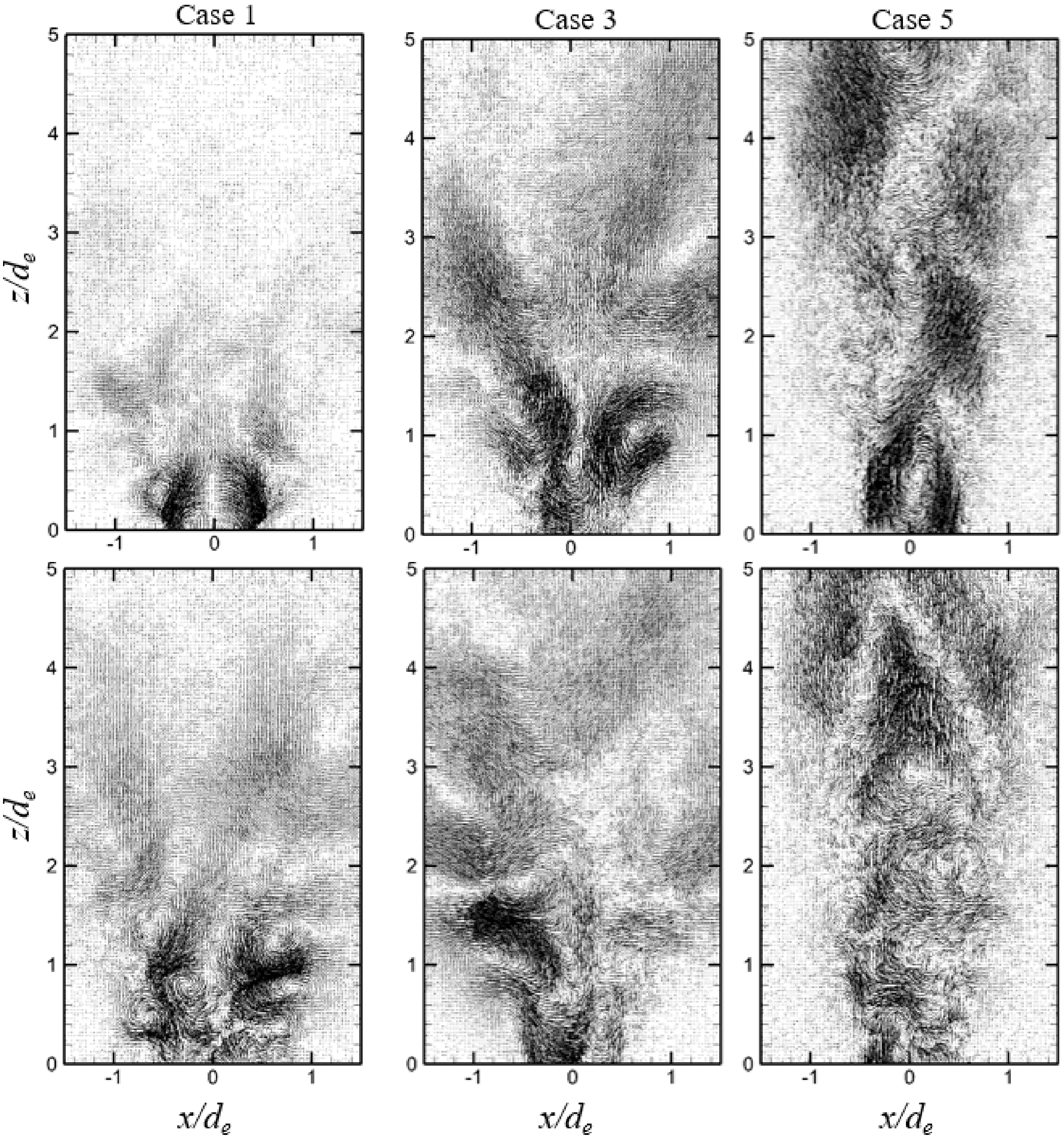

Figure 6.12 Reconstructed velocity field for POD modes of the three cases, mode 4 (top) and mode 10 (bottom).

6.3 Modification of Swirling the Jet

From the above discussion, it can be concluded that the jet exiting from the cyclonic chamber is highly swirl-dominated with reduced axial momentum accompanied by rapid decay. In order to recover the axial momentum, an auxiliary tube is installed inside the chamber to shroud the braided vortices from extracting energy from the radial flow and isolating it from the surrounding rotating fluid in the chamber before its exit as shown in Figure 6.13. A shrouding tube of internal diameter, d_t = 0.25 in and $4d_t$ length was mounted inside the chamber on the exit plate to shroud the core flow prior to its exit.

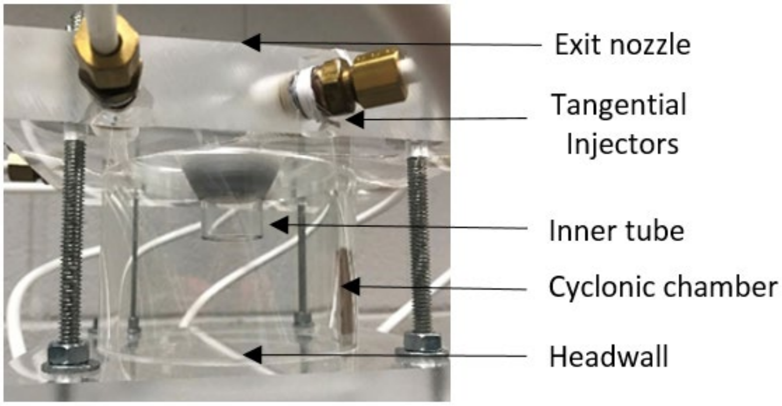

Figure 6.13 Assembled cyclonic chamber with the inner tube.

The axial velocity contours of Case 1 without and with the shrouding tube are presented in Figure 6.14. It is observed that the inner shrouding tube results in better symmetry while restricting the spread of the jet. The reverse flow in the core of the jet also decreases for the case with the inner tube. This can be attributed to the flow alignment in the inner tube and boundary layer buildup on the shrouding tube's inner wall, while separating the outward-directed flow from the surrounding rotating fluid. Similar observations are made from the velocity profiles presented in Figure 6.15, the latter compares the velocity profiles for Case 1 and the configuration with a shrouding tube at downstream distances of z/d_e =1.0 and 2.0.

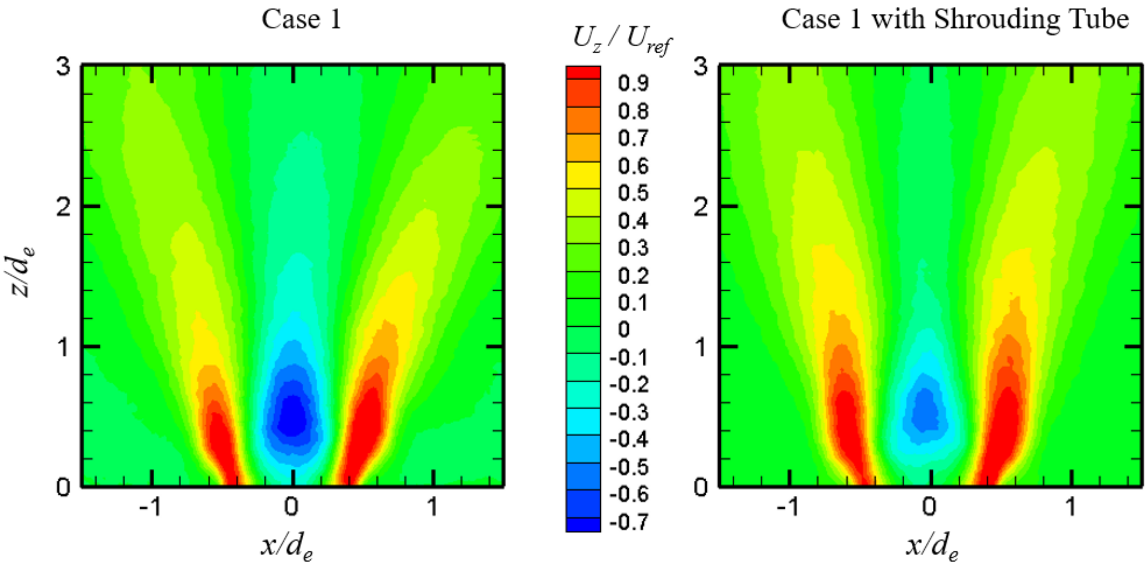

Figure 6.14 Axial velocity contours of the jet emanating from the cyclonic chamber.

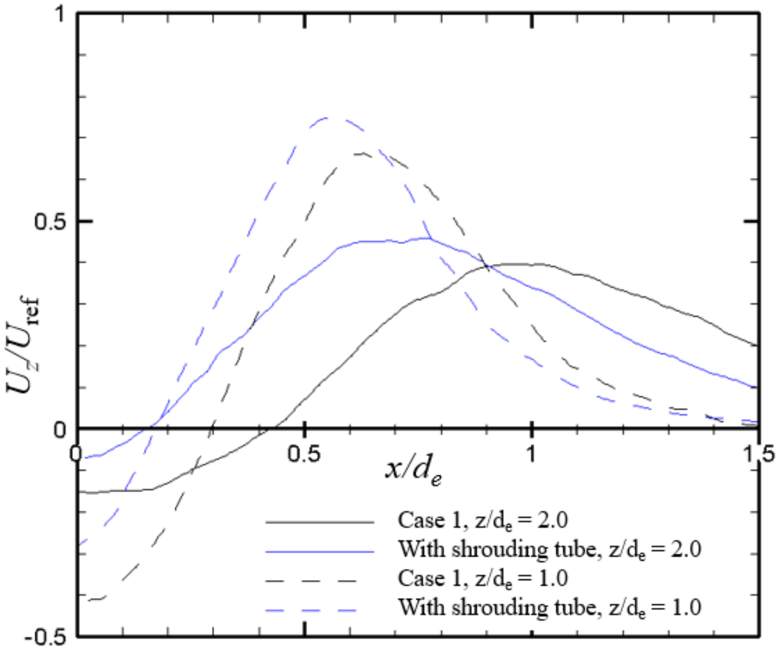

Figure 6.15 Axial velocity profiles at z/d_e of 1.0 and 2.0.

Figure 6.16 shows the distribution of the turbulent kinetic energy for the baseline and the shrouding tube configurations. The TKE distribution of the swirling jet is in agreement with Dulin et. al. [91] where both the inner and outer shear layers surround the region with the highest TKE. The shrouding tube not only results in reducing the magnitude of reverse flow but also reduces the turbulent intensity of rising vortices, therefore reducing the TKE as well.

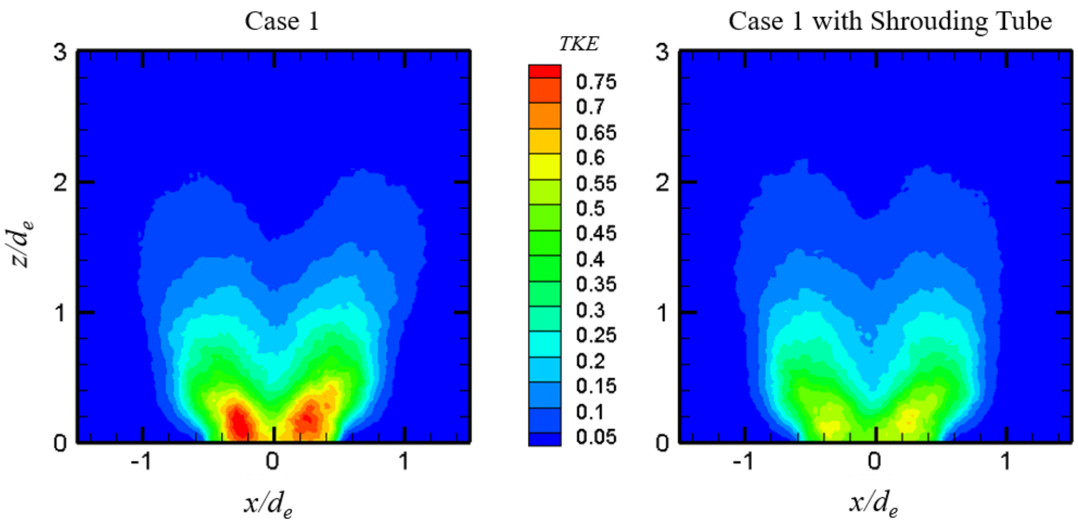

Figure 6.16 Axial distribution of turbulent kinetic energy.

The mean mode energy fraction is also larger for the configuration with the inner shrouding tube, as evident from the cumulative modal energy presented in Figure 6.17. However, the increase in the mean mode energy, which is also representative of the recovery of the axial momentum is marginal as compared to the mean mode energy of Case 5; naturally, the latter resembles an axial jet.

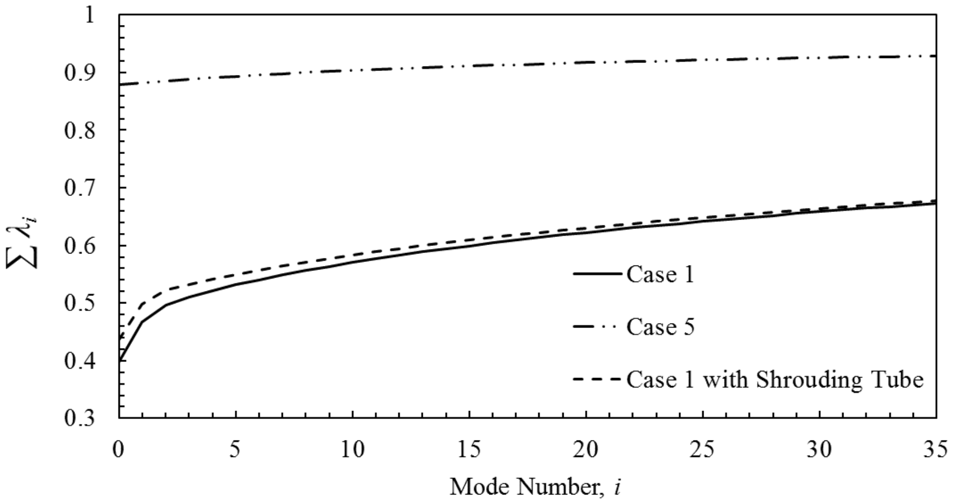

Figure 6.17 Cumulative sum of the energy content of the axial POD modes.

The recovery of the axial momentum can also be inferred from the reduced velocities in the transverse plane of the jet. Figure 6.18 presents a comparison of the flowfield in the transverse plane at a distance of two exit diameters from the nozzle exit for the baseline and with shrouding tube configurations. It is evident that the presence of the inner tube resulted in the reduced transverse velocities and spread of the jet.

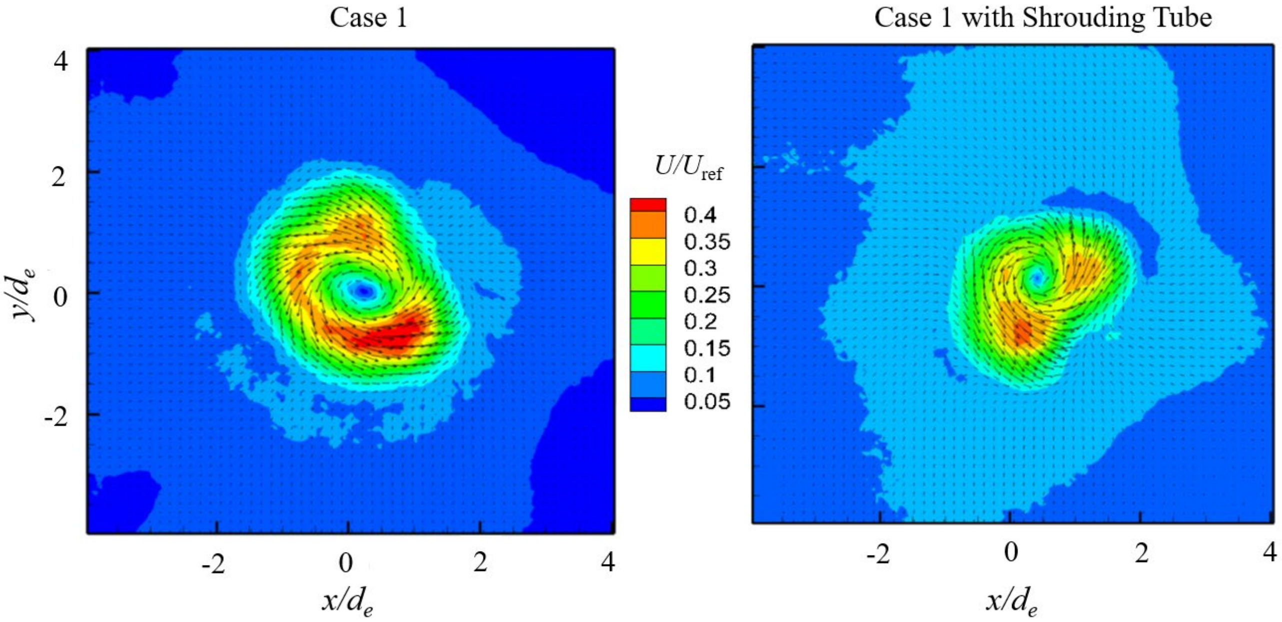

Figure 6.18 Contours of velocity in the transverse plane.

It can be inferred that the use of an auxiliary tube inside the chamber installed to shroud the inner core vortex results in reduced swirl and increased axial momentum of the jet. However, this gain in the axial momentum is marginal, even for an inner shrouding tube that spans half of the chamber and would affect the inner flowfield of the cyclonic chamber. Therefore further experimentation with shrouding tubes was not undertaken.

6.4 Summary

The inner flowfield of the confined cyclonic chambers has a significant effect on the ensuing jet. The swirl-dominated exiting jet possesses reverse flow/backflow along the jet axis, which extends into the cyclonic chamber due to very low pressures in the inner vortex core. Two separate shear layers are observed in the swirling jet with reverse flow, which concentrates the vorticity and turbulent kinetic energy in the core of the ensuing jet, resulting in reduced axial momentum and increased spread. The configuration and operating condition of the axial head port greatly influence the flowfield of the jet. Opening the head port and any subsequent injection reduce the axial adverse pressure gradient, thereby eliminating the reverse flow region along the chamber centerline. However, the unconstrained expansion of the swirling flow in the radial direction, outside the chamber, leads to the bubble-type vortex breakdown of the jet. Further increase in the axial injection ratio inhibits the breakdown and an axial jet is observed. Proper orthogonal analysis shows a progressive increase in the mean mode energy with a higher fraction of axial injection.

The use of an inner tube to shroud the core of the cyclonic chamber vortex successfully reduces the swirl and spread of the jet. The shrouding tube reduced the magnitude of the reversed flow near the jet exit. It also reduces the overall level of turbulent kinetic energy compared to the jet without an inner tube. However, the velocity distribution remains bimodal and, consequently, the distribution of turbulent kinetic energy as well. Proper orthogonal decomposition analysis also shows a marginal increase in the mean mode energy of the axial velocity and a decrease in the transverse velocity for the configurations with an inner tube. However, the effectiveness of the shrouding tube for axial momentum recovery remains limited.

7. Conclusions

7.1 Flow Dynamics

The formation of a bidirectional vortex flow has been observed in the cyclonic chamber with tangential inlets under varying operating conditions. In addition to the two characteristic flow features of the bidirectional vortex, namely the bidirectional axial velocity and the combination of the free-forced vortex, two additional flow features have been identified. These are the head-induced flow and the central recirculation zone.

The central recirculation zone (CRZ) is created due to the adverse pressure gradient along the chamber centerline. The range of swirl number ($S = 1.37 – 4.0$) for the baseline configuration of the present experiments is well beyond the critical swirl number of 0.6. At such high levels of swirl, the CRZ develops into a columnar structure along the chamber centerline and is responsible for the reverse flow from the chamber exit. The reverse flow region has been observed in all the configurations tested in the present experiments. It is contingent, however, on the use of an incompressible fluid with a closed headwall port.

The other noteworthy flow feature of the head-induced flow, which is a direct consequence of the viscous interaction between the vortex-dominated flowfield and the stationary headwall of the chamber, resulting in a rotating boundary layer at the chamber headwall. Within the boundary layer, the equilibrium between the centrifugal force and the radial pressure gradient is disturbed, which drives the fluid within the boundary layer towards the center of the chamber, resulting in a jet-like flow that surrounds the central reverse flow region along the chamber centerline. The axial velocity of the head-induced flow is significantly higher than the exit-bound inner vortex and the central reverse flow region, which gives rise to azimuthal vorticity due to the Kelvin-Helmholtz instability in the vicinity of the chamber centerline.

7.2 Axial and Tangential Velocity Profiles

In an effort to characterize the flowfield of the confined cyclonic chamber, a large data set in the form of axial and tangential velocity profiles for various operating conditions and geometric configurations were generated. The analysis of the axial velocity profiles shows the bidirectional behavior of the axial velocity in the complete range of the operating conditions, with the minimum vortex Reynolds number of ~1200 being investigated. A good qualitative agreement with the analytical solutions in the outer, head-bound vortex region is found, including the location of the mantle. However, the high exit bound velocity region of the head-induced flow and the reverse flow region is not discussed in the existing literature for bidirectional cyclonic chambers. The tangential velocity profile captures both the forced vortex core and the free vortex tail. The invariance of tangential velocity with respect to the axial (*z/L*) location, and its dependence on the vortex Reynolds number, is also been demonstrated in conformance with theory [10]. The variational trend in the characteristic parameters of the tangential velocity profile such as the core thickness, maximum tangential velocity, and angular velocity of the forced vortex is also found to be in agreement with Majdalani's analytical solutions. An attempt is made to use the eddy-viscosity approach to quantitatively compare the present experimental results with available analytical solutions, and is determined that a constant eddy-viscosity ratio, l_t, does not effectively scale the effective vortex Reynolds number. However, defining an eddy-viscosity ratio, l_t, in terms of the vortex Reynolds number yields very good agreement between the analytical and experimental data.

7.3 Effect of Geometric Conditions

This study also characterizes the effect of the geometric parameters on the confined cyclonic flowfield and associated characteristics. Four geometric parameters, including the head injector configuration, exit contraction ratio, injection area, and chamber aspect ratio are investigated. The vortex breakdown and resulting reverse flow region are eliminated by allowing passive flow entrainment or active injection from the axial head port. The influence of the head port configuration remains confined within the inner exit-bound vortex only and does not affect the mantle location or the velocity distribution in the outer head-bound vortex. Proper orthogonal decomposition reveals the presence of coherent structures in the vicinity of the head injection port. The distribution of turbulent kinetic energy also suggests efficient mixing of the injected fluid.

In addition to the head port configuration, the exit contraction ratio is also found to significantly affect both the axial and tangential velocity profiles, in magnitude as well as distribution. The influence of both the exit contraction ratio and the injection area can be characterized together with the help of the swirl number. Although considerable variation in the flowfield is observed with the swirl number, the effect of swirl is not presented in the analytical solutions. Also, the effect of the chamber aspect ratio can be adequately characterized with the help of non-dimensional quantities, such as the vortex Reynolds number, V, and off-swirl number, κ.

7.4 Swirl Dominated Jet

The inner flowfield of the confined cyclonic chambers has a significant effect on the ensuing jet. Using a subsonic converging nozzle in a water tank, the swirl-dominated exiting jet possesses reverse flow/backflow along the jet axis, which extends into the cyclonic chamber due to very low pressures in the inner vortex core. Two separate shear layers are observed in the swirling jet with reverse flow, which concentrates the vorticity and turbulent kinetic energy in the core of the ensuing jet, resulting in reduced axial momentum and increased spread. The configuration and operating conditions of the axial head port greatly influence the flowfield of the jet. The opening of the head port and any subsequent injection reduce the axial adverse pressure gradient, thereby eliminating the reverse flow region along the chamber centerline. However, the unconstrained expansion of the swirling flow in the radial direction outside the chamber leads to the bubble-type vortex breakdown of the jet. Further increase in the axial injection ratio inhibits the breakdown and an axial jet is observed. The proper orthogonal decomposition shows a progressive increase in the mean modal energy with a higher fraction of axial injection.

The use of an inner tube to shroud the core of the cyclonic chamber vortex successfully reduces the swirl and spread of the jet. The shrouding tube reduces the magnitude of the reverse flow near the jet exit. It also reduces the overall level of turbulent kinetic energy compared to the jet without an inner tube. However, the velocity distribution remains bimodal, and consequently the distribution of turbulent kinetic energy as well. The use of proper orthogonal decomposition analysis also projects a marginal increase in the mean modal energy of the axial velocity and a decrease in the transverse velocity for the configurations with an inner tube. However, the effectiveness of the shrouding tube for axial momentum recovery remains limited.

7.5 Future Work

The natural extension to the present research is to implement the time-resolved, three-dimensional volumetric or stereoscopic PIV measurements in order to resolve the unsteady, asymmetric structures that are expected in high swirling flows. Such time-resolved data can also provide an insight into the growth and decay of flow features with the implementation of dynamic mode decomposition with high temporal resolution. In addition to PIV, three-dimensional hotwire anemometry can also resolve local time-sensitive flow features.

Although, the effect of geometric modifications, across a limited parameter space, has been examined, several parameters may be useful to characterize what remained out of the scope of the present research. The location and angle of injection, which have the potential to yield the bidirectional flow without the formation of CRZ or reverse flow regions may be explored. In the same vein, the sizing and contouring of the exit nozzle can be explored in detail such that the exit nozzle matches the mantle location for an ideal scenario. This, no doubt will be a challenging undertaking as the mantle location varies with the exit nozzle size as shown in this study.

Another avenue that lies ahead is to characterize and subsequently control the flowfield in response to perturbations or active control inputs, to produce a flowfield suitable for vortex injection hybrid/liquid rocket engine operations. In the same vein, high fidelity numerical simulations can be validated against the present experimental data and perused to achieve a fully transient solution with enhanced spatial and temporal resolution. The ensuing jet, which is strongly influenced by the internal flowfield of the cyclonic chamber, can be actively controlled to maximize its axial momentum and its extension to propulsive applications.

Bibliography

[1] Linden, A. J. ter. "Investigations into Cyclone Dust Collectors." *Proceedings of the Institution of Mechanical Engineers.*, Vol. 160, No. 1, 1949, pp. 233–251. https://doi.org/10.1243/PIME.

[2] Bloor, M. I. G., and Ingham, D. B. "The Flow in Industrial Cyclones." *Journal of Fluid Mechanics*, Vol. 178, 1987, pp. 507–519. https://doi.org/DOI: 10.1017/S0022112087001344.

[3] Hsieh, K. T., and Rajamani, R. K. "Mathematical Model of the Hydrocyclone Based on Physics of Fluid Flow." *AIChE Journal*, Vol. 37, No. 5, 1991, pp. 735-746.

[4] Hoekstra, A. J., Derksen, J. J., and Van Den Akker, H. E. A. "An Experimental and Numerical Study of Turbulent Swirling Flow in Gas Cyclones." *Chemical Engineering Science*, Vol. 54, Nos. 13–14, 1999, pp. 2055–2065. https://doi.org/10.1016/S0009-2509(98)00373-X.

[5] Gloyer, P. W., Knuth, W. H., and Goodman, J. "Overview of Initial Research into the Effects of Strong Vortex Flow on Hybrid Rocket Combustion and Performance." *In its Center for Space Transportation and Applied Research Fifth Annual Technical Symposium Proceedings 00004 p (SEE N96-16940 04-20)*, 1993.

[6] Knuth, W. H., Quavering, M. J., Gramer, D. J., and Sauer, J. A. "Experimental Investigation of a Vortex-Driven High-Regression Rate Hybrid Rocket Engine." *34th AIAA/ASME/SAE/ASEE Joint Propulsion Conference and Exhibit*, 1998. https://doi.org/10.2514/6.1998-3348.

[7] Knuth, W. H., Chiaverini, M. J., Gramer, D. J., Sauer, J. A., Whitesides, R. H., and Dill, R. A. "Preliminary Computational Fluid Dynamics Analysis of the Vortex Hybrid Rocket Chamber and Nozzle Flowfield." *34th AIAA/ASME/SAE/ASEE Joint Propulsion Conference and Exhibit*, 1998. https://doi.org/10.2514/6.1998-3351.

[8] Knuth, W. H., Bemowski, P. A., Gramer, D. J., Majdalani, J., and Rothbauer, W. J. "Gas-Fed, Vortex Injection Hybrid Rocket Engine." *SBIR Phase I, NASA Final Technical Contract No. NAS8-40679, Orbital Technolodies Corporation*, 1996.

[9] Chiaverini, M. J., Malecki, M. J., Sauer, J. A., Knuth, W. H., Gramer, D. J., and Majdalani, J. "Vortex Thrust Chamber Testing and Analysis for O2-H2 Propulsion Applications." *39th*

AIAA/ASME/SAE/ASEE Joint Propulsion Conference and Exhibit, Vol. 39, No. July, 2003, pp. 1–20. https://doi.org/10.2514/6.2003-4473.

[10] Majdalani, J. “Unified Framework for Modeling Swirl Dominated Helical Motions.” *50th AIAA/ASME/SAE/ASEE Joint Propulsion Conference and exhibit 2014*, 2014. https://doi.org/10.2514/6.2014-3677.

[11] Vyas, A. B., and Majdalani, J. “Exact Solution of the Bidirectional Vortex.” *AIAA Journal*, Vol. 44, No. 10, 2006, pp. 2208–2216. https://doi.org/10.2514/1.14872.

[12] Maicke, B. A., and Majdalani, J. “A Constant Shear Stress Core Flow Model of the Bidirectional Vortex.” *Proceedings of the Royal Society A: Mathematical, Physical and Engineering Sciences*, Vol. 465, No. 2103, 2009, pp. 915–935. https://doi.org/10.1098/rspa.2008.0342.

[13] Akiki, G., and Majdalani, J. “On the Viscous Bidirectional Vortex with Arbitrary Endwall Injection.” *47th AIAA/ASME/SAE/ASEE Joint Propulsion Conference & Exhibit*, 2011. https://doi.org/10.2514/6.2011-5692.

[14] Maicke, B. A., Cecil, O. M., and Majdalani, J. “On the Compressible Bidirectional Vortex in a Cyclonically Driven Trkalian Flow Field.” *Journal of Fluid Mechanics*, Vol. 823, 2017, pp. 755–786. https://doi.org/10.1017/jfm.2017.310.

[15] Maicke, B. A., and Majdalani, J. “On the Compressible Bidirectional Vortex.” *44th AIAA/ASME/SAE/ASEE Joint Propulsion Conference & Exhibit 21 - 23 July 2008, Hartford, CT*, No. July, 2008, pp. 1–13. https://doi.org/10.2514/6.2008-4834.

[16] Turner, A. E. “Aquarius Low Cost Launch Main Engine Study.” *3rd Responsive Space Conference*, 2005.

[17] Flinn, E. D. “Cooling off a Hot New Engine.” *Aerospace America*, Vols. 39(9):26–2.

[18] Chiaverni, M. J., Malecki, M. J., Sauer, J. A., and Knuth, W. H. “Vortex Combustion Chamber Development for Future Liquid Rocket Engine Applications.” *38th AIAA/ASME/SAE/ASEE Joint Propulsion Conference and Exhibit*, No. July, 2002. https://doi.org/10.2514/6.2002-4149.

[19] Majdalani, J., and Chiaverini, M. J. “On Steady Rotational Cyclonic Flows: The Viscous Bidirectional Vortex.” *Physics of Fluids*, Vol. 21, No. 10, 2009, pp. 1–15. https://doi.org/10.1063/1.3247186.

[20] Batterson, J. W., and Majdalani, J. “Sidewall Boundary Layers of the Bidirectional Vortex.”

Journal of Propulsion and Power, Vol. 26, No. 1, 2010, pp. 102–112. https://doi.org/10.2514/1.40442.

[21] Majdalani, J. "Exact Eulerian Solutions of the Cylindrical Bidirectional Vortex." *45th AIAA/ASME/SAE/ASEE Joint Propulsion Conference & Exhibit*, No. August, 2009, pp. 1–30. https://doi.org/10.2514/6.2009-5306.

[22] Batterson, J. W., and Majdalani, J. "On the Viscous Bidirectional Vortex . Part 1 : Linear Beltramian Motion." *46th AIAA/ASME/SAE/ASEE Joint Propulsion Conference & Exhibit*, 2010. https://doi.org/10.2514/6.2010-6763.

[23] Vyas, A. B., Majdalani, J., and Chiaverini, M. J. "The Bidirectional Vortex. Part 2: Viscous Core Corrections." *39th AIAA/ASME/SAE/ASEE Joint Propulsion Conference and Exhibit, USA*, 2003. https://doi.org/10.2514/6.2003-5053.

[24] Akiki, G., and Majdalani, J. "On the Bidirectional Vortex with Arbitrary Endwall Velocity." *46th AIAA/ASME/SAE/ASEE Joint Propulsion Conference and Exhibit*, Vol. 2010. https://doi.org/https://doi.org/10.2514/6.2010-6652.

[25] Maicke, B., and Majdalani, J. "On the Compressible Bidirectional Vortex. Part 1: A Bragg-Hawthorne Stream Function Formulation." *50th AIAA Aerospace Sciences Meeting including the New Horizons Forum and Aerospace Exposition*, No. January, 2012, pp. 1–11. https://doi.org/10.2514/6.2012-1103.

[26] Knuth, W., Chiaverini, M., Gramer, D., and Sauer, J. "Solid-Fuel Regression Rate and Combustion Behavior of Vortex Hybrid Rocket Engines." *Journal of Propulsion and Power*, Vol. 18, No. 3, 2002. https://doi.org/10.2514/6.1999-2318.

[27] Ozawa, K., Kitagawa, K., Aso, S., and Shimada, T. "Hybrid Rocket Firing Experiments at Various Axial–Tangential Oxidizer-Flow-Rate Ratios." *Journal of Propulsion and Power*, Vol. 35, No. 1, 2019, pp. 1–15. https://doi.org/10.2514/1.B36889.

[28] Rom, C. J. "Flow Field and Near Nozzle Fuel Spray Characterizations for a Cold Flowing Vortex Engine." *Department of Engineering Mechanics and Engineering Physics*, 2006.

[29] Wall, N. *Characterisation of Multiple Concentric Vortices in Hybrid Rocket Combustion Chambers*. Department of Mechanical Engineering, The University of Shefield, 2013.

[30] Ahmed, A., and Weiner, A. J. "Axisymmetric Jet Subjected to Radial and Azimuthal Forcing." *Journal of Propulsion and Power*, Vol. 32, No. 2, 2016, pp. 311–324. https://doi.org/10.2514/1.B35690.

[31] Meyer, K. E., Pedersen, J. M., and Özcan, O. "A Turbulent Jet in Crossflow Analysed with Proper Orthogonal Decomposition." *Journal of Fluid Mechanics*, Vol. 583, 2007, pp. 199–227. https://doi.org/10.1017/S0022112007006143.

[32] Knuth, W. H., Chiaverini, M. J., Gramer, D. J., and Sauer, J. A. "Final Report on Vortex Combustion Ramjet - a Phase I SBIR Project." *SBIR Phase I, NASA Final Technical Contract No. NAS3-99039, OTC-GS075-FR-99-1, Orbital Technologies Corporation, Madison, Wisconsin,* 1999.

[33] Michaels, R. S., and Wilson, B. F. "Multiple Impinging Stream Vortex Injector, US Patent No. 5,622,046." *April 22 1997.*

[34] Chiaverini, M. J., Sauer, J. A., and Knuth, W. H. "Final Report on Vortex Combustion Combined Cycle Engine a Phase I SBIR Project." *AFRL Contract No. F04611-99-C-0063, OTC-GS082-FR-99-1, Orbital Technologies Corporation, Madison, Wisconsin*, 1999.

[35] Rice, E. E., Chiaverini, M. J., Malecki, M. J., St. Clair, C. P., Knuth, W. H., Gustafson, R. J., and Gramer, D. J. "Status Report on Mars ISRU CO/O2 Hybrid Engine Development and Testing." *NASA Interim Technical Contract No. NASA CP-2001-210826, Orbital Technologies Corporation, Madison, Wisconsin*, 2001, pp. 189–192.

[36] Shepherd, C. B., and Lapple, C. E. "Flow Pattern and Pressure Drop in Cyclone Dust Collectors: Cyclone without Inlet Vane." *Industrial and Engineering Chemistry*, Vol. 32, No. 9, 1940, pp. 1246–1248. https://doi.org/10.1021/ie50369a042.

[37] Smith, J. L. "An Experimental Study of the Vortex in the Cyclone Separator." *Journal of Basic Engineering Transactions of the ASME*, Vol. 84, No. 4, 1962, pp. 602–608. https://doi.org/10.1115/1.3658721.

[38] Smith, J. L. "An Analysis of the Vortex Flow in the Cyclone Separator." *Journal of Basic Engineering Transactions of the ASME*, Vol. 84D, 1962, pp. 609–618. https://doi.org/10.1115/1.3658722.

[39] Reydon, R. F., and Guavin, W. H. "Theoretical and Experimental Study of Confined Vortex Flow." *Journal of Applied Mechanics*, Vol. 36, No. 4, 1969, pp. 687–692.

[40] Ogawa, A. *Vortex Flow*. Crc Series on Fine Particle Science and Technology, CRC Press, Boca Raton, Florida, 1993.

[41] Hu, L. Y., Zhou, L. X., Zhang, J., and Shi, M. X. "Studies on Strongly Swirling Flows in the Full Space of a Volute Cyclone Separator." *AIChE Journal*, Vol. 51, No. 3, 2005, pp.

740–749. https://doi.org/10.1002/aic.10354.

[42] Krepec, T., and Cwok, C. K. "Vortex Flow Pattrens in Cylindrical Chambers." *4th Joint Fluid Mechanics, Plasma Dynamics and Lasers Conference*, 1986. https://doi.org/10.2514/6.1986-1098.

[43] Vatistas, G. H., Lin, S., and Kwok, C. K. "Theoretical and Experimental Studies on Vortex Chamber Flows." Vol. 24, No. 4, 1986, pp. 635–642. https://doi.org/10.2514/3.9319.

[44] Knuth, W. H., Gramer, D. J., Chiaverini, M. J., and Sauer, J. A. "Development and Testing of a Vortex-Driven, High-Regression Rate Hybrid Rocket Engine." *34th AIAA/ASME/SAE/ASEE Joint Propulsion Conference and Exhibit, July,* 1998. https://doi.org/10.2514/6.1998-3507.

[45] Haag, G. S. "SSC99-XII-2 Low Cost Propulsion Development for Small Satellites at The Surrey Space Centre." *13th AIAA/USU Conference on Small Satellites*, 1993, pp. 1–10.

[46] Anderson, M., Valenzuela, R., Rom, C., Bonazza, R., and Chiaverini, M. J. "Vortex Chamber Flow Field Characterization for Gelled Propellant Combustor Applications." *39th AIAA/ASME/SAE/ASEE Joint Propulsion Conference and Exhibit*, 2003. https://doi.org/10.2514/6.2003-4474.

[47] Rom, C. J., Anderson, M. H., and Chiaverini, M. J. "Cold Flow Analysis of a Vortex Chamber Engine for Gelled Propellant Combustor Applications." *40th AIAA/ASME/SAE/ASEE Joint Propulsion Conference and Exhibit*, 2004. https://doi.org/10.2514/6.2004-3359.

[48] Maicke, B. A., and Majdalani, J. "Particle Image Velocimetry in Confined Vortex Flows." *Journal of Physics: Conference Series*, Vol. 548, No. 1, 2014. https://doi.org/10.1088/1742-6596/548/1/012060.

[49] Liew, R., Zeegers, J. C. H., Kuerten, J. G. M., and Michałek, W. R. "3D Velocimetry and Droplet Sizing in the Ranque–Hilsch Vortex Tube." *Experiments in Fluids*, Vol. 54, No. 1, 2012, p. 1416. https://doi.org/10.1007/s00348-012-1416-z.

[50] Saffman, P. G., Ablowitz, M. J., J. Hinch, E., Ockendon, J. R., and Olver, P. J. *Vortex Dynamics*. Cambridge University Press, 1992.

[51] Burgers, J. M. "A Mathematical Model Illustrating the Theory of Turbulence." *Advances in Applied Mechanics*, Vol. 1, 1948, pp. 171–199. https://doi.org/doi.org/10.1016/s0065-2156(08)70100-5.

[52] Sullivan, R. D. “A Two-Cell Vortex Solution of the Navier-Stokes Equations.” *Journal of the Aerospace Sciences*, Vol. 26, No. 11, pp. 767–768.

[53] Kuo, H. L. “On the Dynamics of Convective Atmospheric Vortices.” *Journal of the Atmospheric Sciences*, Vol. 23, No. 1, 1966, pp. 25–42. https://doi.org/10.1175/1520-0469(1966)023<0025:OTDOCA>2.0.CO;2.

[54] Bloor, M. I. G., and Ingham, D. B. “Theoretical Investigation of the Flow in a Conical Hydrocyclone.” *Transactions of the Institution of Chemical Engineers*, Vols. 51a, No. 1, 1973, pp. 36–41.

[55] Barber, T. A., and Majdalani, J. “On the Beltramian Motion of the Bidirectional Vortex in a Conical Cyclone.” *Journal of Fluid Mechanics*, Vol. 828, 2017, pp. 708–732. https://doi.org/10.1017/jfm.2017.494.

[56] Hoffmann, A. C., and Stein, L. E. *Gas Cyclones and Swirl Tubes: Principles, Design and Operation.* Springer Verlag, 2002.

[57] Nolan, D. S., and Farrell, B. F. “Generalized Stability Analyses of Asymmetric Disturbances in One- and Two-Celled Vorticies Maintained by Radial Inflow.” *Journal of the Atmospheric Sciences*, Vols. 56, No. 10, 1999, pp. 1282–1307.

[58] Akiki, G. “On the Bidirectional Vortex Engine Flowfield with Arbitrary Endwall Injection.” *Master’s Thesis, University of Tennessee*, 2011.

[59] Majdalani, J. “Helical Solutions of the Bidirectional Vortex in a Cylindrical Cyclone: Beltramian and Trkalian Motions.” *Fluid Dynamics Research*, Vol. 44, No. 6, 2012. https://doi.org/10.1088/0169-5983/44/6/065506.

[60] Maicke, B. A., and Majdalani, J. “On the Compressible Bidirectional Vortex . Part 2 : A Beltramian Flowfield Approximation.” *50th AIAA Aerospace Sciences Meeting including the New Horizons Forum and Aerospace Exposition*, 2012. https://doi.org/10.2514/6.2012-1104.

[61] Batterson, J. W., and Majdalani, J. “Biglobal Instability of the Bidirectional Vortex . Part 1 : Formulation.” *47th AIAA/ASME/SAE/ASEE Joint Propulsion Conference & Exhibit*, 2011, pp. 1–20. https://doi.org/10.2514/6.2011-5648.

[62] Batterson, J., and Majdalani, J. “Biglobal Instability of the Bidirectional Vortex. Part 2: Complex Lamellar and Beltramian Motions.” *47th AIAA/ASME/SAE/ASEE Joint Propulsion Conference & Exhibit*, 2011. https://doi.org/10.2514/6.2011-5649.

[63] Hall, P. “The Linear Development of Gortler Vortices in Growing Boundary Layers.” *Journal of Fluid Mechanics*, Vol. 130, 1983, pp. 41–58. https://doi.org/10.1017/S0022112083000968.

[64] Maicke, B. A., and Majdalani, J. Characterization of the Bidirectional Vortex Using Particle Image Velocimetry. In *The Particle Image Velocimetry - Characteristics, Limits and Possible Applications*, In Tech, 2012, pp. 149–176.

[65] Gupta, A. ., Lilley, D. G., and Syred, N. *Swirl Flows*. Abacus Press, England, 1984.

[66] Lilley, D. G. “Swirl Flows in Combustion-A Review.” *AIAA Journal*, Vol. 15, No. 8, 1977, pp. 1063–1078. https://doi.org/10.2514/3.60756.

[67] 1977 - Lilley - AIAAJ - Swirl Flows in Combustion-A Review.Pdf.

[68] Tropea, A., Yarin, A., and Foss, J. *Springer Handbook of Experimental Fluid Mechanics*. Springer, 2007.

[69] Lynch, K. P. *Fluere for Particle Image Velocimetry : User Manual*. 2011.

[70] Maicke, B. A., and Talamantes, G. “Numerical Investigation of Injection Variation in the Bidirectional Vortex.” *AIAA Journal*, Vol. 55, No. 8, 2017, pp. 1–11. https://doi.org/10.2514/1.J055807.

[71] Elsayed, K. *Analysis and Optimization of Cyclone Separators Geometry Using RANS and LES Methodologies Khairy Elsayed*. 2011.

[72] Liu, Z., Zheng, Y., Jia, L., and Zhang, Q. “An Experimental Method of Examining Three-Dimensional Swirling Flows in Gas Cyclones by 2D-PIV.” *Chemical Engineering Journal*, Vol. 133, Nos. 1–3, 2007, pp. 247–256. https://doi.org/10.1016/j.cej.2007.02.015.

[73] Liu, Z., Jiao, J., and Zheng, Y. “Study of Axial Velocity in Gas Cyclones by 2D-PIV, 3D-PIV, and Simulation.” *China Particuology*, Vol. 4, Nos. 3–4, 2006, pp. 204–210. https://doi.org/10.1016/s1672-2515(07)60262-0.

[74] Sarkies, J. M., and Otto, S. R. “Görtler Vortices in Compressible Mixing Layers.” *Journal of Fluid Mechanics*, Vol. 427, 2001, pp. 359–388.

[75] Tatro, P. R., and Mollo-Christensen, E. L. “Experiments on Ekman Layer Instability.” *Journal of Fluid Mechanics*, Vol. 28, No. 3, 1967, pp. 531–543. https://doi.org/10.1017/S0022112067002289.

[76] Caldwell, D. R., and Atta, C. W. V. “Characteristics of Ekman Boundary Layer Instabilities.” *Journal of Fluid Mechanics*, Vol. 44, No. 1, 1970, pp. 79–95.

https://doi.org/10.1017/S0022112070001702.

[77] Faler, J. H., and Leibovich, S. “Disrupted States of Vortex Flow and Vortex Breakdown.” *Physics of Fluids*, Vol. 20, No. 9, 1977, pp. 1385–1400. https://doi.org/10.1063/1.862033.

[78] Wang, Y., Wang, X., and Yang, V. “Evolution and Transition Mechanisms of Internal Swirling Flows with Tangential Entry.” *Physics of Fluids*, Vol. 30, No. 1, 2018. https://doi.org/10.1063/1.5001073.

[79] Hall, M. G. “Vortex Breakdown.” *Annual Review of Fluid Mechanics*, Vol. 4, No. 1, 1972, pp. 195–218. https://doi.org/10.1146/annurev.fl.04.010172.001211.

[80] Barber, T. A., Cecil, O. M., and Majdalani, J. “Complex-Lamellar Cyclonic Vortex in a Cylindrical Chamber with a Hollow Core.” *51st AIAA/SAE/ASEE Joint Propulsion Conference*, 2015, pp. 1–16. https://doi.org/10.2514/6.2015-3848.

[81] Gupta, A., and Kumar, R. “Three-Dimensional Turbulent Swirling Flow in a Cylinder: Experiments and Computations.” *International Journal of Heat and Fluid Flow*, Vol. 28, No. 2, 2007, pp. 249–261. https://doi.org/10.1016/j.ijheatfluidflow.2006.04.005.

[82] Zhang, B., Guo, X., and Yang, Z. “International Journal of Heat and Mass Transfer Analysis on the Fluid Flow in Vortex Tube with Vortex Periodical Oscillation Characteristics.” *International Journal of Heat and Mass Transfer*, Vol. 103, 2016, pp. 1166–1175. https://doi.org/10.1016/j.ijheatmasstransfer.2016.08.063.

[83] Faler, J. H., and Leibovich, S. “An Experimental Map of the Internal Structure of a Vortex Breakdown.” *Journal of Fluid Mechanics*, Vol. 86, No. 2, 1978, pp. 313–335. https://doi.org/10.1017/S0022112078001159.

[84] Escudier, M. P., Bornstein, J., and Zehnder, N. “Observations and LDA Measurements of Confined Turbulent Vortex Flow.” *Journal of Fluid Mechanics*, Vol. 98, No. 1, 1980, pp. 49–63. https://doi.org/10.1017/S0022112080000031.

[85] Lumley, J. L. “The Structure of Inhomogeneous Turbulent Flows.” *Atmospheric Turbulence and Radio Propagation*, 1967, pp. 166–178.

[86] Vyas, A. B., Majdalani, J., and Chiaverini, M. J. “The Bidirectional Vortex. Part 3: Multiple Solutions.” *39th AIAA/ASME/SAE/ASEE Joint Propulsion Conference and Exhibit*, 2003. https://doi.org/10.2514/6.2003-5054.

[87] Liang, H., and Maxworthy, T. “An Experimental Investigation of Swirling Jets.” *Journal of Fluid Mechanics*, Vol. 525, 2005, pp. 115–159.

https://doi.org/10.1017/S0022112004002629.

[88] Billant, P., Chomaz, J. M., and Huerre, P. “Experimental Study of Vortex Breakdown in Swirling Jets.” *Journal of Fluid Mechanics*, Vol. 376, 1998, pp. 183–219. https://doi.org/10.1017/S0022112098002870.

[89] Faler, J. H., and Leibovich, S. “Disrupted States of Vortex Flow and Vortex Breakdown.” *Physics of Fluids*, Vol. 20, No. 9, 1977, pp. 1385–1400. https://doi.org/10.1063/1.862033.

[90] Cala, C. E., Fernandes, E. C., Heitor, M. V., and Shtork, S. I. “Coherent Structures in Unsteady Swirling Jet Flow.” *Experiments in Fluids*, Vol. 40, No. 2, 2006, pp. 267–276. https://doi.org/10.1007/s00348-005-0066-9.

[91] Dulin, V., and Lobasov, A. Coherent Structures in the Near Field of Swirling Turbulent Jets and Flames Investigated by PIV and PLIF. In *Swirling Flows and Flames*, 2018, pp. 137–144.

[92] Raffel, C. W. and Kompenhans, J. *Particle Image Velocimetry: A Practical Guide*. 2007.

[93] Scharnowski, S., Bross, M., and Kähler, C. J. “Accurate Turbulence Level Estimations Using PIV/PTV.” *Experiments in Fluids*, Vol. 60, No. 1, 2019, pp. 1–12. https://doi.org/10.1007/s00348-018-2646-5.

[94] Timmins, B. H., Wilson, B. W., Smith, B. L., and Vlachos, P. P. “A Method for Automatic Estimation of Instantaneous Local Uncertainty in Particle Image Velocimetry Measurements.” *Experiments in Fluids*, Vol. 53, No. 4, 2012, pp. 1133–1147. https://doi.org/10.1007/s00348-012-1341-1.

[95] Sciacchitano, A., Wieneke, B., and Scarano, F. “PIV Uncertainty Quantification by Image Matching.” *Measurement Science and Technology*, Vol. 24, No. 4, 2013. https://doi.org/10.1088/0957-0233/24/4/045302.

[96] Charonko, J. J., and Vlachos, P. P. “Estimation of Uncertainty Bounds for Individual Particle Image Velocimetry Measurements from Cross-Correlation Peak Ratio.” *Measurement Science and Technology*, Vol. 24, No. 6, 2013. https://doi.org/10.1088/0957-0233/24/6/065301.

[97] Xue, Z., Charonko, J. J., and Vlachos, P. P. “Particle Image Velocimetry Correlation Signal-to-Noise Ratio Metrics and Measurement Uncertainty Quantification.” *Measurement Science and Technology*, Vol. 25, No. 11, 2014. https://doi.org/10.1088/0957-0233/25/11/115301.

[98] Stanislas, M., Okamoto, K., Kähler, C. J., and Westerweel, J. "Main Results of the Second International PIV Challenge." *Experiments in Fluids*, Vol. 39, No. 2, 2005, pp. 170–191. https://doi.org/10.1007/s00348-005-0951-2.

[99] World Wide Cooperation on Particle Image Velocimetry (PIV) Challenge 2003. https://www.pivchallenge.org/pub03/index.html#a.

[100] World Wide Cooperation on Particle Image Velocimetry (PIV) Challenge 2005. https://www.pivchallenge.org/pub05/.

APPENDIX - A Additional Experimental Results

In addition to the results presented in the main body of the dissertation, a number of experiments were conducted for different operating and geometric conditions, which support the discussion and conclusions presented. For conciseness, the supplementary results were not presented in the main body of the dissertation. However, the same are presented here in Appendix "A" for completeness.

Case “A”

Table A.1 Geometrical and operating conditions for Case “A”

<table>
<tr><th colspan="2">Geometric Parameters</th><th colspan="2">Operating Parameters</th></tr>
<tr><td>Chamber Radius, a</td><td>1 in</td><td rowspan="2">Modified Swirl #
$\sigma = a^2 / A_i$</td><td rowspan="2">2.6</td></tr>
<tr><td>Contraction Ratio, β</td><td>0.353</td></tr>
<tr><td>Inlet Diameter, d_{inlet}</td><td>0.35 in</td><td rowspan="2">Geometric Swirl #
$S = (\pi d_e a) / (2 A_i)$</td><td rowspan="2">2.89</td></tr>
<tr><td>Chamber AR, $l = L/a$</td><td>3</td></tr>
<tr><td colspan="4">Vortex Re (Qi / vL)</td></tr>
<tr><td>820</td><td colspan="2">2470</td><td>4120</td></tr>
</table>

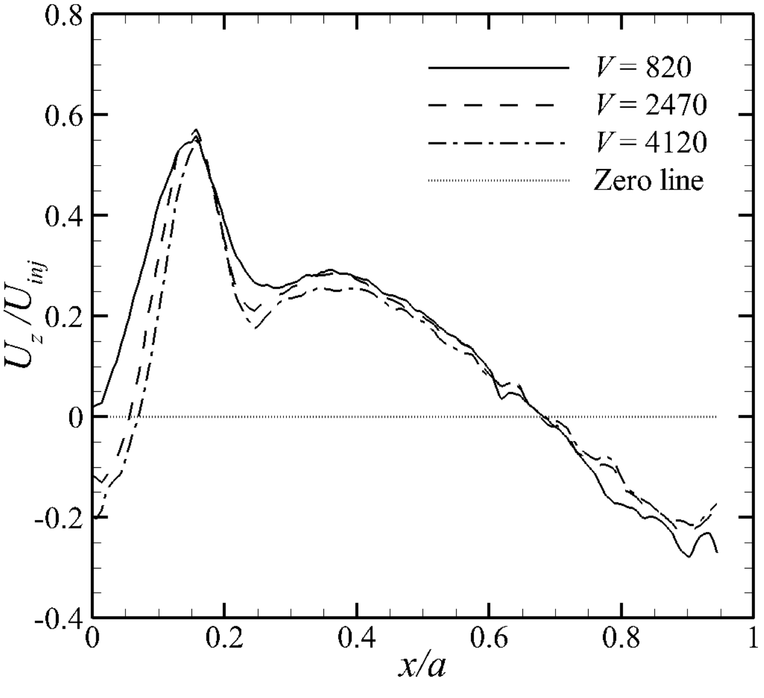

Figure A0.1 Distribution of the axial velocity for Case “A”

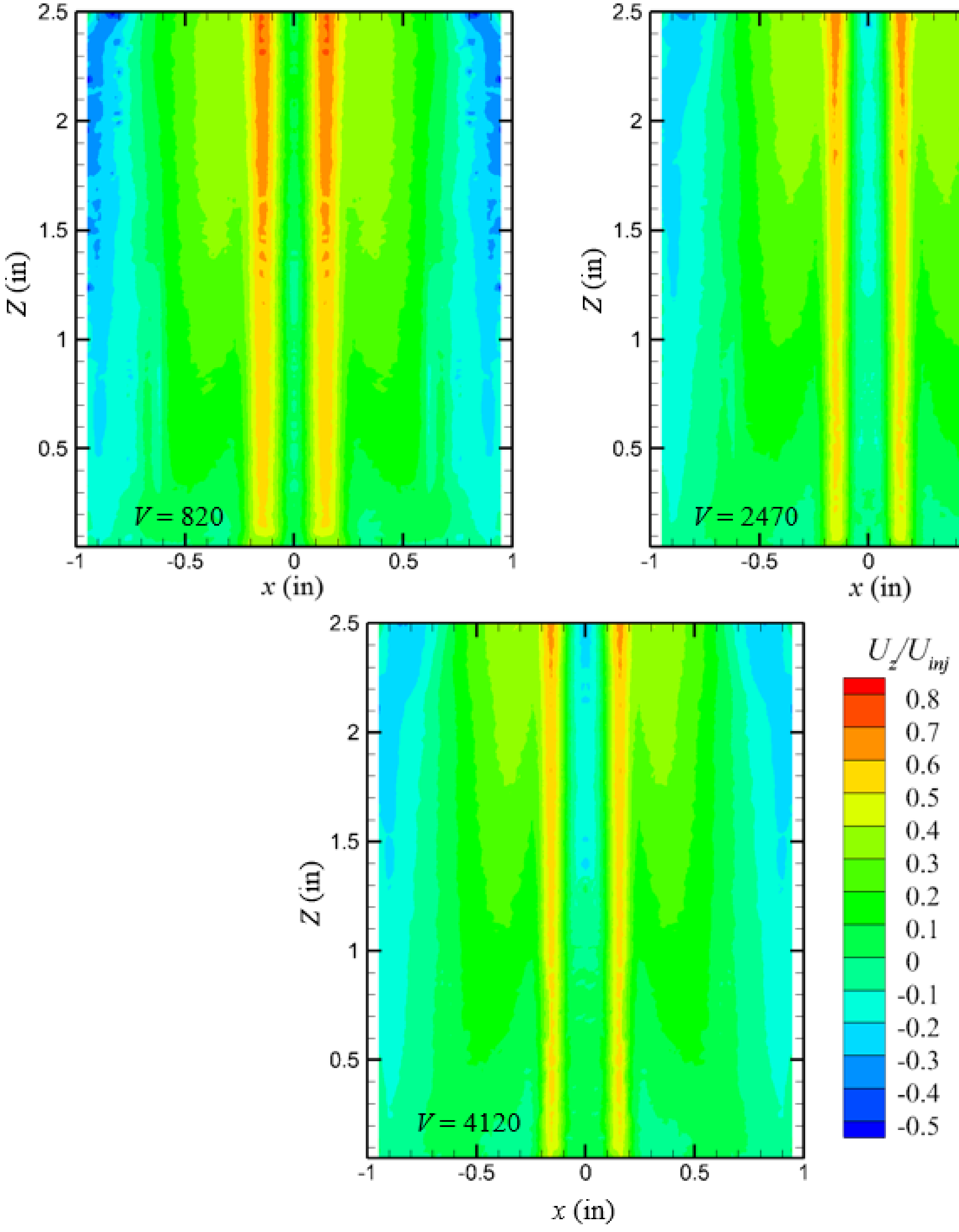

Figure A0.2 Contour of axial velocity for Case “A”

Case “B”

Table A.2 Geometrical and operating conditions for Case “B”

Geometric Parameters		**Operating Parameters**	
Chamber Radius, a	1 in	Modified Swirl # $\sigma = a^2 / A_i$	5.10
Contraction Ratio, β	0.25		
Inlet Diameter, d_{inlet}	0.25 in	Geometric Swirl # $S = (\pi\, d_e\, a) / (2\, A_i)$	4.0
Chamber AR, $l = L/a$	2		
Vortex Re ($Qi / \nu\, L$)			
1240		3710	

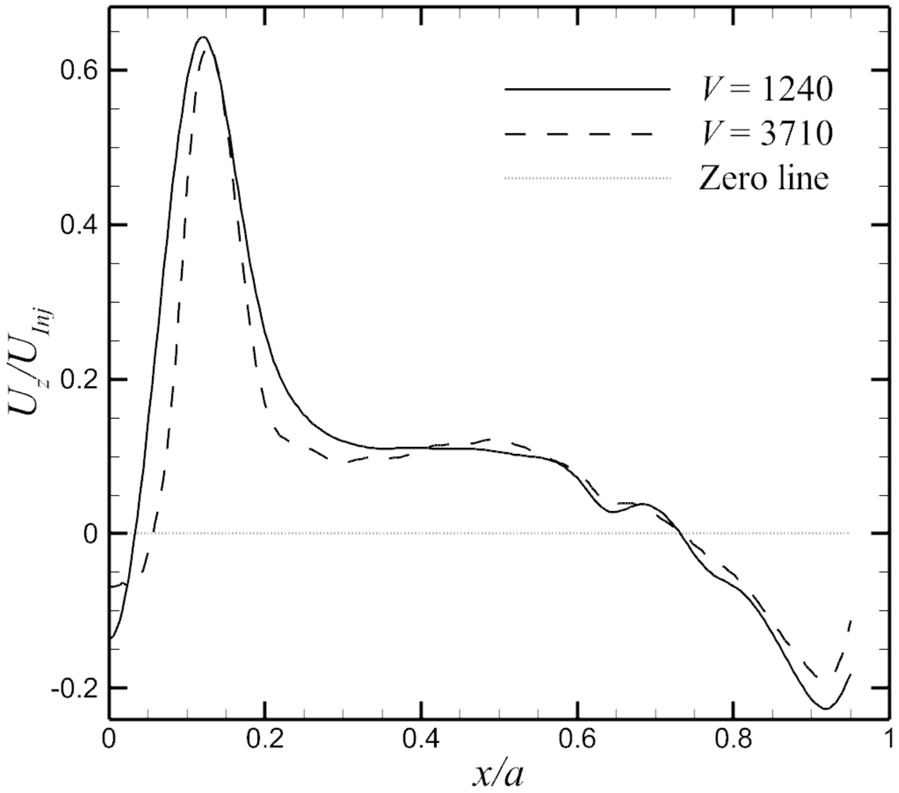

Figure A0.3 Distribution of the axial velocity for Case “B”

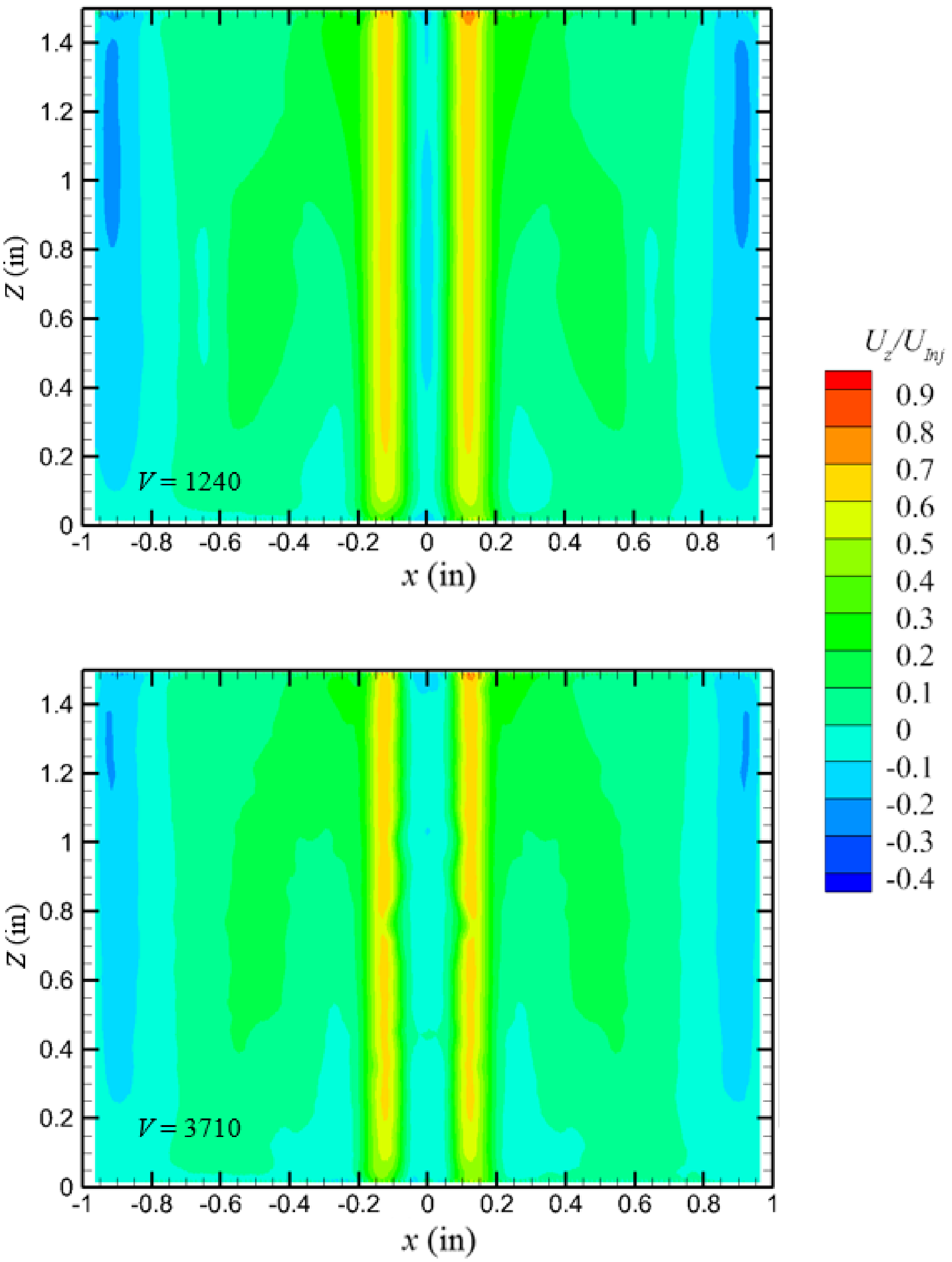

Figure A0.4 Contour of axial velocity for Case "B"

Case “C”

Table A.3 Geometrical and operating conditions for Case “C”

Geometric Parameters		Operating Parameters	
Chamber Radius, a	1 in	Modified Swirl # $\sigma = a^2 / A_i$	2.6
Contraction Ratio, β	0.25		
Inlet Diameter, d_{inlet}	0.35 in	Geometric Swirl # $S = (\pi\, d_e\, a) / (2\, A_i)$	2.04
Chamber AR, $l = L/a$	2		
Vortex Re ($Qi / v\, L$)			
1236		3707	

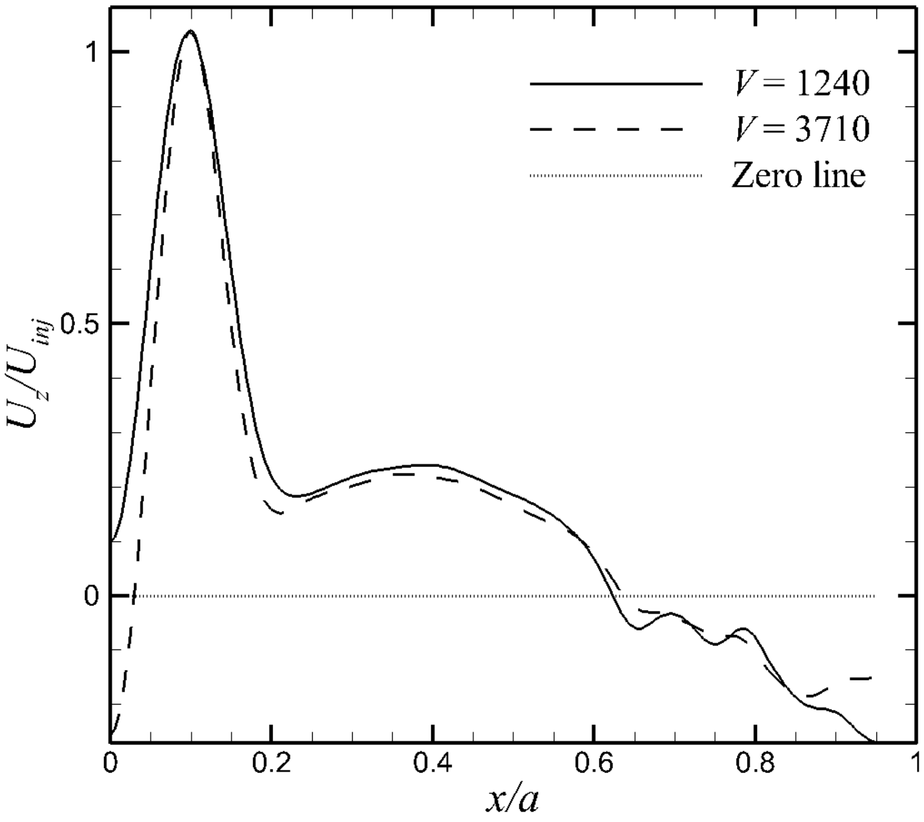

Figure A0.5 Distribution of the axial velocity for Case “C”

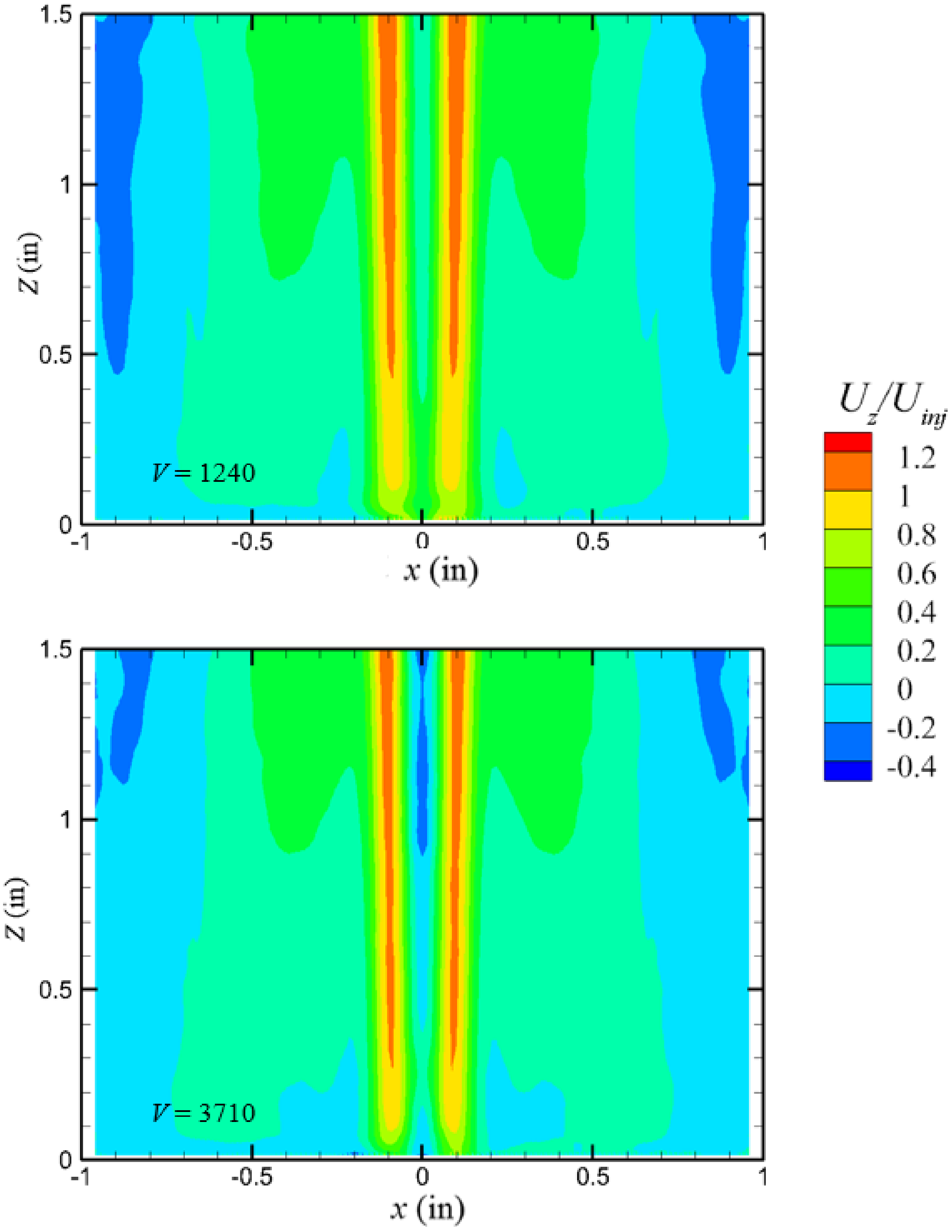

Figure A0.6 Contour of axial velocity for Case "C"

Case “D”

Table A.4 Geometrical and operating conditions for Case “D”

Geometric Variables		Operating Conditions	
Chamber radius, a	1 in	Vortex Re	7410
Chamber AR, $l = L/a$	1	Modified Swirl # $\sigma = a^2 / A_i$	2.6
Inlet Diameter, d_{inlet}	0.35 in		
Contraction ratio, $\beta = d_e/2a$	0.353	Geometric Swirl # $S = (\pi\ d_e\ a) / (2\ A_i)$	2.89
Head Port	Closed	Open	Injection

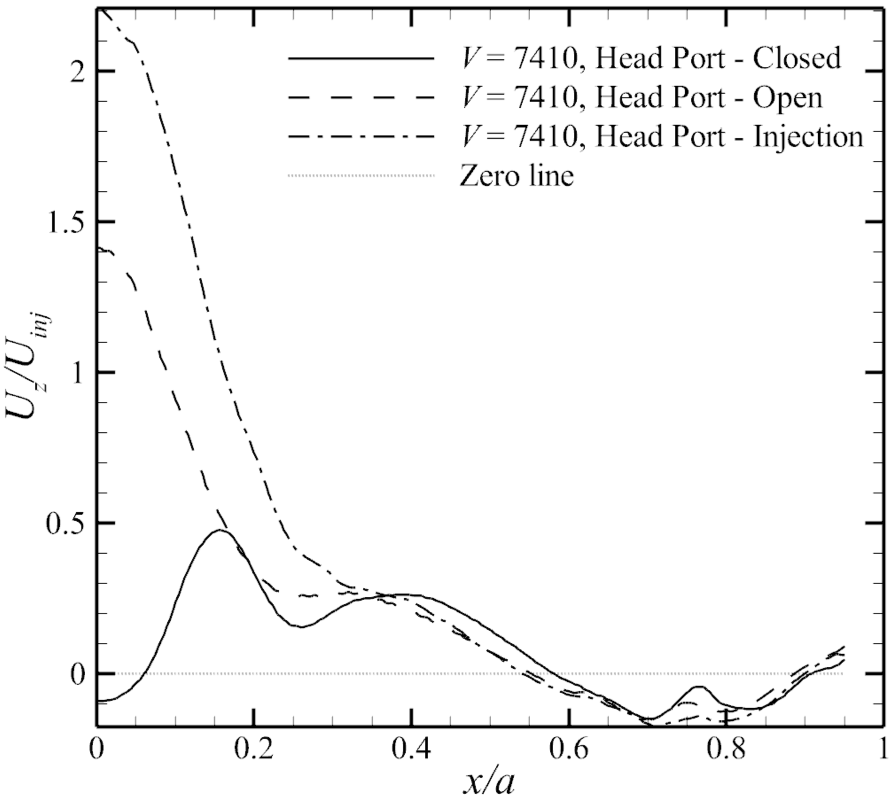

Figure A0.7 Distribution of the axial velocity for Case “D”

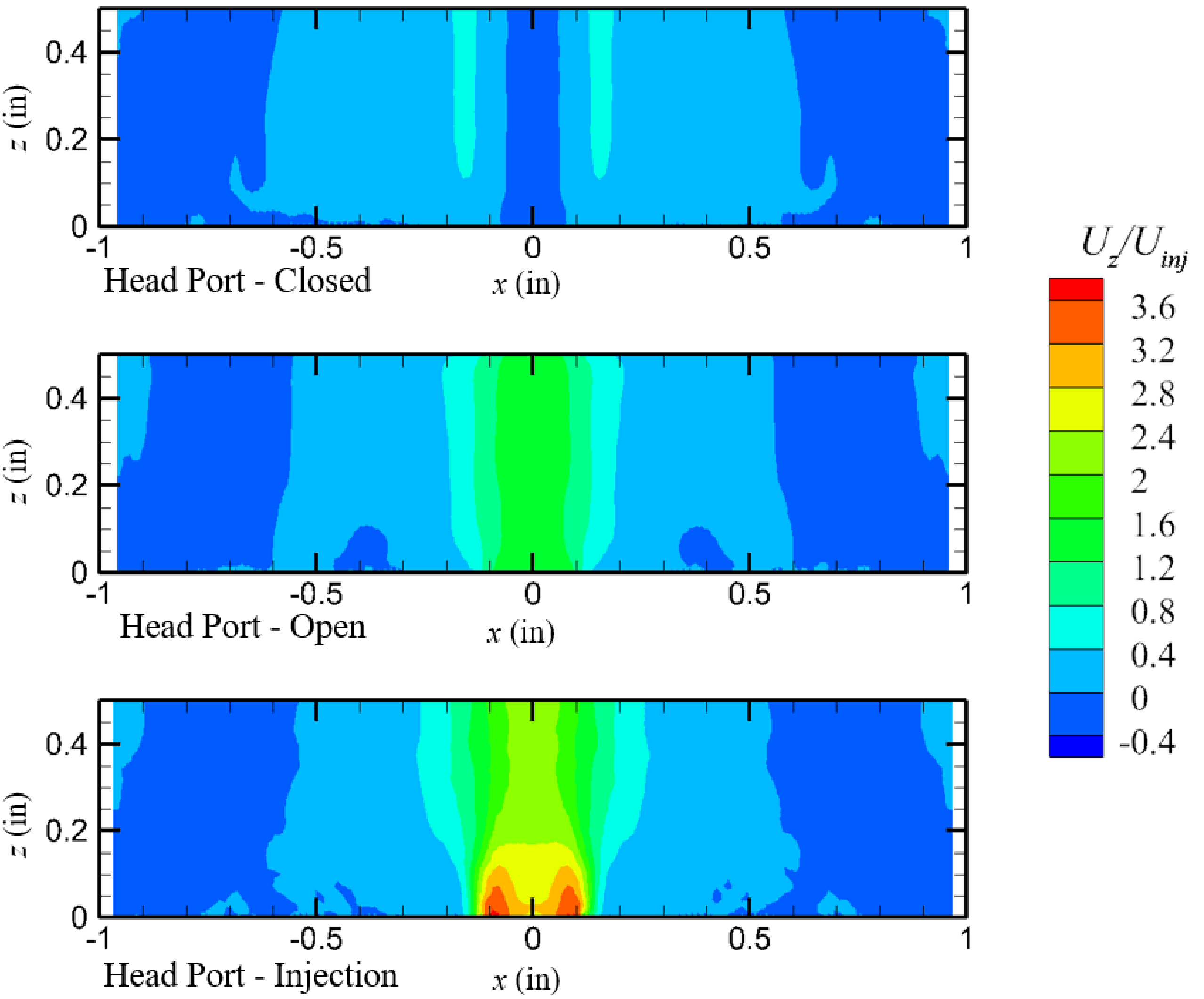

Figure A0.8 Contour of axial velocity for Case "D"

Case “E”

Table A.5 Geometrical and operating conditions for Case “E”

Geometric Parameters		**Operating Parameters**	
Chamber radius, a	1 in	Vortex Re, V	1240
Chamber AR, $l = L/a$	3	Modified Swirl # $\sigma = a^2 / A_i$	2.6
Inlet Diameter, d_{inlet}	0.35 in		
Total Injection Area, A_i	0.385 in^2	Contraction ratio, β	Geometric Swirl No, S
Exit Diameter, d_e	0.336 in	0.168	1.37
	0.5 in	0.a1725	2.04
	0.61 in	0.305	2.53
	0.707 in	0.353	2.89

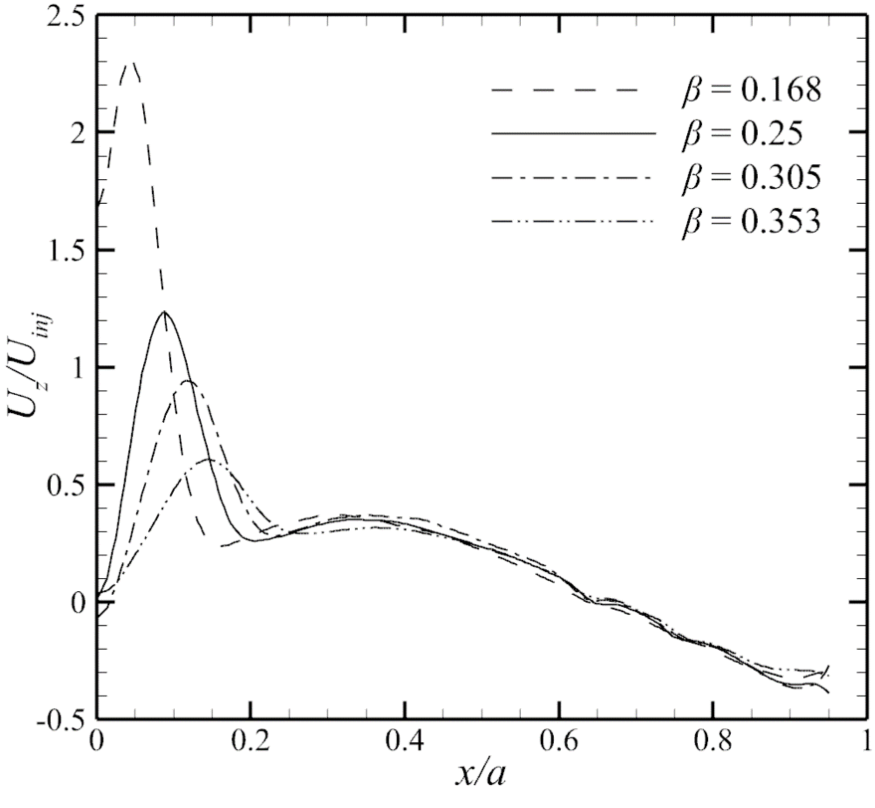

Figure A0.9 Distribution of the axial velocity for Case “E”

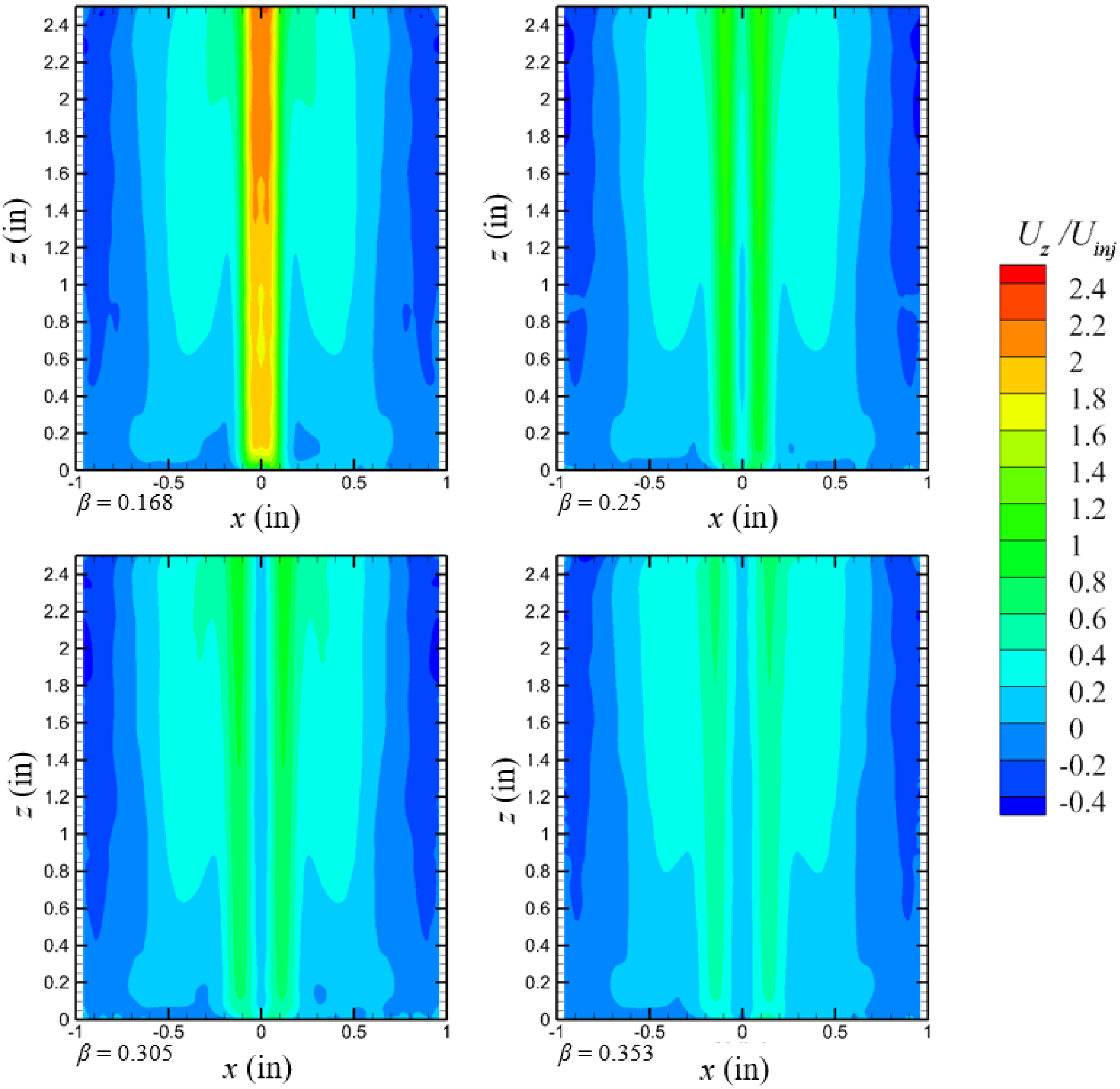

Figure A0.10 Contour of axial velocity for Case "E"

Case “F”

Table A.6 Geometrical and operating conditions for Case “F”

Geometric Parameters		**Operating Parameters**	
Chamber radius, *a*	1 in	Vortex Re, *V*	2470
Chamber AR, $l = L/a$	1	Modified Swirl # $\sigma = a^2 / A_i$	2.6
Inlet Diameter, d_{inlet}	0.35 in		
Total Injection Area, A_i	0.385 in^2	**Contraction ratio, *β***	**Geometric Swirl No, *S***
Exit Diameter, d_e	0.336 in	0.168	1.37
	0.5 in	0.25	2.04
	0.707 in	0.353	2.89

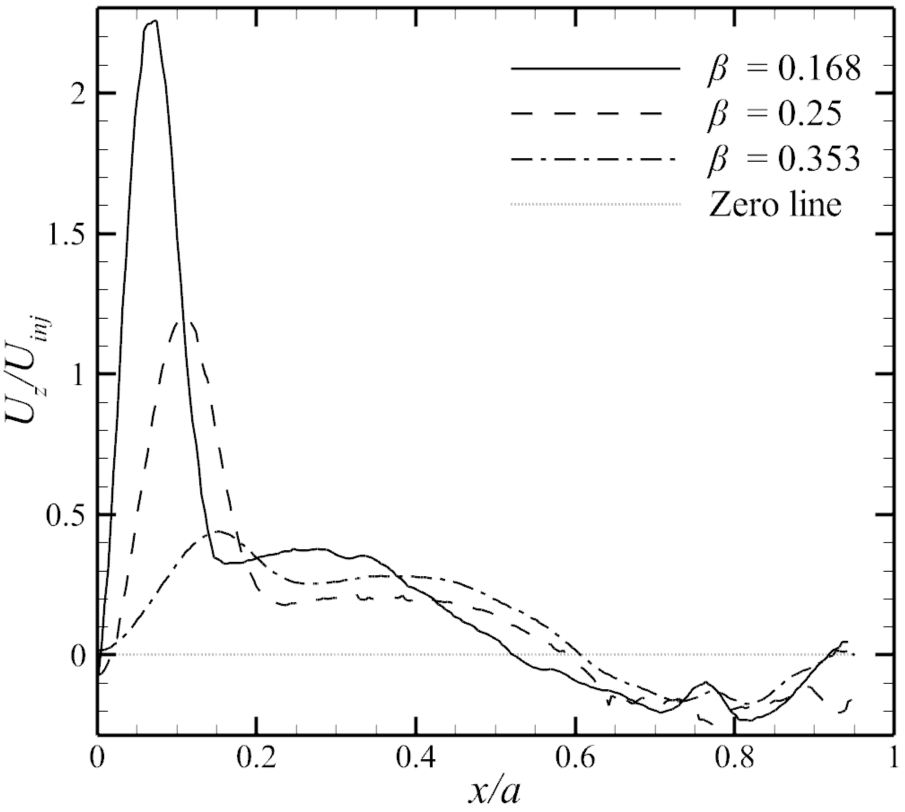

Figure A0.11 Distribution of the axial velocity for Case “F”

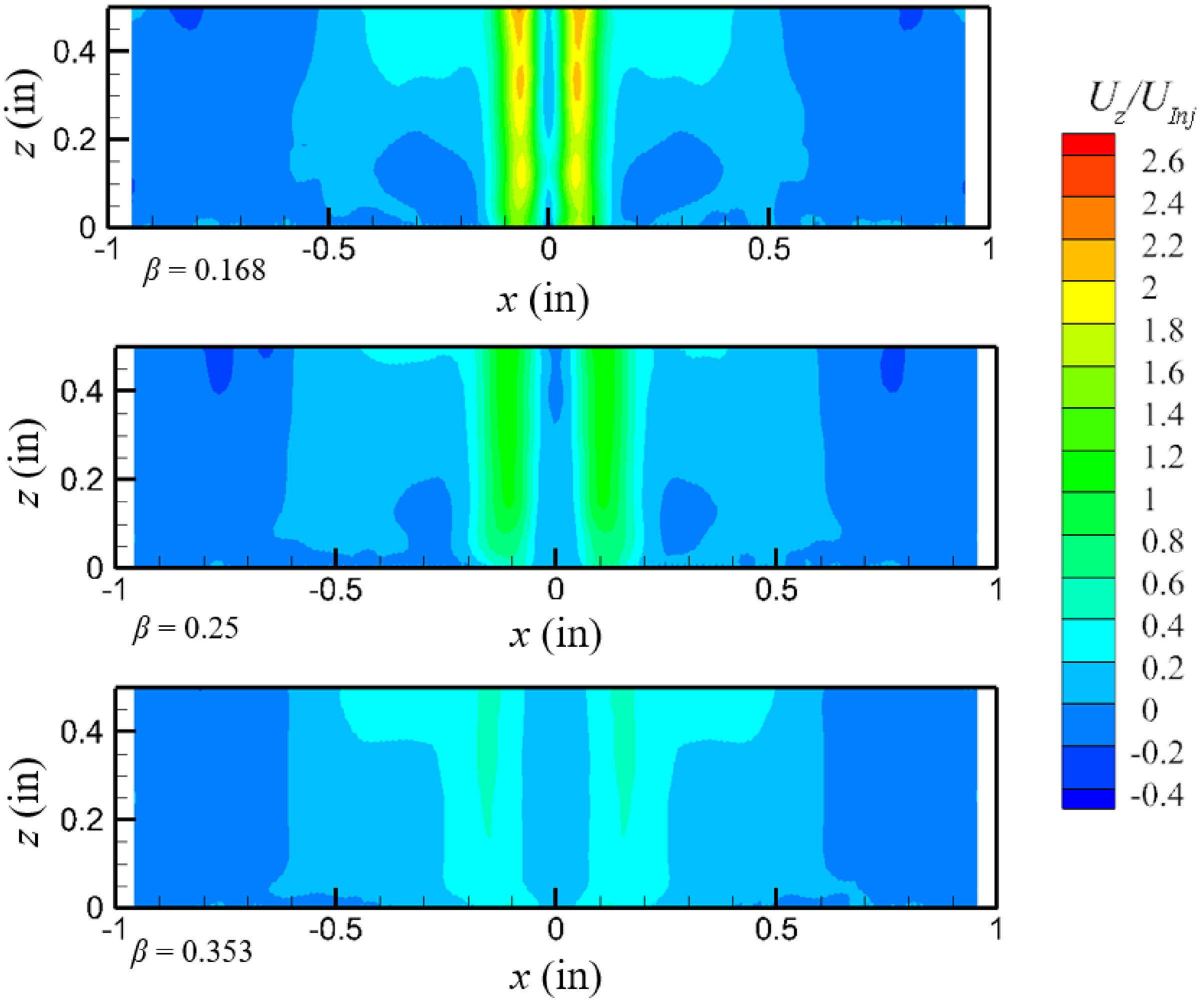

Figure A0.12 Contour of axial velocity for Case "F"

Case “G”

Table A.7 Geometrical and operating conditions for Case “G”

Geometric Parameters		**Operating Conditions**	
Chamber Radius, *a*	1 in	Modified Swirl # $\sigma = a^2 / A_i$	2.6
Contraction Ratio, β	0.353		
Inlet Diameter, d_{inlet}	0.35 in	Geometric Swirl # $S = (\pi\ d_e\ a) / (2\ A_i)$	2.89
Total Inlet Area, A_i	0.385 in^2		
Chamber Aspect Ratio, $l=L/a$		Vortex *Re* ($Qi / \nu L$)	$\kappa = 1 / 2\pi\sigma l$
1.0		7414	0.061
2.0		3707	0.0306
3.0		2471	0.0204

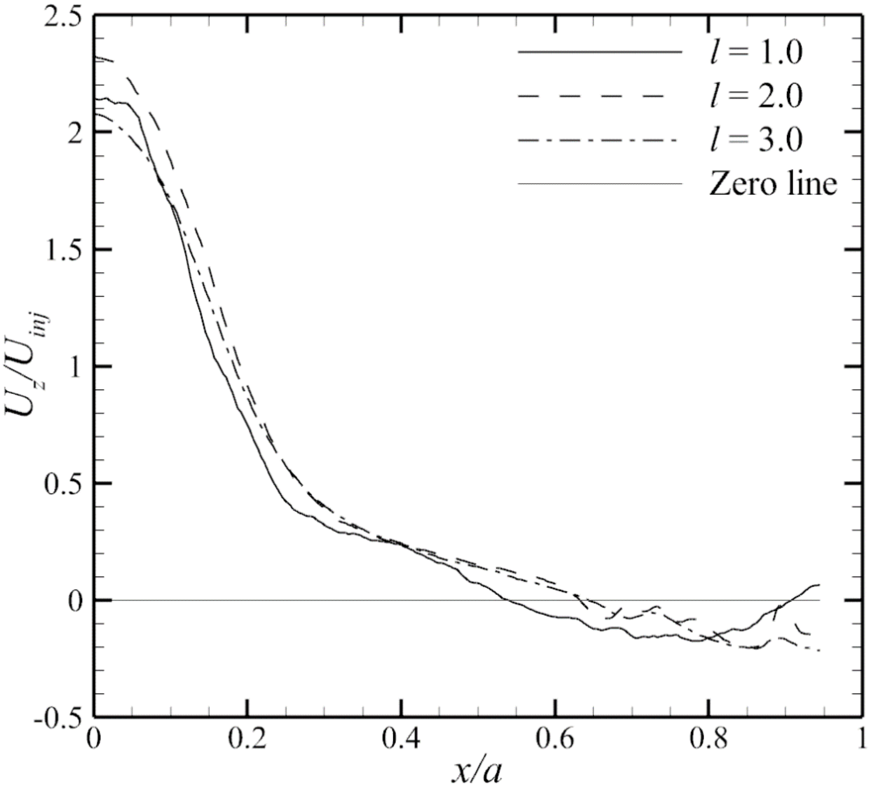

Figure A0.13 Distribution of the axial velocity for Case “G”

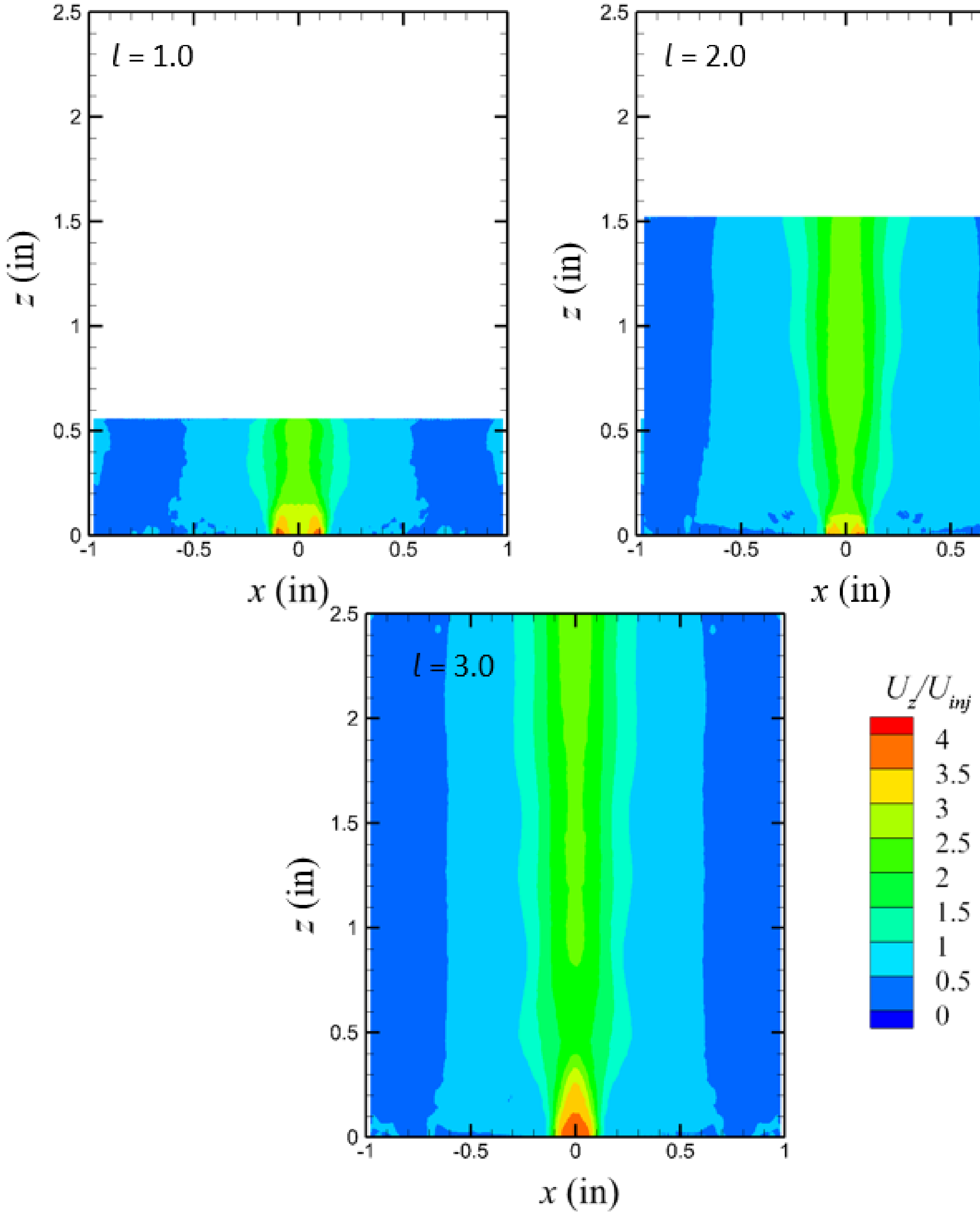

Figure A0.14 Contour of axial velocity for Case "F"

APPENDIX - B Uncertainty Calculations for PIV Correlation

There are multiple sources of possible errors in the velocity distributions calculated by PIV. These sources include particle response, particle dropout, laser flare, light refractions, image aberration, spatial resolutions, calibration errors, pixel locking, and correlation errors, among others. Therefore the goodness of PIV measurement is always in question and needs to be established by quantifying the uncertainty. In the literature, various principles of PIV have been established to reduce these uncertainties [92,93]

The measure of PIV particles ability to truly represent the fluid motions is governed by the Stokes particle number, in the present experiment, the particle size and material were selected such that the resultant Stokes particle number was 0.03, which entails the tracing uncertainty of below 1% [68]. Similarly, the particle density and laser sheet thickness was selected in the view of the particle dropout rate, both in-plane and out of plane [92]. The calibration uncertainty and the required spatial resolution were ensured by selecting appropriate magnification and spatial calibration, which resulted in the minimum detectable displacement of one pixel equal to 2.3×10^{-5} meters. The noise generated by reflections and residual light was reduced by background subtractions as detailed in Sec. 3.3.

The lower bound of the acceptable particle image is limited by peak-locking, which results in the tendency of the measured displacements to be biased towards integral values, such as 1, 2 ... n. The peak locking effect can be detected by plotting the displacement histogram, such as presented in Figure B.1 [92].

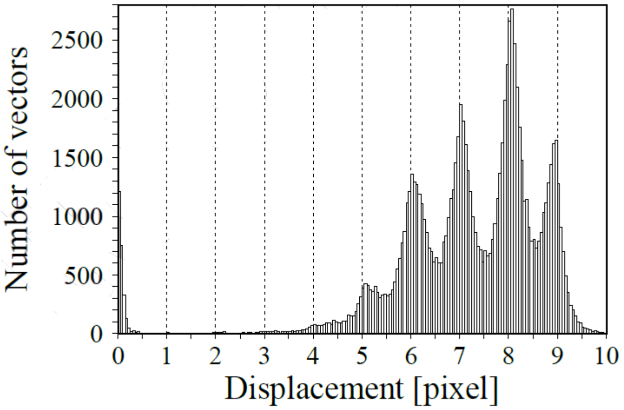

Figure B.1 Histogram of PIV displacement data illustrating the peak locking effect [92]**.**

The alignment of local peaks with the whole number pixel displacement represents the peak locking effect. In the present experiment, the magnification was selected such that a particle image was approximately 3-4 pixels as shown in Figure 3.4. In order to ensure that the results obtained were free of the peak locking effect, the histogram for both axial and tangential particles displacement were plotted and are presented in Figure B.2 and B.3, respectively.

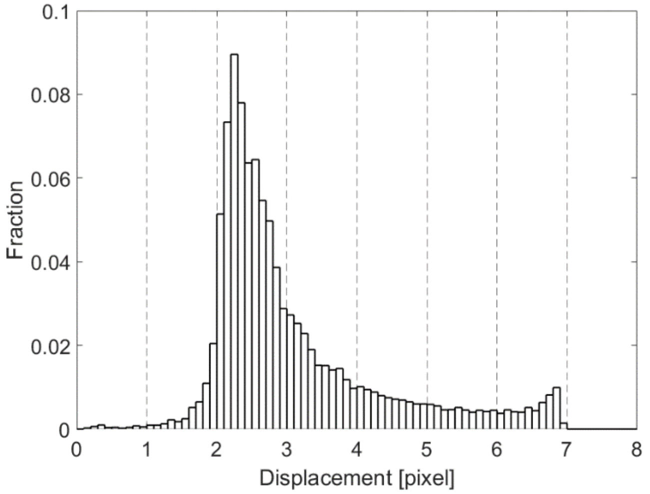

Figure B.2 Histogram of PIV displacement data of the axial velocity in the *r-z* plane on midplane.

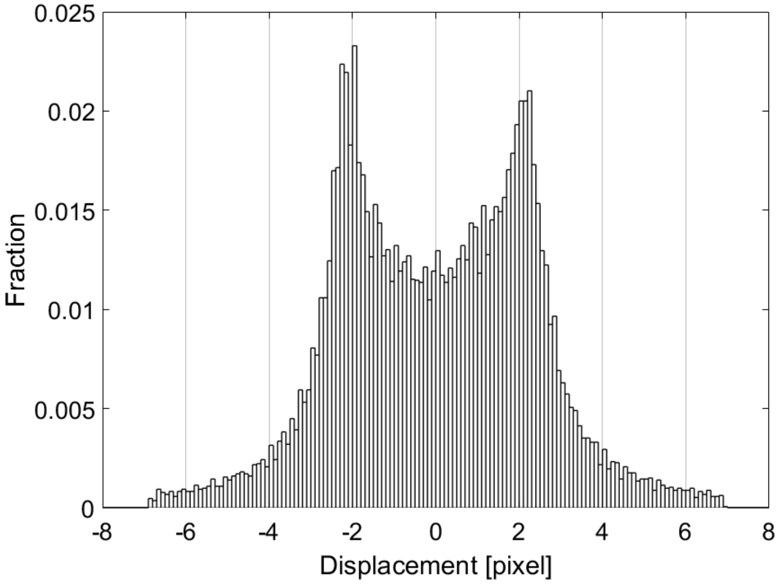

Figure B3 Histogram of PIV displacement data of the tangential velocity in the *r-θ* plane on midplane.

The absence of local peaks in the particle displacement confirm that the data is free of peak locking. Since, PIV essentially is a data reduction method that uses a statistical approach to develop correlation among the particle images to create a velocity field, a level of uncertainty is always associated with this correlation. Various methods have been presented in order to quantify this uncertainty e.g. uncertainty surface method [94], particle disparity methods [95], and correlation statistics method. However, the most commonly used method which accounts for various sources of uncertainty in the measurement of the velocity field is the peak ratio method [96,97], which establishes the uncertainty from the information extracted from the correlation to noise ratio. The peak in the correlation plane is the measure of the probability of a particle pattern to displace by a relative distance. In an ideal scenario, the correlation peak would be of a size of a single-pixel that would entail the probability of 100%. However, in any real case, the correlation plane has a peak distributed over a range of the interrogation window and may have many peaks and valleys which represent multiple fluctuations in the velocity field in addition to the noise in the data. Thus a wider peak or multiple peaks in a correlation plane represent a higher uncertainty, whereas a tall and narrow peak denotes an accurate measurement. Charonko and Vlachos [96] utilized the peak ratio method for the quantification of uncertainty on various data sets provided at the World Wide Cooperation on Particle Image Velocimetry, PIV Challenge 2003 and 2005 [98–100] and found that the uncertainty can be modeled as a function of the peak ratio by the following equation:

$$\delta_d = M \exp\left[-\frac{1}{2}\left(\frac{Q-1}{s}\right)^2\right] + A\,Q^{-1} + c \qquad (B1)$$

here δ_d is the uncertainty in the velocity measurement, Q is the peak ratio, and M, A and c, are the coefficients that are evaluated by calibration against synthetic data. Charonko and Vlachos proceeded to plot the uncertainty for various data sets as a function of peak ratio, presented in Figure B.4.

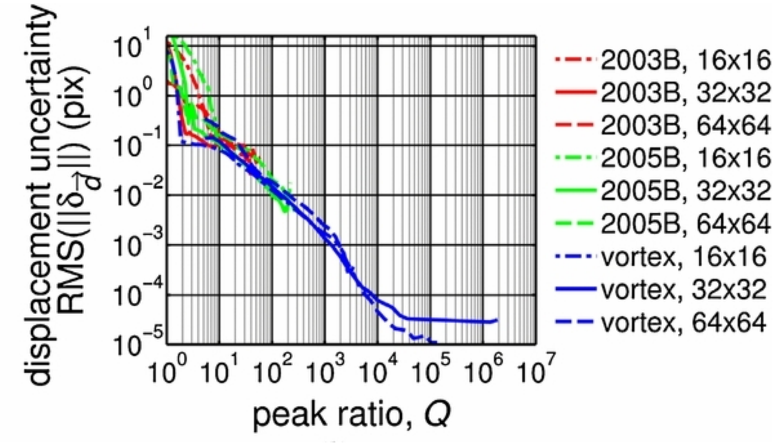

Figure B.4 Plots of the relationship of the calculated standard uncertainty on displacement magnitude versus peak ratio [96]**.**

And evaluated the coefficients of the Eq. (B1) for selected cases, presented in Figure B.5.

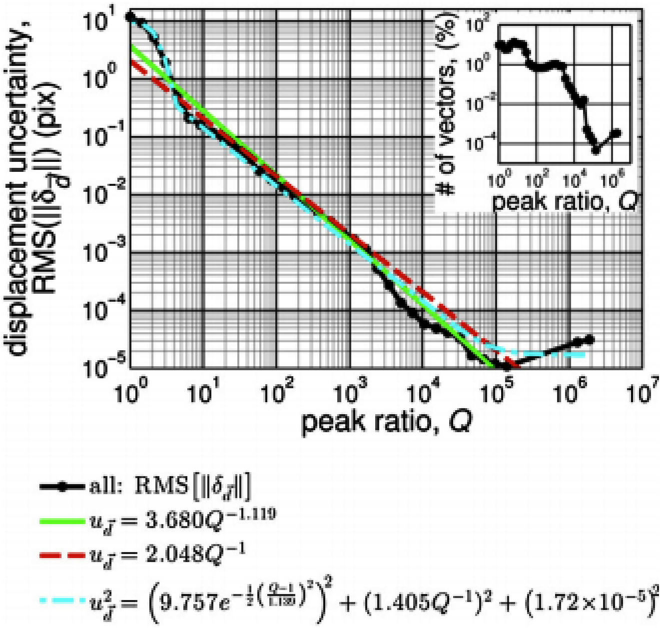

Figure B.5 Plots of the relationship of the calculated standard uncertainty on displacement magnitude versus peak ratio and calculated coefficients [96].

In the current experiment, although the synthetic data/error-free data is not available to determine the coefficients of Eq. (B1) but the peak ratio can be determined by the results of the PIV correlation for each interrogation window, which spans 32 x 32 pixels in the present experiment. Selected representative correlation peaks are shown in Figures B.6 and B.7 for the representative transverse and axial planes, respectively.

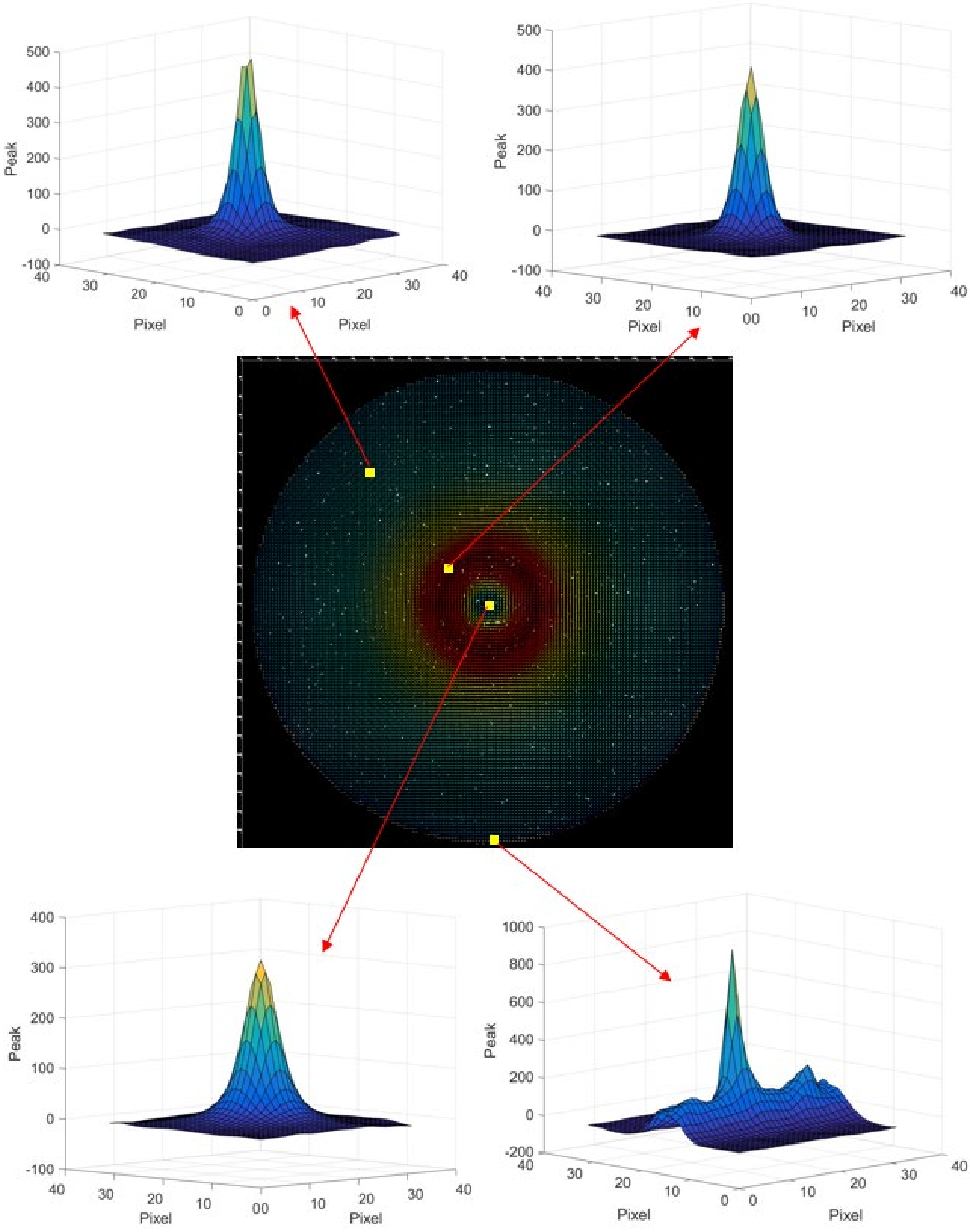

Figure B.6 Selected interrogation windows and associated correlation peak on the representative r-θ plane.

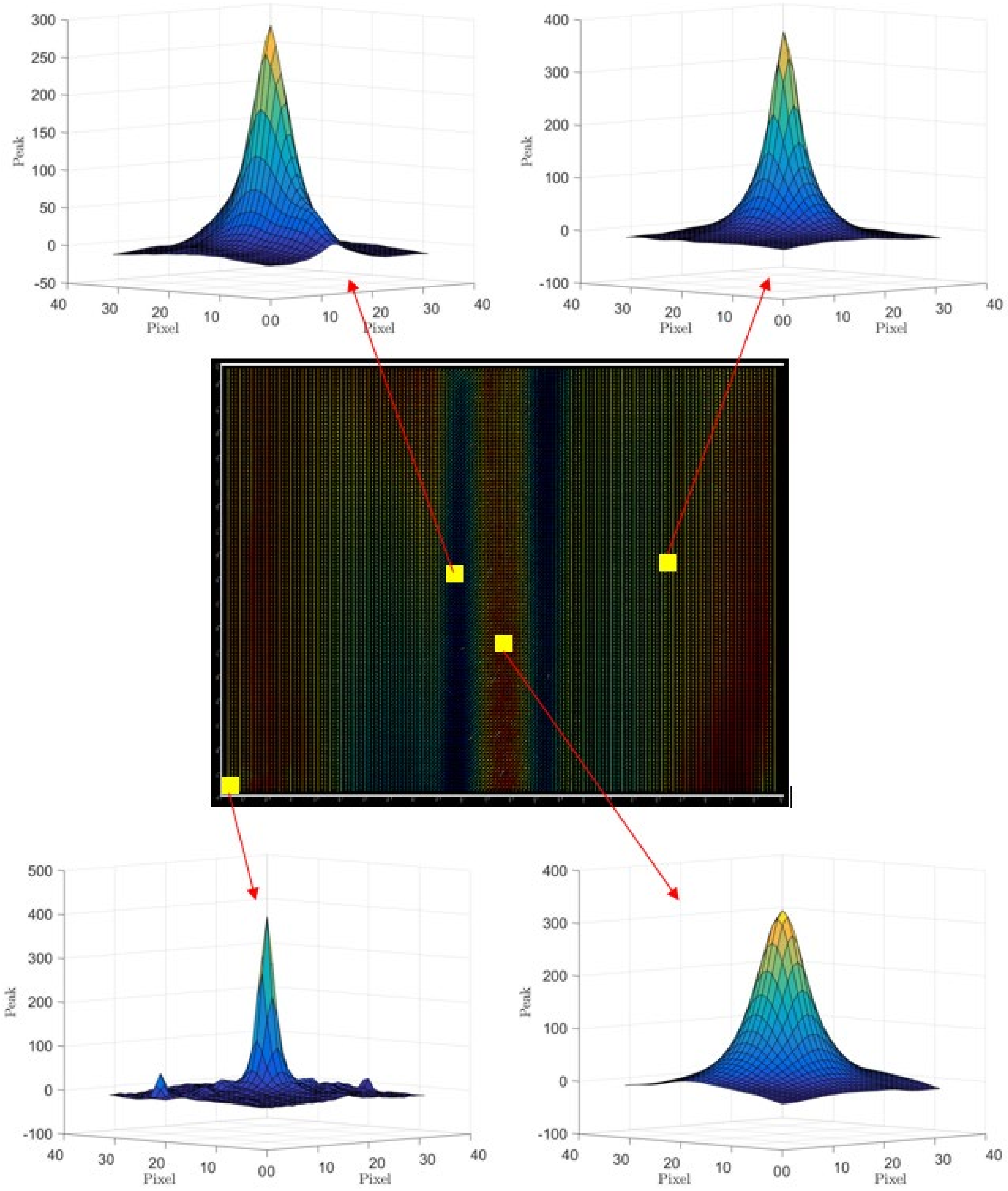

Figure B.7 Selected interrogation windows and associated correlation peak on the representative *r-z* plane.

It can be seen that in most cases a clear peak is observed. However, in the tangential plane, the correlation plane for the interrogation window on the periphery of the vortex chamber shows distributed secondary peaks. These are observed due to the circular masking that is applied while performing the cross-correlation in a square interrogation window. This is only observed on the periphery of the vortex chamber. Similarly, a distributed peak is observed in the centerline of the chamber for the *r-z* plane. This relatively reduced correlation peak is due to the recirculation and the unsteady flow features in the CRZ. However, the peak ratio, Q, remains above 100 for all the cases. Comparing the peak ratio to the data presented in Figures B.4 and B.5, it is concluded that the uncertainty remains below 3%.